Contributions to the statistical mechanics of ideal two and a half dimensional flows

Simon Thalabard




THÈSE

Présentée pour obtenir :

LE GRADE DE DOCTEUR EN SCIENCES DE L'UNIVERSITÉ PARIS-SUD XI

Spécialité : Physique

Ecole Doctorale de Physique de la Région Parisienne - ED 107

par

Simon THALABARD

Contributions to the statistical mechanics of ideal two-and-a-half dimensional flows

Soutenue le 28 octobre 2013 devant le jury composé de :

M.	Julien BARRÉ	Rapporteur
M.	Freddy BOUCHET	Invité
M.	Marc-Etienne BRACHET	Rapporteur
Mme.	Bérengère DUBRULLE	Directrice de thèse
M.	Frédéric MOISY	Examinateur
Mme.	Annick POUQUET	Invitée
M.	Bruce TURKINGTON	Rapporteur

Entendu le 29 Octobre 2013 :

“Tu as assisté à la thèse hier ? Celle avec la moitié d’une dimension manquante ? ”

“ Oui... Enfin, je vais être honnête : je n’ai pas vraiment écouté. Mais j’ai parcouru le manuscript. Tout du moins les remerciements.”

“Et alors ?”

“ Bah, je ne les ai pas lus en entier non plus, car il y en avait sur plusieurs pages. Ils étaient assez conventionnels. Un peu foutraques aussi. Débordant d’émotion of course. [ST] commencait par remercier sa directrice de thèse, Bérengère Dubrulle, dont l’enthousiasme avait su le revigorer plus d’une fois. Il remerciait Freddy Bouchet qui lui avait expliqué patiemment les subtilités de la physique statistique : au Nouveau Mexique d’abord, ensuite à Lyon. Il remerciait également Annick Pouquet, ainsi que Duane Rosenberg et Pablo Mininni, avec qui il avait travaillé dans le Colorado, et de qui il avait beaucoup appris. ”

“Et ensuite les membres de son jury, Julien Barré, Frédéric Moisy, Marc Brachet et Bruce Turkington ?”

“Oui. Il était désolé d’avoir troublé la fin de leur été, avec un manuscript de xxx pages. Mais sincèrement honoré qu’ils aient accepté de prendre le temps d’y porter attention, de le lire, de le rapporter.”

“...”

“S’ensuivait un remerciement exhaustif des membres du SPEC, et du SPHYNX. En particulier, Brice Saint-Michel, Cécile Wiertel-Gasquet, Hervé Bercegol, Marco Bonetti, Pablo Gutierrez, Sébastien Aumaître, Francois Daviaud, Francois Ladieu, Davide Farranda et leur bienveillance au cours de récentes répétitions de soutenance.”

“ ...”

“ Plus loin, il était question d’une histoire de vélos – avec un “s” – avec tout ce qu’ils évoquent de freins, dérailleurs, tubes désemmanchés, pédaliers en vrac, sprints dramatiques, barres mythiques de 45 minutes sur le Paris-Saclay, Tremblayries et autres Bièvreries. Je n’ai pas tout compris, c’était un peu confus. Mais il y avait sans ambiguité à cet endroit là des “special thanks” pour Vincent Padilla, Eric Herbert et Corentin Coulais – voire parfois une pointe de défi. ”

“ ...”

“Et puis (j’allais dire déjà) les remerciements se sont éparpillés. Comme dans une cérémonie des Oscars, la famille y est passée. Reum, Reup, Reums [2], Bros, Sis, Bros et al,

Sis et al, and so on. Il ne s'agissait pas là d ' un exercice de style."

"Et les amis ?"

" Ouaip. Itou. Avec un petit mot pour chacun. Si je me souviens bien, Baptiste, Christelle, Corentin, Claire, Damien, Florent, George, Guillaume, Hugo, Isaac, Jérôme and the Fleurus band, Jake, Jon, Keith, Marc, Mary, Marine, Mylène, Nico, Preden, Seb, Sen Seb, ... J'en oublie ... Tu y étais aussi. "

"Et Fanny ?"

" Et Fanny ! Qui ... A vrai dire, la phrase avait l'air croustillante mais je ne l'ai pas lue : elle ne me regardait pas. "

Abstract

The present manuscript deals with the statistical mechanics of some inviscid fluid models which are possibly relevant in the context of geophysics and astrophysics. We investigate the case of axially symmetric flows, two-dimensional Boussinesq flows, and two-dimensional magneto-hydro fluids. Those flows can be loosely referred to as two-dimensional flows with three components ("2D3C"). In addition to the two-dimensional velocity field, they describe the evolution of an additional field variable, which represents either a magnetic current, a salinity, a temperature or a swirl depending on the situation. In common with the dynamics of strictly two-dimensional hydrodynamical flows, the non-linear dynamics of 2D3C flows is constrained by the presence of an infinite number of Casimir invariants, which emerge as dynamical invariants in the limit of a vanishing forcing and a vanishing dissipation . In common with three-dimensional flows, the vorticity is not only mixed but also stretched by the dynamics. The additional field may act as a source or a sink of kinetic energy. It is commonly believed that such flows have the propensity to develop large scale coherent structures. Whether those long lived structures are equilibrium or metastable structures is however not so clear, nor are the exact conditions of their emergence. The role of the Casimir invariants in constraining those is not so obvious either.

In the first part of the manuscript, we try to clarify those questions, by investigating the equilibrium properties of 2D3C fluids, using statistical mechanics arguments both in Fourier and in physical space, theoretically when possible; numerically when needed.
A second part deals with the interpretation of "real" turbulence, as observed in laboratory Von Kármán experiments or in numerical simulations, using tools borrowed from statistical mechanics.

Keywords : Ideal flows, Statistical Mechanics, two-and-a-half Turbulence, Axi-symmetry, Magneto-fluids

Résumé court

Dans cette thèse, nous nous intéressons à la mécanique statistique d'une classe d' écoulements "quasi-bidimensionnels". Nous nous penchons plus particulièrement sur le cas des écoulements tri-dimensionnels axisymétriques, bidimensionnels stratifiés et bidimensionnels magnéto hydrodynamiques. La dynamique de ces écoulements est génériquement décrite par les équations d'évolution d'un champ de vitesses incompressible bidimensionnel, couplées à une équation d'évolution d'un champ scalaire. Ce dernier représente tantôt une température, tantôt un courant électrique, tantôt un mouvement tourbillonnaire transverse. Ces écoulements ont un intérêt géophysique ou astrophysique : ils peuvent être utilisés pour modéliser grossièrement les ouragans, les courants océaniques à l'échelle planétaire, les taches solaires, etc. Ils ont aussi un intérêt plus fondamental. Malgré leur géométrie bidimensionnelle intrinsèque, les écoulements "2D3C" peuvent être en effet tri-dimensionnellement connotés. Dans les cas que l'on regarde, la vorticité n'est pas seulement transportée : elle est aussi étirée. Il n'est ainsi pas évident de savoir si la tendance naturelle des écoulements 2D3C est de s'organiser en structures cohérentes énergétiques à grande échelle comme en deux dimensions, ou plutôt de répartir leur énergie sur les petites échelles comme en trois dimensions. Il n'est a priori pas clair non plus de savoir si une forme d'énergie (cinétique ou magnétique/tourbillonnaire) y est privilégiée aux dépends de l'autre.

Pour répondre à ces questions de manière très générale, nous étudions et décrivons la mécanique statistique d'équilibre des écoulements 2D3C sus-mentionnés, en nous plaçant d'abord dans le cadre des "ensembles d'équilibre absolu" considérés par Robert Kraichnan à la fin des années 1960, puis dans le cadre plus moderne des "mesures microcanoniques stationnaires" introduites par Raoul Robert, Jonathan Miller et Joël Sommeria pour les fluides bidimensionnels au début des années 1990. Les équilibres 2D3C sont décrits dans la première partie de ce manuscript.
La seconde partie du manuscript est plus pratique, et également plus spéculative. Nous nous servons d' outils de la mécanique statistique d'équilibre pour interpréter des données turbulentes expérimentales provenant d'expériences de type Von Kármán . Nous utilisons ensuite des résultats récents de théorie de probabilité pour montrer que des régimes de turbulence quasi-bidimensionnelle (turbulence tri-dimensionnelle avec rotation, turbulence dans des couches savonneuses) ont des propriétés d'invariance conforme statistique, analogues à celles observées dans des systèmes de spins ferromagnétiques au point critique.

Mots clés : Fluides idéaux, Mécanique Statistique, Turbulence quasi-bidimensionnelle, Axi-symétrie, fluides conducteurs.

Contents

Special notations

Some more or less standard notations may be found throughout the manuscript. Below is what they mean, provided no abuse is committed in the text.

Probabilities. Associated to a measurable space $(\Omega, \mathcal{A}, \mu)$ with Ω is the underlying space, $\mathcal{A}$ the σ-algebra of measurable sets, μ a probability measure, the following notations may be used.

- $\mathbf{1}_A$ or $\mathbf{1}_{x\in A}$ is the indicator function related to a measurable set A, that takes value 1 on A and 0 elsewhere. With a tiny abusive yet standard notation, if A is defined as something like $\{\omega \in \Omega : f(\omega)\}$ with f a prescribed boolean function defined over Ω, I will often write $\mathbf{1}_{f(\omega)}$ instead of $\mathbf{1}_{\{\omega\in\Omega: f(\omega)\}}$.
- An observable is a function $O : \Omega \to \mathbb{R}$.
- $\langle O\rangle_\mu$ is the average of the observable O with respect to the measure μ, so that formally $\langle O\rangle_\mu = \int_\Omega \mu(\mathrm{d}\omega)O(\omega)$. If the integrating measure is clearly stated in the text, it can be that I simply write $\langle O\rangle$ instead of $\langle O\rangle_\mu$.

Standard symbols.

- *i.f.f* : if and only if
- $(\hat{\mathbf{x}}, \hat{\mathbf{y}}, \hat{\mathbf{z}})$: the canonical base in $\mathbb{R}^3$.
- $(\hat{\mathbf{r}}, \hat{\boldsymbol{\theta}}, \hat{\mathbf{z}})$: the canonical base using cylindrical coordinates.
- $\mathcal{D}$,$\partial\mathcal{D}$: a domain in physical space and its frontier.
- $\int_\mathcal{D} \mathrm{d}\mathbf{r}$: domain integration.
- $\oint_{\partial\mathcal{D}} \mathbf{dS}\cdot$: Surface integration. $\mathbf{dS}$ is then unit vector surface element, whose direction is locally normal to $\partial\mathcal{D}$, and pointing outwards the domain $\mathcal{D}$.
- The determinant of a matrix M is denoted as $\det M$ or $|M|$, provided there is no confusion between $|M|$ and $|\det M|$.
- $\log$: logarithm, defined as the inverse of the exponential : $\log \circ \exp = Id$.
- $\sharp\mathcal{E}$: the number of elements in the finite ensemble $\mathcal{E}$.

Mathematical tools

- $\delta_{\mathbf{r}_0}$ denotes a delta function defined over a domain $\mathcal{D}$, so that $\int_{\mathcal{D}} \mathrm{d}\mathbf{r}\delta_{\mathbf{r}_0}(\mathbf{r})f(\mathbf{r}) = f(\mathbf{r}_0)$ for any test function $f : \mathcal{D} \to \mathbb{R}$.
- A functional $\mathcal{F}$ is a function whose arguments are functions, typically written as $\mathcal{F} = \mathcal{F}(\omega(\mathbf{r}))$ for $\omega : \mathcal{D} \to \mathbb{R}$ defined over a prescribed domain $\mathcal{D}$.
- For such a function $\mathcal{F}$, $\dfrac{\delta\mathcal{F}}{\delta\omega(\mathbf{r})}$ denotes the functional derivative $\mathcal{F}$, formally defined as $\dfrac{\delta\mathcal{F}}{\delta\omega(\mathbf{r})} = \lim\limits_{\epsilon\to 0} \dfrac{\mathcal{F}(\omega + \epsilon\delta_r) - \mathcal{F}(\omega)}{\epsilon}$.

Introduction

> Alors j'ai décidé, à mes riques et périls, de m'acheter une chose qui paraitrait puérile : une paire de jumelles, et je vous ai observés. Dieu que vous me paraissez aimables et cultivés !

[Tisserand and Reggiani, 1970]

2D3C flow in geophysics : The Venusian and the seagull. Observed from the binoculars of an inhabitant from Venus, the Earth's oceans and atmosphere may seem confined on the Earth's surface, resulting in motions being purely two-dimensional. A contemporary Venusian anthropologist with a working knowledge of English might corroborate this observation by finding out that many scientific papers published by Human Geophysicists over the last hundred (Venusian) days do indeed relate to a so-called "two-dimensional turbulence".
The two-dimensional (2D) incompressible Navier-Stokes equations describe the advection of the scalar vorticy field $\omega = \hat{\mathbf{z}} \cdot \nabla \times \mathbf{v}$ [(a)] by the incompressible two-component velocity field $\mathbf{v}$, subject to a forcing F and a dissipation D :

$$\partial_t \omega + \mathbf{v} \cdot \nabla \omega = F + D, \quad \text{with} \quad \mathbf{v} = -\nabla \times \Big((\nabla^{-2} \omega) \hat{\mathbf{z}} \Big). \tag{1}$$

Human (Geo)physicists are no earth-flatters. But they have recognized for long that the two-dimensional incompressible Navier-Stokes equations had some relevance to describe atmospheric or oceanic planetary motions. In a 1953 paper for example, the Danish geophysicist Ragnar Fjørtofft considered the 2D Navier-Stokes equation on the surface of a sphere. Due the presence of two "conservation theorems" in the limit of vanishing forcing and dissipation, one regarding the kinetic energy, and the other one regarding the square of the vorticity, Fjørtofft argued that most of the kinetic energy in 2D needed to be transferred to the large scales of the problem [Fjørtoft, 1953]. The observation was later made more quantitative by Robert H. Kraichan, who argued about the existence of a dual cascade process [Kraichnan, 1967] in forced 2D turbulence. In Kraichnan's scenario, there exists an inverse cascade of energy yielding a $k^{-5/3}$ spectrum for scales larger than the injection scales. There also exists a direct cascade of total vorticity squared, which yields a k^{-3} energy spectrum for scales smaller than the injection scales. The relevance of 2D turbulence to understand large scale ($\gtrsim 1000$ km) and mesoscale ($\lesssim 500$ km) respective -3 and $-5/3$ law behaviors of the horizontal spectra of tropospheric wind spectra was

[(a)] $\hat{\mathbf{z}}$ denotes a vector perpendicular to the 2D plane on which the motion is confined.

initially discussed by Gage [Gage, 1979] and further explored by Lilly [Lilly, 1983, Lindborg, 1999]. Whether 2D turbulence allows a complete and unambiguous interpretation of atmopheric spectra is a subtle question and is still controversial [Herring, 1999, Lindborg, 1999]. But the essential reasons why 2D turbulence is thought to have some relevance to describe large scale motions in the oceans and in the atmosphere are (i) the intrinsic geometry of the domains (the height of the troposphere is at most of the order of 10 km; the depths of the oceans are also at most 10 km, which is very small compared to their horizontal extent of several thousand kilometers) but also (ii) the presence of strong sources of stratification such as temperature gradients, gravity forces, and rotation. In presence of strong stratification, a theorem called the Taylor-Proudman theorem tells that the pressure gradients parallel to the direction of the stratification are essentially vanishing, therefore confining the motions onto planes perpendicular to the direction of stratification. The picture is quite crude, but may account for the stratification of the largest scales of the motion. The theorem can be refined to account for smaller scales and finite Reynolds or Rossby number effects [Julien et al., 1998].

(a)

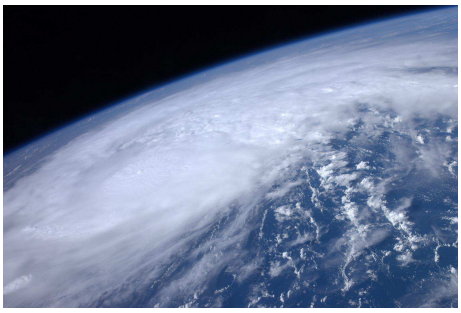

(b)

Figure 1: (a) The Great Red Spot of Jupiter from Voyager 1 in 1979 and (b) Hurricane Irene from the International Space Station in 2011 [nasa.gov, 2013]

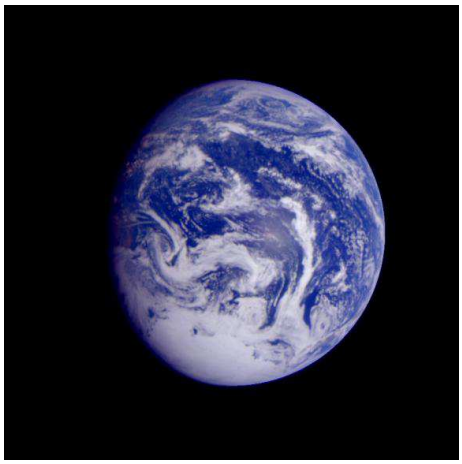

(a)

(b)

Figure 2: (a) Earth from the NASA Galileo Spacecraft satellite [nasa.gov, 2013]. (b) Earth from a seagull perspective, shot by Alessandro di Benedetto during Vendée-Globe 2012-2013.

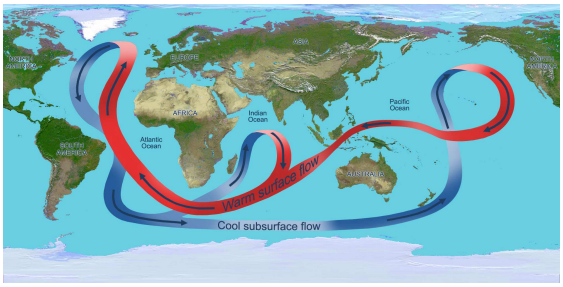

(a)

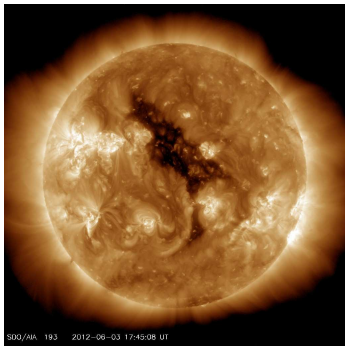

(b)

Figure 3: (a) The thermohaline circulation [nasa.gov, 2013] (b) the solar corona shot with X-ray telescopes in June 2012 [nasa.gov, 2013].

Many geophysical and astrophysical toy models involve a flat two-dimensional space. The two-dimensional turbulent Navier-Stokes equations can be taken as a minimalistic model of planetary atmospheres, and may be used to explain why large-scale, long-lived, swirling and stormy patterns naturally emerge in those [Sommeria, 2001], be it on Jupiter or on Earth – see Figure 1. In other models, interesting physics may come from the interplay between the kinetic vorticity field and additional scalar fields. From the point of view of a seagull (Figure 2), the height of the oceans, however small compared to the extent of the oceans, may be a relevant scalar field to consider. Such a consideration might yield the "Saint-Venant" or "Shallow-Water" equations. To obtain insights about the global thermohaline oceanic circulation – see Figure 3a –, one may want to include an interplay between the kinetic field and the salinity of water or its temperature, hereby obtaining a "Boussinesq model of the zonally averaged thermohaline circulation" [Dijkstra and Molemaker, 1997, Fleury, 2006], or more simply two-dimensional baroclinic Boussinesq flows. To describe geo and astrophysical dynamos (Figure 3b), the inclusion of a magnetic field or of an electric current is necessary, in which case one deals with magneto-hydrodynamical equations [Zeldovich, 1957, Spiegel and Zahn, 1992].

"The number of fields needed to describe the complete situation will depend on how complicated the problem is", tells Richard Feynman in [Feynman et al., 1964]. Current Global Circulation Models such as NASA's "model E" take into account not less than nineteen additional fields [(a)], describing the role of clouds, radiation, moisture, Arctic ice, and so on. Were we to include those effects, we could wind up with a model of a "2D flow with N components", which we could casually refer to as a "2DNC" flow. But this is not our intention. We will modestly focus on purely hydrodynamical "2D2C" flows, and "2D3C" flows : two-dimensional hydrodynamical flows supplemented by an additional scalar field. In the latter situation, the interplay between the kinetic and the additional field is by no mean generically prescribed. Interesting physics may emerge when the additional field (the height, the salinity, or the electric current) is not simply advected by the kinetic field , but also provides a mechanism to enhance or deplete the kinetic field. In such cases, the additional field acts as an "active scalar".

[(a)] http://www.giss.nasa.gov/tools/modelE/modelE.html

2D3C flows from symmetry considerations. At a more fundamental level, 2D3C flows naturally emerge as continuously symmetric solutions of the three-dimensional Navier-Stokes equations in a prescribed domain $\mathcal{D}$.

$$\partial_t \mathbf{v} + \mathbf{v} \cdot \nabla \mathbf{v} = -\nabla p + \mathbf{F} + \mathbf{D}, \qquad \nabla \cdot \mathbf{v} = 0. \tag{2}$$

A natural symmetry to consider is translational symmetry along a prescribed direction. Using Cartesian coordinates (x, y, z) and a domain periodic along the "z" direction, we may choose to consider a z-independent forcing term $\mathbf{F} = (\mathbf{F}_\perp(x, y), F_z(x, y))$ combined with a z-independent initial condition $\mathbf{v} = (\mathbf{v}_\perp(x, y), v_z(x, y))$. In such a case, the equations governing the evolution of the velocity fields describe a 2D3C flow. The evolution of the "perpendicular" velocity field $\mathbf{v}_\perp = (v_x, v_y)$ is described by the two-dimensional Navier-Stokes equations confined onto the perpendicular plane (x, y). The z or " parallel " component of the velocity is then simply advected by the perpendicular velocity field – in addition to being possibly forced and dissipated.

More interesting is the situation of axi-symmetry, which may be imposed in the case of a cylindrical domain $\mathcal{D}$, described with cylindrical coordinates (r, θ, z). Axisymmetric flows are obtained by considering an initial condition and a forcing term independent of the azimuthal coordinate θ. The analogue of the parallel/perpendicular decomposition is a poloidal/toroidal decomposition. The poloidal velocity field is a two-component velocity field $\mathbf{v}_{\text{pol}} = (v_r(r, z), v_z(r, z))$, whose evolution is confined onto a meridional plane. The toroidal velocity field is the scalar field $v_\theta(r, z)$. Unlike the parallel velocity field in the translational-symmetric case, the toroidal velocity field is an active scalar, whose feedback on the the poloidal field is closely analogous to the feedback of the salinity or the temperature on the kinetic field in 2D Boussinesq flows.

More subtle symmetries can also be imposed, an example of which is the so-called "helical symmetry" considered in [Mahalov et al., 1990]. The helical symmetry requires an infinitely long or a z periodic cylindrical domain. The symmetry is obtained by (i) switching from cylindrical to helical coordinates $(r, \theta, z) \to (r, \xi, \eta)$, through $\xi = n\theta + \alpha z$ and $\eta = n\theta - \alpha z$ with n a non vanishing integer and α a real number (ii) considering velocity fields independent of either ξ or η. Doing so, helical flows are obtained. They are described by three components of the velocities but only two coordinates, r and ξ or r and η. They therefore also provide examples of 2D3C flows.

Are symmetric flows interesting to consider ? It is a matter of taste. As surprising as it may seem though, there is an abundant literature about axisymmetric solutions of the Navier-Stokes equations [(a)]. One could think that the interest for the axi-symmetry is historical : Theodore Von Kármán 's 1929 axisymmetric stationary solutions for the problem of a viscous flow over an infinite rotating disk triggered many contributions throughout the twentieth century – see [Zandbergen and Dijkstra, 1987] and references therein. One

[(a)] At the time of redaction of this introduction, an informal query on Scholar Google yielded 59,300 results for "MHD turbulence", 93,600 for "axisymmetric turbulence", 129 000 for isotropic turbulence and 1,030,000 for "two-dimensional turbulence".

could think that the interest for the axi-symmetry is geophysical : axisymmetric flows have been considered by Douglas Lilly as toy models of tornadoes [Lilly, 1969]. However, the main reason why axi-symmetry has been widely considered in the literature is more probably due to industrial jets. Spacecraft nozzles, plane turbines, fire hoses, garden hoses are as many devices for which a cylindrical geometry prevails. Axi-symmetry may serve as a zero-level approximation to gain insights about the flows generated within those devices. Besides, it has been well-known that axisymmetric flows give rise to the phenomenon of "vortex breakdown" [Hall, 1972], which describes an abrupt geometric change in the topology of – non necessarily turbulent – axisymmetric flows far from their sources. The issue has focused the attention of many people, as it "emerged as a serious problem at high angle of attack for highly manoeuvrable military aircraft" [Brown and Lopez, 1990].

Ideal 2D3C flows and "two-and-a-half turbulence" Since 2D3C flows live in a two-dimensional space, it may be natural to wonder whether the properties of such flows are close to strictly two-dimensional hydrodynamical flows. The answer is certainly not generic, as it depends on the kind of feedback which the advected scalar exerts on the advecting field. If the scalar is passive, as it is the case for translational -symmetric solutions of the Navier-Stokes equations, the perpendicular/kinetic advecting field is fundamentally not different from a strictly two-dimensional hydrodynamical field. The presence of an active scalar may however seriously alter the behavior of the two-dimensional (kinetic) fluid as well as the long time evolution of the kinetic energy. This altering is visible at the level of the cascades for forced dissipated turbulent flows. In numerical simulations of forced two-dimensional magneto hydro turbulence for example, an inverse cascade of magnetic potential squared has frequently been observed [Pouquet, 1978, Biskamp and Bremer, 1994], which could be thought of as being analogous to Kraichnan's inverse cascade of energy in two-dimensional hydro turbulence . However, the systematic emergence of such a cascade is not so clearly established [Biskamp and Bremer, 1994], nor are the directions of possible energy cascades. The possibility of a direct or inverse transfer of energy, depending on the nature of the forcing has been suggested [Kim and Dubrulle, 2002].

The differences between 2D and 2D3C fluids are also revealed by switching from the world of real fluids to the world of ideal fluids.

Ideal fluids, – Feynman's "dry water" – are fluids that are subject neither to forcing nor to dissipation. Their dynamics is governed by the Euler equations, which are formally obtained from the Navier-Stokes equations by crudely setting the forcing and the dissipation term to zero. The dynamics of ideal fluids – or at least of "sufficiently regular" ideal fluids – is constrained by the presence of infinitely many invariants of motion : the total energy and the Casimir invariants. The Casimir invariants are well known in the two-dimensional hydrodynamical situation : in 2D, any power of the vorticity integrated over the domain is a constant of motion. This prescribes in particular that the total vorticity remains bounded throughout time. Just like the two-dimensional hydrodynamical flows, ideal 2D3C dynamics is constrained by the presence of infinitely many Casimir

invariants. Yet, those invariants may less severely constrain the dynamics. In particular, for axisymmetric, Boussinesq and MHD flows, no obvious Casimir constraint exists that would bound the vorticity field. This feature gives 2D3C flows a very three-dimensional flavor.

The absence of a vorticity bound is likely to have some dramatic consequences for the regularity and for the long-time existence of 2D3C ideal flows. A series of numerical work at the beginning of the nineties gave strong hints that initially smooth ideal axisymmetric and two-dimensional Boussinesq flows tend to develop finite time singularities, even when the initial poloidal/vorticity field is vanishing [Grauer and Sideris, 1991,Pumir and Siggia, 1992a,Pumir and Siggia, 1992b,Caflisch, 1993,Grauer and Sideris, 1995]. Similar conclusions have been reached from the simulations of slightly decaying two-dimensional MHD flows [Pouquet, 1978, Orszag and Tang, 1979]. Despite today's petascale numerical possibilities, the conditions under which the three-dimensional Euler equations may or may not develop finite time singularities are still a matter of scientific debate [Gibbon, 2008]. However, the possible existence of a singularity for the ideal axisymmetric and the ideal two-dimensional magneto-hydro equations shows that in spite of their obvious "2Dness", 2D3C flows may also carry with them an intrinsic "3Dness". They are likely to describe a "two-and-a-half" turbulence [Orszag and Tang, 1979], whose properties are in between 2D and 3D turbulence. As such, those flows are worth of interest.

Questions that we may wish to answer are the following : do the invariants generically prescribe a direction for the energy transfers ? Should we expect the energy to pile up at large scales, or spread out over the smallest scales ? In any case, does the dynamics favor a form of energy at the expense of the other ? Those questions can be addressed from the angle of statistical mechanics.

Statistical mechanics and ideal flows Understanding turbulence through the prism of statistical physics and Boltzmann's counting is an ancient idea, that can be attributed to Theodore Von Kármán or Jan Burgers [Martinus et al., 1995]. The difficulties of the approach were soon identified. In 1929, Burgers writes [Burgers, 1929] :

> "[...] the hydrodynamical case presents the difficulty that the system is not a conservative one.[...] A second difficulty is that it is not immediately clear what elementary processes or types of motion can be used as objects to be counted in order to arrive at a definition of the probability of a given type of flow".

The first difficulty can be crudely bypassed by focusing on ideal flows. In the case of 2D turbulence, Lars Onsager [Onsager, 1949, Eyink and Sreenivasan, 2006], had understood that trends about the large-scale long-time organization of two-dimensional turbulence could be obtained from ideal models. But the second difficulty remains. Boltzmann's kinetic theory is designed to account for the statistical behavior of large but finite assemblies of molecules, while the degrees of freedom of an ideal fluid span a continuous

range and are therefore infinitely many. In a 1955 paper, the Swedish geophysicist Pierre Welander acknowledges [Welander, 1955]:

> "It seems to be a general impression that no decisive advancement can be made along this line until the mathematical apparatus of statistical mechanics has been improved, so that it can effectively tackle continuous systems also."

Quite remarkably, Welander depicts in the same paper the gist of the modern developments regarding the statistical mechanics of ideal flows. He illustrates the relevance of the concepts of "coarse-grained" and "fine-grained" observables as regards to fluids, by monitoring the numerical evolution of small patches of fluid colored in black and white embedded within an atmospheric quasi-2D flow.

Idealized ideal flows, Onsager's theory. One way to circumvent the continuum difficulty is to approximate the dynamics of ideal fluids by a well-chosen finite dimensional dynamics, for which "standard" statistical mechanics can be used to yield at least some qualitative trends. This is the idea followed by Onsager in [Onsager, 1949]. Onsager considers the description of a two-dimensional fluid in terms of N "very playful" Kirchhoff's vortices of strengths $\kappa_1, ...\kappa_N$ obeying a Hamiltonian dynamics :

> "They were enclosed by a boundary but could play ring-around-the-rosy otherwise. The rule of that game was $\kappa_i \dfrac{\mathrm{d}x_i}{\mathrm{d}t} = \dfrac{\partial W}{\partial y_i}; \kappa_i \dfrac{\mathrm{d}y_i}{\mathrm{d}t} = -\dfrac{\partial W}{\partial x_i}$.[...] The function W is something like this : $W = -\dfrac{1}{2\pi} \sum_{i,j} \kappa_i \kappa_j \log(r_{ij})$+(potential of image forces) and the image forces are finite except near the boundary",

informally described Onsager , in a 1945 note to Linus Pauling [Eyink and Sreenivasan, 2006].

In the context of turbulence this further "idealization of the two-dimensional ideal fluid" [Aref, 2007] allows to interpret large scale coherent structures in the light of a mutual pairing between the strongest vortices. Typical configurations of vortices in which some vortices are "paired" are more energetic than typical configurations of randomly distributed vortices. As such, they describe a negative temperature microcanonical state. More quantitatively, the description of turbulence through a Boltzmann-Gibbs statistics of point vortices has led to the celebrated Joyce-Montgomery "$\sinh$-Poisson" law between the vorticity and the stream function [Joyce and Montgomery, 1973, Montgomery and Joyce, 1974, Eyink and Spohn, 1993], which was observed in decaying numerical simulations of two-dimensional turbulence [Montgomery et al., 1992].

Point- vortices may provide some insights about two-dimensional turbulence, but are heavily anchored in Flatland. Some models of point vortices have been studied that include an interaction with a background flow [Nazarenko and Zakharov, 1992]. However, since the vorticity of the flow is in a sense frozen within each point-vortex, it is not very clear whether adequate point-vortices could be used to describe systems in which the vorticity is likely to be stretched. A "blob model" of the shallow water equations has been proposed in [Salmon, 1983], and is reminiscent of the point-vortex spirit. Subtle

quasi-2D filament-vortex models have also been proposed, whose properties bear some intriguing analogies both with 3D turbulence and polymer physics [Chorin, 1993].

Kraichnan's theory. Kraichnan's derivation of two-dimensional "absolute equilibria" is similar to the point-vortex theory in the sense that its starting point is an approximation of the ideal equations [Kraichnan, 1967]. In Kraichnan's approach, the approximation is not carried out in physical space but in Fourier space, by the means of a spectral, low-band filtering truncation. The filtering yields a set of truncated equations, describing the evolution of a finite number of modes. The truncated equations generically preserve the quadratic invariants, which are termed "rugged" invariants. Statistical absolute equilibria are then obtained by considering grand canonical Gibbs ensembles in Fourier space, with one inverse temperature for each quantity identified as a rugged invariant.

Absolute equilibria provide a ready-to-use statistical theory that have been studied widely beyond the scope of two-dimensional turbulence. One reason for this is that many Direct Numerical Situations (DNS) of Turbulence rely on the use of Galerkin spectral truncations, which are precisely the truncations for which Kraichnan's theory is tailored. A second reason is that for forty years, absolute equilibria have proven extremely valuable in indicating the existence and the direction of many rugged invariants cascades, among them the inverse cascade of magnetic potential in 2D MHD [Pouquet, 1978], inverse magnetic helicity cascades in 3D MHD [Frisch et al., 1975, Alexakis et al., 2006], and so on. A third reason is their simple, almost trivial derivation. Crudely put, it suffices to know how to compute Gaussian integrals to derive the desired set of absolute equilibria. The trivial derivation has however a cost : (i) absolute equilibria artificially single out the rugged invariants, and say nothing about the role of the un-rugged ones in constraining the –untruncated– dynamics. Therefore, by essence, absolute equilibria can only give partial insights about the class of equilibria relevant for untruncated ideal flows. (ii) the canonical description that they provide for finite dimensional systems is likely to break down in the limit of an infinite number of modes. This is the case when a condensation regime emerges. (iii) When more than three invariants are involved in the theory, the absolute equilibria regimes may be quite challenging to decipher [Fyfe and Montgomery, 1976, Montgomery and Turner, 1982].

The Robert-Miller-Sommeria theory. The modern way of using statistical mechanics to describe continuous fluids is provided using "invariant Young measures". The description was introduced very mathematically by Raoul Robert and Joel Sommeria [Robert and Sommeria, 1991] and more pedagogically by Jonathan Miller in the beginning of the 1990's [Miller, 1990]. Subsequent work from then [Michel and Robert, 1994, Ellis et al., 2000, Boucher et al., 2000] has revealed that the Robert-Miller-Sommeria theory does indeed provide the "mathematical apparatus" insighted by Welander. In the Robert-Miller-Sommeria approach, one works directly at the level of the ideal equations, cutting through the steps of defining finite-dimensional dynamics [Bouchet and Corvellec, 2010]. In 2D, Kraichnan's and Onsager's theories emerge as particular cases of the Robert-Miller-Sommeria theory [Miller et al., 1992]. Many attempts have been made to widen the scope of the Robert-Miller-Sommeria theory, beyond the two-dimensional hydrody-

namical case. It has for example been used successfully to describe quasi-geostrophic flows: two-dimensional flows including a "β-effect" and a topography – see [Bouchet and Venaille, 2011] and references therein. Descriptions of equilibria relevant to 2D3C flows have also been made : bi-dimensional MHD equilibria under some simplifying assumptions [Jordan and Turkington, 1997,Weichman, 2012], shallow-water equations [Weichman and Petrich, 2001], and non-swirling axisymmetric flows [Mohseni, 2001]. The generalization is however not straightforward, and technical difficulties are often encountered, which require the use of simplifying assumptions be it a separation of scale hypothesis, a nontrivial change of coordinates or the use of subtle counting theorems.

The Robert-Miller-Sommeria theory has also given rise to an alternative, systematic use of maximum entropy principle derivation of the equilibria of a wide variety of quasi-2D flows, in which an entropy is maximized, which plays both roles of a "Jaynes -like" information-theory coarse-grained entropy and an Arnold function. The approach is extremely fruitful in making a link between stationary equilibria of fluid models and statistical mechanics. It provides a practical use of the maximum entropy principle, and has been used to describe some equilibria related to two-dimensional flows with and without topography, shallow-water flows [Chavanis and Sommeria, 2000, Chavanis, 2005, Majda and Wang, 2006], axisymmetric flows [Leprovost et al., 2006, Naso et al., 2010a]. Such theories are closely related to the Robert-Miller-Sommeria theory but may however fail to give a clear and thorough account of the equilibria, in the case where the vorticity is not bounded, as is precisely the case here.

Comment. The theories described in the previous paragraph all bring a solution to Burger's second difficulty of defining the "probability of a given type of flow" : Onsager counts some vortices, Kraichnan some wave numbers, Robert, Miller and Sommeria some locally defined quantities. However, they fail to bring an answer to Burger's first objection of the statical mechanics of a [forced-dissipated] hydrodynamical field. Whether and how ideal invariants do constrain the dynamics of turbulent, forced and dissipated fluids is a difficult question, which requires fine investigations about the connections between the solutions of the Navier-Stokes equations and the solutions of the Euler equations. In the strictly two-dimensional "2D2C" case, however some very specific mathematical results do continuously link (weak) solutions of the Navier-Stokes to ideal solutions of the Euler equations. It is the case for example when a stochastic forcing is imposed [Kuksin, 2007], or doubly-periodic or non standard Boundary conditions are imposed [Bellout et al., 2009]. A thorough description would require to open a Pandora's box. However, in 2D, under specific conditions, one may hope that the statistical solutions obtained through the Robert-Miller-Sommeria theory can both provide long time solutions for the ideal equations and be reasonably "close" to Navier-Stokes long time solutions [Robert, 2004]. I am not aware of the existence of such mathematical results for 2D3C flows in their full extent. Such fine mathematical results won't concern us in the present work. Therefore, most of the theoretical work will rely on formal computations and analogies.

Aims of the present manuscript. The present manuscript aims at exploring general trends regarding 2D3C flows, and in particular about axisymmetric flows, bi-dimensional Boussinesq flows and bi-dimensional magneto hydrodynamical flows. At a formal level, we will revisit and/or extend Kraichnan and Miller's theory to those flows. We will wonder whether there is any chance that a 2D3C equilibrium statistical mechanics may account for some of the large scale physics observed in quasi 2D3C real flows. The underlying geophysical questions are modest and can be summarized as : " What kind of energy ?", "What Scale/Organization ?", "So What ?". The first two questions will be tackled in the course of the manuscript. The third one will be further commented on in the final discussion.

Layout of the manuscript. The chapters of the present manuscript are divided into two main parts.

In the first part of the manuscript, we investigate the equilibrium properties of 2D3C fluids in the light of ideal statistical theories, both in Fourier and in physical space, theoretically when possible; numerically when needed.

In Chapter 1, the equations describing the dynamics of ideal axisymmetric flows, Boussinesq flows and two-dimensional magneto fluids are recalled. Their ideal invariants are described.

Chapter 2 is devoted to the theorem of Liouville. I present a formal straightforward generalization of the theorem for the dynamics of a field, which may be of relevance for the statistical mechanics of ideal flows, at least at a physicist level. This chapter stems from discussions with Freddy Bouchet, Oleg Zaboronski and Philip J. Morrison about whether the theorem of Liouville is or is not a generic feature of truncated and untruncated fluid models.

Chapter 3 is a reminder of the theory of absolute equilibria, as derived for 2D flows and 2D MHD flows. I show that for axisymmetric flows, absolute equilibria are not very insightful.

In Chapter 4, we build a microcanonical measure for the axisymmetric Euler equations using a construction *à la* Miller. The construction is original. As opposed to Kraichnan's theory, it gives non trivial insights about axisymmetric flow –and two-dimensional Boussinesq flows. The chapter stems from a collaboration with Freddy Bouchet and Bérengère Dubrulle. It has given rise to a paper, that was submitted to *Journal of Statistical Mechanics* in June 2013.

In Chapter 5, I use a Monte-Carlo microcanonical algorithm, the "Creutz Algorithm" to give a numerical illustration of the axisymmetric microcanonical equilibria derived in Chapter 4. I use the algorithm to illustrate qualitative considerations about the microcanonical equilibria of a lattice model, referred to as a "MHD Ising Model".

The model is possibly relevant to describe different classes of inviscid equilibria for bi-dimensional magneto-fluids.

The second part of the manuscript is more practical. It is also more speculative.

In Chapter 6, we look at data obtained from a highly turbulent Von Kármán experiment using the prism of two axisymmetric inviscid theories : one is a mixing theory derived from a maximum entropy principle, originally derived by Nicolas Leprovost [Leprovost et al., 2006] during his PhD at the former-GIT-now-SPHYNX laboratory. The other is a quenched avatar or of the microcanonical theory described in Chapter 4. Strictly speaking, neither theories describe axisymmetric equilibria. Yet, both theories give insights about the experiment.

In Chapter 7, I mention the existence of a possible analogy between rotating turbulence and quasi-2D turbulence on the one hand, and ferromagnetic models at critical temperature on the other hand. The analogy is heuristic. It relies on two articles accounting for the observation of a potential hints of conformal invariance in quasi-2D numerical and experimental data. Those two papers were obtained through a collaboration with Annick Pouquet's Turbulence Numerics Team at the National Center for Atmospheric Research, in Boulder, Colorado.

At the end of Chapter 7, I give a general conclusion to the manuscript.

Chapter 1

Equations for ideal two-dimensional flows with two and three components

In this technical chapter, the equations governing the dynamics of ideal axisymmetric flows, MHD flows and Boussinesq flows are recalled, and derived from their three-dimensional counterparts using elementary symmetric considerations. The Casimir invariants of the 2D3C flows listed. The whole chapter is summarized in Table 1.1.

Contents

1.1 Hydrodynamical flows with symmetries

To derive the equations for ideal 2D and axisymmetric flows, one may start from the incompressible three dimensional Euler equations for the velocity field inside a domain $\mathcal{D}$.

$$\partial_t \mathbf{v} + \mathbf{v} \cdot \nabla \mathbf{v} = -\nabla P \quad \text{and} \quad \nabla \cdot \mathbf{v} = 0. \tag{1.1}$$

They need to be supplemented by boundary conditions, such as periodic boundary conditions, or an impermeability condition at the walls if the domain is finite. They imply the following evolution for the (incompressible) vorticity field $\boldsymbol{\omega} = \nabla \times \mathbf{v}$:

$$\partial_t \boldsymbol{\omega} = \nabla \times (\mathbf{v} \times \boldsymbol{\omega}) = \boldsymbol{\omega} \cdot \nabla \mathbf{v} - \mathbf{v} \cdot \nabla \boldsymbol{\omega}. \tag{1.2}$$

1.1.1 Translational invariant flows

Derivation. We consider a domain $\mathcal{D}$, infinite or doubly periodic in the z-direction, and use cartesian coordinates (x,y,z) to describe the flow. Translational invariant flows are obtained by considering solutions of the form $\mathbf{v} = (v_x(x,y), v_y(x,y), v_z(x,y)) = (\mathbf{v}_\perp(x,y), v_z(x,y))$, which are independent on the z coordinate. Their evolution is then obtained by setting $\partial_z \equiv 0$ in the set of equations (1.1). Writing $\nabla_\perp = (\partial_x, \partial_y)$:

$$\begin{aligned} &\partial_t \mathbf{v}_\perp + \mathbf{v}_\perp \cdot \nabla_\perp \mathbf{v}_\perp = -\nabla_\perp P \quad \text{and} \quad \partial_t \mathbf{v}_z + \mathbf{v}_\perp \cdot \nabla_\perp \mathbf{v}_z = 0, \\ &\nabla_\perp \cdot \mathbf{v}_\perp = 0. \end{aligned} \tag{1.3}$$

Stream function formulation. Those equations have a stream function formulation. Since $\nabla_\perp \cdot \mathbf{v}_\perp = 0$, there exists a stream function ψ such that $\mathbf{v} = -\nabla \times (\psi \hat{\mathbf{z}})$; *e.g* such that $v_x = -\partial_y \psi$ and $v_y = \partial_x \psi$. It follows that (i) the z-component of the vorticity field satisfies : $\omega_z = -\nabla_\perp^2 \psi$ and (ii) the advection of a scalar field can be written in terms of inner-brackets : $\mathbf{v}_\perp \cdot \nabla . = [\psi, .]$, with $[f,g] = \partial_x f \partial_y g - \partial_x g \partial_y f$.

By taking the rotational of the perpendicular evolution equation, or alternatively by setting the z-derivatives to zero in the evolution equation of the z-component of the vorticity equation (1.2), one obtains the evolution of ω_z :

$$\partial_t \omega_z = -\mathbf{v}_\perp \cdot \nabla \omega_z = -[\psi, \omega_z]. \tag{1.4}$$

There exists a one-to-one relation between (ω_z, ψ) and the two-components of the perpendicular velocity field. The system of equations (1.3) is therefore equivalent to the system :

$$\begin{aligned} &\partial_t \omega_z + [\psi, \omega_z] = 0 \quad \text{and} \quad \partial_t v_z + [\psi, v_z] = 0, \\ &\quad \text{with} \quad \omega_z = -\Delta_{2D} \psi. \end{aligned} \tag{1.5}$$

Δ_{2D} is the two-dimensional Laplacian : $\Delta_{2D} = \partial_{xx}^2 + \partial_{yy}^2$. One observes that $\mathbf{v}_z$ does not exert any kind of retro-action on the perpendicular evolution equation. It is a passive scalar.

1.1.2 2D flows

2D ideal flows are obtained from translational invariant solutions of the 3D-Euler equations : they describe the evolution equation of the perpendicular velocity field, confined on a perpendicular plane (x,y), as given by the first line of the system of equations (1.6).

$$\partial_t \mathbf{v}_\perp + \mathbf{v}_\perp \cdot \nabla_\perp \mathbf{v}_\perp = -\nabla_\perp P \quad \text{and} \quad \nabla_\perp \cdot \mathbf{v}_\perp = 0. \tag{1.6}$$

Alternatively, they can be described with the stream function formalism of equation (1.5) :

$$\partial_t \omega_z + [\psi, \omega_z] = 0 \quad \text{with} \quad \omega_z = -\Delta_{2D} \psi. \tag{1.7}$$

Since there is no 3D-dimensionality left in those equations, we will usually let aside the "$\perp$", "$2D$", and "z" subscripts.

1.1.3 Axisymmetric flows

Geometry. Equations for ideal axisymmetric flows are obtained along the same line, except that they require the slightly more cumbersome use of differential operators within cylindrical coordinates (r, θ, z). Let us suppose that $\mathcal{D}$ is a domain with a cylindrical geometry, for example a domain delimited by two cylindrical walls, at minimal distances R_{in} and R_{out} from the axial symmetry axis. It is convenient – but not mandatory – to suppose that R_{in} is non-vanishing. It may turn convenient to suppose that the domain has an infinite vertical extent, or that it is periodic along the z (axial) direction, but one can also wish to work with horizontal top and bottom walls, and prescribe an impermeability condition for the velocity field.

Poloidal/toroidal. We consider an axisymmetric solution of the Euler equations : $\mathbf{v} = (v_r(r,\theta), v_\theta(r,\theta), v_z(r,\theta))$. The vorticity of such a solution reads

$$\boldsymbol{\omega} = -\partial_z v_\theta \hat{\mathbf{r}} + (\partial_z v_r - \partial_r v_z)\hat{\boldsymbol{\theta}} + \frac{1}{r}\partial_r(r v_\theta)\hat{\mathbf{z}}. \tag{1.8}$$

A standard description of the velocity field involves the two-component *poloidal* velocity field $\mathbf{v}_{\rm pol} = (v_r, v_z)$ and the scalar *toroidal* velocity field : v_θ. With axi-symmetry, the incompressibility condition only involves the poloidal velocity field :

$$0 = \nabla \cdot \mathbf{v} = \frac{1}{r}\partial_r(r v_r) + \partial_z(v_z). \tag{1.9}$$

Hence, the poloidal velocity field can be derived from a stream-function ψ, which is conveniently taken as :

$$\mathbf{v}_{\rm pol} = \nabla \times (r^{-1}\psi\hat{\boldsymbol{\theta}}), \quad \text{so that} \quad v_r = -\frac{1}{r}\partial_z\psi \text{ and } v_z = \frac{1}{r}\partial_r\psi. \tag{1.10}$$

The stream function is related to the θ-component of the vorticity field, through $\omega_\theta = \hat{\boldsymbol{\theta}} \cdot \nabla \times (\nabla \times (r^{-1}\psi\hat{\boldsymbol{\theta}}))$. The poloidal velocity field is entirely prescribed by ω_θ and ψ. Hence, the axisymmetric equations can be written in terms of the toroidal field v_θ and the poloidal vorticity ω_θ only. The axisymmetric equations are more compactly written using the pair of variables $(\sigma, \xi) = (r v_\theta, \omega_\theta / r)$.

Equations. An equation for σ is obtained directly from the Euler equations (1.1). The pressure gradient is independent from θ. Hence:

$$\partial_t \sigma = r\hat{\boldsymbol{\theta}} \cdot (\mathbf{v} \times \boldsymbol{\omega}) = r v_z \omega_r - r v_r \omega_z = -v_z \partial_z \sigma - v_r \partial_r \sigma. \tag{1.11}$$

An equation for ω_θ stems from (1.2) :

$$\begin{aligned}\partial_t \xi &= \frac{1}{r}\partial_z\left(\frac{\sigma}{r}\omega_z - v_z r\xi\right) - \frac{1}{r}\partial_r\left(v_r r\xi - \frac{\sigma}{r}\omega_r\right) \\ &= \frac{1}{r}\left(\partial_z\frac{\sigma}{r^2}\partial_r\sigma - \partial_r\frac{\sigma}{r^2}\partial_z\sigma\right) - (v_z\partial_z\xi + v_r\partial_r\xi) - \xi\underbrace{\left(\partial_z v_z + \frac{1}{r}\partial_r(rv_r)\right)}_{=0}.\end{aligned} \tag{1.12}$$

We define an axisymmetric inner bracket $[,]^\odot$ through $[f,g]^\odot = \frac{1}{r}\left(\partial_r f\partial_z g - \partial_r g\partial_z f\right)$. We can then use the axisymmetric incompressibility (1.9), and recast the advection terms in equations (1.11) and (1.11) in terms of the axisymmetric bracket. The axisymmetric Euler equations are then compactly written as :

$$\begin{aligned}&\partial_t\sigma + [\psi,\sigma]^\odot = 0 \quad \text{and} \quad \partial_t\xi + [\psi,\xi]^\odot = \left[\frac{\sigma}{r^2},\sigma\right]^\odot, \\ &\text{with} \quad \xi = -\left\{\frac{1}{r^2}\partial^2_{zz} + \frac{1}{r}\partial_r\left(\frac{1}{r}\partial_r\right)\right\}\psi \underset{def}{=} -\Delta_\star\psi.\end{aligned} \tag{1.13}$$

This form of the Axisymmetric Euler equations can be found for example in [Szeri and Holmes, 1988] and more recently in [Leprovost et al., 2006].

The field σ will in general be referred to as the "toroidal" field, but also sometimes as the "swirl" or the "azimuthal" field. The field ξ will be referred to as the "poloidal" field. We note that contrarily to the translational-symmetric case, the swirl is an active scalar. This feature is not an artifact of the cylindrical geometry. The generation of vorticity by the swirling field can be interpreted as an effect of the centrifugal forces acting on the fluids [Vladimirov et al., 1997].

Remark. We will usually omit the "$\odot$" superscript. It will also sometimes prove more convenient to work with the radial coordinate $y = r^2/2$ instead of r. With such a choice, the differential operator $\Delta_\star$ reads : $\Delta_\star = \frac{1}{2y}\partial^2_{zz} + \partial^2_{yy}$.

1.2 Equations for Boussinesq flows

(Three-Dimensional) Boussinesq flows are obtained by supplementing the strictly hydrodynamical equations (1.1) with a buoyancy term, that acts along a prescribed direction, say along the y direction (in Cartesian coordinates). In the absence of viscous and forcing terms, their evolution is governed by the ideal Boussinesq equations, which in normalized units and in the absence of rotation read [Abarbanel et al., 1986]:

$$\begin{aligned}&\partial_t\mathbf{v} + \mathbf{v}\cdot\nabla\mathbf{v} = -\nabla p + \theta\nabla y, \qquad \partial_t\theta + \mathbf{v}\cdot\nabla\theta = 0, \\ &\text{and} \quad \nabla\cdot\mathbf{v} = 0.\end{aligned} \tag{1.14}$$

θ is a scalar field, built in to be an active scalar. It can be thought of as a temperature, but also as a density, a salinity or a combination of several such effects [Fleury, 2006].

In Boussinesq flows, the vorticity evolves as

$$\partial_t \boldsymbol{\omega} = \nabla \times (\mathbf{v} \times \boldsymbol{\omega}) + \nabla\theta \times \nabla y. \tag{1.15}$$

Two-dimensional Boussinesq flows can be obtained from translational-symmetric solutions. A simple symmetry for which the buoyancy remains active is a translational symmetry along a direction different from the one prescribed by the stratification, say along the z direction. Considering fields depending on the x and the y coordinates only (so that "$\partial_z \equiv 0$"), it is straightforward to generalize the little game played in the purely hydrodynamical situation. The solutions can be described in terms of (i) the z-component of the velocity $v_z(x, y)$, (ii) the z-component of the vorticity ω_z, (iii) the stream function ψ defined through $v_\perp = -\nabla \times (\psi \hat{\mathbf{z}})$ (iv) the buoyancy $\theta(x, y)$. This yields the "2D4C" system of equations,

$$\begin{array}{c} \partial_t \omega_z + [\psi, \omega_z] = [\theta, y], \qquad \partial_t v_z + [\psi, v_z] = 0, \qquad \partial_t \theta + [\psi, \theta] = 0 \\ \text{with} \quad \omega_z = -\Delta_{2D}\psi. \end{array} \tag{1.16}$$

As in the two-dimensional case, the inner bracket is defined through $[f, g] = \partial_x f \partial_y g - \partial_x g \partial_y f$. The active effect of the buoyancy is simply given by $[\theta, y] = \partial_x \theta$. The vertical velocity field is passive. By restricting our attention to the active interplays, we obtain a 2D3C model of a buoyancy-driven flow, known as a "2D Boussinesq flow" (the subscripts have been omitted) :

$$\begin{array}{c} \partial_t \omega + [\psi, \omega] = [\theta, y], \qquad \partial_t \theta + [\psi, \theta] = 0 \\ \text{with} \quad \omega = -\Delta\psi. \end{array} \tag{1.17}$$

1.3 Equations for magneto-hydrodynamical flows

Three-dimensional ideal incompressible magneto-fluids are thought to be described by the magneto-hydrodynamical (MHD) equations. They describe the joint evolution of a three-component magnetic field $\mathbf{B}$ and of the velocity $\mathbf{v}$ of an incompressible conducting fluid. They read [Biskamp, 1993] :

$$\begin{array}{c} \partial_t \mathbf{v} + \mathbf{v} \cdot \nabla \mathbf{v} = -\nabla P + \mathbf{B} \cdot \nabla \mathbf{B} \quad \text{and} \quad \partial_t \mathbf{B} = \nabla \times (\mathbf{v} \times \mathbf{B}), \\ \text{with} \quad \nabla \cdot \mathbf{v} = 0 \quad \text{and} \quad \nabla \cdot \mathbf{B} = 0, \end{array}. \tag{1.18}$$

They prescribe the evolution of the kinetic vorticity as :

$$\partial_t \boldsymbol{\omega} = \nabla \times (\mathbf{v} \times \boldsymbol{\omega}) + \nabla \times (\mathbf{j} \times \mathbf{B}), \tag{1.19}$$

where $\mathbf{j} = \nabla \times \mathbf{B}$ is defined as the density of electric current. An other important quantity is the magnetic potential $\mathbf{A}$. It is defined as $\mathbf{B} = \nabla \times \mathbf{A}$. Its existence stems from the divergence-free condition on $\mathbf{B}$. Its evolution is obtained directly from the equation on $\mathbf{B}$ in Equation (1.18) :

$$\partial_t \mathbf{A} = \mathbf{v} \times (\nabla \times \mathbf{A}) + \nabla\phi. \tag{1.20}$$

A Gauge condition on $\mathbf{A}$, such as the standard Coulomb Gauge ($\nabla \cdot \mathbf{A} = 0$), allows to completely specify the field ϕ by taking the divergence of the latter equation.

Two-dimensional magneto-fluids are standardly obtained from translational-symmetric flows. The specification of a translational symmetric solutions requires the specification of the two perpendicular fields : $\mathbf{v}_\perp(x,y)$, $\mathbf{B}_\perp(x,y)$, as well as of the two parallel fields : $v_z(x,y)$, $B_z(x,y)$. As for translational symmetric solutions in the hydrodynamical situation, the perpendicular velocity field is entirely prescribed by the z-component of the vorticity field ω_z, and the scalar stream function defined through $\mathbf{v}_\perp = -\nabla \times (\psi\hat{\mathbf{z}})$. Similarly, the perpendicular magnetic field is entirely prescribed by the z-component of the electric current j_z, and the scalar magnetic potential A_z defined through $\mathbf{B}_\perp = -\nabla\times(A\hat{\mathbf{z}})$. Those solutions are then entirely prescribed by the six scalar fields : v_z, B_z, ω_z, j_z, A_z. The final form of the translational symmetric magneto-hydrodynamical equations describe a "2D6C" fluid :

$$\begin{aligned} &\partial_t v_z + [\psi, v_z] = [A, B_z], \qquad \partial_t B_z + [\psi, B_z] = [A, v_z], \\ &\partial_t \omega_z + [\psi, \omega_z] = [A, j_z], \qquad \partial_t A_z + [\psi, A_z] = 0, \\ &\quad \text{with} \quad j_z = -\Delta_{2D} A_z, \quad \text{and} \quad \omega_z = -\Delta_{2D}\psi. \end{aligned} \tag{1.21}$$

The bracket is still $[f,g] = \partial_x f \partial_y g - \partial_x g \partial_y f$. $[A,.] = \mathbf{B}_\perp \cdot \nabla.$ and $[\psi,.] = \mathbf{v}_\perp \cdot \nabla.$ respectively represent perpendicular magnetic and kinetic advections. The two equations describing the evolution of the z-component of the velocity and of the magnetic fields are passive. Therefore, it is relevant to focus on the motions within the perpendicular plane. This natural restriction yields the two-dimensional magneto-hydrodynamical equations, which read (without subscripts) :

$$\begin{aligned} &\partial_t \omega + [\psi, \omega] = [A, j], \qquad \partial_t A + [\psi, A] = 0, \\ &\quad \text{with} \quad j = -\Delta A, \quad \text{and} \quad \omega = -\Delta\psi. \end{aligned} \tag{1.22}$$

These are not "2D3C" but rather "2D4C"equations. Howere , the "2D3C" denomination is mostly a matter of vocabulary and is quite subjective. Due to the incompressibility condition, two-dimensional (hydrodynamical) flows describe the evolution of a single component (the scalar vorticity) to which all the other fields (stream function and velocities) relate: they could therefore be relabeled as "2D1C". The axisymmetric, the translational symmetric, the two-dimensional Boussinesq and the magneto-hydrodynamical flows just described would then all fall into the same category of "2D2C" flows. Such a labeling would be more accurate but also less self-explanatory.

1.4 Ideal dynamical invariants.

Description. The analogy between two-dimensional Boussinesq , magneto-hydro and three-dimensional axisymmetric flows is manifest when comparing the sets of equations (1.13), (1.17) and (1.22). Those three flows have many invariants associated to them. Their evolution preserve an Energy, which can be written as the sum of a poloidal/kinetic energy with a toroidal/(available) potential/magnetic energy. They also preserve two families of Casimir invariants. The first family is a toroidal/buoyant/magnetic family of Casimirs C_F : every function of the toroidal /buoyancy/magnetic potential scalar only integrated over the domain is preserved. The second family could be called a family of Helical Casimirs H_G: every function of the toroidal /buoyancy/magnetic potential scalar multiplied by the poloidal/kinetic/kinetic field is also conserved when integrated over the domain.

The energy and the Casimirs invariants of the various models are made explicit and summarized on Table 1.1.

Flow	2D Hydro	3D Axisymmetric	2D Boussinesq	2D Magneto-Hydro
Fields	$\omega \ (= -\Delta\psi)$	$\xi \ (= -\Delta_\star\psi)$	$\omega \ (= -\Delta\psi)$	$\omega \ (= -\Delta\psi)$
		σ	θ	$A \ (= -\Delta^{-1} j)$
Energy	$E = E_{\text{kin}}$	$E = E_{\text{tor}} + E_{\text{pol}}$	$E = E_{\text{buoy}} + E_{\text{kin}}$	$E = E_{\text{mag}} + E_{\text{kin}}$
	$E_{\text{kin}} = \frac{1}{2}\int_{\mathcal{D}} \omega\psi$	$E_{\text{pol}} = \frac{1}{2}\int_{\mathcal{D}} \xi\psi$	$E_{\text{kin}} = \frac{1}{2}\int_{\mathcal{D}} \omega\psi$	$E_{\text{kin}} = \frac{1}{2}\int_{\mathcal{D}} \omega\psi$
		$E_{\text{tor}} = \frac{1}{2}\int_{\mathcal{D}} \frac{\sigma^2}{r^2}$	$E_{\text{buoy}} = \int_{\mathcal{D}} \theta y$	$E_{\text{mag}} = \frac{1}{2}\int_{\mathcal{D}} jA$
Casimirs	$C_F = \int_{\mathcal{D}} F(\omega)$	$C_F = \int_{\mathcal{D}} F(\sigma)$	$C_F = \int_{\mathcal{D}} F(\theta)$	$C_F = \int_{\mathcal{D}} F(A)$
		$H_G = \int_{\mathcal{D}} \xi G(\sigma)$	$H_G = \int_{\mathcal{D}} \omega G(\theta)$	$H_G = \int_{\mathcal{D}} \omega G(A)$

Table 1.1: Invariants for 2D and 2D3C ideal fluids.

Derivation It is very easy to check directly from equations (1.13), (1.17) and (1.22) that those quantities are indeed preserved by the 2D3C dynamics of relevance. The proof relies on the use of the following quasi-transparent properties of the inner brackets $[,]$ – representing either the axisymmetric or the bi-dimensional brackets :

for sufficiently regular scalar fields χ, ϕ, ζ: $\mathcal{D} \to \mathbb{R}$ and scalar function F :$\mathbb{R} \to \mathbb{R}$,

(i) $[\chi, \phi] = -[\phi, \chi]$,

(ii) $[F \circ \phi, \chi] = (F' \circ \phi)[\phi, \chi]$,

(iii) $\int_{\mathcal{D}} \zeta[\phi,\chi] = \int_{\mathcal{D}} [\zeta\phi,\chi] + \int_{\mathcal{D}} \phi[\chi,\zeta]$,

(iv) $\int_{\mathcal{D}} [\phi,\chi] = 0$ for periodic fields, or if either ϕ or χ vanishes at the boundary.

As an example, the conservation of the magnetic Helical Casimirs in a doubly periodic domain is obtained through :

$$\begin{aligned} \frac{\mathrm{d}}{\mathrm{dt}} \int_{\mathcal{D}} \omega G(A) &= \int_{\mathcal{D}} \left\{ G(A)[A,j] + G(A)[\omega,\psi] + \omega G'(A)[A,\psi] \right\} \\ &= \int_{\mathcal{D}} jG'(A)[A,A] + \int_{\mathcal{D}} G(A) \left\{ [\omega,\psi] + [\psi,\omega] \right\} = 0. \end{aligned} \tag{1.23}$$

Rugged Invariants Note, that the Casimir invariants include the familiar rugged invariants. For example, taking G as the identity function ($G(x) = x$) gives one half of the hydrodynamical helicity $H = \int \mathbf{v} \cdot \boldsymbol{\omega}$ for axi-symmetry and one half of the cross- helicity $H_c = \int \mathbf{B} \cdot \mathbf{v}$ for two-dimensional magneto-hydrodynamics. A quadratic F ($F(x) = x^2$) yields the enstrophy for two-dimensional hydrodynamical flows and the magnetic potential squared in the magneto-hydrodynamical case. The enstrophy $\int_{\mathcal{D}} \omega^2$ is not conserved for 2D3C models.

"Casimirs" The Casimir invariants are "Casimir" invariants in the Hamiltonian meaning. At a formal level, ideal fluids are Hamiltonian systems, although of an infinite dimensional kind [Morrison, 1998].

The Casimir invariants emerge as a consequence of Noether's theorem and of the relabeling symmetry of "fluid parcels" when switching from Lagrangian to Eulerian coordinates and from the continuous symmetry (translational/axial) considered [Salmon, 1988, Shepherd, 1990, Morrison, 1998].

We note that the Hamiltonian representation of the two-dimensional Boussinesq, two-dimensional magento-hydrodynamical and three-dimensional axisymmetric flows can be achieved using the same Lie-Poisson Structure, but not the same Hamiltonian. This explains why the Casimir invariants are the same in the three situations [Morrison and Hazeltine, 1984, Abarbanel et al., 1986, Szeri and Holmes, 1988].

1.5 A side remark on Shallow-Water flows

The various flows that have been derived here have in common that they are incompressible. Such is not the case for example for Shallow-Water flows, which we will sometimes allude to, and which also describe a 2D3C situation. The Shallow-Water equations describe a quasi-2D fluid whose height may be slightly varying. The fluid is described in terms of a two-component velocity field $\mathbf{v} = (v_x(x,y), v_z(x,y))$ and of a height $h(x,y)$. In the absence of rotation, the governing equations are [Pedlosky, 1982]:

$$\partial_t \mathbf{v} + \mathbf{v} \cdot \nabla \mathbf{v} = -g \nabla h, \quad \text{and} \quad \partial_t h + \nabla \cdot (h\mathbf{v}) = 0. \tag{1.24}$$

Shallow water flows can also be derived from a Hamiltonian formalism [Salmon, 1983]. The total energy is the sum of a kinetic energy $E_{\text{kin}} = \int_{\mathcal{D}} h\mathbf{v} \cdot \mathbf{v}$ and of a potential energy

$E_p = \int_{\mathcal{D}} gh^2$. It is conserved by the dynamics. The velocity field transports the potential vorticity $q = \omega/h$. However, the velocity is not divergence free. Hence, the family of invariants $\int_{\mathcal{D}} F(q)$ are not conserved. Only Casimirs "of helical type" $\int_{\mathcal{D}} hf(q)$ are indeed conserved by the dynamics [Weichman and Petrich, 2001]. In a sense, shallow water flows are truely "2D3C": the velocity field cannot be derived from a scalar quantity, as was the case for the incompressible equations previously described. From this point of view, they can be be expected to be more delicate to handle.

Part I

Ideal theory

Chapter 2

Invariant measures and Theorem of Liouville

The present chapter aims at defining the concepts of measures and invariant measures in the context of dynamical systems. For finite dimensional systems, I briefly review the connection between the Theorem of Liouville and microcanonical or canonical measures. I then define a formal counterpart to the theorem, which may be relevant for the dynamics of continuous fields. The formal Theorem of Liouville is shown to hold for the ideal flows described in the first chapter. I briefly comment on the "Hamiltonianity" of those flows. The chapter stems from discussions with Freddy Bouchet, Oleg Zaboronski and Philip J. Morrison.

Contents

2.1 (Brief) Introduction.

An informal survey performed at the coffee room of the SPHYNX laboratory[(a)] makes it clear. " The Theorem of Liouville, huh ? This is something you learn at school ! It tells you something about the contraction – or more precisely the absence thereof – of the phase

[(a)] Room 205, Building 772, Orme des Merisiers, 91191 Gif-Sur-Yvette, France.

space , doesn't it ? ", a head scientist from the SPHYNX laboratory – whose anonymity is here preserved – spontaneously replies when asked about the Theorem of Liouville. This pavlovian description of the Theorem of Liouville is self-sufficient. However, because the Theorem of Liouville is essential for statistical mechanics and because many textbooks on statistical mechanics quite often crudely summarize it as a cryptic condition of the kind "$\sum_i \frac{\partial \dot{x}_i}{\partial x_i} = 0$", I feel that it is worth to spend a short time giving a brief overview of this theorem, in the context of finite dimensional dynamical systems and using the language of invariant measures. This is done in Section 2. In Section 3, I will argue that the Theorem of Liouville has a very simple and very natural formal counterpart for infinite dimensional dynamical systems, describing the time evolution of a field. The existence of such a "Formal Theorem of Liouville" – too be defined below – might be of direct relevance to the statistical mechanics description of ideal flows, at least from a Physicist's perspective.

2.2 Theorem of Liouville for a dynamical system in finite dimensions

2.2.1 Definitions

Dynamical system. Let us consider an autonomous set of ordinary differential equations describing the instantaneous evolution of potentially many, yet a finite number n of degrees of freedom z_i over a finite dimensional manifold $\mathbb{R}^n$, *viz*

$$\begin{array}{c} \dot{\mathbf{z}} = \mathbf{F}(\mathbf{z}) \quad \text{with} \quad \mathbf{F} : \mathbb{R}^n \to \mathbb{R}^n \quad \text{(vector field)} \\ \text{and initial conditions} \quad \mathbf{z}(t=0) = \mathbf{z_0}. \end{array} \tag{2.1}$$

Let us write $\mathcal{Z} = \mathbb{R}^n$ the space of all possible initial states $\mathbf{z} = (z_1, ..., z_n)$. If for any initial condition $\mathbf{z_0} \in \mathcal{Z}$ and any time $t \in \mathbb{R}$, there exists a uniquely defined solution $\mathbf{z}(t, \mathbf{z_0})$ to the Cauchy problem defined by (2.1), then one can unambiguously define the flow map :

$$\phi : \begin{cases} \mathcal{Z} \times \mathbb{R} \to \mathcal{Z} \\ (\mathbf{z_0}, t) \mapsto \phi_t(\mathbf{z_0}) = \mathbf{z}(t, \mathbf{z_0}) \end{cases}. \tag{2.2}$$

The flow map naturally satisfies

$$\begin{array}{c} \phi_0(\mathbf{z_0}) = \mathbf{z_0}, \qquad \phi_{t+t'} = \phi_t(\phi_{t'}(\mathbf{z}0), t), \\ \text{and} \quad \partial_t \phi(\mathbf{z_0}, t) = F(\phi(\mathbf{z_0}, t)) \ \text{ for all } \ \mathbf{z_0} \in \mathcal{Z} \text{ and } t, t' \in \mathbf{R}. \end{array} \tag{2.3}$$

Equations (2.2) and (2.3) then define a dynamical system $\mathcal{S} = (\mathcal{Z}, \phi)$, whose dynamics is given by (2.1), and phase space is $\mathcal{Z}$. It stems from Equation (2.3) that for any t, the map $\phi_t : \mathcal{Z} \to \mathcal{Z}$ is bijective and has inverse $\phi_t^{-1} = \phi_{-t}$.

Measures and invariant measures. In the context of dynamical systems, what do we expect to learn from statistical mechanics, and more particularly from equilibrium sta-

tistical mechanics ? Colloquially, the idea is to consider non-trivial sets of solutions – if any– , whose statistical properties are left unaltered by the dynamics (2.2). Those "invariant" sets of solutions are in a sense a generalization of dynamical fixed points, whose systematical study allows a classification of bifurcations for low dimensional dynamical systems. An old idea beneath the use of statistical mechanics is that if the invariant set of solutions is well-chosen, then it is possible to compute "time - averages" of the kind $\lim_{T\to\infty} \frac{1}{T} \int_0^T$ dt along any trajectory in terms of well-defined "ensemble averages", whose treatment may vary in difficulty but may also be made possible by a century of developments in the field of statistical mechanics and the use of powerful techniques such as saddle-point approximations, large-deviations theorems, renormalization groups, and so on. Except in some very specific situations, there is however no mathematical proof in general that such a crude replacement is justified. This problem is known as "the ergodic problem" and has kept mathematicians busy for more than a century now. The ergodic problem in the context of ideal flows is out of the scope of the present manuscript except for some brief comments in Chapter 3. Following Khinchin's prescription, we shall take the more pragmatic approach of " attempt[ing] as the 'ergodic hypothesis' the very possibility of such a replacement, and [...] judg[ing] the theory by its practical success or failure" [Khinchin, 1949, p.53]. Let us now define precisely what we mean by "invariant sets of solutions".

Definitions. We suppose that we can define a probability measure on the phase space $\mathcal{Z}$, so that $(\mathcal{Z}, \mathcal{O}, \mu)$ is a measurable space for some suitably defined measurable sets in $\mathcal{O}$. This is obviously the case in the simple case $\mathcal{Z} = \mathbb{R}^n$. For any time t, ϕ_t maps $\mathcal{Z}$ onto itself. Hence, ϕ_t can be interpreted as a random variable on $\mathcal{Z}$, whose distribution law μ_t is defined by

$$\mu_t(A) = \mu(\phi_t^{-1}(A)) \quad \text{for any measurable set A of } \mathcal{Z} \quad . \tag{2.4}$$

In other words, μ_t is simply defined as the image measure of μ by ϕ_t, sometimes written as $\mu_t = \phi_t^\sharp \, \mu$ [Villani, 2006].

An invariant measure for the dynamical system $(\mathcal{S} = \mathcal{Z}, \phi)$ is then simply a measure μ such that

$$\forall t \in \mathbb{R}, \mu_t(A) = \mu(A) \quad \text{for any measurable set A of } \mathcal{Z} \quad . \tag{2.5}$$

Vocabulary. In the language of statistical mechanics, a probability measure defined over phase space is most often called a "statistical ensemble", and an invariant measure sometimes denoted as a "stationary statistical solution". Also, since the fine mathematical properties of measurable ensembles is not really the subject of the present study, I will often talk of "observables" instead of "measurable sets" to describe the properties of the ensembles at stake. An observable is simply defined as a function $\mathcal{Z} \to \mathbb{R}$. The measure $\mu(A)$ of a measurable set A belonging to a suitably defined probability space $(\mathcal{Z}, \mathcal{A}, \mu)$, can therefore be seen as the ensemble average of the "observable" $O = \mathbf{1}_A$ so

that $\langle O \rangle_\mu = \int_{\mathcal{Z}} \mu(\mathrm{dz}) \mathbf{1}_A(\mathbf{z}) = \mu(A)$. I will extensively use this terminology throughout the manuscript.

2.2.2 The Theorem of Liouville

Ensembles. Celebrated examples of statistical ensembles include the "microcanonical ensemble" which corresponds to uniform weighting over a finite region of phase space, or the "canonical" and related "grand-canonical" ensembles whose weighting are specified by Boltzmann weights. However, when studying a dynamical system of the kind described by Equations (2.3) and (2.2), there is no reason why in general microcanonical nor canonical nor even grand-canonical ensembles should be singled out. It may very well be that neither of those ensembles are invariant measures. The reason why they naturally emerge in the context of finite dimensional Hamiltonian systems owes to the Theorem of Liouville [(a)], which is a statement of the incompressibility of the flow ϕ_t. I give below a general version of the theorem, akin to the one described for example in [Majda and Wang, 2006, Chapter 7].

More definitions. Let us first introduce two more notations. Unless stated otherwise, $(\mathcal{Z}, \phi)$ denotes a dynamical system, whose dynamics is prescribed by the vector field $\mathbf{F}(\mathbf{z}) = \partial_t \phi(\mathbf{z}, t)$, as described by Equations (2.3) and (2.1).

(i) Divergence with respect to a density of probability : to any function $f : \mathcal{Z} \to \mathbb{R}$ defined over the phase space $\mathcal{Z}$ that has n dimensions, we associate a f-divergence operator ∇_f that converts a vector field $\mathbf{F} : \mathcal{Z} \to \mathcal{Z}$ into a scalar field, as

$$\nabla_f \cdot \mathbf{F} \underset{\text{def}}{=} \sum_{i=1}^{n} \frac{\partial f F_i}{\partial z_i} \quad \text{for any vector field} \quad \mathbf{F}(\mathbf{z}) = (F_1(\mathbf{z}), ..., F_n(\mathbf{z}))\,. \tag{2.6}$$

(ii) Jacobian determinant : it is useful to introduce $J(t, \mathbf{z}) = \left| \frac{\partial \mathbf{z}_t}{\partial \mathbf{z}} \right| = \frac{\partial(\phi_t(\mathbf{z})_1, ..., \phi_t(\mathbf{z})_n)}{\partial(z_1, .., z_n)}$ the Jacobian determinant associated to the mapping $\mathbf{z} \to \phi_t(\mathbf{z})$. It is easily checked that

$$\forall \mathbf{z} \in \mathcal{Z}, \qquad \partial_t J(t, \mathbf{z}) = J(t, \mathbf{z}) \sum_{i=1}^{n} \frac{\partial F_i(\phi_t(\mathbf{z}))}{\partial z_i}. \tag{2.7}$$

Proof : Using the compact notation $\mathbf{z}_t = \phi_t(\mathbf{z})$, and the multi-linearity of the determinant

[(a)] The denomination "Theorem of Liouville" sounds slightly outdated but is also more charming than the common"Liouville Theorem" or its variant "Liouville's theorem". The former denomination is the one chosen by George Gamow in his translation of Khinchin's monograph [Khinchin, 1949]. So, I will stick to it.

form, we obtain

$$J(t+\delta t,\mathbf{z}) = \left|\frac{\partial \mathbf{z}_{t+\delta t}}{\partial \mathbf{z}_t}\right| \left|\frac{\partial \mathbf{z}_t}{\partial \mathbf{z}}\right| = J(t,\mathbf{z}) \sum_{i=1}^{n} \frac{\partial(\mathbf{z}_{t1}+\delta t F_1(\mathbf{z}),...,\mathbf{z}_{tn}+\delta t F_n(\mathbf{z}))}{\partial(\mathbf{z}_{t1},...,\mathbf{z}_{t1})}$$
$$\underset{\delta t\to 0}{=} J(t)\left(1+\delta t\sum_{i=1}^{n}\frac{\partial F_i(\mathbf{z}_t)}{\partial z_i}\right)+o(\delta t^2),$$
$$\text{so that}\quad \partial_t J(t,\mathbf{z}) = J(t,\mathbf{z})\sum_{i=1}^{n}\frac{\partial F_i(\mathbf{z}_t)}{\partial z_i}. \tag{2.8}$$

■

Theorem of Liouville. The Theorem of Liouville can then be formulated in the following way:

Theorem 1 (*Theorem of Liouville*)

- *Let $(\mathcal{Z},\phi)$ be a dynamical system, whose dynamics is prescribed by the vector field $\mathbf{F}(\mathbf{z}) = \partial_t\phi(\mathbf{z},t)$.*
- *Assume there exists a probability measure μ defined over $\mathcal{Z}$, that admits a density of probability $f(\mathbf{z})$ – with respect to the Lebesgue measure–, so that formally $\mu(dz) = f(\mathbf{z})dz$.*

If the vector field has a vanishing f-divergence, e.g. satisfies $\nabla_f\mathbf{F} = 0$, then μ is an invariant measure for the dynamics.

Proof : We use the notations of the theorem. Let $X = \phi_t(Z)$ a measurable set. It stems from $\mu_t = \phi_t^\sharp\mu$ that $\mu_t(X) = \mu(Z) = \int_Z \mathrm{d}\mathbf{z} f(\mathbf{z})$. Besides, $\mu(X) = \mu(\phi_t(Z)) = \int_{\phi_t(Z)} \mathrm{d}\mathbf{x}\, f(\mathbf{x}) = \int_{\mathbf{Z}} \mathrm{d}\mathbf{z}\ |\mathbf{J}(\mathbf{t},\mathbf{z})|\, \mathbf{f}\left(\phi_{\mathbf{t}}(\mathbf{z})\right)$. Hence, the following equivalences hold :

$$\begin{aligned}\mu \text{ is invariant} &\iff \mu_t(X) = \mu(X) \quad \text{for any measurable set } X \text{ and any time } t\\ &\iff \int_Z \mathrm{d}\mathbf{z} f(\mathbf{z}) = \int_Z \mathrm{d}\mathbf{z}\ |J(t,\mathbf{z})|\, f\left(\phi_t(\mathbf{z})\right) \qquad (2.9)\\ &\qquad \text{for any measurable set } Z \text{ and any time } t \quad .\end{aligned}$$

Since f is non-negative, the latter condition is surely satisfied if $\partial_t\left(J(t,\mathbf{z})f\left(\phi_t(\mathbf{z})\right)\right)$ vanishes for any time t and $z\in\mathcal{Z}$. It is easy to check using (2.7), that $\partial_t\left(J(t,\mathbf{z})f\left(\phi_t(\mathbf{z})\right)\right) = J(t,\mathbf{z})\nabla_f\cdot\mathbf{F}$. Hence a vanishing divergence of the vector field $\mathbf{F}$ with respect to f ensures that μ is invariant. ■

(a)

(a) A more compact but more formal proof can be written in terms of observables. We first notice that that μ is invariant *iff* $\frac{d}{dt}\langle\mathcal{O}\rangle_{\mu_t} = 0$ for any observable $\mathcal{O}$. We then compute $\langle\mathcal{O}\rangle_{\mu_t} = \int_{\mathcal{Z}}\mu_t(\mathrm{d}\mathbf{x})\,\mathcal{O}(\mathbf{x}) = \int_{\phi_{-\mathbf{t}}(\mathcal{Z})}\mu(\mathrm{d}\mathbf{z})\,\mathcal{O}(\phi_{\mathbf{t}}(\mathbf{z})) = \int_{\mathcal{Z}}\mathrm{d}\mathbf{z}\,\mathbf{f}(\mathbf{z})\,\mathcal{O}(\phi_{\mathbf{t}}(\mathbf{z}))$. We can now estimate $\frac{d}{dt}\langle\mathcal{O}\rangle_{\mu_t} = \int_{\mathcal{Z}}\mathrm{d}\mathbf{z}f(\mathbf{z})\sum_i\frac{\partial\mathcal{O}(\phi_t(\mathbf{z}))}{\partial z_i}F_i(\mathbf{z}) = -\int_{\mathcal{Z}}\mathrm{d}\mathbf{z}\sum_i\frac{\partial fF_i}{\partial z_i}\mathcal{O}(\phi_t(\mathbf{z}))$. The last equality is obtained with an integration by part. We conclude that a vanishing f-divergence for the vector field ensures μ to be invariant.

Dynamical Invariants and invariant measures. An immediate corollary to the Theorem of Liouville relates to the use of dynamical invariants to define a family of "natural" invariant measures :

Corollary 1

- *Let $S = (\mathcal{Z}, \phi)$ a dynamical system, and $\mathcal{F} = \partial_t \phi$.*
- *Let μ be a measure with density of probability f such that $\nabla_f \cdot \mathcal{F} = 0$.*
- *Assume there exists a dynamical invariant for the dynamics, $C(\mathbf{z})$ satisfying $\partial_t C(\phi_t(\mathbf{z})) = 0$ for any $\mathbf{z} \in \mathcal{Z}$.*

Then, for any positively valued scalar and sufficiently regular function g, the measure μ_g, defined through $\mu_g(d\mathbf{z}) = f(\mathbf{z})g(C(\mathbf{z}))d\mathbf{z}$ is also an invariant measure for the dynamics.

Proof : The corollary stems from the following observation :

$$\nabla_{f(g\circ C)} \cdot \mathbf{F} = [g \circ C] \underbrace{\nabla_f \cdot \mathbf{F}}_{=0} + (g' \circ C)\, f \underbrace{\mathbf{F} \cdot \nabla C(\mathbf{z})}_{=\partial_t C} = 0. \tag{2.10}$$

■

2.2.3 Examples

2.2.3.1 Canonical Hamiltonian systems

Definition. The "canonical" illustration of the Theorem of Liouville involves a finite-dimensional Hamiltonian system, whose dynamics is written in terms of so-called canonical coordinates $\mathbf{q} = (q_1 ... q_n)$ and $\mathbf{p} = (p_1 ... p_n)$ together with a Hamiltonian function $H(\mathbf{q}, \mathbf{p})$ as

$$\dot{q}_i = \frac{\partial H}{\partial p_i} \quad \text{and} \quad \dot{p}_i = -\frac{\partial H}{\partial q_i} \quad \text{for } i \in [\![1; N]\!] \quad . \tag{2.11}$$

Microcanonical ensemble. In this case, the phase space can be identified as $\mathbb{R}^{2n}$. If the q_i and the p_i are respectively taken as the first and second sets of n coordinates, than the vector-field $\mathbf{F} = (F_1 ... F_{2n})$ is given by $F_i = \dfrac{\partial H}{\partial p_i}$ and $F_{i+n} = -\dfrac{\partial H}{\partial q_i}$ for $i \in [\![1; N]\!]$, so that $\nabla \cdot F = \sum_{i=1}^{n} \dfrac{\partial^2 H}{\partial p_i q_i} + \dfrac{\partial^2 H}{\partial q_i p_i} = 0$. The uniform (Lebesgue) measure $\mu(\mathrm{d}\mathbf{q}\,\mathrm{d}\mathbf{p}) = \mathrm{d}\mathbf{q}\,\mathrm{d}\mathbf{p}$ is then an invariant measure for the dynamics. In the case of canonical Hamiltonian systems, it is easily checked that the energy $E = H(\mathbf{q}, \mathbf{p})$ is a dynamical invariant. We conclude that the microcanical measures $\mu_0(\mathrm{d}\mathbf{q}\,\mathrm{d}\mathbf{p}) = \mathrm{d}\mathbf{q}\,\mathrm{d}\mathbf{p}\ \mathbf{1}_{H(\mathbf{q},\mathbf{p})=E_0}$ defined as the uniform measures over the energy shells $H(\mathbf{q}, \mathbf{p}) = E_0$ are invariant measures.

Canonical ensemble. Note that it also stems from Corollary (1) that the canonical measures $\mu_\beta(\mathrm{d}\mathbf{q}\,\mathrm{d}\mathbf{p}) = \dfrac{\mathrm{d}\mathbf{q}\,\mathrm{d}\mathbf{p}\ \exp(-\beta H(\mathbf{q}, \mathbf{p}))}{\int_{\mathcal{Z}} \mathrm{d}\mathbf{q}\,\mathrm{d}\mathbf{p}\ \exp(-\beta H(\mathbf{q}, \mathbf{p}))}$ do also correspond to invariant measures, for the values of β such that the partition function $\int_{\mathcal{Z}} \mathrm{d}\mathbf{q}\,\mathrm{d}\mathbf{p}\ \exp(-\beta H(\mathbf{q}, \mathbf{p}))$ is not infinite.

2.2.3.2 Noncanonical Hamiltonian systems

Definition. A somewhat less trivial example, and which besides has some relevance in the context of fluid dynamics and plasma physics is given by "noncanonical Hamiltonian systems" [Marsden and Morrison, 1984, Morrison, 1998, Morrison, 2005]. Heuristically, a noncanonical Hamiltonian system can be seen as a Hamiltonian system of the kind (2.11), whose "Hamiltonianity" is obscured by a change of variables $\mathbf{z}_c = (\mathbf{q}, \mathbf{p}) \to \mathbf{z}(\mathbf{z}_c)$. More precisely, it is a system whose dynamics reads

$$\dot{z}_i = \sum_{j=1}^{n'} J_{ij} \frac{\partial H}{\partial z_j}. \tag{2.12}$$

J is called a "symplectic" operator. J is bilinear, antisymmetric ($J_{ij} + J_{ji} = 0$) and satisfies the Jacobi identity $\sum_l J_{il}\frac{\partial J_{jk}}{\partial z_l} + J_{kl}\frac{\partial J_{ij}}{\partial z_l} + J_{jl}\frac{\partial J_{ki}}{\partial z_l} = 0$. If the underlying phase space $\mathcal{Z}$ has a finite even dimension, $n' = 2n$, the specific choice

$$J_c = \begin{pmatrix} 0_n & I_n \\ -I_n & 0_n \end{pmatrix}, \quad \text{with } 0_n \text{ and } I_n \text{ respectively denoting the } n \text{ by } n \text{ zero and unit matrix,} \tag{2.13}$$

yields the canonical dynamics (2.11).

Microcanonical ensembles. The vector-field associated to the dynamics (2.12) is $\mathcal{F}(\mathbf{z}) = J\nabla H(\mathbf{z})$. Unlike the canonical situation, this vector field is in general not divergence-free, since $\nabla \cdot H = \sum_{ij} \frac{\partial J_{ij}}{\partial z_i}\frac{\partial H}{\partial z_j}$ may very well be non vanishing. Then, one cannot conclude that the Lebesgue measure $\mathrm{d}\mu = \prod_i \mathrm{d}z_i$ is invariant. However, if J is invertible ($\det J \neq 0$), a theorem called the Darboux theorem [Morrison, 1998] says that there exists a local change of coordinates $\mathbf{z}_c = \mathbf{z}_c(\mathbf{z})$, such that the dynamics of the system written in terms of the $\mathbf{z}_c$ variables is canonical, *e.g.* satisfies (2.12) with the canonical operator (2.13). The natural invariant measure that emerges from the Theorem of Liouville is then $\mathrm{d}\mu = \prod_i \mathrm{d}z_{ci}$. It can be recast in terms of the z_i variables as $\mathrm{d}\mu = \prod_i \mathrm{d}z_i \left|\frac{\partial \mathbf{z}_c}{\partial \mathbf{z}}\right| = \frac{1}{\sqrt{|\det J|}} \prod_i \mathrm{d}z_i$. [(a)]

Side note : the case of "Lie-Poisson" systems. In the special case where J is a linear function of z, J can be defined in terms of structure constants C_{ij}^k as $J_{ij} = \sum_{k=1}^n C_{ij}^k z_k$. Such systems are known as "Lie-Poisson" systems, and for those, the Theorem of Liouville may hold without having to insert the extra factor $\sqrt{|\det J|}$. [(b)]

[(a)] In the case $\det J = 0$, the Darboux theorem does not hold any longer, but has a generalization, called the Darboux-Lie theorem. The theorem states that $\mathcal{Z}$ can be written as the direct sum of the kernel of J with a space of even dimension, on which the dynamics is canonical. It is of no concern to us for this specific point.

[(b)] To determine whether this is actually the case, one has to consider the quadratic form of Killing defined by the matrix elements $g_{ij} = \sum_{p,q} C_{iq}^p C_{pj}^q$. If it is negative definite, than the Theorem of Liouville holds on any basis of $\mathcal{Z}$ [Morrison, 1998].

2.2.3.3 Truncated Euler equations

In the context of turbulence, it is well-known that the Theorem of Liouville holds for truncated Euler equations, be it in two , two and and a half or three dimensions. An early demonstration of the theorem can be found in [Lee, 1952] for three-dimensional dynamics decomposed over a set of Fourier modes. Let us here take as a landmark example the case of the two-dimensional Euler equations written in terms of the vorticity field.

Two-dimensional case. Let us consider a domain $\mathcal{D}$ for which the bidimensional Laplacian Δ admits a countable and orthonormal set of eigenmodes $\phi_{I\in\mathbb{Z}^2}$ – for a prescribed scalar product $(.)$. The corresponding eigenmodes are denoted $-\kappa_I^2$. We write the vorticity field as

$$\begin{aligned} \omega(\mathbf{r}) &= \sum_{I\in\mathbb{Z}^2} \omega_I \phi_I(\mathbf{r}), \\ \text{with} \quad \omega_I &= (\phi_I, \omega) \text{ and } (\phi_I, \phi_J) = \delta_{IJ}, \end{aligned} \tag{2.14}$$

and set to zero all but a finite number of modes in a set S_M. S_M may for instance include all the modes whose eigenvalues are less than a given cutoff k_M. An ideal dynamics for the non-zero modes of the vorticity is then directly obtained from Equation (1.7) of Chapter 1. It reads

$$\dot{\omega}_I = \sum_{(J,K)\in S_M^2} C_{JK}^I \omega_J \omega_K \quad \text{with} \quad C_{JK}^I = \kappa_J^{-2}(\phi_I, [\phi_J, \phi_K]). \tag{2.15}$$

It stems from the latter equation that

$$\frac{\partial \dot{\omega}_I}{\partial \omega_I} = \sum_{J\in S_M} \left(C_{JI}^I + C_{IJ}^I \right) \omega_I. \tag{2.16}$$

In a doubly periodic domain, the eigenmodes are $\phi_{\mathbf{k}}(\mathbf{r}) = \exp(i\mathbf{k}\mathbf{r})$, the scalar product is defined as $(f,g) = \int_{\mathcal{D}} f^\star g$, and $\omega_{\mathbf{0}} = 0$ (no net flow). Hence, $C_{\mathbf{k}'\mathbf{k}''}^{\mathbf{k}} = \delta(\mathbf{k}' + \mathbf{k}'' - \mathbf{k})$ and for all $\mathbf{k}$ in S_M,

$$\frac{\partial \dot{\omega}_{\mathbf{k}}}{\partial \omega_{\mathbf{k}}} = \sum_{\mathbf{k}'\in S_M} \left(C_{\mathbf{k}'\mathbf{k}}^{\mathbf{k}} + C_{\mathbf{k}\mathbf{k}'}^{\mathbf{k}} \right) \omega_{\mathbf{k}} = 2 \sum_{\mathbf{k}'\in S_M} \delta(\mathbf{k}') \omega_{\mathbf{k}'} = 2\omega_{\mathbf{0}} = 0. \tag{2.17}$$

The uniform measure $\prod_{\mathbf{k}} \mathrm{d}\omega(\mathbf{k}) = 0$ is therefore an invariant measure for the truncated Euler equations.

2.3 Formal Theorem of Liouville for the dynamics of a field

2.3.1 Dynamics of a field

Definition. Let us now consider the continuous counterpart to Equation (2.1) in order to describe the dynamics of a vector field $\mathbf{z} : \mathcal{D} \to \mathbb{R}^d$ (here, $d = 1, 2$ or 3) defined over a prescribed continuous domain $\mathcal{D}$. $\mathbf{z}(\mathbf{r})$ denotes the value of the vector field at position $(\mathbf{r})$ and $\mathbf{z}_\alpha(\mathbf{r})$ its component along the α-direction. The dynamics of $\mathbf{z}$ can then be formally

written as

$$\dot{\mathbf{z}}_\alpha(\mathbf{r}) = \mathcal{F}_\alpha[\mathbf{r}](\mathbf{z}). \tag{2.18}$$

Issues. $\mathcal{F}$ is the continuous counterpart of the vector-field $\mathbf{F}$. It associates to any $\mathbf{z}$ another vector field $\mathcal{F}(\mathbf{z})$. $\mathcal{F}_\alpha[\mathbf{r}](\mathbf{z})$ denotes the value of the α component of the the vector field $\mathcal{F}(\mathbf{z})$ at position $\mathbf{r}$. A general question is : does this kind of dynamics give rise to a dynamical system ? In general the answer is no. In the context of ideal flows, this issue is related to the "blow-up" problem. As mentioned in the introduction, the existence of a solution to the Cauchy problem is not guaranteed to exist at all time for Eulerian dynamics [Bardos and Titi, 2013, Frisch, 1996]. The issue might be of relevance for 2D3C flows. The existence of a phase space map ϕ_t is not guaranteed. Besides, it involves the use functional derivatives, which are not well-defined mathematical objects. It is therefore awkward to look for an infinite-dimensional version of the Theorem of Liouville and study 2D3C ideal dynamics using a dynamical system analogy. This is however what we do. The idea is to find a condition analogue to the vanishing f-divergence of the vector field in finite dimensions through formal algebraic computations. The "result" will be called a Formal Theorem of Liouville. The hope is that the existence of a formal Theorem of Liouville might serve as a guideline to build appropriate measures related to ideal quasi two-dimensional flows.

2.3.2 Formal derivation of a Theorem of Liouville

Formal divergence in phase space. Let us suppose that we can see the space of vector-fields as an infinite dimensional phase space manifold $\mathcal{Z}$. The elements of $\mathbf{z} \in \mathcal{Z}$ are functions $\mathcal{D} \to \mathbb{R}^d$, so that they associate to any position $\mathbf{r} \in \mathcal{D}$ a d-dimensional vector $\mathbf{z}(\mathbf{r}) = (\mathbf{z}_1(\mathbf{r}), ..., \mathbf{z}_d(\mathbf{r}))$. The counterpart to the finite dimensional f-divergence (2.6) involves a mapping $\mathcal{F} : \mathcal{Z} \to \mathcal{Z}$ and any sufficiently regular function $f : \mathcal{Z} \to \mathbb{R}$ and reads

$$\nabla_f \cdot \mathcal{F}(\mathbf{z}) = \sum_{\alpha=1}^{d} \int_{\mathcal{D}} \mathrm{d}\mathbf{r} \frac{\delta}{\delta \mathbf{z}_\alpha(\mathbf{r})} \left[f \mathcal{F}_\alpha[\mathbf{r}] \right](\mathbf{z}). \tag{2.19}$$

Formal derivation of a Theorem of Liouville. Let us now suppose that we can define a measure μ defined over $\mathcal{Z}$, that has density f with respect to the formal measure $\mathcal{D}[\mathbf{z}]$. It is not clear whether this object is properly defined, and if it is, it should be defined through an appropriate discretization and limiting process. Anyhow, the average of an observable $\mathcal{A}$ for this measure could then be formally written as

$$\langle \mathcal{A} \rangle = \int \mathfrak{D}[\mathbf{z}] f(\mathbf{z}) \mathcal{A}(\mathbf{z}). \tag{2.20}$$

Formally,

$$\frac{\mathrm{d}}{\mathrm{dt}}\langle A\rangle = \int \mathfrak{D}[\mathbf{z}] f(\mathbf{z}) \frac{\mathrm{d}}{\mathrm{dt}}\mathcal{A}(\mathbf{z}) \tag{2.21}$$

$$= \int \mathfrak{D}[\mathbf{z}] f(\mathbf{z}) \int_{\mathcal{D}} \mathbf{dr} \sum_{\alpha=1}^{d} \frac{\delta \mathcal{A}(\mathbf{z})}{\delta \mathbf{z}_\alpha(\mathbf{r})} \mathcal{F}_\alpha[\mathbf{r}](\mathbf{z}) \tag{2.22}$$

$$= -\int \mathfrak{D}[\mathbf{z}] \mathcal{A}(\mathbf{z}) \underbrace{\int_{\mathcal{D}} \mathbf{dr} \sum_{\alpha=1}^{d} \frac{\delta}{\delta \mathbf{z}_\alpha(\mathbf{r})} \left(f \mathcal{F}_\alpha[\mathbf{r}]\right)(\mathbf{z})}_{\nabla_f \cdot \mathcal{F}}. \tag{2.23}$$

The last equality is obtained with an integration by part. Just as in the finite dimensional case, a simple condition for μ to be an invariant measure reads

$$\nabla_f \cdot \mathcal{F} = 0. \tag{2.24}$$

We call such a condition a Formal Theorem of Liouville.

Dynamical invariants and formal invariant measures. If one can identify an invariant $C(\mathbf{z})$ for the dynamics (2.18), then for any sufficiently regular g, the probability densities $g(C(\mathbf{z}))f(\mathbf{z})$ also define formal probability measures μ_g which are invariant for the dynamics. The formal proof relies on the following identities :

$$\begin{aligned}
\nabla_{(g\circ C)f} \cdot \mathcal{F}(\mathbf{z}) &= \int_{\mathcal{D}} \mathbf{dr} \sum_{\alpha=1}^{d} \frac{\delta}{\delta \mathbf{z}_\alpha(\mathbf{r})} \left((g\circ C) f \mathcal{F}_\alpha[\mathbf{r}]\right)(\mathbf{z}) \\
&= g(C(\mathbf{z})) \underbrace{\int_{\mathcal{D}} \mathbf{dr} \sum_{\alpha=1}^{d} \frac{\delta}{\delta \mathbf{z}_\alpha(\mathbf{r})} \left(f \mathcal{F}_\alpha[\mathbf{r}]\right)(\mathbf{z})}_{\nabla_f \cdot \mathcal{F}(\mathbf{z}) = 0} \\
&\qquad + f(\mathbf{z}) g'(C(\mathbf{z})) \underbrace{\int_{\mathcal{D}} \mathbf{dr} \sum_{\alpha=1}^{d} \frac{\delta C(\mathbf{z})}{\delta \mathbf{z}_\alpha(\mathbf{r})} \mathcal{F}_\alpha[\mathbf{r}](\mathbf{z})}_{= \frac{\mathrm{d}C(\mathbf{z})}{\mathrm{dt}} = 0}.
\end{aligned}$$

2.3.3 Examples

Condition (2.24) is satisfied for the quasi two-dimensional ideal fluid models presented in the first chapter.

2.3.3.1 Ideal 2D flows

The transport equation for the scalar vorticity ($\omega = (\nabla \times \mathbf{v}) \cdot \hat{\mathbf{z}}$) reads

$$\partial_t \omega = -\nabla \cdot (\mathbf{v}\omega) \underset{\text{def}}{=} \mathcal{F}(\omega). \tag{2.25}$$

It is supplemented by the incompressibility condition $\nabla \cdot \mathbf{v} = 0$. The formal divergence in phase space of the vector field $\mathcal{F}(\omega)$ is

$$\nabla \cdot \mathcal{F}(\omega) = \int_{\mathcal{D}} \mathrm{d}\mathbf{r} \, \frac{\delta \mathcal{F}[\mathbf{r}](\omega)}{\delta \omega(\mathbf{r})} = -\int_{\mathcal{D}} \mathrm{d}\mathbf{r} \nabla \cdot \frac{\delta(\mathbf{v}\omega)}{\delta \omega(\mathbf{r})} = -\oint_{\partial \mathcal{D}} \mathbf{dS} \cdot \frac{\delta}{\delta \omega(\mathbf{r})} \omega \mathbf{v}. \tag{2.26}$$

If the domain is doubly periodic, or has rigid walls, so that a no-slip condition is enforced at the boundaries, the integral vanishes. In that case, we conclude that a formal Theorem of Liouville holds, and that the formal measure $\mathfrak{D}[\omega]$ is invariant.

2.3.3.2 Ideal axisymmetric flows

In terms of the microscopic variables $\sigma = r u_\theta$ and $\xi = r^{-1}\omega_\theta$, the ideal axisymmetric equations in a cylindrical domain $\mathcal{D}$ (1.13) can be recast as

$$\partial_t \xi = -\nabla_\odot \cdot \xi \mathbf{v} + \frac{1}{r^4} \partial_z \sigma^2 \underset{\text{def}}{=} \mathcal{F}_\xi(\sigma, \xi) \quad \text{and} \quad \partial_t \sigma = -\nabla_\odot \cdot \sigma \mathbf{v} \underset{\text{def}}{=} \mathcal{F}_\sigma(\sigma, \xi). \tag{2.27}$$

$\nabla_\odot \cdot = r^{-1}\partial_r r + \partial_z$ is the divergence operator in cylindrical geometry with no dependence on the coordinate θ. The incompressibility condition reads $\nabla_\odot \cdot \mathbf{v} = 0$. The vector-field $\mathcal{F}(\sigma, \xi) = (\mathcal{F}_\sigma(\sigma, \xi), \mathcal{F}_\xi(\sigma, \xi))$ is divergence-free in phase space. Indeed, the contribution from σ to the vector field divergence is

$$\int_{\mathcal{D}} \mathrm{d}\mathbf{r} \frac{\delta \mathcal{F}_\sigma[\mathbf{r}]}{\delta \sigma(\mathbf{r})} = -\oint_{\partial \mathcal{D}} \mathbf{dS} \cdot \frac{\delta(\sigma \mathbf{v})}{\delta \sigma(\mathbf{r})}. \tag{2.28}$$

It is therefore vanishing if one considers standard no-slip boundary conditions on the domain boundaries for the velocity field.

The contribution from ξ to the vector field divergence vanishes as well. It reads

$$\int_{\mathcal{D}} \mathrm{d}\mathbf{r} \frac{\delta \mathcal{F}_\xi[\mathbf{r}]}{\delta \xi(\mathbf{r})} = -\oint_{\partial \mathcal{D}} \mathbf{dS} \cdot \frac{\delta(\xi \mathbf{v})}{\delta \xi(\mathbf{r})} + \int_{\mathcal{D}} \mathrm{d}\mathbf{r} \frac{\delta}{\delta \xi(\mathbf{r})} \partial_z (r^{-4}\sigma^2). \tag{2.29}$$

The first term of the r.h.s of (2.29) vanishes with no-slip boundary conditions and the second term vanishes because the quantity $\partial_z \sigma^2$ is independent from $\xi(\mathbf{r})$. Hence, we conclude that the formal measure $\mathfrak{D}[\xi]\mathfrak{D}[\sigma]$ is an invariant measure for the dynamics which describes the motion of axially symmetric ideal flows.

Note: A similar computation shows that in the case of ideal 2D magneto fluids , the formal measure $\mathfrak{D}[A]\mathfrak{D}[\omega]$ satisfies a formal Theorem of Liouville.

2.3.3.3 Shallow water flows

In the case of the Shallow-Water model, a formal Liouville Theorem holds, but the variables involved must be carefully chosen. The formal theorem of Liouville can for example easily be demonstrated for the set of variables $(M_x = h v_x, M_y = h v_y, h)$. In

terms of those variables, the Shallow-Water equations read

$$\partial_t M_x + \partial_x \left(\frac{M_x^2}{h} \right) + \partial_y \left(\frac{M_x M_y}{h} \right) + \partial_x \left(\frac{gh^2}{2} - f M_y = 0 \right), \tag{2.30}$$

$$\partial_t M_y + \partial_x \left(\frac{M_x My}{h} \right) + \partial_y \left(\frac{M_y^2}{h} \right) + \partial_y \left(\frac{gh^2}{2} + f M_x = 0 \right), \tag{2.31}$$

$$\text{and} \quad \partial_t h + \partial_x M_x + \partial_y M_y = 0. \tag{2.32}$$

The contribution to the formal divergence of the vector field coming from the field h is clearly vanishing. The contribution from the field M_x reads

$$\int_{\mathcal{D}} \mathbf{dr} \, \frac{\delta}{\delta M_x(\mathbf{r})} \left[-\nabla \cdot (M_x \frac{\mathbf{M}}{h} + \partial_x \left(\frac{1}{2} g h^2 \right) + f M_y \right]. \tag{2.33}$$

The second and third terms in Equation (2.33) vanish because they are independent from M_x. The first term can be integrated using Green theorem. It vanishes for doubly-periodic domains or no-slip boundary conditions. For similar reasons, the M_y contribution to the formal divergence also vanishes and hence a formal Theorem of Liouville holds for the formal measure $\mathfrak{D}[M_x]\mathfrak{D}[M_y]\mathfrak{D}[h]$.

2.3.4 Formal Theorem of Liouville and Hamiltonian structure of the ideal Euler equations

Is the Formal Theorem of Liouville obvious ? It may seem surprising that the derivation of a formal theorem of Liouville is so direct for all the models that we considered. This is – I think – a direct consequence of the infinite dimensional Hamiltonian structure of those ideal flows. The Hamiltonian description of the Euler equations was thoroughly explored and exhibited in a series of papers in the 80's and 90's in the context of plasma physics [Morrison and Hazeltine, 1984,Marsden and Morrison, 1984] and geophysics [Salmon, 1983,Salmon, 1988,Shepherd, 1990]. It is now well-known that the Eulerian description of ideal fluids can be described in terms of a non-canonical Hamiltonian structure. It turns out that the Hamiltonian structure that accounts for the description of the ideal 2D, 2D-MHD, axisymmetric, and shallow-water flows involve the exact same sets of variables than the ones for which a Formal Theorem of Liouville holds. This may be related to the infinite dimensional symplectic operator involved in the Hamiltonian description of those flows being of "Lie-Poisson" type, *e.g.* linear with respect to the variables describing the dynamics.

Illustrative Lie-Poisson dynamics and the ideal axisymmetric case. Let me just illustrate this comment with the Hamiltonian description of ideal axisymmetric flows. Infinite Hamiltonian dynamics is a subtle topic. I don't want to – and I can't – discuss the topic in details nor in full rigor.

The parallel between finite and infinite dimensional noncanonical hamiltonian dynamics (2.12) and the infinite dimensional is made suggestive if we introduce Poisson brackets. In the finite dimensional case, the dynamical variable $\mathbf{z} = (z_1..z_n)$ belongs to

$\mathbb{R}^n$. Upon defining the Poisson Bracket $\{,\}$ as:

$$\begin{gathered}\{f,g\} = \sum_{i,j\in[\![1;n]\!]^2} \frac{\partial f}{\partial z_i} J_{ij} \frac{\partial f}{\partial z_j} \\ \text{for any functions} \quad f = f(\mathbf{z},t) \text{ and } g = g(\mathbf{z},t) : \mathbb{R}^n \times \mathbb{R} \to \mathbb{R},\end{gathered} \tag{2.34}$$

the dynamics (2.12) can be recast into

$$\dot{f} = \{f, H\}\,. \tag{2.35}$$

In the infinite dimensional case, $\mathbf{z} = (\mathbf{z}_\alpha)_{\alpha\in[\![1;d]\!]}$, and each $\mathbf{z}_\alpha$ is a field, namely $\mathbf{z}_\alpha : \mathcal{D} \to \mathbb{R}$. The counterpart to the bracket (2.34) is [Morrison, 1998]

$$\begin{gathered}\{F,G\} = \int_{\mathcal{D}} \mathrm{d}\mathbf{r} \frac{\delta F}{\delta \mathbf{z}_\alpha} \mathcal{J}^{\alpha\alpha'} \frac{\delta G}{\delta \mathbf{z}_{\alpha'}}, \\ \text{for any functionnals} \quad F(\mathbf{z}_\alpha, t) \text{ and } G(\mathbf{z}_\alpha, t) : (\mathcal{D} \to \mathbb{R}) \times \mathbb{R} \to \mathbb{R}.\end{gathered} \tag{2.36}$$

$\mathcal{J}$ is now a differential operator acting on the space of functionals . In order for $\{,\}$ to describe an actual Poisson Bracket, $\{,\}$ i/ needs to be antisymmetric ($\{F,G\}+\{G,F\} = 0$) and ii/ needs to satisfy the Jacobi identity $\{F,\{G,H\}\} + \{H,\{F,G\}\} + \{G,\{H,F\}\} = 0$. In an infinite dimensional Hamiltonian system, the dynamics of a field functional F can then be compactly written in terms of the relevant Hamiltonian H as :

$$\dot{F} = \{F, H\}\,. \tag{2.37}$$

The axisymmetric Lie-Poisson bracket. The "axisymmetric bracket" yielding the ideal three-dimensional axisymmetric dynamics in terms of the poloidal and toroidal variables ξ and σ can be found for example in [Szeri and Holmes, 1988] and reads

$$\begin{aligned}\{F,G\}^{\odot} = \int_{\mathcal{D}} \mathrm{d}\mathbf{r} \Bigg(&\xi(\mathbf{r}) \left[\frac{\delta G}{\delta \xi(\mathbf{r})}, \frac{\delta F}{\delta \xi(\mathbf{r})}\right] + \sigma(\mathbf{r}) \left[\frac{\delta G}{\delta \xi(\mathbf{r})}, \frac{\delta F}{\delta \sigma(\mathbf{r})}\right] \\ &+ \sigma(\mathbf{r}) \left[\frac{\delta G}{\delta \sigma(\mathbf{r})}, \frac{\delta F}{\delta \xi(\mathbf{r})}\right]\Bigg).\end{aligned} \tag{2.38}$$

The inner bracked $[,]$ is here given by

$$[f,g] = \frac{1}{r}\frac{\partial f}{\partial r}\frac{\partial g}{\partial z} - \frac{1}{r}\frac{\partial g}{\partial r}\frac{\partial f}{\partial z}. \tag{2.39}$$

The axisymmetric bracket (2.38) is a particular case of (2.36). In this case, $d = 2$, $\mathbf{z} = (\xi, \sigma)$, and the $\mathcal{J}^{\alpha\alpha'}$ are defined by

$$\begin{gathered}\mathcal{J}^{\xi\xi}\begin{bmatrix}\xi(\mathbf{r})\\ \sigma(\mathbf{r})\end{bmatrix} = [\xi(\mathbf{r}), \cdot], \qquad \mathcal{J}^{\sigma\sigma}\begin{bmatrix}\xi(\mathbf{r})\\ \sigma(\mathbf{r})\end{bmatrix} = 0, \\ \text{and} \quad \mathcal{J}^{\xi\sigma}\begin{bmatrix}\xi(\mathbf{r})\\ \sigma(\mathbf{r})\end{bmatrix} = \mathcal{J}^{\sigma\xi}\begin{bmatrix}\xi(\mathbf{r})\\ \sigma(\mathbf{r})\end{bmatrix} = [\sigma(\mathbf{r}), \cdot].\end{gathered} \tag{2.40}$$

The bilinearity of each of those operators make the axisymmetric bracket of "Lie-Poisson" type, and is the infinite dimensional analogue of the finite-dimensional Lie-Poisson structure briefly alluded to in Section (2.2.3.2) of the previous Chapter.

The same kind of brackets yields the equations for ideal two-dimensional magneto-hydrodynamics in terms of the magnetic potential and kinetic vorticity variables ([Morrison and Hazeltine, 1984, Marsden and Morrison, 1984]) , and for ideal two-dimensional Boussinesq flows in terms of density and vorticity variables [Abarbanel et al., 1986, Szeri and Holmes, 1988]. One only needs to replace the inner bracket, and use $[f, g] = \partial_x f \partial_y g - \partial_y f \partial_x g$ with standard cartesian coordinates instead of (2.39). The only substantial difference between ideal two-dimensional magnetohydrodynamics , two-dimensional Boussinesq flows and three-dimensional axisymmetric dynamics relies on the choice of the Hamiltonian to be used in combination with the bracket to actually describe the appropriate dynamics (2.37). For the three-dimensional axisymmetric dynamics , the Hamiltonian is $\mathcal{H}^{\odot}(\xi, \sigma) = \int_{\mathcal{D}} \mathbf{dr}\ (\xi(\mathbf{r})\psi(\mathbf{r}) + (4y)^{-1}\sigma(\mathbf{r})^2)$. For the two-dimensional magnetohydrodynamics , it is $\mathcal{H}^{\mathrm{mag}}(\omega, A) = \int_{\mathcal{D}} \mathbf{dr}\ (\omega(\mathbf{r})\psi(\mathbf{r}) + A(\mathbf{r})j(\mathbf{r}))$.

2.4 Conclusion

What have we learned so far ? Well, basically nothing very new. We have briefly explained what invariant measures are and why they emerge as natural objects to study in the context of finite-dimensional dynamical systems. We have argued that the existence of a Theorem of Liouville for time continuous dynamical systems allows one to easily identify some of those invariant measures. We have then identified a Formal version of the Theorem of Liouville, and argued that this theorem is satisfied for basically all the ideal flows that we are concerned with in the present work, provided that the sets of variables are properly chosen. The extension is purely formal. It nevertheless suggests that microcanonical measures should be worth investigating provided one can find a way to construct them. Such a construction will be described in chapter 3. Whether those measures do indeed turn out to be physically interesting and describe relevant features of quasi-bidimensional flows is not clear at this point.

Chapter 3

Statistical mechanics *à la* Kraichnan.

This chapter aims at describing the statistical mechanics of *truncated* 2D3C flows in the spirit of Kraichnan's derivation of absolute equilibria for two-dimensional turbulence. The absolute equilibria for two-dimensional magnetohydrodynamics were derived in [Fyfe and Montgomery, 1976] but I am unaware of any work describing the axisymmetric case. The comparison is however instructive. In spite of the close analogy between the axisymmetric and the magneto-hydro ideal fluid, the regimes of statistical equilibria are different from each other. The discussion is then extended to a wider family of 2D3C flows, which possess the same quadratic Casimir invariants as axisymmetric and two-dimensional magneto-hydro flows. It is illustrated by the numerical integration of a low-dimensional model of 2D3C turbulence.

Contents

3.1 Introduction: Statistical mechanics for finite-dimensional approximation of ideal flows.

Strategy. The Formal Theorem of Liouville which we described in the previous chapter suggests that one should try to build up some kinds of "formal" microcanonical ensembles to account for the statistical equilibrium properties of ideal flows. The word "formal" hides at least two major difficulties. First, as opposed to the discrete description of a gas of particles, ideal flows are intrinsically continuous. It is not clear how to define an appropriate thermodynamic limit. Second, ideal dynamics are usually constrained by an infinite set of dynamical invariants. It is not obvious how to use this infinite set to describe relevant statistical ensembles. One way to circumvent those two difficulties is to forget about the true ideal dynamics, and instead work on finite-dimensional approximations of the original equations. That way, classical statistical mechanics arguments can be used. The program to follow is then clear. One needs to i/ approximate the dynamics by a truncated dynamics with a finite number of degrees of freedom N, ii/ identify a Theorem of Liouville for the truncated dynamics, iii/ identify the dynamical invariants that survive the truncation, iv/ describe some statistical ensembles that are invariant for the truncated dynamics. One could also add a fifth point that would be v/ discuss the limit $N \to \infty$ of the truncated ensembles.

Absolute equilibria. A systematic and natural way to approximate the dynamics of ideal flows is to decompose the relevant fields of the dynamics over a convenient orthonormal set of modes and set to zero all but a finite set of the coefficients. If Fourier modes are used, and if only the modes whose wave numbers are below a prescribed cutoff k_{max} are kept, the approximation is referred to as a "Galerkin truncation". The aforementioned approach is the one taken by Kraichnan to build energy-enstrophy canonical ensembles relevant two-dimensional turbulence. In his 1967 paper [Kraichnan, 1967], Kraichnan mentions the existence of negative temperature Gibbs states for Galerkin truncations as a hint "towards an upward flow of vorticity, and therefore by the conservation laws, a downward flow of energy. of two-dimensional ideal flows". The equilibrium ensembles are labeled "absolute equilibria" [Kraichnan, 1967, Kraichnan and Montgomery, 1980, Frisch, 1996] and sometimes referred to as (inviscid) "equipartition ensembles" [Orszag, 1974].

Brief historical comment. Before Kraichnan, other physicists had tried to use this approach and describe Galerkin truncated ideal flows in terms of statistical ensembles. In a short, (nowadays) seldom -distributed but much cited paper, T.D. Lee considers truncations of three-dimensional flows, for which he proves the existence of a theorem of Liouville in the space of the Fourier coefficients. He then obtains the equipartition spectrum for the energy density $E(\mathbf{k}) \propto k^2$ [Lee, 1952] – corresponding to a statistical description in the microcanonical ensemble based on the energy. Lee writes the footnote remark that in the two-dimensional case the equipartition of energy should not hold because of the

"existence of a conservation law on vorticity". Even though the term "enstrophy" was not coined yet, the existence of the total "vorticity squared" as an inviscid invariant in two dimension was known – unlike for instance the helicity for the three-dimensional inviscid case. Its role in preventing the energy from leaking towards smaller scales of the problem was explained by Fjørtoft in his 1953 paper [Fjørtoft, 1953] and an argument can also be found on the last page of Batchelor's monograph [Batchelor, 1953]. The ingredients (i)-(ii)-(iii) for a statistical mechanics *à la* Kraichnan were therefore already known in 1953 but somehow not put together until 1967. It was not only a matter a vocabulary, as the term "enstrophy" was not used in Kraichnan's 1967 paper. It first appeared in a paper published by Leith a couple of months later [Leith, 1968, Eyink and Frisch, 2011]. [(a)]

Layout. In the next section, I briefly review the theory of absolute equilibria for the landmark cases of two-dimensional hydro and magnetohydrodynamical flows. In Section 3, I describe the axisymmetric case, for which the theory is *stricto sensu* not so insightful. Comments are made about Boussinesq flows. In Section 4, the discussion is widened to include a class of generalized 2D3C flows, and a shell model of 2D3C turbulence is used to illustrate some regimes of 2D3C absolute equilibria.

3.2 Two-dimensional hydro and magneto-hydro absolute equilibria.

3.2.1 Absolute equilibria for ideal two-dimensional flows.

I here briefly describe Kraichnan's theory of equipartition ensembles as applied to the two-dimensional case. The case has been thoroughly commented on since Kraichnan's original paper, but is useful to bear it in mind as a landmark example.

(i) Truncated dynamics. We consider a simply connected domain $\mathcal{D}$ – with say either impermeability or doubly periodic boundary conditions and decompose the vorticity field over a complete and orthonormal set of eigenfunctions $(\phi_{\mathbf{k}})_{\mathbf{k}\in\mathbb{Z}}$ satisfying $\nabla^2\phi_{\mathbf{k}} = -\kappa_{\mathbf{k}}^2\phi_{\mathbf{k}}$. We therefore write $\omega(\mathbf{r}) = \sum_{\mathbf{k}\in\mathbb{Z}^2}\omega_{\mathbf{k}}\phi_{\mathbf{k}}(\mathbf{r})$ with $\omega_{\mathbf{k}} = \phi_{\mathbf{k}}, \omega$. We introduce a high wave number cutoff κ_c and approximate the vorticity field as $\omega(\mathbf{r}) = \sum_{|\kappa_{\mathbf{n}}|<\kappa_c}\omega_{\mathbf{n}}\phi_{\mathbf{n}}(\mathbf{r})$. We write $N = N(\kappa_c)$ the number of modes $\kappa_{\mathbf{k}}$ such that $|\kappa_{\mathbf{k}}| \leq \kappa_c$. A truncated dynamics for two-dimensional flows is obtained from the Equation for the vorticity transport (1.7).

[(a)] The word "enstrophy" comes directly from the ancient Greek verb ενστρέφω ("enstrephô"), in which one can spot the root στροφή ("strophê"), which yields the poetic "strophe", or the less poetic "catastrophe". The prime sense of ενστρέφω is "to turn within" and is hence obviously related to the notion of vorticity. Note that by extension ενστρέφω also means "to retreat" (from the meditative point of view). Is this secondary meaning a hidden allusion to Robert H. Kraichnan's personal situation, who was working in 1967 as a self-employed physicist in the small town of Peterborough, New Hampshire – 2,963 residents in 1960 according to the 1960 US census ?

It describes the evolution of the set of modes $\omega_{\mathbf{k}}$ as

$$\begin{aligned}\dot{\omega_{\mathbf{k}}} &= \sum_{\mathbf{l},\mathbf{m}} C_{\mathbf{klm}}\kappa_{\mathbf{m}}^{-2}\omega_{\mathbf{l}}\omega_{\mathbf{m}} \text{ with } C_{\mathbf{klm}} = (\phi_{\mathbf{k}}, [\phi_{\mathbf{l}}, \phi_{\mathbf{m}}]) \quad \text{if } |\kappa_{\mathbf{l}}| \leq \kappa_c \\ &= 0 \quad \text{otherwise.}\end{aligned} \tag{3.1}$$

$\sum_{\mathbf{m}}$ is used as a short-hand notation for $\sum_{\mathbf{m}:|\kappa_{\mathbf{m}}|\leq\kappa_c}$. The scalar product $(,)$ is defined through $(f,g) = |\mathcal{D}|^{-1}\int_{\mathcal{D}} \mathbf{dr}\, f(\mathbf{r})g(\mathbf{r})$. [(a)]

(ii) Liouville property. The underlying phase space is identified as $\mathbb{R}^N$, with coordinates given by the $\omega_{\mathbf{k}_1}$,...,$\omega_{\mathbf{k}_N}$. Using integrations by parts, it is immediate to see that $C_{\tau(\mathbf{k})\tau(\mathbf{l})\tau(\mathbf{m})} = -C_{\mathbf{klm}}$ for any odd permutation τ and $C_{\tau(\mathbf{k})\tau(\mathbf{l})\tau(\mathbf{m})} = C_{\mathbf{klm}}$ for any even permutation τ. Therefore $C_{\mathbf{klm}}$ is zero whenever two indices coincide. A detailed theorem of Liouville stems directly from this observation :

$$\frac{\partial\dot{\omega_{\mathbf{k}}}}{\partial\omega_{\mathbf{k}}} = \sum_{\mathbf{m}} \underbrace{C_{\mathbf{kkm}}}_{=0}\kappa_{\mathbf{m}}^{-2}\omega_{\mathbf{m}} + \sum_{\mathbf{l}} \underbrace{C_{\mathbf{klk}}}_{=0}\kappa_{\mathbf{k}}^{-2}\omega_{\mathbf{l}} = 0. \tag{3.2}$$

Therefore, $\displaystyle\sum_{\mathbf{k}:\kappa_{\mathbf{k}}\leq\kappa_c} \frac{\partial\dot{\omega_{\mathbf{k}}}}{\partial\omega_{\mathbf{k}}} = 0$ for any cutoff κ_c.

(iii) Quadratic invariants.

Definitions. The symmetries of the coefficients $C_{\mathbf{klm}}$ imply that the truncated Energy $\mathcal{E}_N(\{\omega_{\mathbf{k}}\}) = \frac{1}{2}\sum_{\mathbf{k}}\kappa_{\mathbf{k}}^{-2}\omega_{\mathbf{k}}^2$ and the truncated enstrophy $\mathcal{G}_N(\{\omega_{\mathbf{k}}\}) = \frac{1}{2}\sum_{\mathbf{k}}\omega_{\mathbf{k}}^2$ are conserved by the truncated dynamics (3.2). A crude differentiation indeed yields

$$\dot{\mathcal{G}}_N = \sum_{\mathbf{k}} \omega_{\mathbf{k}}\dot{\omega_{\mathbf{k}}} = \sum_{\mathbf{k},\mathbf{l},\mathbf{m}} \omega_{\mathbf{k}}C_{\mathbf{klm}}\omega_{\mathbf{l}}\omega_{\mathbf{m}}\kappa_{\mathbf{m}}^{-2} = \frac{1}{2}\sum_{\mathbf{k},\mathbf{l},\mathbf{m}} \underbrace{(C_{\mathbf{klm}} + C_{\mathbf{lkm}})}_{=0}\omega_{\mathbf{k}}\omega_{\mathbf{l}}\omega_{\mathbf{m}}\kappa_{\mathbf{m}}^{-2} = 0, \tag{3.3}$$

and similarly $\dot{\mathcal{E}}_N = 0$.

Geometry of phase space. From a geometrical point of view, the presence of the aforesaid invariants put very strong constraints on the dynamics. Any trajectory in phase space is constrained to lie at the intersection of a N-sphere $\sum_{i=1}^N \omega_{\mathbf{k}_i} = 2G$ with a N-dimensional ellipsoid $\sum_{i=1}^N \kappa_{\mathbf{k}_i}^{-2}\omega_{\mathbf{k}_i} = 2E$ – see Figure 3.1 for an illustration in the case $N = 3$. Writing $\kappa_{\min} = \min_{|\kappa|<\kappa_c}|\kappa|$ and $\kappa_{\max} = \max_{|\kappa|<\kappa_c}|\kappa|$ the smallest and largest wavelengths of the truncated problem, it is visually clear (see Figure 3.1) that (i) The values of E and G for which the accessible phase space is non empty are the ones for which $\kappa_{\max}^{-2}G \leq E \leq \kappa_{\min}^{-2}G$. (ii) Within those bounds, if the total energy is low, say $E \simeq G\kappa_{\max}^{-2}$, then the motion will be confined to small scales – see Figure 3.1b. By contrast, if the total energy is high, say $E \simeq G\kappa_{\min}^{-2}$, the motion will be confined the largest scales available (Figure 3.1c).

[(a)] To obtain the dynamics 3.1, it suffices to write : $\omega = \sum_{\mathbf{k}}\dot{\omega}_{\mathbf{k}}\phi_{\mathbf{k}} = [\omega,\psi] = \sum_{\mathbf{l},\mathbf{m}}\omega_{\mathbf{l}}\psi_{\mathbf{m}}[\phi_{\mathbf{l}},\phi_{\mathbf{m}}] =$

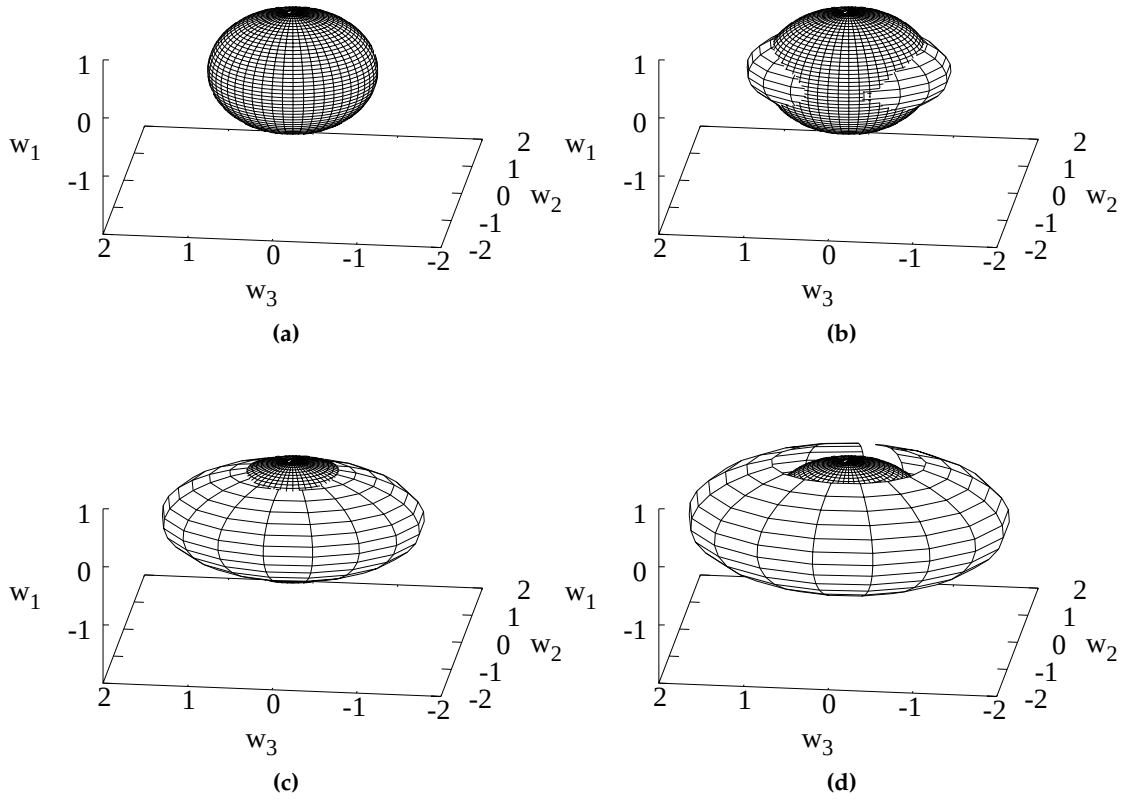

Figure 3.1: (a) A surface of constant enstrophy $\omega_1^2 + \omega_2^2 + \omega_3^2 = 2G = 1$ in a three dimensional phase space. The axes are sorted by increasing values of the eigenmodes κ_i. Here, $\kappa_1 = 1$, $\kappa_2 = \sqrt{2}$, $\kappa_3 = \sqrt{3}$. ($\kappa_1 < \kappa_2 < \kappa_3$). The surface is intersected by surfaces of constant energies ($\kappa_1^{-2}\omega_1^2 + \kappa_2^{-2}\omega_2^2 + \kappa_3^{-2}\omega_3^2 = 2E$) for $E = E_b = 0.35$ (b), $E = E_c = 0.45$ (c) and $E = E_d = 0.55$ (d). Note that $\kappa_3^{-2}G \leq E_b < E_c \leq \kappa_1^{-2}G$ and $E_d > \kappa_1^{-2}G$. The intersection between the surfaces is non empty provided $\kappa_3^{-2}G \leq E \leq \kappa_1^{-2}G$.

(iv) Invariant measures.

Finite dimensional microcanonical measures. In order to refine those two simple geometrical considerations, and get quantitative estimates for the distribution of the energy among the modes, it is extremely natural to investigate energy-enstrophy microcanonical ensembles. The finite dimensional microcanonical probability measures $\mu^{\text{micro}}_{N,E,G}$ are defined as the uniform probability measures over surfaces of constant energies and enstrophies. They can be written in terms of the accessible phase space volume $\Omega_N(E,G)$ as

$\sum_{\mathbf{k},\mathbf{l},\mathbf{m}} \omega_{\mathbf{l}}\psi_{\mathbf{m}}(\phi_{\mathbf{k}},[\phi_{\mathbf{l}},\phi_{\mathbf{m}}])\phi_{\mathbf{k}}$.

$$\mu^{\text{micro}}_{N,E,G}(\{\omega_{\mathbf{k}}\}) = \frac{1}{\Omega_N(E,G)}\delta(\mathcal{E}_N(\{\omega_{\mathbf{k}}\}) - E)\,\delta(\mathcal{G}_N(\{\omega_{\mathbf{k}}\}) - G)\prod_{\mathbf{k}:\kappa_{\mathbf{k}}\leq\kappa_c}\mathrm{d}\omega_{\mathbf{k}} \tag{3.4}$$

$$\text{with}\quad \Omega_N(E,G) = \int_{\mathbb{R}^N}\prod_{\mathbf{k}:\kappa_{\mathbf{k}}\leq\kappa_c}\mathrm{d}\omega_{\mathbf{k}}\;\delta(\mathcal{E}_N(\{\omega_{\mathbf{k}}\}) - E)\,\delta(\mathcal{G}_N(\{\omega_{\mathbf{k}}\}) - G). \tag{3.5}$$

From the Theorem of Liouville, we know that those measures are invariant for the truncated dynamics. Besides, they have a clear geometrical interpretation. As commonly the case in statistical mechanics, computations within microcanonical ensembles may however turn out to be very difficult to do. As noted in [Khinchin, 1949, P.113], the difficulty comes from the fact that within the microcanonical ensemble "the various components are mutually dependent due to the constancy of total energy" – and here also of total enstrophy. Except in the two limiting cases $E/G = \kappa_{\text{min}}^{-2}$ and $E/G = \kappa_{\text{max}}^{-2}$ and in the trivial cases $E/G > \kappa_{\text{min}}^{-2}$ and $E/G < \kappa_{\text{max}}^{-2}$, the difficulty is apparent. It is much simpler to consider averages within a canonical ensemble.

Finite dimensional canonical measures. To define canonical ensembles for the truncated two-dimensional dynamics, an inverse energy temperature β and an inverse enstrophy temperature α [Kraichnan and Montgomery, 1980] are introduced. The canonical distribution is then defined as

$$\begin{aligned}\mu^{\text{cano}}_{N,\alpha,\beta}(\{\omega_{\mathbf{k}}\},\{\mathrm{d}\omega_{\mathbf{k}}\}) &= \frac{1}{\mathcal{Z}_N(\alpha,\beta)}\prod_{\mathbf{k}:\kappa_{\mathbf{k}}\leq\kappa_c}\mathrm{d}\omega_{\mathbf{k}}\,e^{-\beta\mathcal{E}_N(\{\omega_{\mathbf{k}}\})-\alpha\mathcal{G}_N(\{\omega_{\mathbf{k}}\})}\\ \text{with}\quad \mathcal{Z}_N(\alpha,\beta) &= \int_{\mathbb{R}^N}\prod_{\mathbf{k}:\kappa_{\mathbf{k}}\leq\kappa_c}\mathrm{d}\omega_{\mathbf{k}}\,e^{-\beta\mathcal{E}(\{\omega_{\mathbf{k}}\})-\alpha\mathcal{G}(\{\omega_{\mathbf{k}}\})}.\end{aligned} \tag{3.6}$$

The quantity $\beta\mathcal{E}_N(\{\omega_{\mathbf{k}}\})+\alpha\mathcal{G}_N(\{\omega_{\mathbf{k}}\})$ is preserved by the truncated dynamics. Hence, those canonical measures are also invariant measures for the truncated dynamics. In order for the canonical measures to define appropriate probability measures over the phase space, β and α must be such that the partition function $\mathcal{Z}_N(\alpha,\beta)$ is not infinite. In this case, the average of an observable $\mathcal{O}(\{\omega_{\mathbf{k}}\})$ within the canonical ensemble is naturally defined as :

$$\langle\mathcal{O}\rangle^{\text{cano}}_{N,\alpha,\beta} = \int_{\mathbb{R}^N}\mu^{\text{cano}}_{N,\alpha,\beta}(\{\omega_{\mathbf{k}}\},\{\mathrm{d}\omega_{\mathbf{k}}\})\,\mathcal{O}(\{\omega_{\mathbf{k}}\}). \tag{3.7}$$

Observables of particular interest will be single-mode observables such as the single-mode enstrophy $G_{\mathbf{k}} = \omega_{\mathbf{k}}^2$ or the single-mode energy $E_{\mathbf{k}} = \kappa_{\mathbf{k}}^{-2}\omega_{\mathbf{k}}^2$.

Canonical measures or microcanonical measures ? For *small* values of the energies $E_{\mathbf{k}}$ and the enstrophies $G_{\mathbf{k}}$, it is a traditional textbook exercise to show that microcanonical distributions are well approximated by canonical distributions. Here, because the energy and the enstrophy are sums of squares, the microcanonical probability $\mu^{\text{micro}}_{\mathbf{k}}(e,g)$ that the single mode $\mathbf{k}$ has an energy e and an enstrophy g is simply the probability that

all the other modes have energy $E-e$ and enstrophy $G-g$:

$$\mu^{\text{micro}}_{\mathbf{k}}(e,g)=\frac{\Omega_{N,\mathbf{k}}(E-e,G-g)}{\Omega_N(E,G)}. \tag{3.8}$$

Here, $\Omega_{N,\mathbf{k}}$ simply denotes the restricted phase space volume, obtained from equation (3.5) with an integration running on all the N modes but the mode $\mathbf{k}$. Upon introducing the entropies $S_N(E,G)=\frac{1}{N}\log\Omega_N(E,G)$ and $S_{N,\mathbf{k}}(E,G)=\frac{1}{N}\log\Omega_N(E,G)$ one can write down, if $e\ll E$ and $g\ll G$, that

$$\mu^{\text{micro}}_{\mathbf{k}}(e,g)\simeq\frac{\Omega_{N,\mathbf{k}}(E,G)}{\Omega_N(E,G)}\exp\left\{-\overbrace{N\frac{\partial S_{N,\mathbf{k}}}{\partial E}}^{\beta(N)}e-\overbrace{N\frac{\partial S_{N,\mathbf{k}}}{\partial G}}^{\alpha(N)}g\right\}\propto e^{-\beta e-\alpha g}; \tag{3.9}$$

and a canonical distribution is retrieved.

The case $N=3$ may give misleading insights for the case $N=\infty$. However, the geometrical considerations of paragraph (iii) can make us already anticipate that at least for some specific values of E and G – $E\lesssim G/\kappa^2_{\text{min}}$ as in Figure 3.1c for instance – the requirement $e\ll E$ and $g\ll G$ will not hold.

Description of the canonical absolute equilibria. The energy and the enstrophy are sums of squares. Hence, the canonical partition function $\mathcal{Z}_N(\alpha,\beta)$ can be completely factorized as

$$\mathcal{Z}_N(\alpha,\beta)=\prod_{\mathbf{k}:|\kappa_{\mathbf{k}}|\leq\kappa_c}\mathcal{Z}_{N,\mathbf{k}}(\alpha,\beta),\quad\text{where}\quad\mathcal{Z}_{N,\mathbf{k}}(\alpha,\beta)=\int_{\mathbb{R}}\mathrm{d}\omega_{\mathbf{k}}\,e^{-\left(\beta\kappa_{\mathbf{k}}^{-2}+\alpha\right)\frac{\omega^2_{\mathbf{k}}}{2}}. \tag{3.10}$$

The partition function takes a finite value provided that $\beta+\alpha\kappa^2_{\mathbf{k}}>0$ for any wave number $\mathbf{k}$ such that $|\kappa_{\mathbf{k}}|<\kappa_c$. If such is the case, the one-point functions $\mathcal{Z}_{N,\mathbf{k}}(\alpha,\beta)$ can be computed with a standard Gaussian integration :

$$\mathcal{Z}_{N,\mathbf{k}}(\alpha,\beta)=\sqrt{\frac{2\pi\kappa^2_{\mathbf{k}}}{\beta+\alpha\kappa^2_{\mathbf{k}}}}. \tag{3.11}$$

Within the canonical ensemble, the average energy and enstrophy per mode are directly obtained from the $\mathcal{Z}_{N,\mathbf{k}}(\alpha,\beta)$ as

$$\begin{aligned}&\langle E_{\mathbf{k}}\rangle^{\text{cano}}_{N,\alpha,\beta}=-\frac{\partial\log\mathcal{Z}_{N,\mathbf{k}}}{\partial\beta}=\frac{1}{2\left(\beta+\alpha\kappa^2_{\mathbf{k}}\right)}\quad\text{(average energy per mode)},\\ \text{and}\quad&\langle G_{\mathbf{k}}\rangle^{\text{cano}}_{N,\alpha,\beta}=-\frac{\partial\log\mathcal{Z}_{N,\mathbf{k}}}{\partial\alpha}=\frac{\kappa^2_{\mathbf{k}}}{2\left(\beta+\alpha\kappa^2_{\mathbf{k}}\right)}\quad\text{(average enstrophy per mode)}.\end{aligned} \tag{3.12}$$

A typical wavelength $\kappa_{\alpha\beta}=|\beta/\alpha|^{1/2}$ can be defined, and used to make a distinction between the equilibrium regimes, which are summarized on Figure 3.2 :

(a) $\alpha > 0$ and $-\alpha\kappa_{\min}^2 < \beta < 0$, in which

$$\langle E_{\mathbf{k}}\rangle_{N,\alpha,\beta}^{\text{cano}} = \kappa_{\mathbf{k}}^{-2}\langle G_{\mathbf{k}}\rangle_{N,\alpha,\beta}^{\text{cano}} = \frac{1}{2(-\beta)\left(\dfrac{\kappa_{\mathbf{k}}^2}{\kappa_{\alpha\beta}^2} - 1\right)}. \tag{3.13}$$

(b) $\beta > 0$ and $\alpha > 0$, in which

$$\langle E_{\mathbf{k}}\rangle_{N,\alpha,\beta}^{\text{cano}} = \kappa_{\mathbf{k}}^{-2}\langle G_{\mathbf{k}}\rangle_{N,\alpha,\beta}^{\text{cano}} = \frac{1}{2\beta\left(1 + \dfrac{\kappa_{\mathbf{k}}^2}{\kappa_{\alpha\beta}^2}\right)}. \tag{3.14}$$

(c) $\beta > 0$ and $-\beta\kappa_{\max}^{-2} < \alpha < 0$, in which

$$\langle E_{\mathbf{k}}\rangle_{N,\alpha,\beta}^{\text{cano}} = \kappa_{\mathbf{k}}^{-2}\langle G_{\mathbf{k}}\rangle_{N,\alpha,\beta}^{\text{cano}} = \frac{1}{2\beta\left(1 - \dfrac{\kappa_{\mathbf{k}}^2}{\kappa_{\alpha\beta}^2}\right)}. \tag{3.15}$$

In regime (a), the distribution of energy is peaked for $\kappa_{\mathbf{k}} \to \kappa_{\alpha\beta}^{+}$. The energy is confined on the large scales. In regime (c), the distribution of energy peaks for $\kappa_{\mathbf{k}} \to \kappa_{\alpha\beta}^{-}$: hence most of the energy is typically located on small scales. $\beta = 0$ is a limiting case between regime (a) and regime (b) and corresponds to an equipartition of enstrophy among the modes. The case $\alpha = 0$ is in between regime (b) and regime (c) and corresponds to an equipartition of the energy among the modes – see Figure 3.2 [(a)].

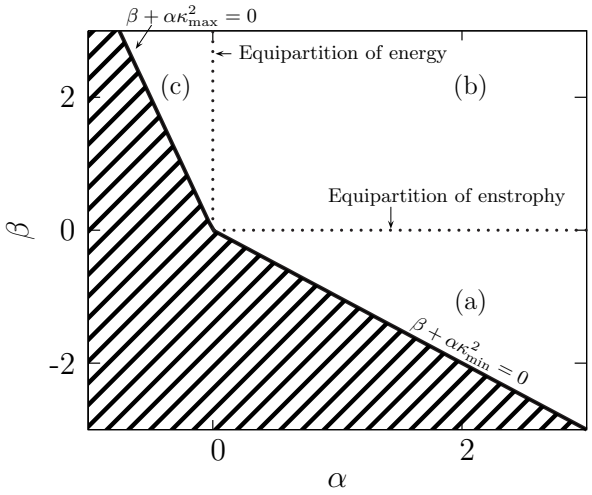

Figure 3.2: Regimes of absolute equilibria in the two-dimensional case, represented in the $\alpha - \beta$ plane.

(v) Discussion of the limit $N \to \infty$.

[(a)] One may also want to think in terms of spectra of energy, $e(\kappa) = \dfrac{\mathrm{d}}{\mathrm{d}\kappa}\displaystyle\sum_{\mathbf{k}:\kappa_{\mathbf{k}}\le|\kappa|}\langle E_{\mathbf{k}}\rangle_{N,\alpha,\beta}^{\text{cano}}$. The equipartition of energy yields $e(\kappa) \propto \kappa$ and the equipartition of enstrophy yields $e(\kappa) \propto \kappa^{-1}$.

Within the canonical ensemble. Until now, we have described finite-dimensional measures, and have not been concerned by any kind of thermodynamic limit. Simply letting $N \to \infty$ in equations (3.12) either yields a trivial limit (the total energy is zero) or an ultraviolet catastrophe (the total energies and enstrophies become infinite). A slightly artificial way to avoid the catastrophe is to ask the following question : can we find a scaling for the Lagrange multipliers as a function of N or $\kappa_{\max}$ such that the averaged total energy and total enstrophy remain finite ? To answer this question, let us first evaluate the average enstrophy and energy per mode (3.12) in the limit of a large, but finite cutoff $\kappa_c = \kappa_{\max}$.

We write $\langle \mathcal{E}_N \rangle^{\text{cano}}_{N,\alpha,\beta} = \sum_{\mathbf{k}:|\kappa_\mathbf{k}|\leq\kappa_c} \langle E_\mathbf{k} \rangle^{\text{cano}}_{N,\alpha,\beta}$ and $\langle \mathcal{G}_N \rangle^{\text{cano}}_{N,\alpha,\beta} = \sum_{\mathbf{k}:|\kappa_\mathbf{k}|\leq\kappa_c} \langle G_\mathbf{k} \rangle^{\text{cano}}_{N,\alpha,\beta}$ and liberally estimate the sum $\displaystyle\sum_{\mathbf{k}:|\kappa_\mathbf{k}|\leq\kappa_c}$ with a continuous integration in the space of eigenmodes $\dfrac{|\mathcal{D}|}{2\pi}\displaystyle\int_{\kappa_{\min}}^{\kappa_{\max}} \kappa \mathrm{d}\kappa$, hereby obtaining :

$$\begin{aligned} \langle \mathcal{E}_N \rangle^{\text{cano}}_{N,\alpha,\beta} &\underset{N\to\infty}{\sim} \frac{|\mathcal{D}|}{8\pi\alpha} \log \frac{\beta + \alpha\kappa^2_{\max}}{\beta + \alpha\kappa^2_{\min}} \\ \text{and} \quad \langle \mathcal{G}_N \rangle^{\text{cano}}_{N,\alpha,\beta} &\underset{N\to\infty}{\sim} \frac{|\mathcal{D}|}{4\pi\alpha} \left\{ \frac{\kappa^2_{\max} - \kappa^2_{\min}}{2} - \frac{\beta}{2\alpha} \log \frac{\beta + \alpha\kappa^2_{\max}}{\beta + \alpha\kappa^2_{\min}} \right\}. \end{aligned} \tag{3.16}$$

[(a)] To work out a thermodynamic limit as $\kappa_{\max} \to \infty$, we look now for an asymptotic expansion of the inverse temperatures that makes the average enstrophies and energies converge to finite values G and E :

$$\alpha(\kappa_{\max}) = \kappa^2_{\max}(\alpha^\star + o(1)) \quad \text{and} \quad \beta(\kappa_{\max}) = \beta^\star \alpha(\kappa_{\max})(1 + \eta(\kappa_{\max})). \tag{3.18}$$

$\alpha^\star$ and $\beta^\star$ are two yet undetermined constants, that can be thought of as normalized inverse temperatures. η is a function that vanishes at ∞. Plugging (3.18) into (3.16), and requiring that E and G are finite impose to choose

$$\begin{aligned} \alpha^\star = \frac{|\mathcal{D}|}{8\pi}(G - \kappa^2_{\min} E)^{-1}, \qquad \beta^\star = -\kappa^2_{\min}, \\ \text{and} \quad \eta(\kappa_{\max}) = \kappa^2_{\min} \exp\left(-\frac{\kappa^2_{\max} E}{G - \kappa^2_{\min} E} \right). \end{aligned} \tag{3.19}$$

Thermodynamically stated, the limit corresponds to $\beta \to -\infty$, $\alpha \to +\infty$ and $\beta/\alpha \to -\kappa^2_{\min}$. In this limit, there is a one-to-one relationship between the renormalized inverse temperatures and the values of the energies and enstrophies. The thermodynamic limit describes a condensation regime, in which all the energy concentrates on the largest scale available. The enstrophy temperature $\alpha^\star$ measures the excess enstrophy on scales smaller than the largest one. The smallest wavelength – *ie* the largest scale – acts as an energy

[(a)] For example, the formula for the average enstrophy simply comes from the identity, valid for $\alpha \neq 0$,

$$\frac{1}{2}\int_{\kappa_{\min}}^{\kappa_{\max}} \mathrm{d}\kappa \frac{\kappa^3}{\beta + \alpha\kappa^2} = \frac{1}{2\alpha}\int_{\kappa_{\min}}^{\kappa_{\max}} \mathrm{d}\kappa \left\{ \kappa - \frac{\beta\kappa}{\beta + \alpha\kappa^2} \right\}. \tag{3.17}$$

which is then integrated – and multiplied by $|\mathcal{D}|/2\pi$ – to yield (3.16).

sink.

Canonical vs microcanonical ensemble. It is not so clear which interpretation should be given to the thermodynamical condensation regime found within the canonical ensemble. "In spite of the fact that for small components the distribution laws based on [the microcanonical distribution] and [the canonical distribution] are almost identical, such is not the case for the large components." [Khinchin, 1949, p.113]. The latter situation precisely occurs in the energy-enstrophy canonical ensemble, since the smallest mode acts as an energy sink on which the energy condensates.

However, a direct asymptotic evaluation of the microcanonical energy-enstrophy measure (3.5) is possible, although more technical. An example of such a calculation is shown in [Bouchet and Corvellec, 2010]. In this paper, it is found that the microcanonical energy-enstrophy microcanonical entropy $S_N(E,G) = \dfrac{\log \Omega_N(E,G)}{N}$ has a well-defined asymptotic limit $S(E,G) = \log 2 + \dfrac{1}{2}\log\left(G - \kappa^2_{\min} E\right)$. The microcanonical inverse temperatures are then $\alpha = \dfrac{\partial S}{\partial G} = \left(G - \kappa^2_{\min} E\right)^{-1}$ and $\beta = \dfrac{\partial S}{\partial E} = -\kappa^2_{\min}\left(G - \kappa^2_{\min} E\right)^{-1}$, exactly akin to the values of the reduced canonical temperatures in the condensation regime (3.19), apart from an unimportant geometric factor $\dfrac{|\mathcal{D}|}{8\pi}$.

The condensation regime obtained through a well-chosen scaling of the canonical inverse temperatures may seem dubious. It does in fact correspond to a physical regime, as it yields the same result than a more technical estimation of the more geometric microcanonical measure. In this regime, whatever the value of the energy compatible with an enstrophy constraint, all the energy condensates on the largest scale. Note, that the geometric picture of paragraph (iii) was useful to understand the construction of the measures but may also provide a misleading intuition for the case $N \to \infty$. In particular, the situation $E \simeq \kappa^2_{\max} G$ depicted on Figure 3.1c – in which energy is at small scales – does not "survive" the thermodynamic limit, unless in the limit of a vanishing energy.

In a nutshell, the enstrophy prevents the ultraviolet catastrophe.

3.2.2 Absolute equilibria for ideal two-dimensional magnetohydrodynamics.

Truncated dynamics and Theorem of Liouville. The previous calculation is readily extended to the case of ideal two-dimensional magnetohydrodynamics , using the magnetic potential A and the vorticity ω as independent Liouville variables. With the same notations as in the two-dimensional case , and upon approximating the magnetic potential as $A = \sum_{\mathbf{k}:|\kappa_\mathbf{k}|\leq\kappa_c} a_\mathbf{k}\phi_\mathbf{k}$ and the vorticity as $\omega = \sum_{\mathbf{k}:|\kappa_\mathbf{k}|\leq\kappa_c} a_\mathbf{k}\phi_\mathbf{k}$, a truncated dynamics is obtained :

$$\dot{a}_\mathbf{k} = \sum_{\mathbf{l},\mathbf{m}} C_{\mathbf{klm}}\kappa_\mathbf{m}^{-2} a_\mathbf{l}\omega_\mathbf{m} \quad \text{and} \quad \dot{\omega}_\mathbf{k} = \sum_{\mathbf{l},\mathbf{m}} C_{\mathbf{klm}}\left(\kappa_\mathbf{m}^{-2}\omega_\mathbf{l}\omega_\mathbf{m} + \kappa_\mathbf{m}^{2} a_\mathbf{l} a_\mathbf{m}\right), \tag{3.20}$$

for which a Theorem of Liouville holds :

$$\frac{\partial \dot{a}_{\mathbf{k}}}{\partial a_{\mathbf{k}}} + \frac{\partial \dot{\omega}_{\mathbf{k}}}{\partial \omega_{\mathbf{k}}} = 2 \sum_{\mathbf{m}} \underbrace{C_{\mathbf{kkm}}}_{=0} \kappa_{\mathbf{m}}^{-2} \omega_{\mathbf{m}} + \sum_{\mathbf{l}} \underbrace{C_{\mathbf{klk}}}_{=0} \kappa_{\mathbf{k}}^{-2} \omega_{\mathbf{l}} = 0. \tag{3.21}$$

Dynamical invariants. The truncated dynamics (3.20) preserve three rugged invariants, which we can identify as

$$\mathcal{E}_N(A,\omega) = \overbrace{\frac{1}{2} \sum_{\mathbf{k}:|\kappa_{\mathbf{k}}|\leq\kappa_c} \kappa_{\mathbf{k}}^2 a_{\mathbf{k}}^2}^{=\mathcal{E}_N^{\text{kin}}(A,\omega)} + \overbrace{\frac{1}{2} \sum_{\mathbf{k}:|\kappa_{\mathbf{k}}|\leq\kappa_c} \kappa_{\mathbf{k}}^{-2} \omega_{\mathbf{k}}^2}^{=\mathcal{E}_N^{\text{mag}}(A,\omega)} \quad \text{(energy)} \quad , \tag{3.22}$$

$$\mathcal{H}_N(A,\omega) = \sum_{\mathbf{k}:|\kappa_{\mathbf{k}}|\leq\kappa_c} a_{\mathbf{k}} \omega_{\mathbf{k}} \quad \text{(cross helicity)} \quad , \tag{3.23}$$

$$\mathcal{A}_N(A,\omega) = \frac{1}{2} \sum_{\mathbf{k}:|\kappa_{\mathbf{k}}|\leq\kappa_c} a_{\mathbf{k}}^2 \quad \text{(magnetic potential squared)} \quad . \tag{3.24}$$

Once again, the preservation of those quantities can be deduced from the antisymmetry properties of the coefficients $C_{\mathbf{klm}}$. For instance, to prove that the truncated helicity is invariant, it suffices to write :

$$\dot{\mathcal{H}}_N = \sum_{\mathbf{k},\mathbf{l},\mathbf{m}} \kappa_{\mathbf{m}}^{-2} a_{\mathbf{k}} \omega_{\mathbf{l}} \omega_{\mathbf{m}} \underbrace{(C_{\mathbf{klm}} + C_{\mathbf{mlk}})}_{=0} + \sum_{\mathbf{m}} \kappa_{\mathbf{m}}^2 a_{\mathbf{m}} \underbrace{\sum_{\mathbf{k},\mathbf{l}} C_{\mathbf{klm}} a_{\mathbf{k}} a_{\mathbf{l}}}_{=0} . \tag{3.25}$$

The conservation of the magnetic potential squared and of the total energy are shown similarly.

Geometrical interpretation. It is less clear than in the two-dimensional case to see how the invariants do indeed constrain the dynamics. One can first observe that the two following inequalities hold :

$$\mathcal{E}_N \geq \kappa_{\min}^2 \mathcal{A}_N + \frac{\mathcal{H}_N^2}{4\kappa_{\max}^2 \mathcal{A}_N} \quad \text{and} \quad \mathcal{E}_N \geq |\mathcal{H}_N|. \tag{3.26}$$

To get a geometrical intuition, one can consider the simple case $N = 2$, for which the phase space is determined by only four degrees of freedom, a_1, ω_1, a_2, ω_2. Four-dimensional surfaces of constant energies and helicities can be projected on hyper surfaces of constant magnetic potential squared $A = a_1^2 + a_2^2$, yielding a three dimensional space, say ω_1,ω_2,a_2. In the projected space, surfaces of constant energies E are ellipsoids. Their equations read $\omega_1^2 \kappa_1^{-2} + \omega_2^2 \kappa_2^{-2} + a_2^2 \kappa_2^2 - \kappa_1^2 = 2(E - A\kappa_1^2)$. The surfaces of constant helicities H are more intricated. Their equations are $\omega_1^2(1 - a_2^2) = (H - \omega_2 a_2)^2$.

In the non-helical ($H = 0$), low-energy situation ($E \simeq A\kappa_{\min^2}$), the energy is purely magnetic and concentrates on the smallest wavelength a_1 (Figure 3.3a). When the helicity is non zero, low-energies ($|H| \lesssim E$) are still large-scale (Figure 3.3d). However the kinetic energy is non zero, and is also large scale ($\omega_1 \neq 0, \omega_2 = 0$). For larger energies ($0 < |H| \ll E$), the motion gets confined on the small scales (Figure 3.3b and 3.3c).

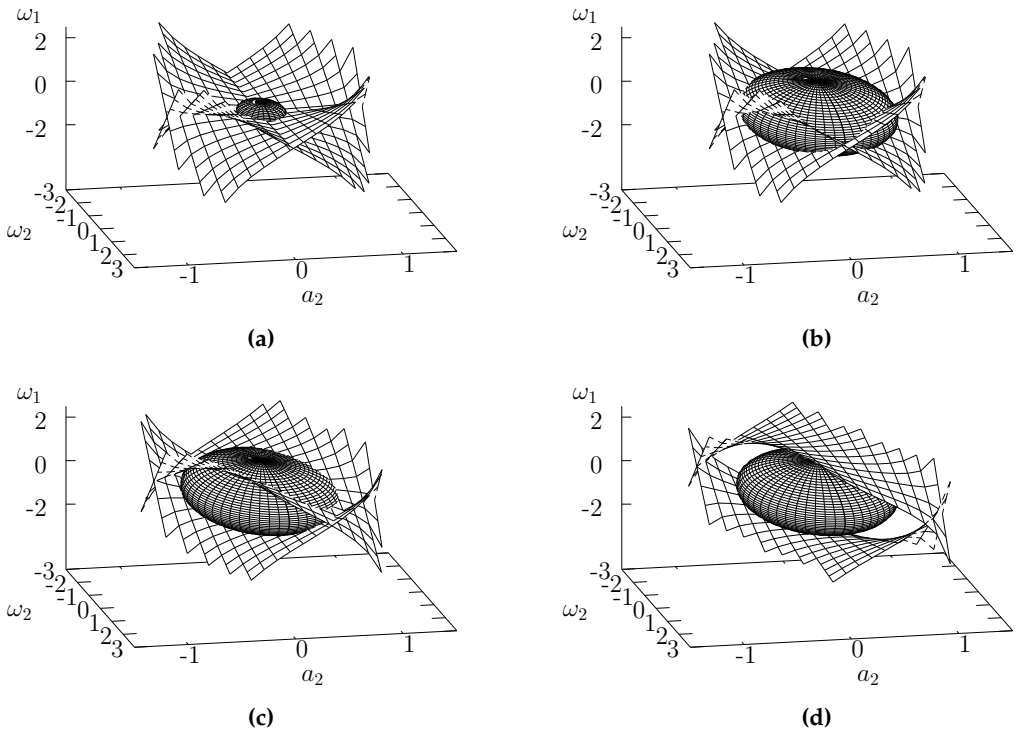

Figure 3.3: For $N = 2$ and $2A = 1$, we use the relation $a_1^2 + a_2^2 = 1$, and represent surfaces of constant helicities and constant energies in the three dimensional space determined by ω_1,ω_2, a_2. The eigenmodes are $\kappa_1 = 1$ and $\kappa_2 = \sqrt{3}$. The surfaces of constant energies are ellipsoids, with equation $\omega_1^2\kappa_1^{-2} + \omega_2^2\kappa_2^{-2} + a_2^2\kappa_2^2 - \kappa_1^2 = 2(E - A\kappa_1^2)$, shown for $2(E - A\kappa_1^2) = 0.1$ (a) and 1 (b,c,d). The surfaces of constant helicities have equation $\omega_1 = \pm\dfrac{H - \omega_2 a_2}{\sqrt{1 - a_2^2}}$ and are here shown for $H = 0$ (a,b), $H = 1$ (c), and $H = 2$ (d).

Absolute equilibria. The counterpart to the canonical measures (3.6) for two-dimensional magnetohydrodynamics are canonical measures $\langle\rangle^{\text{cano}}_{N,\alpha,\beta,\gamma} \equiv \langle\rangle_N$ described in terms of three inverse temperatures α, β, γ respectively associated to the magnetic potential squared, the energy and the Helicity. The generalization of Equation (3.6) is straightforward. As in the two-dimensional case, all the relevant quantities can be expressed in terms of the single-mode partitions functions

$$\begin{aligned}\mathcal{Z}_{N,\mathbf{k}}(\alpha,\beta,\gamma) &= \int_{\mathbb{R}^2} \mathrm{d}a_{\mathbf{k}}\mathrm{d}\omega_{\mathbf{k}} e^{-\frac{1}{2}\left(\beta\kappa_{\mathbf{k}}^{-2}\omega_{\mathbf{k}}^2 + 2\gamma a_{\mathbf{k}}\omega_{\mathbf{k}} + (\alpha+\beta\kappa_{\mathbf{k}}^2)a_{\mathbf{k}}^2\right)} \\ &= \sqrt{\frac{4\pi^2\kappa_{\mathbf{k}}^2}{(\beta^2-\gamma^2)\,\kappa_{\mathbf{k}}^2 + \alpha\beta}}.\end{aligned} \tag{3.27}$$

The conditions on the inverse temperatures for the latter computation to be valid are naturally $\beta > 0$, and $\beta^2 - \gamma^2 + \alpha\beta/\kappa_{\mathbf{k}}^2 > 0$. [(a)] Here, the inverse energy temperature is always positive but the inverse magnetic potential temperature is not. It plays a role analogous to the inverse energy temperature in two-dimension. We can distinguish several

[(a)] We deduce from those two-conditions that $\alpha + \beta\kappa_{\mathbf{k}}^2 > 0$ is necessary.

regimes, depending on the relative values of the coefficients α,β,γ. Those regimes are (a) $\alpha > 0$ and $\beta > \beta_c(\alpha, \gamma, \kappa_{\min})$, (b) $\alpha > 0$ and $\beta > |\gamma|$, and (c) $\alpha > 0$ and $\beta > \beta_c(\alpha, \gamma, \kappa_{\max})$. The critical temperatures $\beta_c(\alpha, \gamma, \kappa)$ are obtained as $\beta_c(\alpha, \gamma, \kappa) = -\frac{\alpha}{2\kappa^2} + (\frac{\alpha^2}{4\kappa^4} + \gamma^2)^{1/2}$ (See Figure 3.4). A characteristic wavelength that emerges from the inverse temperatures is $\kappa_{\alpha,\beta,\gamma} = \left|\frac{\alpha\beta}{\beta^2 - \gamma^2}\right|^{1/2}$. It is smaller than $\kappa_{\min}$ in regime (a) and larger than $\kappa_{\max}$ in regimes (b) and (c).

Note, that in all three regimes, the average helicities, magnetic potentials and energies per mode are easily deduced from the single-mode partition functions as

$$\begin{aligned}
\langle H_{\mathbf{k}} \rangle_N &= -\frac{\partial \log \mathcal{Z}_{N,\mathbf{k}}}{\partial \gamma} = \frac{-\gamma \kappa_{\mathbf{k}}^2}{(\beta^2 - \gamma^2)\,\kappa_{\mathbf{k}}^2 + \alpha\beta} \quad \text{(average helicity per mode)} \quad , \\
\langle A_{\mathbf{k}} \rangle_N &= -\frac{\partial \log \mathcal{Z}_{N,\mathbf{k}}}{\partial \alpha} = \frac{1}{2}\frac{\beta}{(\beta^2 - \gamma^2)\,\kappa_{\mathbf{k}}^2 + \alpha\beta} \quad \text{(average squared magnetic potential per mode)} \quad , \\
\text{and} \quad \langle E_{\mathbf{k}} \rangle_N &= -\frac{\partial \log \mathcal{Z}_{N,\mathbf{k}}}{\partial \beta} = \frac{1}{2}\frac{2\beta\kappa_{\mathbf{k}}^2 + \alpha}{(\beta^2 - \gamma^2)\,\kappa_{\mathbf{k}}^2 + \alpha\beta} \quad \text{(average energy per mode)} \quad .
\end{aligned} \tag{3.28}$$

We can also distinguish between the magnetic and the kinetic contributions to the energy. Their single mode averages respectively read

$$\begin{aligned}
\langle E_{\mathbf{k}}^{\text{mag}} \rangle_N &= \kappa_{\mathbf{k}}^2 \langle A_{\mathbf{k}} \rangle_N = \frac{1}{2}\frac{\beta\kappa_{\mathbf{k}}^2}{(\beta^2 - \gamma^2)\,\kappa_{\mathbf{k}}^2 + \alpha\beta}, \\
\text{and} \quad \langle E_{\mathbf{k}}^{\text{kin}} \rangle_N &= \langle E \rangle_N - \langle E_{\mathbf{k}}^{\text{mag}} \rangle_N = \frac{1}{2}\frac{\beta\kappa_{\mathbf{k}}^2 + \alpha}{(\beta^2 - \gamma^2)\,\kappa_{\mathbf{k}}^2 + \alpha\beta}.
\end{aligned} \tag{3.29}$$

The regime (a) for two-dimensional magnetohydrodynamics is analogous to the regime (a) obtained for two-dimensional flows. In this regime, for $\gamma \simeq 0$, the magnetic part of the energy per mode peaks as $\kappa_{\mathbf{k}} \to \kappa^+_{\alpha\beta,\gamma}$. Within this regime, $\kappa_{\alpha\beta\gamma}$ may is smaller than $\kappa_{\min}$ but may be chosen as close to $\kappa_{\min}$ as wanted. In the case without helicity ($\gamma = 0$), one can notice that values $\kappa_{\alpha\beta\gamma} \lesssim \kappa_{\min}$ describe a regime in which the energy concentrates on the largest mode, and is essentially magnetic$\langle E^{\text{kin}} \rangle_N / \langle E^{\text{mag}} \rangle_N \simeq 0$). If the helicity is non zero, than the kinetic energy of the largest modes is not zero, the ratio $\langle E^{\text{kin}} \rangle_N / \langle E^{\text{mag}} \rangle_N$ can than be estimated as $\langle E^{\text{kin}} \rangle_N / \langle E^{\text{mag}} \rangle_N \simeq \gamma^2/\beta$. Regime (c) describe a concentration of the energy on the smallest scales available, analogous to regimes (b) and (c) described for two-dimensional flows. Note that regime (c) is in a way opposite to regime (a). In regime (c), $\kappa_{\alpha\beta\gamma}$ can be chosen as close to $\kappa_{\max}$ than wanted : $\kappa_{\max} \lesssim \kappa_{\alpha\beta\gamma}$. In the non-helical case, the energy is then essentially kinetic ($\langle E^{\text{mag}} \rangle_N / \langle E^{\text{kin}} \rangle_N \simeq 0$). We can anticipate that regime (c) has no thermodynamic limit unless one allows for infinitely large values of the energy.

Limit $N \to \infty$. In order to work out a thermodynamic limit for fixed values of E, A, H, as in the two-dimensional case, one needs to find a right scaling for the inverse temperatures. In the limit of a large number of modes ($N \gg 1$), and upon replacing the

summation $\sum_{\mathbf{k}:\kappa_{\mathbf{k}}\leq|\kappa_c|}$ by the two-dimensional continuous integration $\frac{|\mathcal{D}|}{2\pi}\int_{\kappa_{\min}}^{\kappa_{\max}}\kappa \mathrm{d}\kappa$ one obtains

$$\langle\mathcal{A}\rangle = \frac{|\mathcal{D}|}{2\pi}\int_{\kappa_{\min}}^{\kappa_{\max}}\kappa \mathrm{d}\kappa\langle A_{\mathbf{k}}\rangle = \frac{|\mathcal{D}|}{8\pi}\frac{\beta}{\beta^2-\gamma^2}\log\frac{\left(\beta^2-\gamma^2\right)\kappa_{\max}^2+\alpha\beta}{\left(\beta^2-\gamma^2\right)\kappa_{\min}^2+\alpha\beta}. \tag{3.30}$$

Similarly,

$$\begin{aligned}\langle\mathcal{H}\rangle &= -\frac{|\mathcal{D}|}{4\pi}\frac{\gamma}{\beta^2-\gamma^2}\left(\kappa_{\min}^2-\kappa_{\max}^2\right)+\frac{|\mathcal{D}|}{4\pi}\frac{\alpha\beta\gamma}{\left(\beta^2-\gamma^2\right)^2}\log\frac{\left(\beta^2-\gamma^2\right)\kappa_{\max}^2+\alpha\beta}{\left(\beta^2-\gamma^2\right)\kappa_{\min}^2+\alpha\beta},\\ \text{and}\quad \langle\mathcal{E}\rangle &= -\frac{\beta}{\gamma}\langle\mathcal{H}\rangle+\frac{\alpha}{\beta}\langle\mathcal{A}\rangle\end{aligned} \tag{3.31}$$

We now look for a thermodynamic limit that ensures $\langle A\rangle$, $\langle H\rangle$ and $\langle E\rangle$ to remain finite as $\kappa_{\max}\to\infty$. We look for an expansion :

$$\alpha=\kappa_{\max}^2\left(\alpha^\star+o(1)\right),\qquad \beta=\kappa_{\max}^2(\beta^\star+o(1))\quad\text{and}\quad \gamma=\kappa_{\max}^2(\gamma^\star+o(1)). \tag{3.32}$$

Plugging the latter equations into (3.30) and (3.31), and requiring finiteness of the dynamical invariants as $\kappa_{\max}\to\infty$, one gets:

$$\begin{aligned}&\left(\beta^{\star2}-\gamma^{\star2}\right)\kappa_{\min}^2+\alpha^\star\beta^\star=0,\qquad E=\frac{|\mathcal{D}|}{4\pi\beta^\star}\left(1-\left(\frac{\gamma^\star}{\beta^\star}\right)^2\right)^{-1}+\kappa_{\min}^2A\left(1+\left(\frac{\gamma^\star}{\beta^\star}\right)^2\right),\\ &\text{and}\quad -H=\frac{\gamma^\star}{\beta^\star}\left(1-\left(\frac{\gamma^\star}{\beta^\star}\right)^2\right)^{-1}\left[\frac{|\mathcal{D}|}{4\pi\beta^\star}+2\left(1-\left(\frac{\gamma^\star}{\beta^\star}\right)^2\right)\kappa_{\min}^2A\right].\end{aligned} \tag{3.33}$$

We conclude that a thermodynamic limit exists. It can be interpreted as a condensation regime. If there is no helicity, then from $H=0$ stems $\gamma^\star=0$ and $E=\frac{|\mathcal{D}|}{4\pi\beta^\star}+\kappa_{\min^2}A$. The energy is then essentially magnetic. The temperature $\frac{1}{\beta^\star}$ measures fluctuations of the kinetic energy. For non vanishing helicities $\gamma\neq0$, both the kinetic and the magnetic energies have a non zero contribution on the largest scale – smallest mode. The geometric pictures which correspond to this condensation regime are shown on Figure 3.3a (for the non helical case) and on Figure 3.3d (for the helical case).

3.3 Absolute equilibria for axisymmetric flows.

Let us now take a look at axisymmetric flows. Because of the close analogy between two-dimensional magnetohydrodynamics and axisymmetric flows, we could expect that absolute equilibria would predict a condensation of the toroidal energy on the largest mode, akin to the condensation of magnetic energy in the magneto hydrodynamical case. Is this actually the case ? Quite surprisingly, no.

For axisymmetric flows, it is fairly easy to write down a truncated Galerkin axisymmetric dynamics for which a Theorem of Liouville holds. However, those truncations

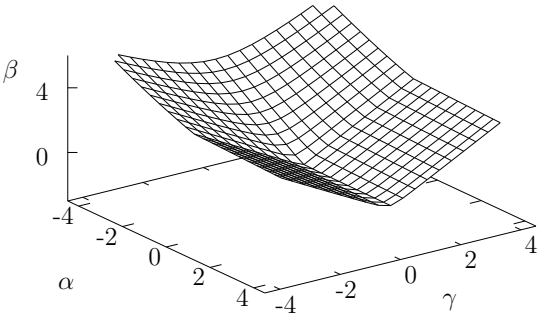

(a)

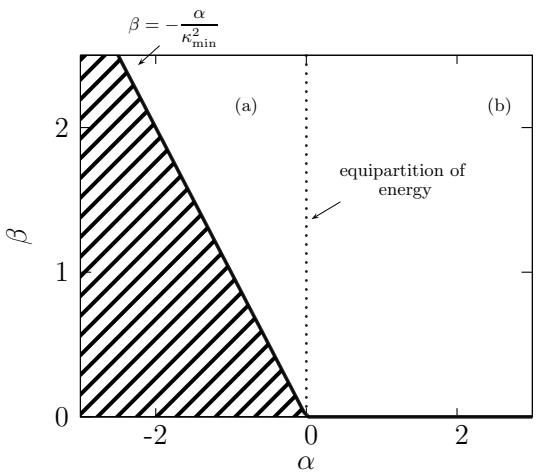

(b) Cut along $\gamma = 0$.

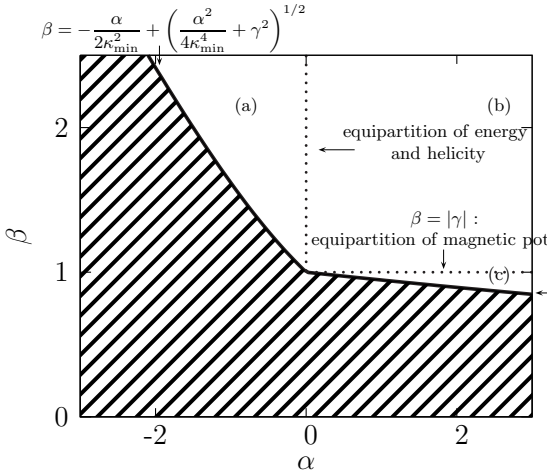

(c) Cut along $\gamma = \pm 1$

Figure 3.4: The different regimes for finite (dimensional) absolute equilibria for two-dimensional magnetohydrodynamics , represented in a $\alpha - \beta - \gamma$ space (a) and in the plane $\gamma = 0$ (b) and $\gamma = 1$ (c).

will fail to conserve both the energy *and* an additional enstrophy-like invariant. They conserve either a truncated energy and truncated helicity or the truncated toroidal field squared – analogous to the magnetic potential squared – and a helicity. Therefore, the axisymmetric absolute equilibria are *stricto sensu* only based on two invariants. The first subsection shows that the insights given by those absolute equilibria is quite limited. It can be skipped in a first reading. In the second subsection, I will argue that even if we were to take into account three invariants, no condensation regime would be obtained.

3.3.1 Two attempts to build absolute equilibria for axisymmetric ideal flows

First attempt : statistical equilibria using toroidal and poloidal variables.

(i) Let us try for instance to approximate and decompose the toroidal field σ and the poloidal field ξ over an orthonormal set of eigenmodes of the differential operator $\Delta_\star$, so that, $\xi = \sum_{\mathbf{k}:\mathbf{k}\leq\kappa_c} \xi_{\mathbf{k}}\phi_{\mathbf{k}}$ and $\sigma = \sum_{\mathbf{k}:\mathbf{k}\leq\kappa_c} \sigma_{\mathbf{k}}\phi_{\mathbf{k}}$, using transparent notations. (i) Truncated axisymmetric equations for the coefficients $\xi_{\mathbf{k}}$ and $\sigma_{\mathbf{k}}$ are easily obtained from

the axisymmetric equations (1.13) as

$$\begin{aligned}&\dot\sigma_{\mathbf{k}}=\sum_{\mathbf{l},\mathbf{m}}C_{\mathbf{klm}}\kappa_{\mathbf{m}}^{-2}\sigma_{\mathbf{l}}\xi_{\mathbf{m}}\quad\text{and}\quad\dot\xi_{\mathbf{k}}=\sum_{\mathbf{l},\mathbf{m}}C_{\mathbf{klm}}\kappa_{\mathbf{m}}^{-2}\xi_{\mathbf{l}}\xi_{\mathbf{m}}+\tilde C_{\mathbf{klm}}\kappa_{\mathbf{m}}^{2}\sigma_{\mathbf{l}}\sigma_{\mathbf{m}}\quad\text{if }|\kappa_{\mathbf{k}}|\le\kappa_c\,;\\&\dot\sigma_{\mathbf{k}}=0\quad\text{and}\quad\dot\xi_{\mathbf{k}}=0\quad\text{otherwise}\quad.\end{aligned}\tag{3.34}$$

Again, "$\sum_{\mathbf{l},\mathbf{m}}$" is a shorthand notation for "$\sum_{\mathbf{l}:|\kappa_{\mathbf{l}}|\le\kappa_c}\sum_{\mathbf{m}:|\kappa_{\mathbf{m}}|\le\kappa_c}$". The coefficients $C_{\mathbf{klm}}$ and $\tilde C_{\mathbf{klm}}$ are obviously defined as $C_{\mathbf{klm}}=\dfrac{1}{|\mathcal{D}|}\displaystyle\int_{\mathcal{D}}\mathbf{r}\mathbf{d}\mathbf{r}\,\phi_{\mathbf{k}},[\phi_{\mathbf{l}},\phi_{\mathbf{m}}]\underset{\text{def}}{=}(\phi_{\mathbf{k}},[\phi_{\mathbf{l}},\phi_{\mathbf{m}}])$ and $\tilde C_{\mathbf{klm}}=\left(\phi_{\mathbf{k}},\left[\phi_{\mathbf{l}},\dfrac{\phi_{\mathbf{m}}}{2y}\right]\right)$. Note the appearance of the position field in the coefficients $\tilde C_{\mathbf{klm}}$.

(ii) The Theorem of Liouville is again painless to derive:

$$\frac{\partial\dot\sigma_{\mathbf{k}}}{\partial\sigma_{\mathbf{k}}}+\frac{\partial\dot\xi_{\mathbf{k}}}{\partial\xi_{\mathbf{k}}}=2\sum_{\mathbf{m}}\underbrace{C_{\mathbf{kkm}}}_{=0}\kappa_{\mathbf{m}}^{-2}\xi_{\mathbf{m}}+\sum_{\mathbf{l}}\underbrace{C_{\mathbf{klk}}}_{=0}\kappa_{\mathbf{k}}^{-2}\xi_{\mathbf{l}}=0.\tag{3.35}$$

(iii) What about the dynamical invariants? It is straightforward to check that the truncated toroidal field squared $\mathcal{G}_N=\dfrac{1}{2}\sum_{\mathbf{k}}\sigma_{\mathbf{k}}^2$ is conserved, as well as the truncated helicity $\mathcal{H}_N=\sum_{\mathbf{k}}\sigma_{\mathbf{k}}\xi_{\mathbf{k}}$. Ideally, we could also want that the truncated dynamics (3.34) conserve a truncated axisymmetric energy, say

$$\mathcal{E}_N=\frac{1}{2}\sum_{\mathbf{k},\mathbf{l}}\underbrace{(\phi_{\mathbf{k}},\frac{\phi_{\mathbf{l}}}{2y})}_{=\alpha_{\mathbf{kl}}}\sigma_{\mathbf{k}}\sigma_{\mathbf{l}}+\frac{1}{2}\sum_{\mathbf{k}}\xi_{\mathbf{k}}^2\kappa_{\mathbf{k}}^{-2}.\tag{3.36}$$

But this is not the case ! Indeed,

$$-\dot{\mathcal{E}}_N=\sum_{\mathbf{n},\mathbf{m},\mathbf{k}}\xi_{\mathbf{n}}\kappa_{\mathbf{n}}^{-2}\sigma_{\mathbf{m}}\sigma_{\mathbf{k}}\left\{\tilde C_{\mathbf{nmk}}+\sum_{\mathbf{l}}\alpha_{\mathbf{kl}}C_{\mathbf{lmn}}\right\},\tag{3.37}$$

which is not zero unless in the limit of an infinite number of modes. [(a)] Therefore, strictly speaking, there are only two obvious invariants that survive the truncations ; the helicity $\mathcal{H}_N$ and the toroidal field squared $\mathcal{G}_N$.

(iv) The absolute canonical equilibria are then just : $\mu^{\text{cano}}\propto e^{-\epsilon\mathcal{G}_N-\gamma\mathcal{H}_N}$. The corresponding single mode partition functions are $\mathcal{Z}_{\mathbf{k}}(\beta,\gamma)=\int_{\mathbb{R}^2}\mathrm{d}\sigma_{\mathbf{k}}\mathrm{d}\xi_{\mathbf{k}}\,e^{-\frac{1}{2}\left(\epsilon\sigma_{\mathbf{k}}^2+2\gamma\sigma_{\mathbf{k}}\xi_{\mathbf{k}}\right)}$, which is non integrable. We conclude, that we need to find truncations for which an

[(a)] Formally, when considering an infinite number of modes :

$$\tilde C_{\mathbf{nmk}}=\left(\phi_{\mathbf{n}}\left[\phi_{\mathbf{m}},\frac{\phi_{\mathbf{k}}}{2y}\right]\right)=\left([\phi_{\mathbf{n}},\phi_{\mathbf{m}}]\,\frac{\phi_{\mathbf{k}}}{2y}\right)=\left(\sum_{\mathbf{l}\in\mathbb{Z}}(\phi_{\mathbf{l}}\,[\phi_{\mathbf{n}},\phi_{\mathbf{m}}])\,\phi_{\mathbf{l}}\frac{\phi_{\mathbf{k}}}{2y}\right)=\sum_{\mathbf{l}\in\mathbb{Z}}C_{\mathbf{lnm}}\alpha_{\mathbf{kl}}=-\sum_{\mathbf{l}\in\mathbb{Z}}C_{\mathbf{lmn}}\alpha_{\mathbf{kl}}.\tag{3.38}$$

axisymmetric energy is conserved in order for axisymmetric absolute equilibria to be fruitful.

Second attempt : statistical equilibria using orthoradial velocity and vorticity variables. In order to conserve the energy, one needs to make the truncated energy local in the space of eigenmodes. This can be done by considering velocity and vorticity variables.

(i) To do so, let us write a truncated dynamics for the axisymmetric equations (1.13) in terms of Bessel-Fourier modes $(\phi_{\mathbf{k}})_{\mathbf{k}\in\mathbb{Z}}$, defined as the (real) eigenmodes of the differential operator $\mathcal{L}(.) = r\Delta_\star(r.)$ – with either one of the boundary conditions discussed in Chapter 1 : $\Delta^\star r\phi_{\mathbf{k}} = -\kappa_{\mathbf{k}}^2\dfrac{\phi_{\mathbf{k}}}{r}$. The eigenvalues $-\kappa_{\mathbf{k}}^2$of $\mathcal{L}$ are all negative (see Appendix A).

Naturally, the modes can be set to form an orthonormal set of modes for the scalar product $(.)$ defined as $(f,g) = |\mathcal{D}|^{-1}\int_{\mathcal{D}} \mathrm{d}\mathbf{r} f(\mathbf{r})g(\mathbf{r})$. We use the coefficients $v_{\mathbf{k}} = (\phi_{\mathbf{k}}, r^{-1}\sigma)$, $\omega_{\mathbf{k}} = (\phi_{\mathbf{k}}, r\xi)$, and approximate the toroidal and poloidal fields as

$$\sigma(\mathbf{r}) = \sum_{\substack{\mathbf{k}\in\mathbb{Z}^2\\ \kappa_{\mathbf{k}}\leq\kappa_c}} rv_{\mathbf{k}}\phi_{\mathbf{k}}(\mathbf{r}) \text{ and } \xi(\mathbf{r}) = \sum_{\substack{\mathbf{k}\in\mathbb{Z}^2\\ \kappa_{\mathbf{k}}\leq\kappa_c}} r^{-1}\omega_{\mathbf{k}}\phi_{\mathbf{k}}(\mathbf{r}). \tag{3.39}$$

The stream function $\psi = -\Delta_\star^{-1}\xi$, is then obtained as $\psi(\mathbf{r}) = \sum_{\substack{\mathbf{k}\in\mathbb{Z}^2\\ \kappa_{\mathbf{k}}\leq\kappa_c}} r\psi_{\mathbf{k}}\phi_{\mathbf{k}}(\mathbf{r})$with $\psi_{\mathbf{k}} = \kappa_{\mathbf{k}}^{-2}\omega_{\mathbf{k}}$.

In terms of the coefficients $v_{\mathbf{k}}$ and $\omega_{\mathbf{k}}$, the axisymmetric ideal dynamics (1.13) reads

$$\dot\omega_{\mathbf{k}} = \sum_{\mathbf{l},\mathbf{m}} A_{\mathbf{klm}}\omega_{\mathbf{l}}\psi_{\mathbf{m}} + \sum_{\mathbf{l},\mathbf{m}} B_{\mathbf{klm}}v_{\mathbf{l}}v_{\mathbf{m}}, \quad \text{and} \quad \dot v_{\mathbf{k}} = \sum_{\mathbf{l},\mathbf{m}} C_{\mathbf{klm}}v_{\mathbf{l}}\psi_{\mathbf{m}}. \tag{3.40}$$

The coefficients $A_{\mathbf{klm}}$,$B_{\mathbf{klm}}$,$C_{\mathbf{klm}}$ are defined as

$$\begin{aligned} A_{\mathbf{klm}} &= \left(r\phi_{\mathbf{k}}\left[r^{-1}\phi_{\mathbf{l}}, r\phi_{\mathbf{m}}\right]\right), B_{\mathbf{klm}} = \left(r\phi_{\mathbf{k}}\left[r\phi_{\mathbf{l}}, r\phi_{\mathbf{m}}\right]\right) \\ \text{and} \quad C_{\mathbf{klm}} &= \left(r^{-1}\phi_{\mathbf{k}}\left[r\phi_{\mathbf{l}}, r\phi_{\mathbf{m}}\right]\right). \end{aligned} \tag{3.41}$$

A truncated axisymmetric dynamics is obtained by setting to zero all the modes above κ_c.

(ii) From the truncated equations (3.40), we easily get the following (detailed) theorem of Liouville :

$$\frac{\partial\dot\omega_{\mathbf{k}}}{\partial\omega_{\mathbf{k}}} + \frac{\partial\dot v_{\mathbf{k}}}{\partial v_{\mathbf{k}}} = 0. \tag{3.42}$$

(a)

(a)To "easily" obtain the theorem, let us first observe that for any functions $f, g, h : \mathcal{D} \to \mathbb{R}$, the equality $(f,[g,h]) = (g,[h,f])$ holds whenever f or g is either periodic or vanishing on the boundaries. This result is immediately obtained from the definition of $(.)$ and $[,]$ with two integrations by parts. Therefore, the

(iii) As for the invariants, it is straightforward to show that the dynamics (3.41) conserve both a truncated Energy $\mathcal{E}_N = \frac{1}{2}\sum_{\mathbf{k}} v_{\mathbf{k}}^2 + \omega_{\mathbf{k}}^2 \kappa_{\mathbf{k}}^{-2}$ and a truncated Helicity $\mathcal{H}_N = \sum_{\mathbf{k}} \omega_{\mathbf{k}} v_{\mathbf{k}}$. The price to pay is that truncations of the toroidal Casimir $\frac{1}{2}\int_{\mathcal{D}} \sigma^2$ now involve non-local couplings between the coefficients $v_{\mathbf{k}}$: $\mathcal{G}_N = \frac{1}{2}\sum_{\mathbf{kl}} (r\phi_{\mathbf{k}} r\phi_{\mathbf{l}})\, v_{\mathbf{k}} v_{\mathbf{l}}$. The latter are therefore *not* conserved by (3.41), unless in the limit of an infinitely large cutoff κ_c, as it was the case for the truncated energy and the dynamics (3.34).

(iv) Absolute equilibria based on solely the truncated energies and the truncated helicities, $\mu_{\text{cano}} \propto e^{-\beta\mathcal{E}_N - \gamma\mathcal{H}_N}$ predict slightly but little more than just an equipartition of helicity. The canonical averages are obtained from the single-point partition functions

$$\mathcal{Z}_{\mathbf{k}}(\beta,\gamma) = \int_{\mathbb{R}} \mathrm{d}\omega_{\mathbf{k}} \mathrm{d}v_{\mathbf{k}} \exp -\frac{1}{2}\left(\beta\omega_{\mathbf{k}}^2\kappa_{\mathbf{k}}^{-2} + \beta v_{\mathbf{k}}^2 + 2\gamma\omega_{\mathbf{k}} v_{\mathbf{k}}\right) = \sqrt{\frac{4\pi\kappa_{\mathbf{k}}^2}{\beta^2 - \gamma^2\kappa_{\mathbf{k}}^2}}. \tag{3.44}$$

The second equality holds provided that $|\beta| > |\gamma|\kappa_{\max}$. Hence, no negative temperature regime is allowed. The average energy per mode is $\langle E_{\mathbf{k}}\rangle = \dfrac{\beta}{\beta^2 - \gamma^2\kappa_{\mathbf{k}}^2}$ and can only peak at small scales ($\kappa_{\mathbf{k}} \lesssim |\beta\gamma^{-1}|$). The ratio of toroidal energy towards poloidal energy is always 1.

3.3.2 Axisymmetric invariants from a " mock absolute equilibria" perspective. The case of a Von Kármán geometry.

Peristrophy and mock equilibria. One may argue that the absolute equilibria that were found in the previous subsection are trivial because only two invariants were taken into account. Let us try to further include truncations of the toroidal field squared $\frac{1}{2}\int_{\mathcal{D}} \sigma^2$. To avoid the use of periphrases, I will refer to this invariant as the "peristrophy". [(a)]

Note that equilibria within a canonical helicity-energy-peristrophy are not invariant distributions for (3.41) unless in the formal limit of an infinitely large cutoff. This is why I will call those equilibria "mock" absolute equilibria. The purpose of the mock equilibria is simply to contrast the physics dictated by the invariants of the axsymmetric dynamics with that of the related two-dimensional magnetohydrodynamics , and to show that the interplay between the peristrophy and the axisymmetric energy is very different from the interplay between the magnetic potential squared and the energy for two-dimensional magnetohydrodynamics . The present analysis is restricted to the case of a Von Kármán geometry (R_{in}=0), with impermeability condition on the walls.

---

coefficients given by (3.41) satisfy in particular :

$$A_{\mathbf{klk}} = -A_{\mathbf{klk}} = 0, \quad \text{and} \quad A_{\mathbf{klm}} = -C_{\mathbf{lkm}}. \tag{3.43}$$

: It follows from these two identities that

$$\frac{\partial\dot{\omega}_{\mathbf{k}}}{\partial\omega_{\mathbf{k}}} + \frac{\partial\dot{v}_{\mathbf{k}}}{\partial v_{\mathbf{k}}} = -\sum_{\mathbf{m}} \underbrace{(A_{\mathbf{kkm}} + C_{\mathbf{kkm}})}_{=0}\psi_{\mathbf{m}} - \sum_{\mathbf{l}} \underbrace{A_{\mathbf{klk}}}_{=0}\omega_{\mathbf{l}}\kappa_{\mathbf{k}}^{-2} = 0.$$

[(a)] From the prefix περι ("around") and the previously described στροφή.

Pseudo-invariants. Let me reuse the "vorticy-velocity" decomposition in terms of Bessel-Fourier modes (3.39) :

$$\sigma(\mathbf{r}) = \sum_{\substack{\mathbf{k}\in\mathbb{Z}^2 \\ \kappa_{\mathbf{k}}\leq\kappa_c}} r v_{\mathbf{k}}\phi_{\mathbf{k}}(\mathbf{r}) \text{ and } \xi(\mathbf{r}) = \sum_{\substack{\mathbf{k}\in\mathbb{Z}^2 \\ \kappa_{\mathbf{k}}\leq\kappa_c}} r^{-1}\omega_{\mathbf{k}}\phi_{\mathbf{k}}(\mathbf{r}) \quad \text{with } \kappa_c \text{ a prescribed cutoff} \quad . \tag{3.45}$$

In addition to the previously considered truncated energy $\mathcal{E}_N = \frac{1}{2}\sum_{\mathbf{k}} v_{\mathbf{k}}^2 + \omega_{\mathbf{k}}^2\kappa_{\mathbf{k}}^{-2}$ and truncated helicity $\mathcal{H}_N = \sum_{\mathbf{k}} v_{\mathbf{k}}\omega_{\mathbf{k}}$, we project the peristrophy $\mathcal{G}/|\mathcal{D}| = \frac{1}{2|\mathcal{D}|}\int_{\mathcal{D}}\sigma^2$ onto the set of modes $\phi_{\mathbf{k}}$ and set to zero the modes with eigenvalues larger than κ_c, and obtain

$$\mathcal{G}_N = \frac{1}{2}\sum_{\mathbf{k},\mathbf{l}} \overbrace{(r\phi_{\mathbf{k}} r\phi_{\mathbf{l}})}^{\alpha_{\mathbf{kl}}} v_{\mathbf{k}} v_{\mathbf{l}} \quad \text{(truncated –renormalized– peristrophy)} \tag{3.46}$$

Again, the casual "$\sum_{\mathbf{k}}$" denotes "$\sum_{\mathbf{k}:|\kappa_{\mathbf{k}}|\leq\kappa_c}$".

$\mathcal{G}_N$ involves a coupling between the velocity modes. Clearly, the physics contained within the peristrophy may sharply depend on what the coefficients $\alpha_{\mathbf{kl}} = (r\phi_{\mathbf{k}} r\phi_{\mathbf{l}})$ actually are. Explicit estimates for those may be found in the case of a Von Kármán geometry. As explained in Appendix A, those estimates are

$$\alpha_{\mathbf{kk}'} \simeq \begin{cases} 0 \quad \text{if } k_z \neq k_z' \\ \dfrac{R^2}{3}\left(1 - \dfrac{3}{2\pi^2\left(k_r+\frac{1}{4}\right)^2}\right) \quad \text{if } \mathbf{k} = \mathbf{k}' \\ \dfrac{2R^2}{\pi^2}\left(\dfrac{(-1)^{k_r-k_r'}}{(k_r-k_r')^2} - \dfrac{(-1)^{k_r-k_r'}}{(k_r+k_r'+1/2)^2} + \dfrac{1}{\pi(k_r+k_r'+1/2)^3}\right) \quad \text{otherwise.} \end{cases} \tag{3.47}$$

To grasp the physics hidden in those coefficients, let us work with approximations.

The peristrophy as a sum of squares. Let us crudely approximate the truncated peristrophy $\mathcal{G}_N$ by setting to zero the non-diagonal coefficients $\alpha_{\mathbf{kk}'}$. Namely, let us take $\alpha_{\mathbf{kk}'} = \frac{R^2}{3}\delta_{\mathbf{kk}'}$ instead of (3.47). $\mathcal{G}_N$ can be renormalized so that $\mathcal{G}_N = \frac{1}{2}\sum_{\mathbf{k}} v_{\mathbf{k}}^2 = E_N^{\text{tor}}$, and matches the toroidal energy. The canonical distribution within an energy-helicity-peristrophy canonical ensemble is entirely determined by the partition function $\mathcal{Z}_N$, written in terms of the inverse temperatures β,γ, and ϵ respectively related to the energy, the helicity and the peristrophy as

$$\mathcal{Z}_N(\beta,\gamma,\epsilon) = \int_{\mathbb{R}^{2N}}\prod_{\mathbf{k}} \mathrm{d}v_{\mathbf{k}}\mathrm{d}\omega_{\mathbf{k}} e^{-\beta\mathcal{E}_N-\gamma\mathcal{H}_N-\epsilon\mathcal{G}_N} = \prod_{\mathbf{k}}\mathcal{Z}_{\mathbf{k},N}(\beta,\gamma,\epsilon). \tag{3.48}$$

The single-mode partition functions $\mathcal{Z}_{\mathbf{k},N}$ are

$$\mathcal{Z}_{\mathbf{k},N}(\beta,\gamma,\epsilon) = \int_{\mathbb{R}^2}\mathrm{d}v_{\mathbf{k}}\mathrm{d}\omega_{\mathbf{k}} e^{-\frac{1}{2}\left((\beta+\epsilon)v_{\mathbf{k}}^2+\beta\kappa_{\mathbf{k}}^{-2}\omega_{\mathbf{k}}^2+2\gamma v_{\mathbf{k}}\omega_{\mathbf{k}}\right)} = \sqrt{\frac{4\pi^2\kappa_{\mathbf{k}}^2}{\beta(\beta+\epsilon)-\gamma^2\kappa_{\mathbf{k}}^2}}. \tag{3.49}$$

The last equality in (3.49) holds provided $\beta > 0$ and $\beta(\beta+\epsilon) - \gamma^2\kappa_{\mathbf{k}}^2 > 0$ for any $\mathbf{k}$. This implies $\beta > 0$ and $\beta(\beta+\epsilon) > \gamma^2\kappa_{\max}^2$. As in the magneto-hydro case, one can distinguish between a regime (a) for which $\epsilon < 0$ and $\beta > \dfrac{-\epsilon + \sqrt{\epsilon^2 + 4\gamma^2\kappa_{\max}^2}}{2}$, a regime (b) for which $\epsilon > 0$ and $\beta > |\gamma\kappa_{\max}|$ and a regime (c) $\epsilon > 0$ and $\dfrac{-\epsilon + \sqrt{\epsilon^2 + 4\gamma^2\kappa_{\max}^2}}{2} < \beta < |\gamma\kappa_{\max}|$ (see Figure 3.5).

Those regimes can be qualitatively discussed by computing the average toroidal and poloidal energies per mode :

$$\begin{aligned} \langle E_{\mathbf{k}}^{\text{tor}} \rangle_N &= -\frac{\partial \log \mathcal{Z}_{N,\mathbf{k}}}{\partial \epsilon} = \frac{1}{2}\frac{\beta}{\beta(\beta+\epsilon) - \gamma^2\kappa_{\max}^2}, \\ \text{and} \quad \langle E^{\text{pol}} \rangle_N &= -\frac{\partial \log \mathcal{Z}_{N,\mathbf{k}}}{\partial \beta} - \langle E_{\mathbf{k}}^{\text{tor}} \rangle_N = \frac{1}{2}\frac{\beta+\epsilon}{\beta(\beta+\epsilon) - \gamma^2\kappa_{\max}^2}. \end{aligned} \tag{3.50}$$

In the non-helical case ($\gamma = 0$), the energy is equiparted between the modes, but the form of the energy is not the same in the three regimes. The ratio of toroidal to poloidal energy is given by $\langle E^{\text{tor}} \rangle_N / \langle E^{\text{pol}} \rangle_N = \beta/(\beta+\epsilon)$. The energy is then essentially toroidal in regime (a) and essentially poloidal in regime (c). In the helical case, the splitting still holds, but the energy concentrates on the largest energy shells (small scales). The inverse characteristic length can indeed be defined as $\kappa_{\beta,\epsilon,\gamma}^2 = \dfrac{\beta(\beta+\epsilon)}{\gamma^2}$, which is larger than $\kappa_{\max}^2$.
This shows, that in the axisymmetric case, the helicity is intrinsically related to small scales, and that in neither regime, does the energy concentrate on the small wavelengths.

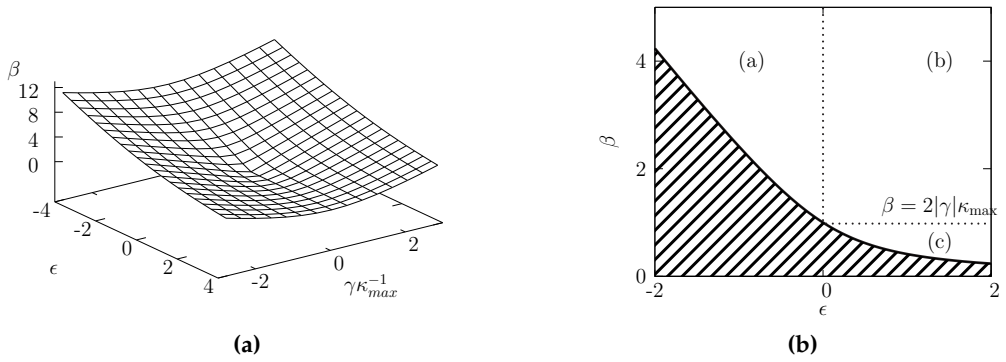

Figure 3.5: The different regimes for the axisymmetric mock equilibria, represented in a $\epsilon - \gamma - \beta$ space (a) and in the plane $\gamma = (\kappa_{\max})^{-1}$ (b). The vertical line $\epsilon = 0$ describes an equal splitting of the energy between its toroidal and poloidal contributions. The horizontal line $\beta = |\gamma|\kappa_{\max}$ corresponds to an equipartition of energy.

Note that we can have an intuitive and geometric interpretation on how the helicity does indeed favor small scales in the axisymmetric case by looking at the case $N = 2$, in which there are only 4 degrees of freedom, v_1, v_2, ω_1 and ω_2 with κ_1<κ_2 (see Figure 3.6). What changes from the magneto-hydro case, is that peristrophy constraint $v_1^2 + v_2^2 = 2G$ makes the surface of constant energies be cylinders in a ω_2, v_2, ω_1 plane and not ellipsoids. In the helical axisymmetric case sketched on Figure 3.6d, the intersection of the surfaces of constant helicities and surfaces of constant energies are obtained for a zero toroidal

contribution for the largest scale ($v_1 = 0$, $v_2 = \pm 1$), hence very different from the helical magnetic case sketched on Figure 3.3d ($a_1 = \pm 1$, $a_2 = 0$).

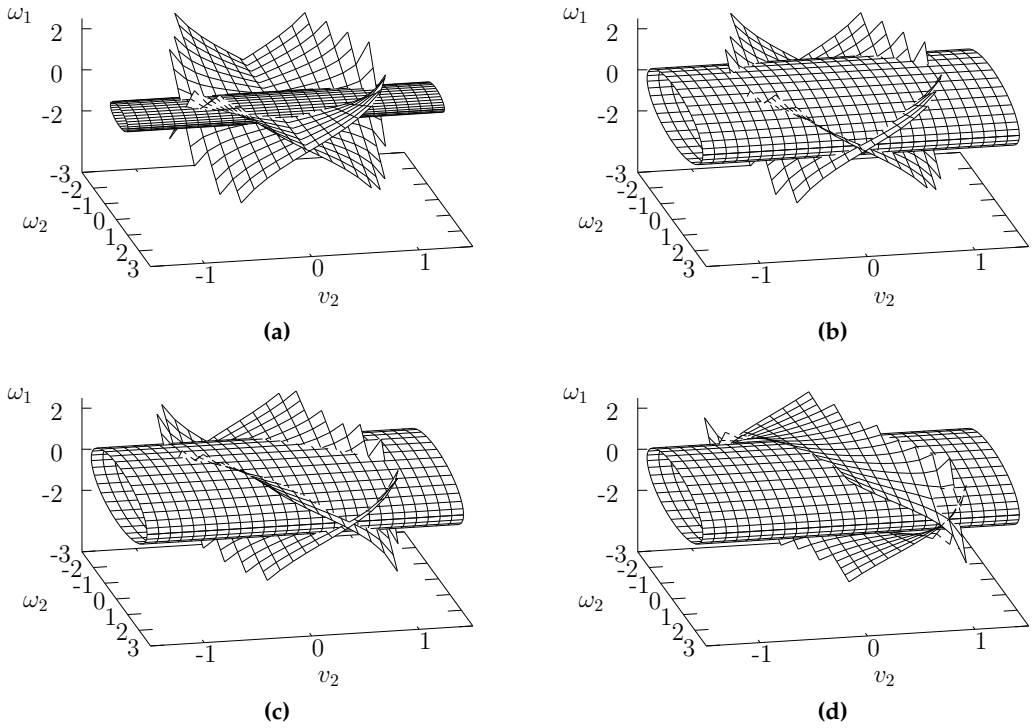

Figure 3.6: For $N = 2$ and $2G = 1$, upon using the relation $v_1^2 + v_2^2 = 1$, we represent surfaces of constant helicities and constant energies in the three dimensional space determined by ω_1,ω_2, v_2. The eigenmodes are $\kappa_1 = 1$ and $\kappa_2 = \sqrt{3}$. The surfaces of constant energies are cylinders, with equation $\omega_1^2 \kappa_1^{-2} + \omega_2^2 \kappa_2^{-2} = 2(E - G) = 2E_{\rm pol}$. Here $2E_{\rm pol} = 0.1$ (a) and 1 (b,c,d). The surfaces of constant helicities have equation $\omega_1 = \pm \dfrac{H - \omega_2 v_2}{\sqrt{1 - v_2^2}}$ and are here shown for $H = 0$ (a,b), $H = 1$ (c), and $H = 2$ (d).

3.3.3 Boussinesq Flows

Galerkin truncations of Boussinesq flows may provide less drama than axisymmetric truncations. If we Fourier approximate the spatial field as $y = \sum_{\mathbf{k}:\kappa_{\mathbf{k}} \leq \kappa_c} \phi_{\mathbf{k}} y_{\mathbf{k}}$, then the active retro-action $[\theta, y]$ of the temperature field on the kinetic field is well behaved in Fourier space. Therefore, the truncated dynamics obtained along the lines previously described will preserve the truncated energy $\mathcal{E}_N = \sum_{\mathbf{k}:\kappa_{\mathbf{k}} \leq \kappa_c} \theta_{\mathbf{k}} y_{\mathbf{k}} + \dfrac{1}{2} \omega_{\mathbf{k}} \psi_{\mathbf{k}}$, the "cross helicity" $\mathcal{H}_N = \sum_{\mathbf{k}:\kappa_{\mathbf{k}} \leq \kappa_c} \theta_{\mathbf{k}} \omega_{\mathbf{k}}$ and the temperature squared $\mathcal{G}_N = \dfrac{1}{2} \sum_{\mathbf{k}:\kappa_{\mathbf{k}} \leq \kappa_c} \theta_{\mathbf{k}}^2$. The single mode partition functions read :

$$\begin{aligned}\mathcal{Z}_{\mathbf{k},N} &= \int_{\mathbb{R}^2} \mathrm{d}\theta_{\mathbf{k}}\mathrm{d}\omega_{\mathbf{k}} e^{-\frac{1}{2}\left\{\beta\kappa_{\mathbf{k}}^{-2}\omega_{\mathbf{k}}+\epsilon\theta_{\mathbf{k}}^2+2\gamma\theta_{\mathbf{k}}\omega_{\mathbf{k}}\right\}-\beta y_{\mathbf{k}}\theta_{\mathbf{k}}} \\ &= \sqrt{\frac{4\pi^2\kappa_{\mathbf{k}}^2}{\beta\epsilon-\gamma^2\kappa_{\mathbf{k}}^2}} e^{\frac{\beta^3 y_{\mathbf{k}}^2}{4(\beta\epsilon-\gamma^2\kappa_{\mathbf{k}}^2)}}.\end{aligned} \tag{3.51}$$

The Gaussian integration requires $\beta > 0$ and $\epsilon > 0$ and $\beta\epsilon > \gamma^2\kappa_{\mathbf{k}}^2$. Contrarily to the axisymmetric case, only positive temperature regimes are allowed. The Boussinesq equilibrium regimes can however be mapped to the mock equilibrium regimes. It suffices to consider the change of variables $(\beta, \epsilon) \to (\beta, \beta + \epsilon)$ in Equation (3.51) to recover the quadratic part of Equation (3.49).

The coefficients β, γ,ϵ are usually interpreted as thermodynamic inverse temperatures. Here, β also appears in the linear stratification term $-\beta y_{\mathbf{k}}\theta_{\mathbf{k}}$. It could therefore also be thought of as analogous to an external thermodynamic field. It breaks the symmetry $\theta \to -\theta$. The values of $\langle\theta_{\mathbf{k}}\rangle = \dfrac{\beta^2 y_{\mathbf{k}}}{2(\beta\epsilon-\gamma^2\kappa_{\mathbf{k}}^2)}$. In the non-helical case($\gamma = 0$), for example, the flow is stratified for ϵ close to 0, and large values of β. However, it is not clear, whether the regime $\beta \to \infty$ and $\epsilon \to 0$, leads to a thermodynamic limit ($\kappa_{\max} \to \infty$). The average temperature squared is indeed in equipartition: the average (total) temperature squared is therefore either 0 or infinite in the limit of an infinitely large cutoff.

3.4 A toy model of ideal 2D3C flows.

In this section, absolute equilibria are illustrated with the numerical integration of a low dimensional dynamical model – a so-called "shell model" – of 2D3C turbulence, whose non-linear interactions involve only nearest or next nearest modes interactions in the space of modes and whose inviscid limit exactly preserves three invariants. Those invariants can be made akin either to the axisymmetric quadratic mock invariants or to the magnetic quadratic invariants, or even to a wider class of 2D3C rugged invariants.

3.4.1 Description of the model

... in terms of explicit equations. We consider the evolution of $2N$ modes $x_1, ...x_N$ and $y_1 ... y_N$ under the following general dynamics

$$\begin{pmatrix}\dot{x}_n \\ y_n\end{pmatrix} = N_n + F_n + D_n. \tag{3.52}$$

N_n is a –non-linear – coupling between the modes, F_n is a forcing term and D_n is a dissipation term.

Let us consider a specific non-linear term involving next-nearest coupling between

the modes. We choose $N_n = (N_n^x, N_n^y)$ as

$$\begin{aligned} N_n^x &= a_1^{(n)} x_{n-1}y_{n-2} + a_2^{(n)} x_{n-1}y_{n+1} + a_3^{(n)} x_{n+2}y_{n+1} + a_4^{(n)} x_{n-2}y_{n-1} \\ &\quad + a_5^{(n)} x_{n+1}y_{n-1} + a_6^{(n)} x_{n+1}y_{n+2}, \\ \text{and} \quad N_n^y &= b_1^{(n)} x_{n-2}x_{n-1} + b_2^{(n)} x_{n-1}x_{n+1} + b_3^{(n)} x_{n+1}x_{n+2} + b_4^{(n)} y_{n-2}y_{n-1} \\ &\quad + b_5^{(n)} y_{n-1}y_{n+1} + b_6^{(n)} y_{n+1}y_{n+2}; \end{aligned} \tag{3.53}$$

where the coefficients $a_i^{(n)}$ and $b_i^{(n)}$ are taken as

$$\left\{ \begin{array}{l} a_1^{(n)} = \{\mathbf{2},\mathbf{3}\}^{(n)} \\ a_2^{(n)} = \{\mathbf{3},\mathbf{1}\}^{(n+1)} \\ a_3^{(n)} = \{\mathbf{1},\mathbf{2}\}^{(n+2)} \\ a_4^{(n)} = \alpha_{n-2}\alpha_n^{-1}\{\mathbf{2},\mathbf{1}\}^{(n)} \\ a_5^{(n)} = \alpha_{n+1}\alpha_n^{-1}\{\mathbf{3},\mathbf{2}\}^{(n+1)} \\ a_6^{(n)} = \alpha_{n+1}\alpha_n^{-1}\{\mathbf{1},\mathbf{3}\}^{(n+2)} \end{array} \right. \quad \text{and} \quad \left\{ \begin{array}{l} b_1^{(n)} = A_3^{(n)}\{\mathbf{1},\mathbf{3}\}^{(n)} \\ b_2^{(n)} = A_1^{(n+1)}\{\mathbf{2},\mathbf{1}\}^{(n+1)} \\ b_3^{(n)} = A_2^{(n+2)}\{\mathbf{3},\mathbf{2}\}^{(n+2)} \\ b_4^{(n)} = \alpha_n\alpha_{n-1}^{-1}\{\mathbf{2},\mathbf{3}\}^{(n)} + \{\mathbf{2},\mathbf{1}\}^{(n)} \\ b_5^{(n)} = \alpha_n\alpha_{n-1}^{-1}\{\mathbf{3},\mathbf{1}\}^{(n+1)} + \{\mathbf{3},\mathbf{2}\}^{(n+1)} \\ b_6^{(n)} = \alpha_n\alpha_{n+2}^{-1}\{\mathbf{1},\mathbf{2}\}^{(n+2)} + \{\mathbf{1},\mathbf{3}\}^{(n+2)} \end{array} \right. . \tag{3.54}$$

The bracket $\{\mathbf{I},\mathbf{J}\}^{(n)} = A_i^{(n)}B_j^{(n)} - A_j^{(n)}B_i^{(n)}$ with which we define the coefficients involves the quantities A_i and B_j which are taken as :

$$\left\{ \begin{array}{l} A_1^{(n)} = \dfrac{\alpha_{n-1}-\alpha_n}{\alpha_{n-1}\gamma_{n-2}} \\ A_2^{(n)} = \dfrac{\alpha_{n-2}-\alpha_{n-1}}{\alpha_{n-2}\gamma_n} \\ A_3^{(n)} = \dfrac{\alpha_n-\alpha_{n-2}}{\alpha_n\gamma_{n-1}} \end{array} \right. \quad \text{and} \quad \left\{ \begin{array}{l} B_1^{(n)} = \dfrac{\alpha_{n-1}\gamma_{n-1}-\alpha_n\gamma_n}{\alpha_{n-1}} \\ B_2^{(n)} = \dfrac{\alpha_{n-2}\gamma_{n-2}-\alpha_{n-1}\gamma_{n-1}}{\alpha_{n-2}} \\ B_3^{(n)} = \dfrac{\alpha_n\gamma_n-\alpha_{n-2}\gamma_{n-2}}{\alpha_n} \end{array} \right. . \tag{3.55}$$

Quantities labeled by an index which is either negative or strictly greater than N are taken as zero. α_n and γ_n can be any arbitrary functions of n.

... in terms of dynamical invariants. Equations (3.53), (3.54) and (3.55) may look both arbitrary and cryptic. They are not arbitrary. As shown in Appendix C , such a choice of a non-linear coupling makes the inviscid dynamics (3.52) – obtained by setting $D_n = F_n = 0$ – conserve the three following quantities :

$$E = \overbrace{\frac{1}{2}\sum_{n=1}^{N} x_n^2}^{E^x} + \overbrace{\frac{1}{2}\sum_{n=1}^{N} \gamma_n y_n^2}^{E^y}, \qquad H = \sum_{n=1}^{N} x_n y_n, \quad \text{and} \quad G = \frac{1}{2}\sum_{n=1}^{N} \alpha_n x_n^2. \tag{3.56}$$

Let us casually remark that the dynamical equations trivially satisfy a Theorem of Liouville. Arguments based on absolute equilibria should therefore be valid to describe the statistical properties of long time integrations of (3.53), (3.54) and (3.55) in the inviscid limit.

Generalized 2D3C flows. Different choices for γ_n and α_n produce different ideal invariants (3.56) for the shell-model. For example, a two-parameter family of 2D3C invariants

can be obtained by choosing

$$\kappa_n = 2^{n-4}, \qquad \gamma_n = \kappa_n^{-g}, \quad \text{and} \quad \alpha_n = \kappa_n^{-a}. \tag{3.57}$$

Different values of a and g produce different toy models of 2D3C flows. If one sets $a = 0$ and $g = 2$ the invariants E, H and G mimic the energy ,the helicity and the – approximated – peristrophy which we used to describe the axisymmetric mock equilibria. Similarly, if one sets $a = 2$ and $g = 0$, then E, H and G match the magneto-hydro rugged invariants [(a)].

More generally, the two-parameter family of inviscid invariants which the toy dynamics preserve match the rugged invariants of the following family of generalized 2D3C flows [(b)] :

$$\begin{gathered} \partial_t \omega + [\psi, \omega] = [A, j] \quad \text{and} \quad \partial_t A + [\psi, A] = 0, \\ \text{with} \quad \omega = -\nabla^{a+g} A \quad \text{and} \quad j = -\nabla^a A. \end{gathered} \tag{3.59}$$

In either one of the two specific magneto-hydro and mock axisymmetric regimes, the coefficients (3.54) are all trivially zeros. This is not the case when a and g are only close to those specific limits. Depending on the regime considered, I will stick to the terminology of magneto-hydro and axisymmetric dynamics to refer to the invariants (3.56).

Absolute equilibrium regimes. The absolute equilibrium regimes based on the three invariants E, H , and G strongly depend on the signs of a and g. They are sketched on Figure 3.7.
In a nutshell, whatever the signs of a and g, there exists a negative temperature peristrophy regime. The negative temperature regime describes a concentration of toroidal/magnetic energy on the largest scale if a is positive and on the smallest scale if a is negative. The helicity favors small scales if g is negative and large scales otherwise. In the positive temperature regime, the situation is somehow reversed : positive (resp. negative) values of a yield a small-scale (resp. large-scale) poloidal/kinetic energy .

3.4.2 Numerical inviscid runs.

3.4.2.1 A close look at a run near the "magnetic regime"

Low dimensional non-helical magnetic runs. As an illustration, let us first consider the case $a = 2$ and $g = 0.5$, which we can consider as a case close to a "magnetic regime". Let us put some energy on the first three "magnetic" modes $x_1 = x_2 = x_3 = \sqrt{2/3}$ and set to zero all the other modes. Such an initial state has a total energy equal to one. Since it is purely magnetic, it is also non helical. The shell model (3.53) is then numerically

[(a)] To see this more explicitly, just consider the change of variables $x_n = a_n {\alpha_n}^{-1/2}$ and $y_n = \omega_n {\alpha_n}^{1/2}$. Then Equation (3.56) becomes

$$E = \frac{1}{2}\sum_{n=1}^{N} \kappa_n^a a_n^2 + \frac{1}{2}\sum_{n=1}^{N} \kappa_n^{-(a+g)} w_n^2, \qquad H = \sum_{n=1}^{N} a_n w_n, \quad \text{and} \quad G = \frac{1}{2}\sum_{n=1}^{N} a_n^2. \tag{3.58}$$

[(b)] Those generalized 2D3C flows might be seen as a the 2D3C generalization of the already generalized surface quasi-geostrophic flows considered in [Pierrehumbert et al., 1994].

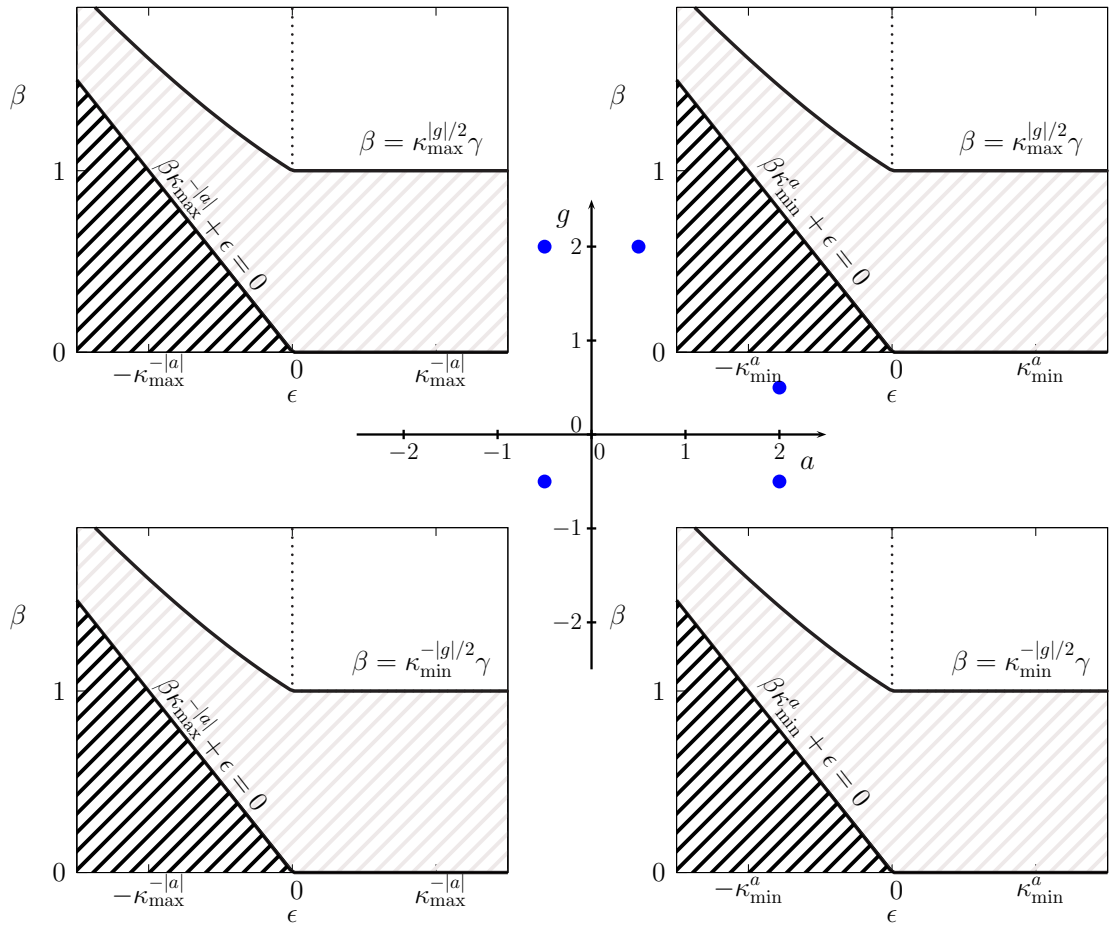

Figure 3.7: Absolute equilibrium regimes, as obtained for different signs of a and g (Equation (3.57). β,γ, and ϵ are the inverse energy, helicity and peristrophy temperatures. The graphs may seem similar between one another but they differ by their labels. The lines that delimit the black hatched regions correspond to the case without helicity. In each case γ is chosen so that the critical β at $\epsilon = 0$ is 1. The blue dots indicate the parameters which we use in section 3.4.2.

integrated with no viscosity nor forcing with N dyadic modes 2^{-4}, 2^{-3} ..., 2^{N-4}, and $N = 7$, 15 and 30. The technical details of the numerical integration are summarized in Table (3.1).

What do we expect to see ? Figure 3.7 tells us that for such a choice of a and g, a purely magnetic large scale initial state should yield a negative ϵ equilibrium. If a statistical equilibrium was to be reached, then most of the energy should remain on the largest scales and the rest of the energy should then be in equipartition. Besides, we also expect the statistics of the single modes x_n and y_n to be Gaussian. The variance of y_n should be proportional to $\gamma_n^{-1} \propto 2^n g$. The variance of x_n should be proportional to $(\beta + \epsilon\alpha_n)^{-1}$. Hence, in the present case, it should scale as 2^{na} for small values of n and be constant for large values of n.

Description of the results. To monitor the evolution of the typical scales of E, G, and H, we compute the "centroids" κ_E, κ_H, κ_G, defined as

$$\kappa_E = \frac{1}{2E}\overbrace{\sum_{n=1}^{N}\kappa_n\gamma_n y_n^2}^{E_y\kappa_{Ey}} + \frac{1}{2E}\overbrace{\sum_{n=1}^{N}\kappa_n x_n^2}^{E_x\kappa_{Ex}}, \qquad \kappa_G = \frac{1}{2G}\sum_{n=1}^{N}\kappa_n y_n^2, \quad \text{and} \quad \kappa_H = \frac{1}{\sum_{n=1}^{N}|x_n y_n|}\sum_{n=1}^{N}\kappa_n|x_n y_n| \tag{3.60}$$

Centroids. As shown on Figure 3.8, the peristrophy centroid κ_G stays close to 2^{-4}, while the other centroids evolve towards the largest wavelengths. Only the peristrophy prevents the flow to be totally small scaled. It is hard to get more than qualitative information from those quantities : since the weight put on the small scales grows exponentially, a small amount of energy on the largest κ_n will make the centroids be essentially close to it. Note in passing the very good conservation of the quantities E,H and G during the run.

Spectra. To have a finer look at the properties of the energies and the helicity, we can take a look at time averaged spectra of energies and helicities. Those are shown on Figure 3.9. As the number of modes increases, the magnetic energy $< E_x >$ become more and more peaked on the gravest mode. What remains of of the energy is spread over all the other modes, with no distinction of its magnetic or kinetic nature. The helicity spectra have positive slopes, this can be interpreted as consequence of the coefficient g being positive, and hence favoring a partitioning of helicity at small scales.

Statistics. Many of the modes display Gaussian statistics (Figure 3.10), as predicted by the absolute equilibria theory. If we probe the Gaussianity of those statistics with a Kolmogorov-Smirnov test, we find out that for the number of modes whose p-values are less than the sharp threshold 0.1 – and hence most likely not Gaussian – is 4 for $N = 7$, 6 for $N = 15$ and 14 for $N = 30$. The variance of each of the distribution scales reasonably well with the wave number, in accordance with the absolute equilibrium scalings. Qualitatively, we can observe that the (scaled) variances roughly decrease by a factor 4 as the number of modes roughly doubles when we double the number of modes from $N = 7$ to $N = 15$ first, and $N = 15$ to $N = 30$ then : the more modes are considered, the less the single modes distributions fluctuate, except for the distribution of the gravest mode.

3.4.2.2 A brief comparison with the other regimes.

Description of the runs. To check whether the good accordance observed between the absolute equilibria and the "nearly magnetic" runs $(a, g) = (2, 0.5)$ is a generic behavior or not, we have investigated other pairs of parameters (a, g). As in the nearly magnetic runs, the runs are initialized by setting $x_1 = x_2 = x_3 = \sqrt{2/3}$ so that the total initial energy is 1. Results are here shown, that correspond to $N = 15$, and $(a, g) = (0.5, 2)$, $(2, 0.5)$, $(2, -0.5)$, $(-0.5, -0.5)$, $(-0.5, 2)$ as indicated by the blue dots of Figure 3.7. More technical details about the runs are summarized on Table 3.1.

	$a=0.5\,;\,g=2$	$a=2\,;\,g=0.5$			$a=2\,;\,g=-0.5$	$a=-0.5\,;\,g=-0.5$	$a=-0.5\,;\,g=2$
N	15	7	15	30	15	15	15
δt	$5\cdot10^{-5}$	$5\cdot10^{-5}$	$5\cdot10^{-5}$	$2\cdot10^{-5}$	$5\cdot10^{-5}$	$5\cdot10^{-4}$	$5\cdot10^{-5}$
τ_c	2.0	1.0	$1.3\cdot10^{-2}$	$6\cdot10^{-6}$	7.4	$8.0\cdot10^{-3}$	$6.6\cdot10^{-1}$
$\tau_{\max}$	$1.5\cdot10^{3}$	$3.0\cdot10^{3}$	$2.3\cdot10^{4}$	$1.9\cdot10^{8}$	$4.1\cdot10^{2}$	$3.8\cdot10^{6}$	$4.6\cdot10^{3}$

Table 3.1: Parameters used for the runs described in section 3.4.2. N is the number of modes, δt is the time step used for the numerical integration, $\tau_c = \left(\kappa_f^E \sqrt{E}\right)^{-1}$ a characteristic time scale based on the value of the energy inverse typical scale κ_f^E for the last iteration. $\tau_{\max}$ is the final time of integration, measured in terms of τ_c. The numerical integration uses a standard explicit 4^{th}-order Runge-Kutta algorithm. For all the runs, the number of iteration steps is 6×10^7 and the initial state is a state of energy 1 with $x_1 = x_2 = x_3 = \sqrt{2/3}$ and all the other modes are set to zero. The modes are taken as $\kappa_n = 2^{n-4}$, with n between 0 and $N-1$.

Brief description of the results. The single modes statistics, energy spectra and helicity spectra for each run are displayed on Figures 3.13, 3.11 and 3.12 respectively. A first look at the energy and the helicity spectra confirms the fact that the respective signs of a and g substantially modify the properties of the long time dynamical equilibria, in the way indicated by the absolute equilibrium arguments. For positive values of a, the energy concentrates on the smallest mode, on which it is mostly magnetic. Contrarily, for negative values of a, we expect the energy to peak on the largest mode and be of kinetic nature. Some hints of such a behavior can be seen for the run $(a,g) = (-0.5,-0.5)$. For the run $(a,g) = (-0.5,2)$, we don't see any peak, but most of the energy has turned into kinetic energy (Figure 3.11).

Similarly, the slopes of the helicity spectra depend on the sign of g. For positive g, the helicity tend to be large-scale, while for negative g it tends to be small-scale. Hence, both the energy and the helicity spectra that we obtained are in reasonable agreement with the absolute equilibria predictions.

What about the single modes statistics ? For positive values of a and g, many modes exhibit Gaussian statistics. This is not the case for the other sets of parameters. For $(a,g) = (2,-0.5)$, the situation is pretty catastrophic, since none of the thirty modes considered can be considered Gaussian. Such a behavior may be heuristically explained : since both the energy and the helicity need to be large scale, the dynamical fluctuations of the small scales are too weak to thermalize the large scales.

The situation is less clear for the runs with a negative value of a. In those two cases, it is found that while most of the toroidal/magnetic modes x_n are Gaussian, almost none of the poloidal/kinetic modes y_n are. This feature might be coherent with the outlook of the corresponding energy spectra. For $(a,g) = (-0.5,2)$, the small kinetic/poloidal scales do not seem to be at equilibrium. This might also be the case for run $(a,g) = (-0.5,-0.5)$. However, such a behavior is also seen in a numerical integration with $N = 7$ modes, implying that a longer integration time would not change the observed behavior.

3.5 Conclusion

The linear inviscid statistical mechanics in the space of eigenmodes has made it clear that in spite of their formal analogy, two-dimensional magnetohydrodynamics and axisymmetric/Boussinesq flows are of very different nature. Simple absolute equilibrium arguments show that axisymmetric dynamics are intrinsically "more" three-dimensional than two-dimensional magnetohydrodynamics , as the rugged invariants do not constrain the initially large-scale motion to remain on the large scales. More generally, the equilibria are not so much sensitive to the presence of extra rugged invariants – in addition to the energy – than to the interplay between those. This conclusion is further emphasized by the description of the equilibrium regimes of a family of generalized 2D3C flows. Those flows possess rugged Casimir invariants which match the axisymmetric/magnetohydro ones but whose Energies are different. The common feature of teh equilibrium regimes is that they describe an energy being either essentially toroidal/magnetic or kinetic/poloidal. Apart from that, all kinds of equilibrium regimes are predicted. As diagnosed by the numerical study of a toy dynamical model for those 2D3C fluids, the axisymmetric case appears to be a limiting case ("a=0"), for which the extra invariant (the "peristrophy") is not anisotropic enough in the space of eigenmodes to yield a regime analogous the the condensation regime of bi-dimensional hydro and magnetohydro flows.

At a more fundamental level, the axisymmetric case has also made it clear that even though it is both simple and systematic, the program that consists in considering equilibria for some kind of truncated dynamics with the hope that the truncated equilibria may possess an accurate thermodynamic limit relevant for the original equations is perhaps not so worth pursuing at all cost. As shown by the axisymmetric case, it may fail in considering relevant invariants, that are not conserved by any of the truncated equations, but which might still be of crucial importance for the physics of the problem.

At this stage, while only two or three invariants are needed to describe a thermodynamic limit for the two-dimensional magnetohydrodynamics and the two-dimensional equations, it is yet not clear whether one can define a suitable thermodynamic limit for the axisymmetric and the Boussinesq flows, even if we were to take into account more invariants. Statistical mechanics *à la* Kraichnan which involves Fourier-like modes and truncated dynamics is not exactly tailored to explore rigorously this problem. It is therefore time to leave the wavelength space and switch to the physical space, using as a guideline the formal Theorem of Liouville which was described in the previous chapter.

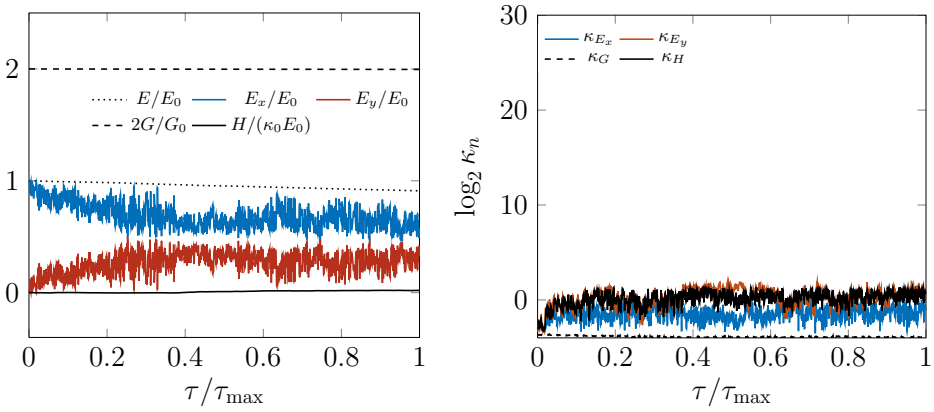

(a) $N = 7$

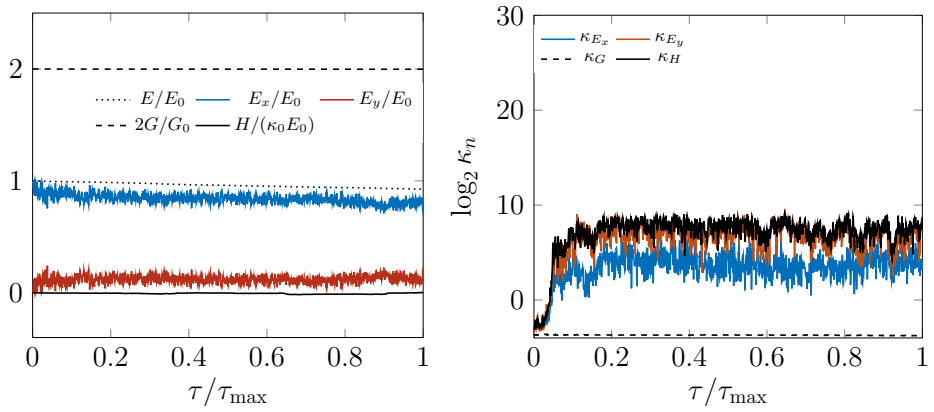

(b) $N = 15$

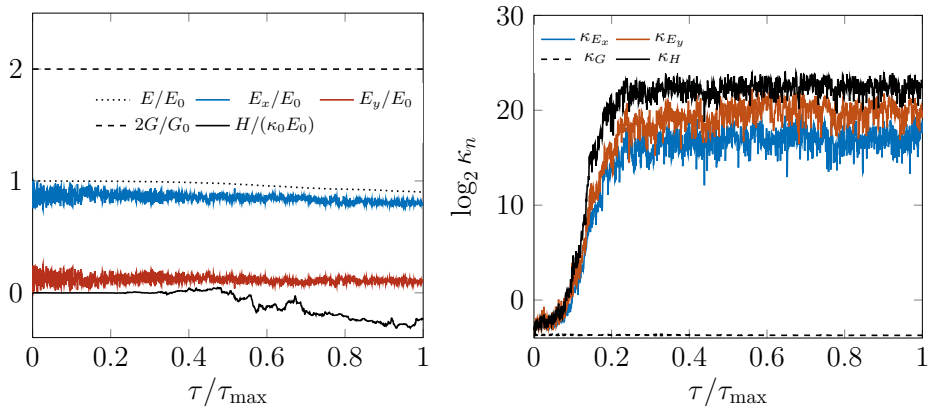

(c) $N = 30$

Figure 3.8: Left : Evolution of the invariants for a nearly magnetic ideal $(a, g) = (2, 0.5)$, between the initial time τ_0 and the final time $\tau_{\max}$ –see Table (3.1). The total (E), magnetic (E_x), and kinetic (E_y) energies are renormalized by the initial energy $E_0 = 1$; G is renormalized by the half of the initial peristrophy G_0. The renormalization of the Helicity involves the typical energy mode at initial time, $K_0 \simeq 2^{-2.7}$. Right : evolution of the typical modes ("centroids") associated to E^x, E^y, G and H – see the text for a definition.

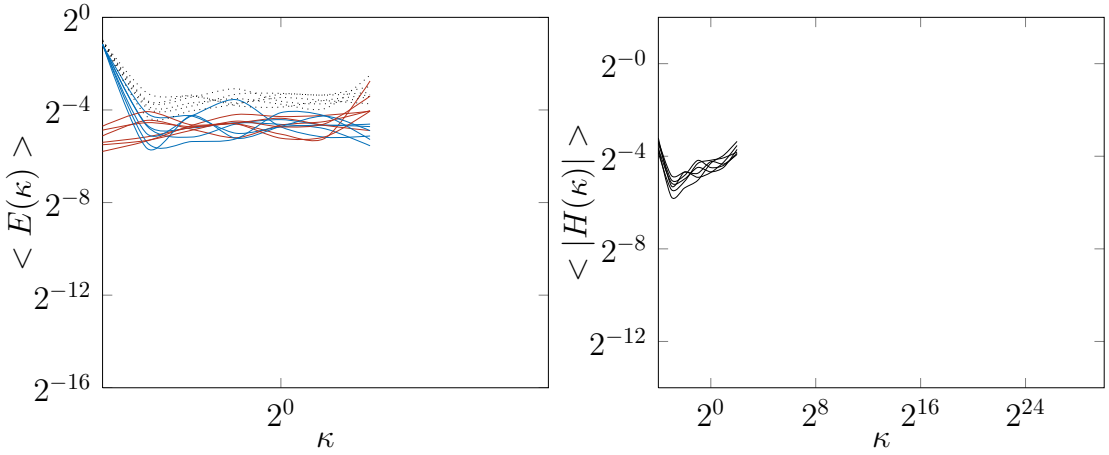

(a) $N = 7$

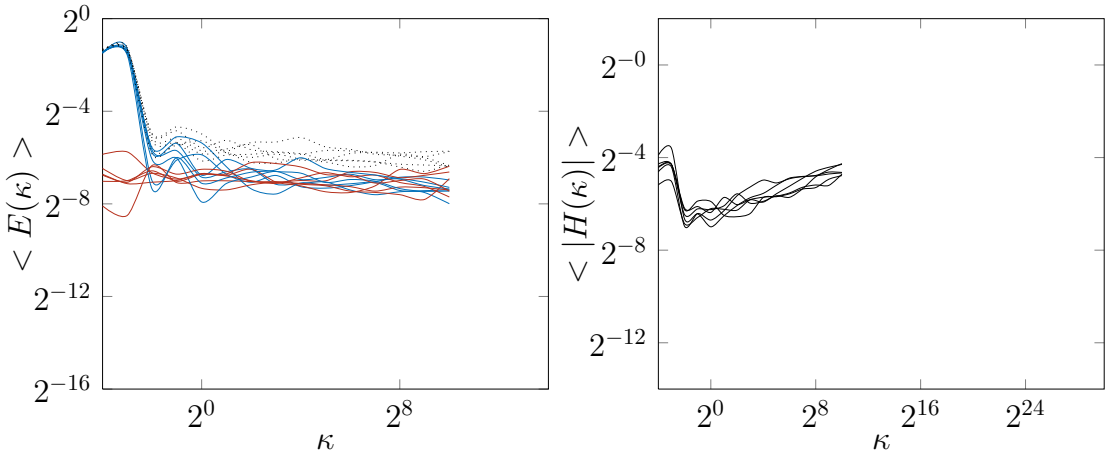

(b) $N = 15$

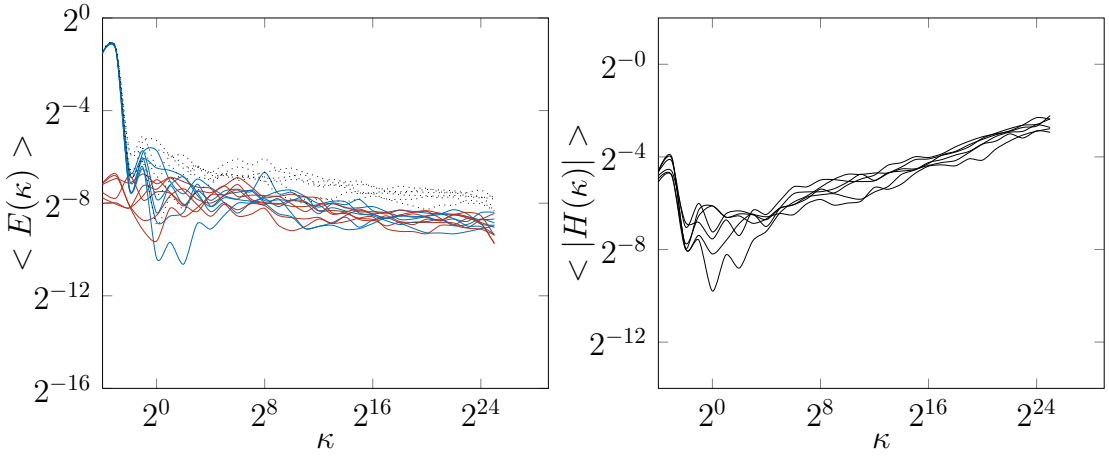

(c) $N = 30$

Figure 3.9: Left: Spectra of magnetic/toroidal energies $< E_x(\kappa) >$ (–), and kinetic/poloidal energies $< E_y(\kappa) >$ (–), and total energy $(\cdots)$ for the runs $a = 2$ and $g = 0.50$. Right : Spectra of absolute Helicity $\langle |H| \rangle$. In both cases, <> denotes a temporal average, computed over $1/12^{th}$ of the final time, and 500 instantaneous spectra. The temporal averages are computed between $\tau = \tau_{\max}/2$ and $\tau_{\max}$.

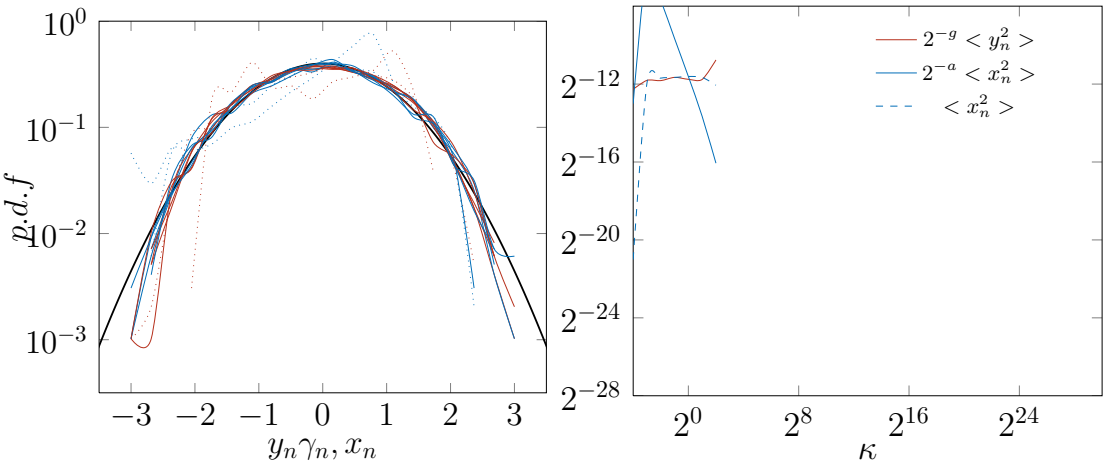

(a) $N = 7$

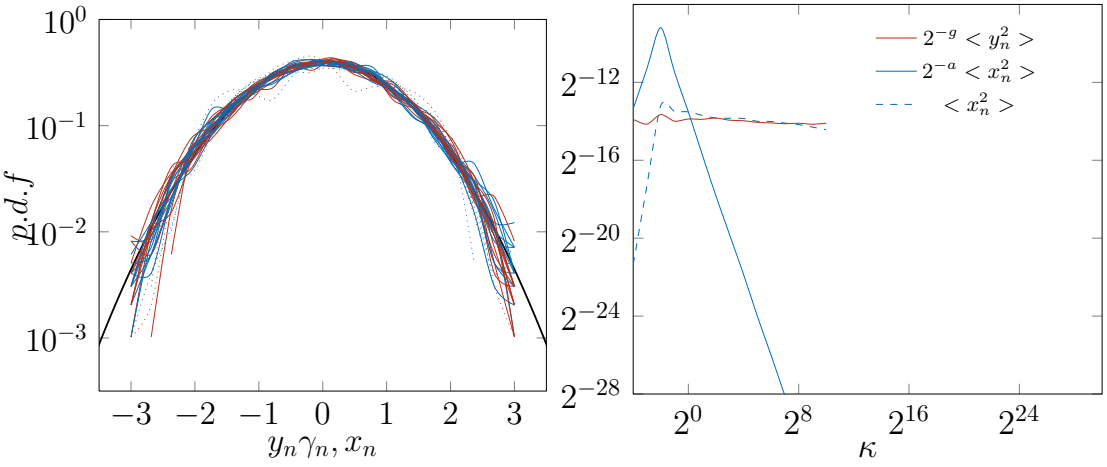

(b) $N = 15$

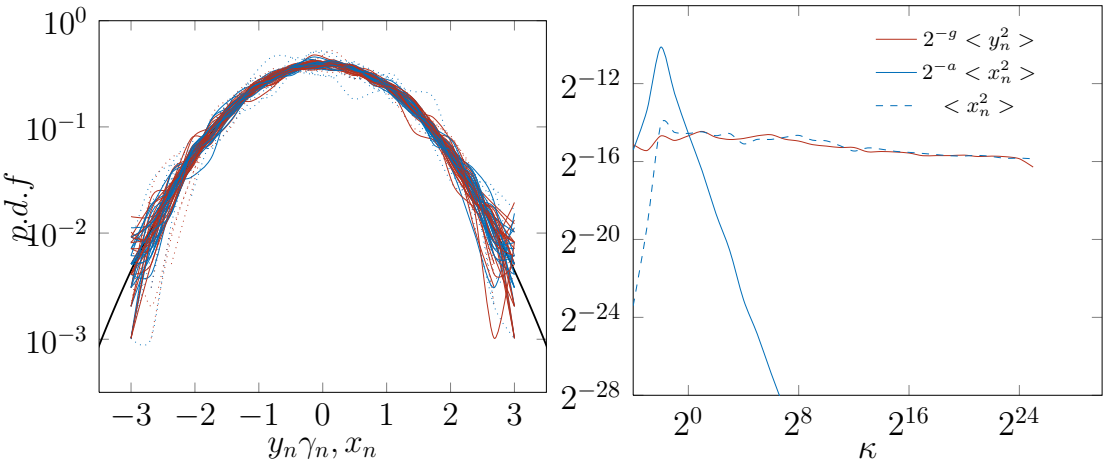

(c) $N = 30$

Figure 3.10: Left: Normalized distributions of each of the $2N$ toroidal/magnetic modes x_n (–) and ploidal/kinetic y_n (–). Dotted and solid lines indicate distributions whose p-values obtained with a Kolmogorov-Smirnov test probing their Gaussianity likelihood are respectively below and above 0.1. The black solid line indicates a Gaussian distribution. Right: Compensated empirical variances as functions of the wave numbers. The temporal averages are computed between $\tau = \tau_{\max}/2$ and $\tau_{\max}$ and involve 3000 data points.

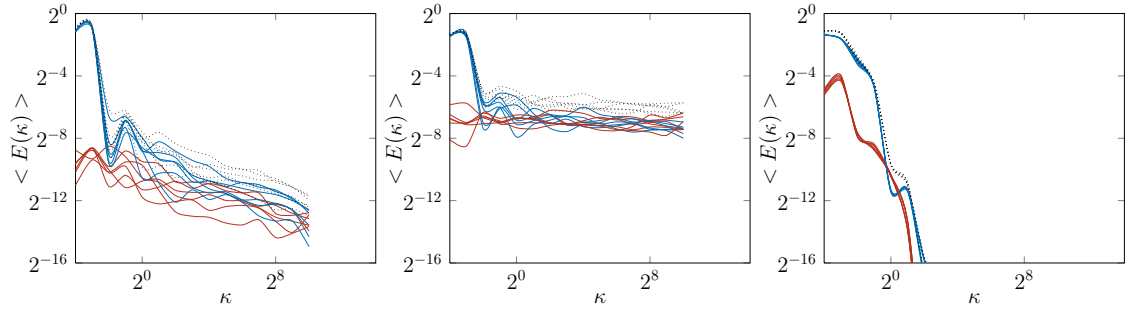

(a) $a = 0.5; g = 2$ **(b)** $a = 2; g = 0.5$ **(c)** $a = 2; g = -0.5$

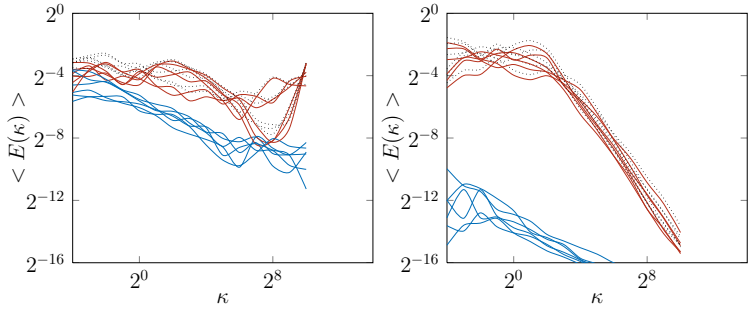

(d) $a = -0.5; g = -0.5$ **(e)** $a = -0.5; g = 2$

Figure 3.11: Energy spectra observed for $N = 15$ and various a and g. The color and the style codes are the ones described in Figure 3.9, as is the definition of the temporal averages $<>$.

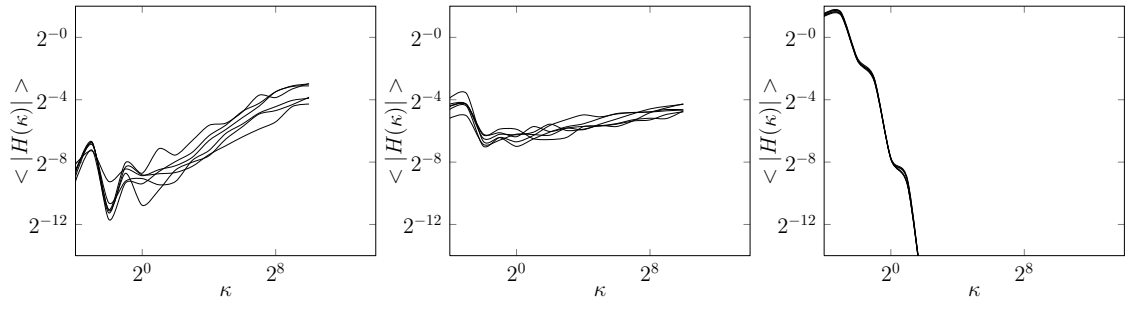

(a) $a = 0.5; g = 2$ **(b)** $a = 2; g = 0.5$ **(c)** $a = 2; g = -0.5$

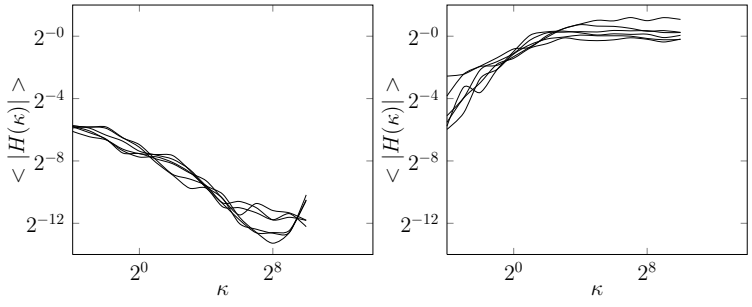

(d) $a = -0.5; g = -0.5$ **(e)** $a = -0.5; g = 2$

Figure 3.12: Absolute Helicity spectra observed for $N = 15$ and various a and g.

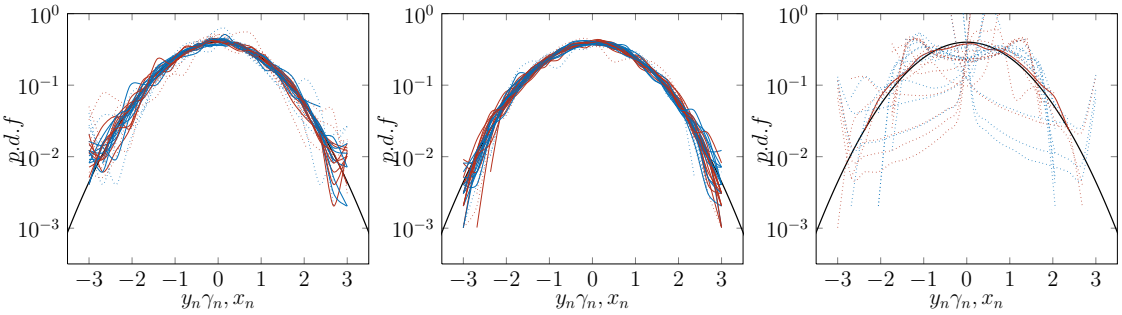

(a) $a = 0.5; g = 2$ **(b)** $a = 2; g = 0.5$ **(c)** $a = 2; g = -0.5$

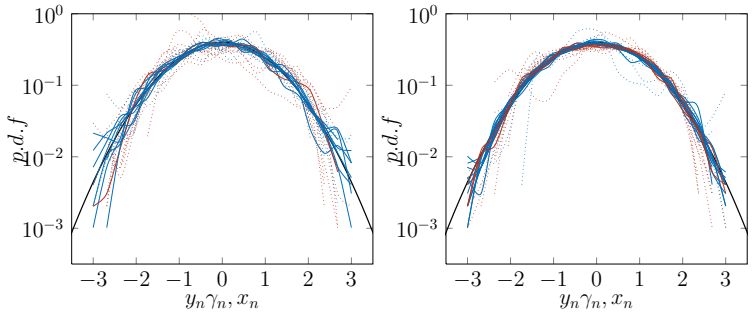

(d) $a = -0.5; g = -0.5$ **(e)** $a = -0.5; g = 2$

Figure 3.13: Normalized distributions of each of the $2N$ modes x_n and y_n for $N = 15$ and various a and g. The color and the style codes are the ones used for Figure 3.10.

Chapter 4

Statistical mechanics in physical space : the axisymmetric case.

In this chapter, we compute microcanonical measures for inviscid (untruncated) axisymmetric flows and take into account all the invariants. The computation is an extension of the Robert-Miller-Sommeria theory to the case of axisymmetric flows. To achieve the computation, we trade off the space of eigenmodes against the physical space, and forget about truncated dynamics. To highlight the construction, we use an analogy with a spin model (Ising like) whose properties are dictated by the dynamical invariants of the axisymmetric equations. The analogy with the lattice model is very much in the spirit of Miller's original papers [Miller, 1990, Miller et al., 1992] about the statistical mechanics of two-dimensional flows. The microcanonical measure can be seen as a well-defined thermodynamic limit of microcanonical ensembles defined on the lattice model. Because of the lack of natural bound for the fluctuations of the poloidal field, the axisymmetric thermodynamic limit needs however to be taken thoughtfully. The physics highlighted by the present construction considerably refines the physics of the mock equilibria described in the previous chapter. The thermodynamics of the axisymmetric flows describes an infinitely warm poloidal field interacting with a colder toroidal field. The same construction applies for two-dimensional Boussinesq flows. The study is described in a paper [Thalabard et al., 2013] written in collaboration with Bérengère Dubrulle and Freddy Bouchet, and which has been accepted for publication in *Journal of Statistical Mechanics*. The paper is mostly self-contained. Its physical content is impressionistically summarized within its five first figures. For completeness, I add some brief comments concerning previous works involving statistical mechanics and axisymmetric flows, as well as a short addendum about the statistical mechanics of two-dimensional flows from the Robert-Miller-Sommeria perspective.

Contents

Notation: In this chapter , I refer to the equations of the paper [Thalabard et al., 2013] as (P1), (P2), and so on.

4.1 Previous statistical mechanic descriptions of axisymmetric flows.

Theoretical works on statistical mechanics and axisymmetric flows are seldom but do exist. Several propositions have be made to extend the Robert-Miller-Sommeria [(a)] to the case of axisymmetric flows. Both the non swirling case and the swirling case have already been investigated. We report those below.

4.1.1 Statistical mechanics of non-swirling flows.

Non-swirling flows. [Mohseni, 2001] and [Lim, 2003] consider axisymmetric flows for which the toroidal field is vanishing. Doing so, they describe so-called "non-swirling" axisymmetric flows. Non-swirling axisymmetric flows can can be used to model jets or vortex rings, fascinating examples of which are shown on Figure 4.1. It is argued in [Mohseni, 2001], that the formation of vortex rings involves " strong mixing between the shear layer and the ambient fluid". Hence, vortex rings can legitimately be seen as non-swirling equilibrium structures.

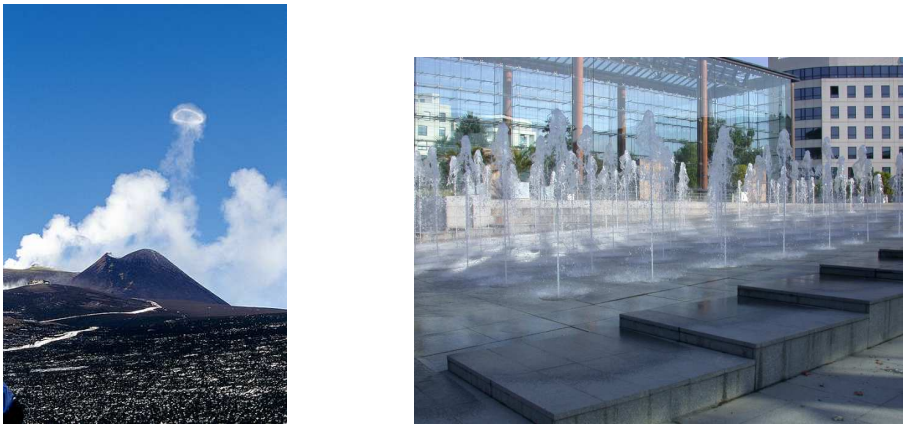

Figure 4.1: Two examples of non swirling flows. Left : A gas ring emitted in 2000 during a volcano eruption at Mount Etna (taken from www.flickr.com/photos/etnaboris/4655808536/). Right : Non swirling fountain jets at the Parc André Citroën in Paris (taken from paris1900.lartnouveau.com).

From a theoretical point of view, one can however remark that the non-swirling case is very specific. It is also very close to the bidimensional situation. Indeed, if one sets σ to 0 in the axisymmetric Equations (1.13) of Chapter (1) – or equivalently in Equations (P3) of the paper –, then one is left with a transport equation for the poloidal field ξ :

[(a)] In order not to beat around the bush, the description of the Robert-Miller-Sommeria theory in the context of two-dimensional flows is not described here, but in a small addendum at the end of the present chapter.

$$\partial_t \xi + [\psi, \xi] = 0 \quad \text{and} \quad \xi = -\Delta_\star \psi, \tag{4.1}$$

where the notations are those introduced in the first chapter.

Hence, the integral of any moment of the poloidal field is conserved by the dynamics. The poloidal field is therefore as constrained as the vorticity field in two dimensions. Hence, the statistical mechanics of non-swirling flows and of two-dimensional flows have a very similar flavor. The large scale structures basically come from the interplay between a purely poloidal energy $E^{\rm pol} = \frac{1}{2}\int_{\mathcal{D}} \xi \Delta_\star^{-1}[\xi]$ and a strong constraint on the moments of the poloidal distribtion, such as a poloidal enstrophy constraint $\frac{1}{2}\int_{\mathcal{D}} {\rm d}r\xi^2$.

Existing Results. In [Mohseni, 2001], it is found that the statistical equilibria only depend on the energy, the impulse and the circulation. Although not many details are given, it is argued that those equilibria correctly account for the formation of ring vortices both experimentally and numerically.

In [Lim, 2003], more attention is given to the description of jets. It is found that both negative and positive temperature equilibria can exist. Negative temperature equilibria are found, that describe large energy, low- poloidal enstrophy equilibria. Physically, those equilibria describe a mean flow uniform in the axial direction. In the positive temperature regime, no large scale structures emerge. The two regimes are physically related to the strength of the flow rate Q. In both cases, the statistical arguments are substantially not different than the ones at play in the two-dimensional case.

4.1.2 Statistical mechanics of swirling flows : the case of Beltrami flows

4.1.2.1 Swirling flows.

Examples. The situation is very different if one considers the axisymmetric equations in their full extent. Let us here not set the toroidal term σ to zero. (Not) doing so, we deal with the more general case of swirling flows. Note that from a practical point of view, real-life examples of swirling flows are very different from non-swirling flows and we expect their physics to be also quite different – compare Figure 4.1 to 4.2 !

Dynamical invariants and the "poloidal catastrophe". At the level of the dynamical invariants, the presence of the toroidal term σ, however small with respect to the poloidal term ξ, makes the axisymmetric swirling inviscid invariants very different from the non-swirling inviscid invariants – see equations (P4) and (P5). The energy has now two components. It can be split into a toroidal contribution and a poloidal contribution. More importantly, the moments of the poloidal field are no longer conserved by the dynamics – see equations (P4), (P8) and (P9) of the paper. Only Helical Casimirs are – see Chapter 1. Hence, the poloidal field is only weakly constrained, and it is not clear at all what statistical mechanics is going to describe. Basically, Miller's appproach of statistical equilibria in two-dimension indeed requires that vorticity has a compact distribution, or decays sufficiently fast.

Figure 4.2: Left: A swirling twister about to hit Dorothy Gale's house in Fleming's 1939 *Wizard of Oz*. Right: the SPHYNX's vón Kárman swirling experiment (also known as the "French Washing Machine") filled with water at the SPHYNX laboratory.

Previous works. The statistical mechanics of swirling flows is considered in a series of papers [Leprovost et al., 2006, Naso et al., 2010a, Naso et al., 2010b], in the context of a Von Kármán experiment, which is depicted on Figure 4.2, and on which more will be said in chapter 6. In those three papers, axisymmetric equilibria are tackled from a very different point of view than the one we discuss in the present paper. It is worth writing a couple of words to describe what was found in those papers.

4.1.2.2 Axisymmetric coarse-grained equilibia and least bias approach.

Context. The papers [Leprovost et al., 2006, Naso et al., 2010a, Naso et al., 2010b] investigate the statistical equilibria from a very pragmatic point of view. Statistical solutions are not investigated within the context of invariant measures but rather from a least bias approach perspective. More precisely, Leprovost et al observe that the axisymmetric Euler equations possess an infinity of stationary solutions. Those solutions are obtained by setting the time derivatives to 0 in the axisymmetric ideal equations (1.13). They read

$$\sigma = F(\psi), \qquad \xi(\mathbf{r}) = r^{-2}F(\psi)F'(\psi) + G(\psi), \quad \text{and} \quad \xi = -\Delta_\star\psi, \tag{4.2}$$

where F and G can be any sufficiently regular functions.

Observe now that ψ is supposed to be a smooth field with low spatial variations over the domain that is considered. Hence, if the flow is stationary and satisfy (4.2) for prescribed F and G, then the relations (4.2) must still hold true at a coarse-grained level. This means, that for "decimated" fields $\bar\sigma$, $\bar\xi$ and $\bar\psi$ defined through a local coarse-graining of the fields σ, ξ and ψ respectively, we can expect to have $\bar\psi = \psi$ and hence

$$\bar\sigma = F(\psi), \qquad \bar\xi = r^{-2}F(\psi)F'(\psi) + G(\psi), \quad \text{and} \quad \bar\xi = -\Delta_\star\psi. \tag{4.3}$$

Now, suppose that you observe an experimental realization of an axisymmetric flow,

and suppose that the information you have access to is only a coarse-grained information. This means that although you might know that the fine-grained dynamics does not distort the distribution of the toroidal field, you do not know what this distribution actually is. What you have access to are coarse-grained quantities like a coarse-grained energy, a toroidal momentum or a poloidal circulation. The question is : can you statistically infer from your coarse grained observation what F and G are ? Can you make an " educated guess" on what the typical stationary toroidal and poloidal field should look like ?

The case of a "mildly fluctuating" poloidal field.

Strategy. Leprovost et al and Naso et al mostly consider the case where the poloidal fluctations are mild. This is tantamount to work under the hypothesis that $\xi = \bar{\xi}$. Then, to make their "educated guess", the authors use the principle of maximum entropy as advocated by Jaynes in his 1957 paper [Jaynes, 1957]. The strategy consists in (i) defining a local probability $\rho(\eta, \mathbf{r})$ that the toroidal field takes the value η at position $\mathbf{r}$ at a fine grained scale , (ii) introducing a mixing entropy, $S^{\text{mix}}(\rho) = \int_{\mathcal{D}} \mathrm{d}\mathbf{r} \int_{\mathbb{R}} \mathrm{d}\eta\, \rho(\eta, \mathbf{r}) \log \rho(\eta, \mathbf{r})$ and (iii) maximizing the mixing entropy S^{mix} over the space of the distributions, subject to various constraints.

Leprovost et al work out the toroidal distributions which maximize S^{mix} when both the toroidal Casimirs $C_n = \int_{\mathcal{D}} \bar{\sigma}^n$, the helicity $H = \int_{\mathcal{D}} \bar{\xi}\bar{\sigma}$, the circulation $\Gamma = \int_{\mathcal{D}} \bar{\xi}$ and a coarse-grained energy $E^{c.g} = \frac{1}{2}\int_{\mathcal{D}} \mathrm{d}\mathbf{r}\, \bar{\xi}\psi + r^{-2}\bar{\sigma}^2$ are prescribed. [(a)] Naso et al consider a simplified case, and work out the maximization of S^{mix} over the set of distributions ρ and coarse-grained field $\bar{\xi}$. The constraints are chosen to be the (fine-grained) energy $E = \frac{1}{2}\int_{\mathcal{D}} \mathrm{d}\mathbf{r}\, \bar{\xi}\psi + r^{-2}\bar{\sigma^2}$, the helicity $H = \int_{\mathcal{D}} \mathrm{d}\mathbf{r}\, \bar{\xi}\bar{\sigma}$ and the toroidal momentum $I = C_1 = \int_{\mathcal{D}} \bar{\sigma}$. The qualitative features found in both cases are pretty similar. Let us for instance further comment on the simplified case of [Naso et al., 2010a, Naso et al., 2010b] where three invariants are taken into account.

Selection of F and G in a "simple case". In the case where only the three invariants E, H and $I = C_1$ are taken into account to constrain the maximization of the mixing entropy, the critical points of the entropy are worked out in terms of three Lagrange multipliers β, γ and α, respectively associated to E, H and I. The critical distributions ρ_e satisfy

$$\rho_e(\eta, \mathbf{r}) = \sqrt{\frac{4\pi y}{\beta}} \exp - \frac{\beta}{4y}\left(\eta + 4y\frac{\alpha + \gamma\bar{\xi_e}}{2\beta}\right)^2, \tag{4.4}$$

and the corresponding coarse-grained typical field satisfy

[(a)] Note that if one neglects the poloidal fluctuations, then both the helicity, the circulation and the momentum are unaltered by the coarse-graining. This is not the case for the energy.

$$\bar{\sigma} = B\psi, \qquad \bar{\xi} = B\frac{\bar{\sigma}}{2y} + C, \quad \text{and} \quad \bar{\xi} = -\Delta_\star \psi, \\ \text{where} \quad B = -\frac{\beta}{\gamma} \quad \text{and} \quad C = -\frac{\alpha}{\gamma}. \tag{4.5}$$

Hence, the prescription of maximal entropy restricts the choice of F and G to respectively linear and constant functions, namely : $F(\psi) = B\psi$ and $G(\psi) = C$. It also gives a closed system of equations for the coarse-grained toroidal and poloidal fields, that we can solve using the generic method described for instance in [Chavanis and Sommeria, 1996]. Is this the end of the story ? Not quite. First, it is noticed that for a given value of the momentum I and H, there can exist infinitely many critical points for the mixing entropy. Those solutions are characterized by the value of the ratio $\Lambda = I^2/H$. From an experimental point of view, those solutions may be distinguished by the values of their coarse-grained energy, measured in terms of the parameter B. A typical phase diagram is shown on Figure 4.3. The value of the initial energy E does not in general prescribe the value of the coarse-grained energy $E^{c.g}$. Secondly, one can try to determine which of the critical points of the mixing entropy are global maximizers of the entropy. But, none of them are. In fact, it is found that all of the critical points of the mixing entropy at fixed E,I,H are saddle points of the entropy. This means, that whatever critical point is considered, one can always find an axisymmetric perturbation, preserving at first order H, I and E such that the perturbed entropy is higher than the unperturbed ones.
(a)

Saddle points of the entropy and unstable equilibria. Link to the work of [Szeri and Holmes, 1988]. From a dynamical point of view, the latter observation implies that none of the statistical equilibria are stable, whether it is for the linear or the non-linear dynamics. This is however not so surprising. To work out the critical points of the mixing entropy using the method of the Lagrange multipliers, one studies the first and the second variation of the quantity $\mathcal{F} = S^{\text{mix}} + \beta E + \gamma H \alpha I$, which we may call a " Free energy" in the context of thermodynamics. Yet, both the mixing entropy, the energy, the helicity and the momentum are invariants of the inviscid axisymmetric dynamics. Hence, in the language of dynamical systems, the free energy $\mathcal{F}$ plays the role of an Arnold functional. By construction, the critical points of $\mathcal{F}$ are stationary solutions of the axisymmetric inviscid dynamics. The definite positiveness (or negativeness) of the quadratic form $\delta^2\mathcal{F}$ computed at a given critical point provides a "formal stability" criterion, which is a necessary condition for both non-linear and linear stability of the corresponding stationary point [Holm et al., 1985]. General Arnold functions for the axisymmetric inviscid dynamics have been studied extensively in Szeri and Holmes' 1988 paper [Szeri and Holmes, 1988]. Their equation (3.15) provides a sufficient condition for formal stability of a stationary axisymmetric flow. In terms of the equilibrium fields σ_e,

(a) Note that this step is non trivial. To study this, Naso et al argue that the original variational problem $\sup_{\rho,\bar{\xi}} \left\{ S^{\text{mix}} | E, H, I \right\}$ is in fact equivalent to the much simpler problem $\inf_{\bar{\sigma},\bar{\xi}} \{E^{\text{c.g.}} | H, I\}$.

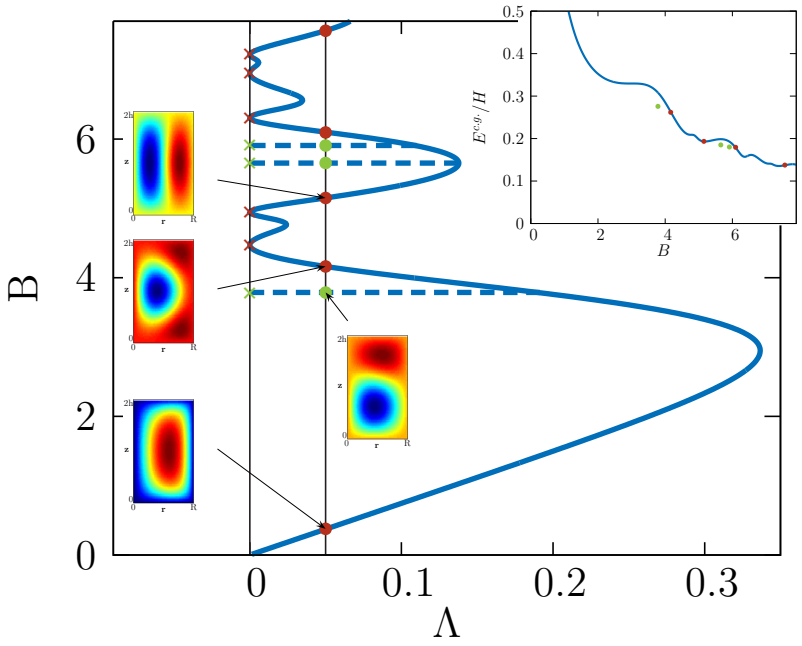

Figure 4.3: Phase diagram describing axisymmetric equilibria from a least bias approach in the case of a mildly fluctuating poloidal field, in the simplified case where only the energy E, the helicity H and the momentum I are taken into account. The present phase diagram is reported in [Naso et al., 2010b]. In the present case $R = 1.4$ and $h = 1.2$. The solutions depend on two parameters B and $\Lambda = I^2/H$. The top right insert shows B as a function of the ratio $E^{c.g}/H$, with $E^{\text{c.g.}}$ being the coarse-grained energy. For a given value of Λ (we have taken here $\Lambda = 0.05$) , the solutions are either "continuum solutions" (•) or "mixed solutions" (•). One observes a multiplicity of solutions : to a given Λ correspond several solutions, each associated to a different value for B. The left insert shows examples of stream function for the four first solutions. The color map ranks from blue (negative) to red (positive). For simplicity, we show at each point only one solution, corresponding to a given sign of I. The solution corresponding to opposite sign of I can be found by a change $\phi \to -\phi$.

ψ_e, ξ_e this condition reads:

$$\frac{\partial \xi_e}{\partial \sigma_e}\frac{\mathrm{d}\psi_e}{\mathrm{d}\sigma_e} + \frac{\sigma_e}{2y^2}\frac{\partial y}{\partial \sigma_e} - \frac{1}{-\Delta_\star^{-1}}\left(\frac{\mathrm{d}\psi_e}{\mathrm{d}\sigma_e}\right)^2 \geq 0. \tag{4.6}$$

The notation $\frac{1}{-\Delta_\star^{-1}}$ can be liberally replaced by $\frac{1}{\kappa_i^2}$ with μ_i either one of the eigenvalue of the operator $-\Delta_\star^{-1}$. Note that $-\Delta_\star^{-1}$ is a positive definite operator so that the $\mu_i = \kappa_i^2$ are real and non-negative (see Appendix PB.1). As noticed by Szeri and Holmes, this inequality "cannot be expected to hold in general, for the simple reason that the eigenvalues of the operator $[\Delta_\star^{-1}]$ have no upper bound". In order to obtain general stability criterion about the formal stability of axisymmetric equilibria, they therefore introduce a high wave-number cut-off for the class of perturbations they consider. Only for very specific flows – such as non-swirling flows – is this cut-off not required to guarantee stability.
In the approach of Leprovost et al , and Naso et al , the presence of a large scale helicity creates a dependence between the extremal entropy typical toroidal field $\bar{\sigma}$ and the stream function ψ. Hence, the term $\left(\frac{\mathrm{d}\psi}{\mathrm{d}\sigma}\right)^2$ is necessarily non-zero. We can foresee, that helicity combined with a mildly fluctuating poloidal field basically prevents stable equilibria to emerge out of a maximal entropy approach.

The case of a fluctuating poloidal field. Note finally that the case of a fluctuating poloidal field is commented on in [Leprovost et al., 2006] as a case where the maximal entropy approach yield non-Gaussian statistics. The authors introduce a cut-off for the fluctuations of the poloidal field. They remark, that taking into account the fluctuation yield an exponential distribution for the poloidal field. If the constraints are treated canonically, the exponential distribution has a dramatic consequence : it makes the distribution of poloidal vorticity become divergent. To deal with the issue, they take as a working hypothesis that the cut-off can be given a physical interpretation, and derive the corresponding axisymmetric canonical equilibria. The equilibria are then very peculiar : the typical field that the maximal entropy theory predicts are *not* stationary solutions of the axisymmetric inviscid equations, while the most probable fields are.

In the present paper, we fix the problem by (i) proposing a different interpretation of the cut-off (ii) considering stricly micro-canonical equilibria.

4.2 Paper: Statistical mechanics of the Axisymmetric Euler equations in a Taylor-Couette geometry.

Statistical mechanics of the 3D axi-symmetric Euler equations in a Taylor-Couette geometry

Simon Thalabard[1] *, Bérengère Dubrulle[1] and Freddy Bouchet[2]

[1] *Laboratoire SPHYNX, Service de Physique de l'Etat Condensé, DSM, CEA Saclay, CNRS URA 2464, 91191 Gif-sur-Yvette, France*
[2] *Laboratoire de Physique de l'Ecole Normale Supérieure de Lyon, Université de Lyon and CNRS, 46, Allée d'Italie, F-69007 Lyon, France*

November 16, 2013

Abstract

In the present paper, microcanonical measures for the dynamics of three dimensional (3D) axially symmetric turbulent flows with swirl in a Taylor-Couette geometry are defined, using an analogy with a long-range lattice model. We compute the relevant physical quantities and argue that two kinds of equilibrium regimes exist, depending on the value of the total kinetic energy. For low energies, the equilibrium flow consists of a purely swirling flow whose toroidal profile depends on the radial coordinate only. For high energies, the typical toroidal field is uniform, while the typical poloidal field is organized into either a single vertical jet or a large scale dipole, and exhibits infinite fluctuations. This unusual phase diagram comes from the poloidal fluctuations not being bounded for the axi-symmetric Euler dynamics, even though the latter conserve infinitely many "Casimir invariants". This shows that 3D axially symmetric flows can be considered as intermediate between 2D and 3D flows.

Contents

*simon.thalabard@cea.fr

1 Introduction

Statistical mechanics provides powerful tools to study complex dynamical systems in all fields of physics. However, it usually proves difficult to apply classical statistical mechanics ideas to turbulence problems. The main reason is that many statistical mechanics theories relie on equilibrium or close to equilibrium results, based on the microcanonical measures. Yet, one of the main phenomena of classical three dimensional (3D) turbulence is the anomalous dissipation, namely the existence of an energy flux towards small scales that remains finite in the inertial limit of an infinite Reynolds number. This makes the classical 3D turbulence problem an intrinsic non-equilibrium problem. Hence, microcanonical measures have long been thought to be irrelevant for turbulence problems.

A purely equilibrium statistical mechanics approach to 3D turbulence is actually pathological. Indeed, it leads for any finite dimensional approximation to an equipartition spectrum, which has no well defined asymptotic behavior in the limit of an infinite number of degrees of freedom [Bouchet and Venaille, 2011]. This phenomena is related to the Rayleigh-Jeans paradox of the equilibrium statistical mechanics of classical fields [Pomeau, 1994], and is a sign that an equilibrium approach is bound to fail. This is consistent with the observed phenomena of anomalous dissipation for the 3D Navier-Stokes and suspected equivalent anomalous dissipation phenomena for the 3D Euler equations.

The case of the 2D Euler equations and related Quasi-Geostrophic dynamics is a remarkable exception to the rule that equilibrium statistical mechanics fails for classical field theories. In this case, the existence of a new class of invariants – the so-called

"Casimirs") and among them the enstrophy – leads to a completely different picture. Onsager first anticipated this difference when he studied the statistical mechanics of the point vortex model, which is a class of special solutions to the 2D Euler equations [Onsager, 1949, Eyink and Sreenivasan, 2006]. After the initial works of Robert, Sommeria and Miller in the nineties [Miller, 1990, Robert and Sommeria, 1991, Robert and Sommeria, 1992] and subsequent work [Michel and Robert, 1994, Jordan and Turkington, 1997, Ellis et al., 2004, Majda and Wang, 2006, Bouchet and Corvellec, 2010], it is now clear that microcanonical measures taking into account all invariants exist for the 2D Euler equations. These microcanonical measures can be built through finite dimensional approximations. The finite dimensional approximate measure has then a well defined limit, which verifies some large deviations properties – see for instance [Potters et al., 2013] for a recent simple discussion of this construction. The physics described by this statistical mechanics approach is a self-organization of the flow into a large scale coherent structure corresponding to the most probable macrostate.

The three dimensional axi-symmetric Euler equations describe the motion of a perfect three dimensional flow, assumed to be symmetric with respect to rotations around a fixed axis. Such flows have additional Casimir invariants, which can be classified as "toroidal Casimirs" and "helical Casimirs" (defined below). By contrast with the 2D Euler equations, the Casimir constraints do not prevent the vorticity field to exhibit infinitely large fluctuations, and it is not clear whether they can prevent an energy towards smaller and smaller scales, although it has been stated that the dynamics of such flows should lead to predictable large scale structures [Monchaux et al., 2006]. Based on these remarks, the three dimensional axi-symmetric Euler equations seem to be an intermediate case between 2D and 3D Euler equations, as previously suggested in [Leprovost et al., 2006, Naso et al., 2010a]. It is then extremely natural to address the issue of the existence or not of non-trivial microcanonical measures.

The present paper is an attempt to write down a full and proper statistical mechanics equilibrium theory for axially symmetric flows in the microcanonical ensemble, directly from first principles, and releasing the simplifying assumptions previously considered in the literature. Examples of such assumptions included either a non-swirling hypothesis [Mohseni, 2001, Lim, 2003], an hypothesis that the equilibria are governed by restricted sets of "robust invariants" [Leprovost et al., 2006] or a deterministic treatment of the poloidal field [Leprovost et al., 2006, Naso et al., 2010a, Naso et al., 2010b]. Those simplifying hypothesis have proved extremely fruitful in giving a phenomenological entropic description of ring vortices or of the large-scale coherent structures observed in swirling flows generated in von Kármán setups [Monchaux et al., 2006, Monchaux, 2007]. As far as the 3D axi-symmetric Euler equations ares concerned though, those treatments were in a sense not completely satisfying. Besides, whether they should lead to relevant invariant measures is not clear.

To derive the axi-symmetric equilibrium measures, we define approximate microcanonical measures on spaces of finite dimensional approximations of axially symmetric flows, compatible with a formal Liouville theorem. As the constrained invariant subspace of the phase space is not bounded, we also have to consider an artificial cutoff M on the accessible vorticity values. From these approximate microcanonical measures, we compute the probability distribution of poloidal and toroidal part of the velocity field. The microcanonical measure of the 3D axi-symmetric equations is defined as a weak limit of sequences of those finite dimensional approximate microcanonical measures, when the

cutoff M goes to infinity. More heuristically stated, we will show that finite dimensional approximations of the Euler equations can be mapped onto a long-range lattice model whose thermodynamic limit, obtained in the limit of the lattice mesh going to zero, defines a microcanonical measure of the Euler equations. We prove that the limit exists and that it describes non-trivial flow structures.

Our treatment of the poloidal fluctuations yields a very thought-provoking phase diagram, which describes the existence of two different regimes of equilibrium. The control parameter is the total kinetic energy. When the kinetic energy is low, the equilibrium flow is characterized by a positive (microcanonical) temperature. In this regime, the typical field is essentially toroidal and is stratified as it depends on the radial coordinate only. When the kinetic energy is higher than a threshold value, the toroidal field is uniform and the poloidal field is both non-vanishing and non-trivial. While the typical poloidal field is dominated by large scales, the equilibrium state exhibits infinitely large fluctuations and is non-gibbsian. As a result, the microcanonical temperature is infinite. In both regimes, it is *found* that the average field is a steady state of the axi-symmetric Euler equations, formally stable with respect to any axially symmetric perturbation.

The paper is organized as follows. In Section 2, we introduce the axi-symmetric Euler equations together with their associated Casimir functions. We then relate the axi-symmetric equilibrium measures to microcanonical ensemble described in the thermodynamic limit of a well-defined long-range lattice model model. Although the main result of our paper concerns the case where all the Casimirs are taken into account, we find it enlightening and pedagogic to consider before hands some toy equilibria obtained by deliberately ignoring all the correlations between the toroidal and the poloidal fields induced by the presence of the helical casimirs. The analysis is carried out in Section 3. Those correlations are restored in Section 4. We find out that the phase diagram obtained in the simplified case of section 3 is exactly the one that describes the full problem. We discuss about the physical content of our results in Section 5.

2 Mapping the axi-symmetric Euler equations onto a spin model

In this section, we introduce the axi-symmetric Euler equations and their invariants. We discretize them in physical space, and observe that the corresponding equilibrium statistical model is described by a lattice model in which the "spins" can be pictured as point-wise Beltrami vortices (to be defined below) with non local interactions. We argue that there exists a natural microcanonical thermodynamic limit for the spin model. It describes a continuous axially symmetric field, and induces an invariant measure of the axi-symmetric Euler equations.

2.1 Axi-symmetric Euler equations and dynamical invariants

2.1.1 Equations

The starting point of the study are the Euler equations for incompressible flows inside a domain $\mathcal{D}$ in between two concentric cylinders of height $2h$, with internal radius R_{in} and

outer one R_{out}, and whose volume we write $|\mathcal{D}| = 2h\pi\,(R_{out}^2 - R_{in}^2)$. The Euler equations read :

$$\partial_t \mathbf{v} + \mathbf{v}.\nabla\mathbf{v} = -\nabla\mathbf{p} \quad \text{and} \quad \nabla.\mathbf{v} = \mathbf{0}. \tag{1}$$

We use cylindrical coordinates (r, θ, z) and consider axi-symmetric flows within a cylindrical geometry. Those flows are defined through their three velocity components v_r, v_θ and v_z depending on r and z only. Instead of the usual velocity variables $\mathbf{v}$, it proves convenient to write the Euler equations for axi-symmetric flows in terms of a toroidal field $\sigma = rv_\theta$, together with a poloidal field $\xi = \dfrac{\omega_\theta}{r} = \dfrac{\partial_z v_r - \partial_r v_z}{r}$. It also proves convenient to use the coordinate $y = \dfrac{r^2}{2}$ instead of r, and we write $\mathbf{dx} = \mathrm{d}y\mathrm{d}\theta\mathrm{d}z$ the infinitesimal cylindrical volume element at position $(\mathbf{x}) = (y, \theta, z)$.

In the present study, we focus on velocity fields which are $2h$-periodic along the vertical direction and which satisfy an impermeability boundary condition on the two cylindric walls, namely $\mathbf{v}.\mathbf{n}|_{\partial\mathcal{D}} = 0$ – with $\mathbf{n}$ the unit vector normal to the boundary $\partial\mathcal{D}$. Since the flow is incompressible ($\nabla.\mathbf{v} = 0$), we know (Helmholtz decomposition) that there exists a periodic stream function ψ and a constant C such that $(2y)^{\frac{1}{2}} v_r = -\partial_z\psi + C$ and $v_z = \partial_y\psi$. The impermeability boundary condition imposes that $C = 0$. Besides, without lack of generality, ψ can be chosen such that it is vanishing on both the inner and the outer walls. [1] The fields ξ and ψ are then related through

$$-\xi = \Delta_\star\psi = \frac{1}{2y}\partial_{zz}\psi + \partial_{yy}\psi, \quad \text{and} \quad \psi = 0 \ \text{ on both the inner and the outer walls.} \tag{2}$$

Therefore, prescribing both the toroidal and the poloidal field (σ, ξ) also completely prescribes the three dimensional axially symmetric velocity field (v_r, v_θ, v_z) – and vice-versa.

The axi-symmetric Euler equations for the (σ, ξ) variables read [Szeri and Holmes, 1988, Leprovost et al., 2006]

$$\partial_t\sigma + [\psi, \sigma] = 0 \quad \text{and} \quad \partial_t\xi + [\psi, \xi] = \partial_z\frac{\sigma^2}{4y}. \tag{3}$$

The inner-brackets represent the advection terms and are defined by $[f, g] = \partial_y f\partial_z g - \partial_z f\partial_y g$. We note that the toroidal field is not only transported by the poloidal field but also exerts a feedback on the poloidal evolution equation. It behaves as an active scalar. The feature is not an artifact of the cylindrical geometry. The generation of poloidal vorticity by the toroidal field can be interpreted as the effect of the centrifugal forces acting on the fluids, which is akin but not completely equivalent to the effect of the Lorentz force on the kinetic vorticity field in 2D magneto-hydrodynamics [Vladimirov et al., 1997], or buoyancy effects in the 2D Boussinesq equations [Abarbanel et al., 1986].

Unless stated otherwise, we will assume from now on that R_{in} is non-zero ($R_{in} > 0$), hereby considering a so-called "Taylor-Couette" geometry.

[1] ψ is defined up to a constant. Since ψ takes a constant value on both the outer and on the inner walls, one of those constants can be set to 0 without lack of generality. Then, using Equation (1) and the boundary conditions, one observes that the quantity $\mathcal{M}_z = (2h)^{-1}\displaystyle\int_{\mathcal{D}} \mathrm{d}y\mathrm{d}z v_z = \psi|_{R_{in}^2/2} - \psi|_{R_{out}^2/2}$ is a conserved by the Eulerian dynamics be it or not axi-symmetric. Therefore, we can choose to consider the referential in which $\mathcal{M}_z$ is zero, and in which $\psi|_{R_{in}^2/2} = \psi|_{R_{out}^2/2} = 0$.

2.1.2 Dynamical invariants

It is straightforward to check that the kinetic energy $E = \frac{1}{2}\int_{\mathcal{D}} \mathbf{dx}\, \mathbf{v}^2$ is a conserved quantity of the axi-symmetric Euler equations (3). The kinetic energy can be written in terms of the fields σ and ξ as

$$E = \frac{1}{2}\int_{\mathcal{D}} \mathbf{dx}\, \left[\frac{\sigma^2}{2y} + \xi\psi\right]. \tag{4}$$

As a consequence of Noether theorem (for the relabelling symmetry) and the degeneracy of its Hamiltonian structure ([Morrison, 1998, Szeri and Holmes, 1988]), the axi-symmetric Euler equations have infinitely many Casimir invariants. They fall into two families: the Toroidal Casimirs C_f and the Helical Casimirs H_g, defined by

$$C_f = \int_{\mathcal{D}} \mathbf{dx}\, f(\sigma) \quad \text{and} \quad H_g = \int_{\mathcal{D}} \mathbf{dx}\, \xi g(\sigma), \tag{5}$$

where f and g can be any sufficiently regular functions.

Note that the well-known invariants of the incompressible Euler equations correspond to specific choices for the functions f and g. The conservation of the usual helicity $H = \int_{\mathcal{D}} \mathbf{dx}\, \mathbf{v}.\omega$ is for instance recovered by setting $g(x) \equiv 2x$ in equation (5). Setting $f(x) \equiv x$ gives the conservation of the z-component of the angular momentum. Setting $g(x) \equiv 1$ gives the conservation of the circulation of the velocity field along a closed loop following the boundary of a meridional plane.

2.2 Dynamical invariants seen as geometrical constraints

We can give an alternative, more geometric, description of the Casimirs constraints (5). We introduce the indicator function $\mathbf{1}_{B(x)}$. This function takes value 1 if $B(x)$ is true and 0 otherwise. Now, given a value q for the toroidal field, let us set $f \equiv g \equiv \mathbf{1}_{\sigma(\mathbf{x})\leq q}$ in equation (5). Doing so, we obtain the specific "Toroidal Casimirs" $\mathcal{C}_q(\sigma) = \int_{\mathcal{D}} \mathbf{dx}\, \mathbf{1}_{\sigma(\mathbf{x})\leq q}$ together with the specific "Helical Casimirs" $\mathcal{H}_q(\sigma,\xi) = \int_{\mathcal{D}} \mathbf{dx}\, \xi(\mathbf{x})\, \mathbf{1}_{\sigma(\mathbf{x})\leq q}$.

$\mathcal{C}_q$ represents the area of $\mathcal{D}$ where the toroidal field is lower than a prescribed value q. $\mathcal{H}_q$ can be interpreted as the poloidal circulation on the contour of the domain corresponding to $\mathcal{C}_q$. Deriving $\mathcal{C}_q$ and $\mathcal{H}_q$ with respect to q, we find that the distribution of the poloidal field $\mathcal{A}_q = \frac{1}{|\mathcal{D}|}\frac{\mathrm{d}\mathcal{C}_q}{\mathrm{d}q}$ together with the partial circulations $\mathcal{X}_q = \frac{1}{|\mathcal{D}|}\frac{\partial \mathcal{H}_q}{\partial q}$ are dynamical invariants of the axi-symmetric equations.

The conservations of the all the areas $\mathcal{A}_q$ together with that of all the partial circulations $\mathcal{X}_q$ is in fact equivalent to the conservations of the whole set of Casimirs – Toroidal and Helical – since for sufficiently regular functions f and g we can write C_f and H_g as

$$C_f[\sigma] = |\mathcal{D}| \int_{\mathbb{R}} \mathrm{d}q \mathcal{A}_q[\sigma]\, f(q) \text{ and } H_g[\sigma,\xi] = |\mathcal{D}| \int_{\mathbb{R}} \mathrm{d}q \mathcal{X}_q[\sigma,\xi]\, g(q). \tag{6}$$

Now, consider a discrete toroidal distribution, say $f(\sigma) = \sum_{k=1}^{K} \frac{A_k}{|\mathcal{D}|} \mathbf{1}_{\sigma=\sigma_k}$. Let $\mathfrak{S}_K = \{\sigma_1, \sigma_2 ... \sigma_K\}$ be the discretized set of possible values for the toroidal field. In this simplified yet general situation, the conservation of the Casimirs is equivalent to the conservation of the K areas and K partial circulations :

$$\mathcal{A}_k[\sigma] = \int \mathbf{dx}\, \mathbf{1}_{\sigma(\mathbf{x})=\sigma_k} \quad \text{and} \quad \mathcal{X}_k[\sigma, \xi] = \int \mathbf{dx}\, \xi \mathbf{1}_{\sigma(\mathbf{x})=\sigma_k}. \tag{7}$$

Let us emphasize here that considering the toroidal field as a discrete set of "toroidal patches" is totally consistent with the ideal axi-symmetric equations. It is completely analogous to the vortex patch treatment of the vorticity field in 2D, on which more details can be found for example in [Robert and Sommeria, 1991, Miller, 1990].

2.3 Analogy with an "axi-symmetric" long-range lattice model

2.3.1 Discretization of the fluid

Let us cut a slice of fluid along a meridional plane $\mathcal{P}$, and draw a $N \times N$ regular lattice on it. We can consider a discretization of the toroidal field and the poloidal field $(\sigma_N, \xi_N) = (\sigma_{N,ij}, \xi_{N,ij})_{1 \le i,j \le N}$. Each node of the grid corresponds to a position $(\mathbf{x_{N,ij}})$ in the physical space, on which there exist a two-degree-of-freedom object that we refer to as an elementary "Beltrami spin". One degree of freedom is related to the toroidal field, while the other is related to the poloidal field. The discretization procedure is sketched on Figure 1. It it simply the axi-symmetric extension to the construction developed in the 2D case in [Miller, 1990, Ellis et al., 2000].

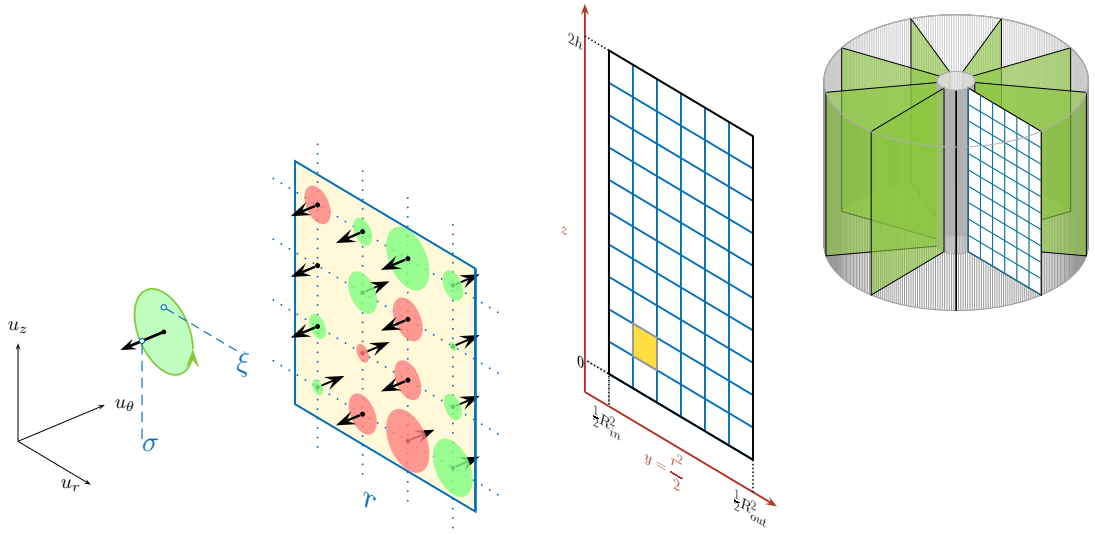

Figure 1: Discretization of the axi-symmetric Euler equations onto an assembly of Beltrami spins (Impressionistic view). For each Beltrami spin, we represent the toroidal degree of freedom by an arrow, and the poloidal degree of freedom by a circle whose radius is proportionnal to the amplitude of the poloidal field. Red (green) circles denote negative (positive) vorticy.

We associate to every spin configuration a discretized version of the axi-symmetric energy (4), that is discretized into the sum of a toroidal energy and a poloidal energy, namely

$$\mathcal{E}[\sigma_N, \xi_N] = \mathcal{E}_{tor}[\sigma_N] + \mathcal{E}_{pol}[\xi_N] \tag{8}$$

$$\text{with } \mathcal{E}_{tor}[\sigma_N] = \frac{1}{4}\frac{|\mathcal{D}|}{N^2}\sum_{(i,j)\in[\![1;N]\!]^2}\frac{\sigma_{N,ij}^2}{y_i} \text{ and } \mathcal{E}_{pol}[\xi_N] = \frac{1}{2}\frac{|\mathcal{D}|}{N^4}\sum_{\substack{(i,j)\in[\![1;N]\!]^2\\(i',j')\in[\![1;N]\!]^2}}\xi_{N,ij}G_{iji'j'}\xi_{N,i'j'}. \tag{9}$$

$G_{iji'j'}$ denotes a discretized version of the Green operator $-(\Delta_\star)^{-1}$ with vanishing boundary conditions on the walls and periodic conditions along the vertical direction.

We now introduce the discretized counterparts of the Casimir constraints (7) as

$$\mathcal{A}_k[\sigma_N] = \frac{|\mathcal{D}|}{N^2}\sum_{(i,j)\in[\![1;N]\!]^2}\mathbf{1}_{\sigma_{N,ij}=\sigma_k} \text{ and } \mathcal{X}_k[\sigma_N,\xi_N] = \frac{|\mathcal{D}|}{N^2}\sum_{(i,j)\in[\![1;N]\!]^2}\xi_{N,ij}\mathbf{1}_{\sigma_{N,ij}=\sigma_k}. \tag{10}$$

Here, the indicator function $\mathbf{1}_{\sigma_{N,ij}=\sigma_k}$ is the function defined over the N^2 nodes of the grid, that takes value 1 when $\sigma_{N,ij} = \sigma_k$ and 0 otherwise. Let us also write the discrete analogue of the total poloidal circulation as $\mathcal{X}[\sigma_N, \xi_N] = \sum_{k=1}^{K}\mathcal{X}_k[\sigma_N, \xi_N]$.

To make the constraints more picturesque, we have sketched on Figure 2 different configurations of an assembly of four Beltrami spins with two toroidal patches ($K = 2$) and symmetric toroidal levels ($\mathfrak{S}_2 = \{-1, 1\}$). Each toroidal area occupies half of the domain : $A_1 = A_{-1} = \frac{|\mathcal{D}|}{2}$. The poloidal circulations conditioned on each one of the patches are also zero : $X_1 = X_{-1} = 0$.

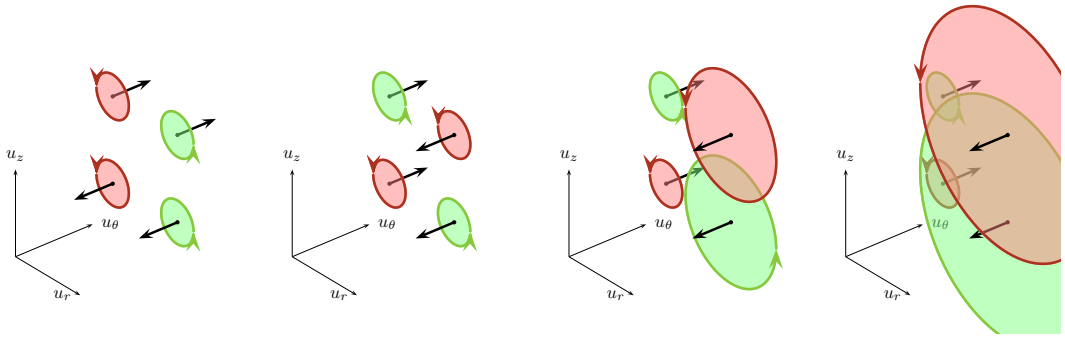

Figure 2: An assembly of four Beltrami Spins satisfying the same constraints on their Toroidal Areas and Poloidal Partial Circulations.

2.3.2 The (helical) axi-symmetric microcanonical measure

The basic idea behind the construction of the microcanonical measure is to translate the dynamical constraints imposed by the axi-symmetric ideal dynamics onto a well defined "microcanonical ensemble". To do so, we consider the set $\mathcal{C}$ of $2K + 1$ constraints given by

$$\mathcal{C} = \{E, \{A_k\}_{1\leq k\leq K}, \{X_k\}_{1\leq k\leq K}\}. \tag{11}$$

Given N, we define the configuration space $\mathcal{G}_N(E, \{A_k\}, \{X_k\}) \subset (K \times \mathbb{R})^{N^2}$ as the space of all the spin-configurations (σ_N, ξ_N) that are such that $E \leq \mathcal{E}[\sigma_N, \xi_N] \leq E + \Delta E$ and $\forall 1 \leq k \leq K$, $\mathcal{A}_k[\sigma_N] = A_k$, and $\mathcal{X}_k[\sigma_N, \xi_N] = X_k$. As will be clear later on, the number of configurations increases exponentially with N. Then, in the limit of large N, due to this large deviation behavior, the microcanonical measure will not depend on ΔE.

The salient properties of the present axi-symmetric lattice model stem from the lack of a natural bound for the poloidal degrees of freedom. Were we to define uniform measures directly on each one of the configuration spaces $\mathcal{G}_N$, we would end up with trivial measures, as each one of the N^2 poloidal degrees of freedom can span the entire $\mathbb{R}$ range. To deal with this issue, we therefore introduce bounded ensembles $\mathcal{G}_{M,N}$ made of the spin-configurations of $\mathcal{G}_N$ that satisfy $(\sup_{ij} |\xi_{N,ij}| \leq M)$. For every ensemble $\mathcal{G}_{M,N}$, we can then define a M, N dependent microcanonical measure $\mathrm{d}\mathcal{P}_{M,N}$ together with a M, N dependent microcanonical average $<>_{M,N}$ by assigning a uniform weight to the spin configurations in $\mathcal{G}_{M,N}$. The construction of $\mathrm{d}\mathcal{P}_{M,N}$ and $<>_{M,N}$ is explicitly carried out in sections (3.1) and (4.1).

M plays the role of an artificial *poloidal cutoff*. *A priori*, it has no physical meaning and is not prescribed by the axi-symmetric dynamics. It is natural to let it go to infinity. The present paper aims at building a thermodynamic limit by letting successively $(N \to \infty)$ and $(M \to \infty)$ for this set of microcanonical measures, and to describe this limit. We will refer to this measure as the (helical) axi-symmetric measure.

Let us emphasize, that the two limits $(N \to \infty)$ and $(M \to \infty)$ most probably do not commute. We argue that the relevant limit is the limit $(N \to \infty)$ first. Taking the limit $(N \to \infty)$ first, we make sure that we describe a microcanonical measure that corresponds to the dynamics of a continuous field (a fluid). The microcanonical measure at fixed M then corresponds to an approximate invariant measure, for which the maximum value of the vorticity is limited. Such a fixed M measure could be relevant as a large, but finite time approximation if the typical time to produce large values of the vorticity is much longer than the typical time for the turbulent mixing. Finally, for infinite time, we recover the microcanonical measure by taking the limit $(M \to \infty)$. For these reasons, we think that the physical limit is the limit $(N \to \infty)$ first.

As for the physics we want to understand out of it, it is the following. Consider an assembly of Beltrami spins with a given energy E. What is the fraction of E that typically leaks into the toroidal part and into the poloidal part ? What does a typical distribution of Beltrami spins then look like ?

2.4 How is the axi-symmetric microcanonical measure related to the axi-symmetric Euler equations ?

Interpreting the invariants as geometrical constraints on a well- defined assembly of spin-like objects has allowed us to map the microcanonical measure of discretized hydrodynamical fields and invariants onto an long-range, "Beltrami Spin", lattice model. Taking the thermodynamical limit $(N \to \infty)$ allows to retrieve continuous hydrodynamical fields and invariants. How is the limit microcanonical measure related to the axi-symmetric Euler equations ? Is it an invariant measure of the axi-symmetric Euler equations ?

The answer is positive but not trivial. The very reason why this should be true relies in the existence of a formal Liouville theorem – *i.e.* an extension of Liouville theorem for infinite dimensional Hamiltonian systems – for the axi-symmetric Euler equations. An elementary proof concerning the existence of a formal Liouville theorem can be found in [Thalabard, 2013]. It is a consequence of the explicit Hamiltonian Lie-Poisson structure of the axi-symmetric Euler equations when written in terms of the toroidal and poloidal fields [Szeri and Holmes, 1988, Morrison, 1998]. The formal Liouville theorem guarantees that the thermodynamic limit taken in a microcanonical ensemble induces an invariant measure of the full axi-symmetric equations.

The same issue arises in the simpler framework of the 2D Euler equations. A similar mapping onto a system of vortices that behaves as a mean-field Potts model, and definition of the microcanonical measure can be found in [Miller, 1990, Ellis et al., 2004, Bouchet and Venaille, 2011]. In [Bouchet and Corvellec, 2010], it is discussed why the microcanonical measure is an invariant measure of the 2D Euler equations. The proof is adaptable to the axi-symmetric case but goes beyond the scope of the present paper.

It is thus expected that the microcanonical measure of ensembles of Beltrami spins is an invariant measure of the Euler axi-symmetric equations, therefore worth of interest. This motivates the present study.

3 Statistical mechanics of a simplified problem without helical correlations

In the present section, we investigate a toy measure which corresponds to a simplified instance of the full (helical) ensemble. In this toy problem, the total poloidal circulation is the only Helical Casimir that is considered. The simplification makes the equilibria more easily and pedagogically derived, and provides some intuitive insights about the physics hidden in the Casimir invariants. Besides, the phase diagram that we obtain in this toy,non-helical problem will turn out to be relevant to describe full, helical one. Impatient readers can skip this section and jump directly to section 4, where the main results of the paper are described.

3.1 Definition of a non-helical toy axi-symmetric microcanonical ensemble

For pedagogic reasons, let us here suppose that the microcanonical measure is not constrained by the presence of the whole set of $2K$ Casimirs and kinetic energy but instead only by the Toroidal Areas , the poloidal circulation X_{tot} and the total kinetic energy. This new problem will be much simpler to understand. The set of $2K+1$ constraints $\mathcal{C}$ is here replaced by a "non-helical" set $\mathcal{C}_{\text{n.h.}}$ of $K+2$ constraints, defined as

$$\mathcal{C}_{\text{n.h.}} = \{E, \{A_k\}_{1\leq k\leq K}, X_{tot} = \sum_{k=1}^{K} X_k\}. \tag{12}$$

In this new problem, the correlations between the toroidal and poloidal degrees of freedom due to the presence of Helical Casimirs are crudely ignored. The only coupling left between the poloidal and the toroidal fields is a purely thermal one: the only way the fields can interact with another is by exchanging some of their energy. In order to

make this statement more rigorous, we now need to get into some finer details and build explicitly the non-helical microcanonical measure.

3.1.1 Explicit construction of a non-helical microcanonical measure

In order to exhibit a configuration of Beltrami spins (σ_N, ξ_N) that satisfies the constraints $\mathcal{C}_{\text{n.h.}}$, it suffices to pick a toroidal configuration $\sigma_N = (\sigma_{N,ij})_{1\leq i,j\leq N}$ with areas A_k and toroidal energy E_{tor} together with a poloidal configuration $\xi_N = (\xi_{N,ij})_{1\leq i,j\leq N}$ with a poloidal circulation X_{tot} and poloidal energy $E_{pol} = E - E_{tor}$. It is therefore natural to introduce the toroidal spaces of configurations $\mathcal{G}_N^{tor}(E, \{A_k\})$ together with the poloidal spaces of configurations $\mathcal{G}_{M,N}^{pol}(E, X_{tot})$ as

$$\mathcal{G}_N^{tor}(E, \{A_k\}) = \{\sigma_N \in \mathfrak{S}_K^{N^2} \mid \mathcal{E}_{tor}(\sigma_N) = E \text{ and } \forall k \in [\![1; K]\!]\, \mathcal{A}_k[\sigma_N] = A_k\}, \quad (13)$$

$$\text{and } \mathcal{G}_{M,N}^{pol}(E, X_{tot}) = \{\xi_N \in [-M; M]^{N^2} \mid \mathcal{E}_{pol}(\xi_N) = E \text{ and } \mathcal{X}[\xi_N] = X_{tot}\}. \quad (14)$$

For finite N, there is only a finite number of toroidal energies E_{tor} for which the space of toroidal configurations $\mathcal{G}_N^{tor}(E, \{A_k\})$ is non empty. The space of bounded Beltrami-spin configurations $\mathcal{G}_{M,N}(E, \{A_k\})$ is then simply a finite union of disjoint ensembles, that can be formally written as

$$\mathcal{G}_{M,N}(E, \{A_k\}, X_{tot}) = \bigcup_{0\leq E_{tor}\leq E} \mathcal{G}_N^{tor}(E_{tor}, \{A_k\}) \times \mathcal{G}_{M,N}^{pol}(E - E_{tor}, X_{tot}). \quad (15)$$

Definition of the M, N-dependent microcanonical measure.

The M, N- dependent microcanonical measure $\mathrm{d}\mathcal{P}_{M,N}$ is defined as the uniform measure on the space of configurations $\mathcal{G}_{M,N}(E, \{A_k\}, X_{tot})$. In order to specify this measure explicitly, we need to define the M, N-dependent volume $\Omega_{M,N}(E, \{A_k\}, X_{tot})$ of $\mathcal{G}_{M,N}(E, \{A_k\}, X_{tot})$. To do so, we write $\Omega_N^{tor}(E, \{A_k\})$ the number of configurations in $\mathcal{G}_N^{tor}(E, \{A_k\})$ and $\Omega_N^{pol}(E, X_{tot})$ the hypervolume in $\mathbb{R}^{N^2}$ of $\mathcal{G}_{M,N}^{pol}(E, X_{tot})$, namely

$$\Omega_N^{tor}(E, \{A_k\}) = \sum_{\sigma_N \in \mathfrak{S}_K^{N^2}} \mathbf{1}_{\sigma_N \in \mathcal{G}_N^{tor}(E, \{A_k\})}, \quad (16)$$

$$\text{and } \Omega_{M,N}^{pol}(E, X_{tot}) = \prod_{(i,j)\in[\![1;N]\!]^2} \int_{-\infty}^{+\infty} \mathrm{d}\xi_{N,ij} \mathbf{1}_{\xi_N \in \mathcal{G}_{M,N}^{pol}(E, X_{tot})}. \quad (17)$$

Note that the integral defining the poloidal volume is finite since $\mathcal{G}_{M,N}^{pol}(E, X_{tot})$ is a bounded subset of $\mathbb{R}^{N^2}$. Using equation (15), the phase-space volume can then be written as

$$\Omega_{M,N}(E, \{A_k\}, X_{tot}) = \int_0^E \mathrm{d}E_{tor}\, \Omega_N^{tor}(E_{tor}, \{A_k\})\, \Omega_{M,N}^{pol}(E - E_{tor}, X_{pol}). \quad (18)$$

The microcanonical weight $\mathrm{d}\mathcal{P}_{M,N}(\mathcal{C})$ of a configuration $\mathcal{C} = (\sigma_N, \xi_N)$ lying in the space $\mathcal{G}_{M,N}(E, \{A_k\}, X_{tot})$ can now be explicitly written as

$$\mathrm{d}\mathcal{P}_{M,N}(\mathcal{C}) = \frac{1}{\Omega_{M,N}(E, \{A_k\}, X_{tot})} \prod_{(i,j)\in[\![1;N]\!]^2} \mathrm{d}\xi_{N,ij}. \quad (19)$$

Provided that $\mathcal{G}$ is a compact subset of ${\mathfrak{S}_K}^{N^2} \times \mathbb{R}^{N^2}$ it is convenient to use the shorthand notation

$$\int_{\mathcal{G}} \mathrm{d}\mathcal{P}_{M,N} \equiv \frac{1}{\Omega_{M,N}\left(E, \{A_k\}, X_{tot}\right)} \sum_{\sigma_N \in \mathfrak{S}_K^{N^2}} \left(\prod_{(i,j)\in[\![1;N]\!]^2} \int_{-\infty}^{\infty} \mathrm{d}\xi_{N,ij} \right) \mathbf{1}_{(\sigma_N,\xi_N)\in\mathcal{G}}, \tag{20}$$

so that the M, N dependent microcanonical average $<>_{M,N}$ of an observable $\mathcal{O}$ can now be defined as

$$\langle \mathcal{O} \rangle_{M,N} = \int_{\mathcal{G}_{M,N}(E,\{A_k\},X_{tot})} \mathrm{d}\mathcal{P}_{M,N}\, \mathcal{O}\left[\sigma_N, \xi_N\right] = \int_0^E \mathrm{d}E_{tor} \int_{\mathcal{G}_N^{tor}(E_{tor},\{A_k\})\times\mathcal{G}_{M,N}^{pol}(E-E_{tor},X_{tot})} \mathrm{d}\mathcal{P}_{M,N}\, \mathcal{O}\left[\sigma_N, \xi_N\right]. \tag{21}$$

Definition of the limit measures.

It is convenient to use observables to define the limit microcanonical measures. We define the M-dependent microcanonical measure $<>_M$ and the microcanonical measure $<>$ by letting successively $N \to \infty$ and $M \to \infty$, so that for any observable $\mathcal{O}$, $< \mathcal{O} >_M$ and $< \mathcal{O} >$ are defined as

$$\langle \mathcal{O} \rangle_M = \lim_{N\to\infty} \langle \mathcal{O} \rangle_{M,N}, \text{ and } \langle \mathcal{O} \rangle = \lim_{M\to\infty} \langle \mathcal{O} \rangle_M. \tag{22}$$

3.1.2 Observables of physical interest

Without any further comment about observables and the kind of observables that we will specifically consider, equations (21) and (22) may appear to be slightly too casual. Let us precise what we mean. In our context, we need to deal both with observables defined for the continuous poloidal and toroidal fields and for their discretized counterparts. Given a continuous field (σ, ξ), we consider observables $\mathcal{O}$ that can be written as $\mathcal{O} = \int_{\mathcal{D}} \mathbf{dx}\, f^{\mathcal{O}}_{(\mathbf{x})}(\sigma, \xi)$ where $f^{\mathcal{O}}_{(\mathbf{x})}$ is a function defined over ${\mathfrak{S}_K}^{\mathcal{D}} \times \mathbb{R}^{\mathcal{D}} \times \mathcal{D}$. The discrete counterpart of $\mathcal{O}$ is then defined as

$$\mathcal{O}(\sigma_N, \xi_N) = \frac{|\mathcal{D}|}{N^2} \sum_{(i,j)\in[\![1;N]\!]^2} f^{\mathcal{O}}_{\left(\mathbf{x_{N,ij}}\right)}(\sigma_N, \xi_N), \tag{23}$$

and the distinction between discrete and continuous observables is made clear from the context.

To learn about the physics described by the microcanonical measure, a first non trivial functional to consider is the toroidal energy functional $\mathcal{E}_{tor}$ defined in equation (9), whose microcanonical average will tell what the balance between the toroidal and poloidal energy for a typical configuration Beltrami spins is. In order to specify the toroidal and poloidal distributions in the thermodynamic limit we will then estimate the microcanonical averages of specific one-point observables, namely

$$\mathcal{O}(\{\sigma\}, \{\xi\}) = \int_{\mathcal{D}} \mathbf{dx}\, \delta\left(\mathbf{x} - \mathbf{x_0}\right) \sigma\left(\mathbf{x}\right)^p \xi\left(\mathbf{x}\right)^k = \mathcal{O}^{tor}(\{\sigma\})\mathcal{O}^{pol}(\{\xi\}) \tag{24}$$

with $\mathcal{O}^{tor}(\{\sigma\}) = \sigma\left(\mathbf{x_0}\right)^p$ and $\mathcal{O}^{pol}(\{\xi\}) = \xi\left(\mathbf{x_0}\right)^k$ defined for any point $(\mathbf{x_0}) \in \mathcal{D}$. The microcanonical averages of those observables provide the moments of the one-point prob-

ability distributions and therefore fully specify them. [2]

Just as for the 2D Euler equations, and slightly anticipating on the actual computation of the microcanonical measures, we can expect the axisymmetric microcanonical measures to behave as Young measures, that is to say that the toroidal and poloidal distributions at positions $(\mathbf{x})$ are expected to be independent from their distributions at position $(\mathbf{x}') \neq (\mathbf{x})$. Therefore, specifying the one-point probability distributions will hopefully suffice to completely describe the statistics of the poloidal and of the toroidal field in the thermodynamic limit.

3.1.3 Specificity of the non-helical toy measure

Looking at equation (21), it is yet not so clear that our non-helical toy problem is easier to tackle than the full pronlem, nor that the limit measures prescribed by equation (22) can be computed. The reason why we should keep hope owes to large deviation theory. Using standard arguments from statistical physics, we argue hereafter that the non-helical problem can be tackled by defining appropriate poloidal and toroidal measures that can be studied separately from each other.

Let us for instance consider the Boltzmann entropies per spin

$$S_N^{tor}(E,\{A_k\}) = \frac{1}{N^2}\log\Omega_N^{tor}(E,\{A_k\}), \quad S_{M,N}^{pol}(E,X_{tot}) = \frac{1}{N^2}\log\Omega_N^{pol}(E,X_{tot}), \tag{25}$$

$$\text{and} \quad S_{M,N}(E,\{A_k\},X_{tot}) = \frac{1}{N^2}\log\Omega_N(E,\{A_k\},X_{tot}). \tag{26}$$

As $N\to\infty$, it can be expected that the toroidal entropies $S_N^{tor}(E,\{A_k\})$ together with the poloidal entropies $S_{M,N}^{pol}(E,X_{tot})$ converge towards a finite limit if they are properly renormalized. If this is the case, then those entropies can be asymptotically expanded as

$$S_N^{tor}(E,\{A_k\}) \underset{N\to\infty}{=} c_N^{tor}(\{A_k\}) + S^{tor}(E,\{A_k\}) + o(1), \tag{27}$$

$$\text{and} \quad S_{M,N}^{pol}(E,X_{tot}) \underset{N\to\infty}{=} c_{M,N}^{pol}(X_{tot}) + S_M^{pol}(E,X_{tot}) + o(1). \tag{28}$$

Plugging the entropies into equation (18), we get, when $N\to\infty$

$$\Omega_{M,N}(E) = e^{N^2\left(c_N^{tor}+c_{M,N}^{pol}\right)+o(N^2)}\int_0^E \mathrm{d}E_{tor}\,\mathrm{e}^{N^2\left(S^{tor}(E_{tor})+S_M^{pol}(E-E_{tor})\right)}. \tag{29}$$

For clarity, we have dropped out the $\{A_k\}$ and X_{tot} dependence of the different entropies. Using Laplace's method to approximate integrals, taking logarithm of both sides of equation (29), dividing by N^2, and setting $c_{M,N}(\{A_k\},X_{tot}) = c_N^{tor}(\{A_k\}) + c_{M,N}^{pol}(X_{tot})$ we obtain

$$S_{M,N}(E) \underset{N\to\infty}{=} c_{M,N} + S^{tor}(E_M^\star) + S_M^{pol}(E-E_M^\star) + o(1),$$

$$\text{where } E_M^\star = \underset{x\in[0;E]}{\arg\max}\{S^{tor}(x) + S_M^{pol}(E-x)\}. \tag{30}$$

[2] One can observe that one-point moments may be ill-defined in the discrete case so that their limit may be ill-defined too. One way to deal with this situation is to consider dyadic discretizations, namely choose $N=2^n$. Then for any point $(\mathbf{x})$ whose coordinates are dyadic rational numbers, the discrete quantities are non trivially zero when n is large enough. The microcanonical averages can then be extended to any position in $\mathcal{D}$ by continuity.

A heuristic way of interpreting equation (30) is to say that when $N \gg 1$, "most of" the configurations in $\mathcal{G}_{M,N}(E, \{A_k\}, X_{tot})$ have a toroidal energy equal to $E^\star_M$ and a poloidal energy equal to $E - E^\star_M$.

We can refine the argument, and ask what the typical value of a one-point observable $\mathcal{O} = \mathcal{O}^{tor}\mathcal{O}^{pol}$ as described in equation (24) becomes in the thermodynamic limit $N \to \infty$. Let us write the M, N dependent toroidal and poloidal partial microcanonical measures as

$$\mathrm{d}\mathcal{P}_N^{tor,E}(\sigma_N) = \frac{1}{\Omega_N^{tor}(E, \{A_k\})} \text{ and } \mathrm{d}\mathcal{P}_{M,N}^{pol,E}(\xi_N) = \frac{1}{\Omega_{M,N}^{pol}(E, X_{tot})} \prod_{(i,j)\in[\![1;N]\!]^2} \mathrm{d}\xi_{N,ij}, \tag{31}$$

and introduce the shorthand notations

$$\begin{aligned} \int_{\mathcal{G}} \mathrm{d}\mathcal{P}_N^{tor,E} &\equiv \frac{1}{\Omega_N^{tor}(E, \{A_k\})} \sum_{\sigma_N \in \mathfrak{S}_K^{N^2}} \mathbf{1}_{\sigma_N \in \mathcal{G}}, \\ \text{and } \int_{\mathcal{G}} \mathrm{d}\mathcal{P}_{M,N}^{pol,E} &\equiv \frac{1}{\Omega_{M,N}^{pol}(E, X_{tot})} \left(\prod_{(i,j)\in[\![1;N]\!]^2} \int_{-\infty}^{\infty} \mathrm{d}\xi_{N,ij} \right) \mathbf{1}_{\xi_N \in \mathcal{G}}. \end{aligned} \tag{32}$$

Respectively defining the M, N dependent toroidal and poloidal partial microcanonical averages as

$$\langle \mathcal{O}^{tor} \rangle_N^{tor,E} = \int_{\mathcal{G}_N^{tor}(E,\{A_k\})} \mathrm{d}\mathcal{P}_N^{tor,E}\, \mathcal{O}^{tor}[\sigma_N] \quad \text{and} \quad \langle \mathcal{O}^{pol} \rangle_{M,N}^{pol,E} = \int_{\mathcal{G}_{M,N}^{pol}(E,X_{tot})} \mathrm{d}\mathcal{P}_{M,N}^{pol,E}\, \mathcal{O}^{pol}[\xi_N], \tag{33}$$

it stems from equation (21) that

$$\langle \mathcal{O} \rangle_{M,N} = \int_0^E \mathrm{d}E_{tor}\, \mathcal{P}_{M,N}(E_{tor}) \langle \mathcal{O}^{tor} \rangle_N^{tor,E_{tor}} \langle \mathcal{O}^{pol} \rangle_{M,N}^{pol,E-E_{tor}}, \tag{34}$$

$$\text{with } \mathcal{P}_{M,N}(E_{tor}) = \frac{\Omega_N^{tor}(E_{tor})\, \Omega_{M,N}^{pol}(E - E_{tor})}{\Omega_{M,N}(E)}. \tag{35}$$

The latter equation means that the full microcanonical measure $<>_{M,N}$ can be deduced from the knowledge of the partial measures $<>_N^{tor,E}$ and $<>_{M,N}^{pol,E}$. As $N \to \infty$, the limit measure can be expected to be dominated by one of the partial measures, provided that the limit measures $<>^{tor,E}$, $<>_M^{pol,E}$ – defined accordingly to equation (22) behave as predicted by equations (27) and (28).

If for example one considers an observable $\mathcal{O}$ that is bounded independently from N , then its microcanonical average can be estimated from equation (34) as

$$\langle \mathcal{O} \rangle_M = \langle \mathcal{O}^{tor} \rangle^{tor,E_M^\star} \langle \mathcal{O}^{pol} \rangle_M^{pol,E-E_M^\star}. \tag{36}$$

Thermodynamically stated, this means that the non-helical statistical equilibria can be interpreted as thermal equilibria between the toroidal and the poloidal fields. It is therefore relevant to first study separately the toroidal and the poloidal problem separately from one another. This is what we do in the next three sections.

3.2 Statistical mechanics of the toroidal field

It is possible to estimate the toroidal entropies $S_N^{tor}(E,\{A_k\})$ for very specific values of the energy using standard statistical mechanics counting methods. We first present those. Then, we show that those specific cases are retrieved with a more general calculation involving the theory of large deviations.

3.2.1 Traditional counting

The contribution to the toroidal energy of a toroidal spin $\sigma_{k_0} \in \mathfrak{S}_K$ placed at a radial distance $y = \dfrac{r^2}{2}$ from the center of the cylinder is $\dfrac{|\mathcal{D}|\,\sigma_{k_0}^2}{4yN^2}$. Clearly, the energy is extremal when the σ_k^2 are fully segregated in K stripes, parallel to the z axis, each of width $w_k = \dfrac{(R_{out}^2 - R_{in}^2)\,A_k}{2\,|\mathcal{D}|} + O\left(\dfrac{1}{N}\right)$. The minimum (resp. maximum) of energy $E_{\min}$ (resp. $E_{\max}$) is obtained when the levels of σ_k^2 are sorted increasingly (resp. decreasingly) from the internal cylinder. The number of toroidal configurations that corresponds to each one of those extremal energy states is therefore at most of order N. Using definition (25) and equation (27) , one therefore finds $S^{tor}(E_{\min},\{A_k\}) = S^{tor}(E_{\max},\{A_k\}) = 0$.

Further assuming that $S^{tor}(E,\{A_k\})$ is sufficiently regular on the interval $[E_{\min};E_{\max}]$, the latter result implies that there exists an energy value $E^\star \in [E_{\min};E_{\max}]$ for which the entropy $S^{tor}(E,\{A_k\})$ is maximal. The value of $S^{tor}(E^\star,\{A_k\})$ can be estimated by counting the total number of toroidal configurations – regardless of their toroidal energies [3]. Indeed,

$$\frac{N^2!}{\prod_{k=1}^K N_k!} = \int_{E_{\min}}^{E_{\max}} \mathrm{d}E\,\Omega_N^{tor}(E,\{A_k\}) = \int_{E_{min}}^{E_{max}} \mathrm{d}E\,e^{N^2 S_N^{tor}(E,\{A_k\})}, \qquad (37)$$

$$\text{where } N_k = \frac{N^2 A_k}{|\mathcal{D}|}.$$

Then, taking the limit $N \to \infty$, using Stirling formula for the l.h.s and estimating the r.h.s with the method of steepest descent, we obtain

$$S^{tor}(E^\star,\{A_k\}) = -\sum_{k=1}^{K} \frac{A_k}{|\mathcal{D}|} \log \frac{A_k}{|\mathcal{D}|}. \qquad (38)$$

This value corresponds to the levels of σ_k^2 being completely intertwined.

3.2.2 Large deviation approach

We can work out the entropy for any value of the energy by using the more modern framework of large deviation theory.

For a given N, let us consider the set of random toroidal configurations that can be obtained by randomly and independently assigning on each node of the lattice a level of σ_k drawn from a uniform distribution over the discrete set $\mathfrak{S}_K$. There are K^{N^2} such different configurations. Among those, there exist some that are such that $\forall k \in [\![1;K]\!]\,\mathcal{A}_k[\sigma_N] = A_k$ together with $\mathcal{E}^{tor}[\sigma_N] = E$. The number of those configurations is precisely what we

[3] We here tacitly work in the case where the σ_k^2 are all distinct –otherwise we need to group the levels with the same value of σ_k^2.

have defined as $\Omega_N^{tor}(E,\{A_k\})$. Can we estimate $\Omega_N^{tor}(E,\{A_k\})$ for $N \gg 1$? The answer is provided by a large deviation theorem called Sanov theorem – see for example [Ellis, 1984, Cover et al., 1994, Touchette, 2009] for material about this particular theorem and the theory of large deviations.

Through a coarse-graining, we define the local probability $p_k(\mathbf{x})$ that a toroidal spin takes the value σ_k in an infinitesimal area $\mathbf{dx}$ around a point $(\mathbf{x})$. With respect to the ensemble of configurations, the functions $(p_1,...,p_K)$ define a toroidal macrostate, which satisfies the local normalization constraint:

$$\forall \mathbf{x} \ \in \mathcal{D}, \sum_{k=1}^{K} p_k(\mathbf{x}) = 1. \tag{39}$$

We denote $\mathcal{Q}^{tor}$ the set of all the toroidal macrostates – the set of all $p = (p_1,...,p_K)$ verifying (39). From Sanov theorem, we can compute the number of configurations corresponding to the macrostate $p = (p_1,...,p_K)$. This number is equivalent for large N to the exponential of N^2 times the macrostate entropy

$$\mathcal{S}^{tor}[p] = -\frac{1}{|\mathcal{D}|}\int_{\mathcal{D}} \mathbf{dx} \sum_{k=1}^{K} p_k(\mathbf{x}) \log p_k(\mathbf{x}). \tag{40}$$

The toroidal areas A_k occupied by each toroidal patch σ_k, as well as the toroidal energy constraint, can be expressed as linear constraints on the toroidal macrostates:

$$\forall k \in [\![1;K]\!]\ \mathcal{A}_k[p] = \int_{\mathcal{D}} \mathbf{dx}\, p_k(\mathbf{x}) \ \text{ and } \mathcal{E}_{tor}[p] = \int \mathbf{dx} \sum_{k=1}^{K} p_k(\mathbf{x}) \frac{\sigma_k^2}{4y}, \tag{41}$$

where $\mathcal{E}_{tor}[p]$ and $\mathcal{A}_k[p]$ are the energy and areas of a macrostate $p = (p_1,...,p_K)$. As the log of the entropy is proportional to the number of configurations, the most probable toroidal macrostate will maximize the macrostate entropy (40) with the constraints $\forall k \in [\![1;K]\!]$, $\mathcal{A}_k[p] = A_k$ and $\mathcal{E}_{tor}[p] = E$. Moreover, using Laplace method of steepest descent, we can conclude that in the limit of large N, the total entropy is equal to the entropy of the most probable macrostate. Therefore,

$$S^{tor}(E,\{A_k\}) = \lim_{N\to\infty} \frac{1}{N^2} \log \Omega_N^{tor}(E,\{A_k\}) \tag{42}$$

$$= \sup_{p\in\mathcal{Q}^{tor}} \{\mathcal{S}^{tor}[p] \mid \forall k \in [\![1;K]\!]\ \mathcal{A}_k[p] = A_k \text{ and } \mathcal{E}_{tor}[p] = E\}. \tag{43}$$

The optimization problem which appears in the r.h.s. of equation (43) can be standardly solved with the help of Lagrange multipliers α_k and β_{tor} to respectively enforce the constraints on the areas A_k and on the energy E. The critical points $p^{\star,E}$ of the macrostate entropy for the constraints E and A_k can then be written as

$$p_k^{\star,E}(\mathbf{x}) = \frac{1}{Z^\star(\mathbf{x})} \exp\{\alpha_k - \beta\frac{\sigma_k^2}{4y}\} \text{ with } Z^\star(\mathbf{x}) = \sum_{k=1}^{K} \exp\{\alpha_k - \beta\frac{\sigma_k^2}{4y}\}. \tag{44}$$

α_k and β_{tor} are such that

$$\int_{\mathcal{D}} \mathbf{dx} \frac{\partial \log Z^\star(\mathbf{x})}{\partial \alpha_k} = A_k \text{ and } -\int_{\mathcal{D}} \mathbf{dx} \frac{\partial \log Z^\star(\mathbf{x})}{\partial \beta_{tor}} = E. \tag{45}$$

Note that if we don't enforce the energy constraint in (43), it is easily checked that the maximum value of the macrostate entropy is $\mathcal{S}^{tor}[p^\star] = -\sum_{k=1}^{K} \frac{A_k}{|\mathcal{D}|} \log \frac{A_k}{|\mathcal{D}|}$ obtained for the macrostate p defined by $p_k^\star(\mathbf{x}) = \frac{A_k}{|\mathcal{D}|}$. This shows the consistency of our calculation since the latter macrostate can also be found by setting $\beta_{tor} = 0$ in (45). A vanishing β_{tor} corresponds to the energy constraint $E = E^\star$, so that $S^{tor}(E^\star, \{A_k\}) = -\sum_{k=1}^{K} \frac{A_k}{|\mathcal{D}|} \log \frac{A_k}{|\mathcal{D}|}$, and equation (38) is retrieved. The value of $E^\star$ can be computed from (41) and (45) as $E^\star = \sum_{k=1}^{K} \frac{A_k \sigma_k^2}{2\,|\mathcal{D}|} \log \frac{R_{out}}{R_{in}}$.

Equation (45) can also be used to numerically estimate the toroidal entropy for abitrary values of E. Such an estimation is shown on Figure 3 for the specific case where $K = 2$, $\mathfrak{S}_2 = \{0, 1\}$, and $A_0 = A_1 = \frac{|\mathcal{D}|}{2}$.

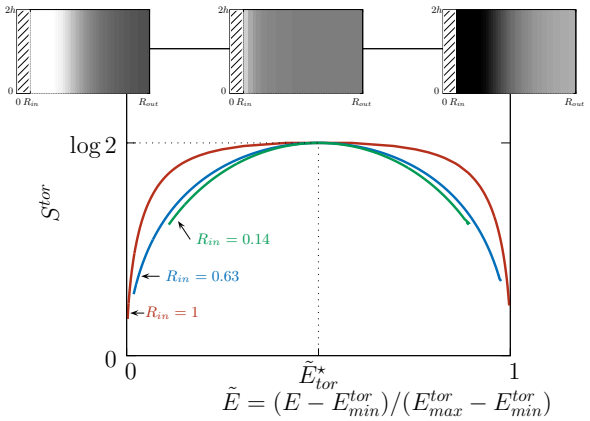

Figure 3: Numerical estimation of the toroidal entropy for K=2 , $\mathfrak{S}_2 = \{0, 1\}$ and $A_0 = A_1 = \frac{\mathcal{D}}{2}$. The height of the domain is $2h = 1$, its outer radius is $R_{out} = \sqrt{2}$ and its inner radius is $R_{in} = 0.14$,0.63 or 1. Insets show typical toroidal fields $\langle \sigma(\mathbf{x}) \rangle^{tor,E}$ for $R_{in} = 0.14$. They correspond to $E = 0.1$, $E = 0.5$, and $E = 0.9$ from left to right. The grayscale ranks from 0 (white pixels) to 1 (black pixels).

Finally, the microcanonical toroidal moments can be deduced from the critical distribution $p^{\star,E}$ that achieves the maximum macrostate entropy. Those moments read

$$\langle \sigma(\mathbf{x})^p \rangle^{tor,E} = \sum_{k=1}^{K} p_k^{\star,E}(\mathbf{x})\, \sigma_k^p. \tag{46}$$

In the thermodynamic limit, the microcanical measure $<>^{tor,E} = \lim_{N\to\infty} <>_N^{tor,E}$ behaves as a product measure, so that equation (46) completely describes the toroidal micocanonical measure.

3.3 Statistical mechanics of the poloidal field

The statistical mechanics for the poloidal field is slightly more subtle than for the toroidal field. It requires two steps: first use a large deviation theorem to compute $<>_M$, then let the cutoff M go to ∞.

3.3.1 Computation of the M-dependent partial measures $<>_M^{pol,E}$

The poloidal energy constraint cannot be exactly expressed as a constraint on the poloidal macrostates. We however argue that Sanov therorem can still be applied because the poloidal degrees of freedom interact through long range interactions, which gives the poloidal problem a mean-field behavior.

We consider the set of random poloidal configurations that can be obtained by randomly and independently assigning on each node of the lattice a random value of ξ from the uniform distribution over the interval $[-M, M]$. We then define through a coarse graining the local probability $p_M(\xi, \mathbf{x})$ that a poloidal spin takes a value between ξ and $\xi + \mathrm{d}\xi$ in an infinitesimal area $\mathbf{dx}$ around a point $(\mathbf{x})$. With respect to the ensemble of poloidal configurations, the distributions $p_M = \{p_M(\xi, \cdot)\}_{\xi\in[-M;M]}$ define a poloidal macrostate. Each poloidal macrostate satisfies the local normalization constraint :

$$\forall \mathbf{x} \ \in \mathcal{D}, \int_{-M}^{M} \mathrm{d}\xi p_M(\xi, \mathbf{x}) = 1. \tag{47}$$

We denote $\mathcal{Q}^{pol}$ the sets of all the poloidal macrostates – the set of all p_M verifying (47). The number of configurations corresponding to the macrostate p_M is then the exponential of N^2 times the poloidal macrostate entropy

$$\mathcal{S}_M^{pol}[p_M] = -\frac{1}{|\mathcal{D}|}\int_{\mathcal{D}} \mathbf{dx} \int_{-M}^{M} \mathrm{d}\xi p_M(\xi, \mathbf{x}) \log p_M(\xi, \mathbf{x}). \tag{48}$$

The constraint on the total circulation X_{tot} can be expressed as a linear constraint on the poloidal macrostates

$$\mathcal{X}_{tot}[p_M] = \int_{\mathcal{D}} \mathbf{dx} \int_{-M}^{M} \mathrm{d}\xi \, \xi p_M(\xi, \mathbf{x}). \tag{49}$$

The subtle point arises when dealing with the constraint on the poloidal energy. The energy of a poloidal macrostate is defined as

$$\mathcal{E}^{pol}[p_M] = \frac{1}{2}\int_{\mathcal{D}} \mathbf{dx}\, \psi(\mathbf{x}) \int_{-M}^{M} \mathrm{d}\xi \, \xi p_M(\xi, \mathbf{x}), \tag{50}$$

$$\text{with} \ \ \psi(\mathbf{x}) = \int_{\mathcal{D}} \mathbf{dx}' G(\mathbf{x}, \mathbf{x}') \langle \xi(\mathbf{x}') \rangle_{\mathbf{M}}^{\mathbf{pol}}, \tag{51}$$

$G(\mathbf{x}, \mathbf{x}')$ being the Green function of the operator $-\Delta_\star$ with vanishing boundary conditions on the walls and periodic boundary conditions along the vertical direction. The energy $\mathcal{E}[\xi_N]$ of a poloidal configuration (9) is therefore not exactly the energy of the corresponding macrostate (50). In order to deal with this situation, one needs to make the coarse-graining procedure more explicit. Dividing the $N \times N$ lattices into $N_b \times N_b$ contiguous blocks each composed of $n^2 = \lfloor N/N_b \rfloor^2$ spins, and taking the limit $N \to \infty$ at fixed N_b, and then letting $N_b \to \infty$, one obtains

$$\mathcal{E}^{pol}[\xi_N] \underset{\substack{N\to\infty \\ N_b\to\infty}}{=} \mathcal{E}^{pol}[p_M] + o\left(\frac{1}{N_b^2}\right). \tag{52}$$

We see that in the continuous limit, the energy of most of the configurations concentrates close to the energy of the macrostate p_M (see [Ellis et al., 2000, Potters et al., 2013] for a more precise discussion in the context of the 2D Euler equations). This is a consequence of the poloidal degrees of freedom mutually interacting through long range interactions. We can therefore enforce the constraint on the configuration energy as a macrostate constraint.

Following the argumentation yielding to (43) in the toroidal case, we conclude that in the limit of large N, the total poloidal entropy is equal to the poloidal entropy of the most probable poloidal macrostate which satisfies the constraints. Therefore,

$$S^{pol}(E, X_{tot}) = \sup_{p_M \in \mathcal{Q}^{pol}} \{\mathcal{S}^{pol}[p] \mid \mathcal{X}_{tot}[p_M] = X_{tot} \text{ and } \mathcal{E}_{pol}[p_M] = E\}. \tag{53}$$

The critical distributions $p_M^\star(\xi, \mathbf{x})$ of the poloidal macrostate entropy can be written in terms of two Lagrange multipliers $\beta_{pol}^{(M)}$ and $h^{(M)}$, respectively related to the constraints on the poloidal energy and on the poloidal circulation as

$$\begin{aligned} p_M^{\star,E}(\xi, \mathbf{x}) =& \frac{1}{M Z_M^\star(\mathbf{x})} \exp\{\left(h^{(M)} - \frac{\beta_{pol}^{(M)} \psi(\mathbf{x})}{2}\right) \xi\}, \\ \text{with } \; Z_M^\star(\mathbf{x}) =& \int_{-1}^{1} \mathrm{d}\xi \exp\{\left(h^{(M)} - \frac{\beta_{pol}^{(M)} \psi(\mathbf{x})}{2}\right) M\xi\}. \end{aligned} \tag{54}$$

The Lagrange multipliers $h^{(M)}$ and $\beta_{pol}^{(M)}$ are defined through

$$X_{tot} = \int_{\mathcal{D}} \mathbf{dx} \, \frac{\partial \log Z_M^\star(\mathbf{x})}{\partial h^{(M)}} \text{ and } E = -\int_{\mathcal{D}} \mathbf{dx} \, \frac{\partial \log Z_M^\star(\mathbf{x})}{\partial \beta_{pol}^{(M)}}. \tag{55}$$

The moments of the one-point poloidal distribution can now be estimated from equation (54) as

$$\forall p \in \mathbb{N}, \langle \xi(\mathbf{x})^p \rangle_M^{pol,E} = \int_{-M}^{M} \mathrm{d}\xi \, p_M^\star(\xi, \mathbf{x}) \, \xi^p = \frac{\partial^p \log Z_M^\star(\mathbf{x})}{\partial h^{(M)p}}. \tag{56}$$

Taking $p = 1$ in equation (56) and using equation (51) yield the M-dependent self-consistent mean-field equation

$$\frac{\partial \log Z_M^\star(\mathbf{x})}{\partial h^{(M)}} = -\Delta_\star \psi. \tag{57}$$

We now need to let $M \to \infty$ to describe the microcanonical poloidal measure. A word of caution may be necessary at this point. For finite M, it is possible to estimate the poloidal energy in terms of a macrostate energy as the correcting term in Equation (52) goes to zero when N goes to ∞. However, the correcting term depends on M, which we now want to let go to ∞. Therefore, there might be a subtle issue in justifying the rigorous and uniform decay of the fluctuations of the stream function to zero in the limit $M \to \infty$. In order to make the theory analytically tractable, we will suppose that that such is the case.

3.3.2 $M \to \infty$: Computation of the partial limit measures $<>^{pol,E}$

We suppose in this section that the energy is non zero. Otherwise $\psi \equiv 0$ and the equilibrium state is trivial.

Scaling for the Lagrange multipliers.

In order for Equation (55) to be satisfied whatever the value of M, the Lagrange multipliers need to be M-dependent. At leading order, the only possible choice is that $\beta_{pol}^{(M)}$ and $h^{(M)}$ both scale as $\frac{1}{M^2}$, when M goes to ∞.

The scaling is crucial to derive the microcanonical equilibria – whether or not helical. Let us briefly detail its origin. It seems reasonable to assume that $\beta^{(M)}$ and $h^{(M)}$ can be developed in powers of M, when $M \to \infty$. Let γ be a yet non-prescribed parameter, and let us define $h^\star$ and $\beta^\star$ as :

$$\beta^\star = \lim_{M\to\infty} M^{-\gamma}\beta_{pol}^{(M)} \text{ and } h^\star = \lim_{M\to\infty} M^{-\gamma}h^{(M)}. \tag{58}$$

$h^\star$ and $\beta^\star$ are the first non-vanishing terms in the asymptotic development of h and β respectively. They can be interpreted as "reduced" or "renormalized" Lagrange Multipliers, associated to the poloidal circulation constraint and the energy constraint respectively.

We now consider a fluid element in the vicinity of a point $(\mathbf{x_0})$ where the quantity $f_0^\star = h^\star - \frac{1}{2}\beta^\star\psi\left(\mathbf{x_0}\right)$ is non zero – this point exists otherwise the stream function ψ would be constant over the domain $\mathcal{D}$ and the poloidal energy would be zero. ψ being continuous in the limit $N \to \infty$, we may assume $\psi\left(\mathbf{x_0}\right) > 0$ on a small volume of fluid $|\mathbf{dx_0}|$ centered around $(\mathbf{x_0})$. To leading order in M, this small volume of fluid contributes to the poloidal energy as

$$E\left(\mathbf{x_0}\right)|\mathbf{dx_0}| = -\frac{\partial \log Z_M^\star\left(\mathbf{x_0}\right)}{\partial\beta_{pol}^{(M)}}|\mathbf{dx_0}| = \frac{M\psi\left(\mathbf{x_0}\right)|\mathbf{dx_0}|}{2}\frac{\int_{-1}^{1} d\xi\xi e^{f_0^\star M^{\gamma+1}\xi}}{\int_{-1}^{1} d\xi e^{f_0^\star M^{\gamma+1}\xi}}. \tag{59}$$

If $\gamma + 1 \geq 0$, then $E\left(\mathbf{x_0}\right)|\mathbf{dx_0}| \to \infty$, and the divergence is exponential when $\gamma > 1$. Therefore, $\gamma + 1 \leq 0$. It stems that $E\left(\mathbf{x_0}\right)|\mathbf{dx_0}| \underset{M\to\infty}{\sim} \frac{M^{\gamma+2}\psi\left(\mathbf{x_0}\right)f_0^\star}{12}|\mathbf{dx_0}|$, so that it is finite and non zero only when $\gamma = -2$.

Therefore, the correct definition of the reduced Lagrange multipliers, in the case where the poloidal energy is non-vanishing is

$$\lim_{M\to\infty} M^2 h^{(M)} = h^\star < +\infty, \quad \text{and} \quad \lim_{M\to\infty} M^2\beta^{(M)} = \beta^\star < +\infty. \tag{60}$$

Mean-field equation and infinite temperature

To describe the microcanonical poloidal measure, we use the scaling (60) and let $M \to \infty$ in Equations (54) and (56). This yields

$$\langle\xi\left(\mathbf{x}\right)\rangle = -\frac{\beta_{pol}^\star\psi\left(\mathbf{x}\right)}{6} + \frac{h^\star}{3}, \quad \text{and} \quad \forall p > 1,\ |\langle\xi\left(\mathbf{x}\right)^p\rangle| = \infty. \tag{61}$$

The limit mean-field equation stems from Equation (61) combined with Equation (57). It reads

$$\Delta_\star\psi = \frac{\beta_{pol}^\star\psi\left(\mathbf{x}\right)}{6} - \frac{h^\star}{3}. \tag{62}$$

The latter equation is very reminiscent of the equation that describes the low energy equilibria or the strong mixing limit of the 2D Euler equations (see e.g. [Chavanis and Sommeria, 1998, Bouchet and Venaille, 2011]). Standard techniques can be used to solve it. Its solutions are thoroughly determined in Appendix A, following a methodology detailed in [Chavanis and Sommeria, 1996]. We qualitatively describe those below.

The differential operator $-\Delta_\star$ is a positive definite operator. We denote by ϕ_{kl} and κ_{kl} the eigenfunctions and corresponding eigenvalues of $-\Delta_\star$, such that $\int_\mathcal{D} \mathbf{dx}\, \phi_{kl} \neq 0$. We denote ϕ'_{kl} and κ'_{kl} the eigenfunctions and corresponding eigenvalues such that $\int_\mathcal{D} \mathbf{dx}\, \phi'_{kl} = 0$. As shown in Appendix A, three kinds of situations can be encountered for a solution ψ of Equation (62).

- If $-\beta^\star/6$ is not one of the eigenvalue κ^2_{kl}, equation (62) has a unique solution $\psi(\beta^\star, h^\star)$, which is non-zero if $h^\star$ is non zero. If $h^\star \neq 0$, each $\psi(\beta^\star, h^\star)$ can be expressed as a sum of contributions on the modes ϕ_{kl} only. This family of solution is continuous for values of $-\beta^\star/6$ between two eigenvalues κ^2_{kl}, and diverge for $-\beta^\star/6$ close to κ^2_{kl}. In particular, it is continuous for $-\beta^\star/6 = \kappa'^2_{kl}$.
- If $\beta^\star = -6\kappa'^2_{k_0 l_0}$, ψ is the superposition of the eigenmode $\phi'_{k_0 l_0}$ with the solution from the continuum at temperature $\beta^\star = -6\kappa'^2_{k_0 l_0}$. In this case, ψ is named a "mixed solution".
- If $\beta^\star = -6\kappa^2_{k_0 l_0}$, ψ is proportional to an eigenmode $\phi_{k_0 l_0}$.

Entropy and phase diagram.

All of the solutions described above are critical points for the macrostate entropy. For given E and X_{tot} we selected among those critical points those that have the correct E and X_{tot}. If more than one solution exist, we select the ones that do indeed maximize the macrostate entropy. The computation of the entropy and the selection of the most probable states is carried out explicitly in Appendix C.

The type of solutions for which the macrostate entropy is maximal depends on the quantity $\dfrac{X^2_{tot}}{2E}$. There exist two threshold values $T_- < T_+$ for this quantity, whose values are here not important but can be found in Appendix C. The value T_- depends on the geometry of the domain. It is close to T_+ for thin cylinders ($h \gg R$) and close to 0 (but not 0) for wide cylinders ($h \ll R$). We recall that κ^2_{01} is the minimal eigenvalue of the operator $-\Delta_\star$. We denote κ'^2 the minimal eigenvalue associated to the eigenfunctions ϕ', so that $\kappa' = \kappa'_{02}$ for wide cylinders and $\kappa' = \kappa'_{11}$ for thin cylinders.

Then:

- For $\dfrac{X^2_{tot}}{2E} > T_+$, there is only one set of values ($\beta^\star$,$h^\star$) such that the critical points $\psi(\beta^\star, h^\star)$ satisfy the constraints on the energy and on the circulation. This is a solution from the continuum with $\beta^\star$ strictly greater than $-6\kappa^2_{01}$. This unique critical point is the entropy maximum. When $\dfrac{X^2_{tot}}{2E} \gg T_+$, the typical poloidal field is uniform. As $\dfrac{X^2_{tot}}{2E} \to T_+^+$, the typical poloidal field gets organized into a single large-scale vertical jet.

- For $\frac{X_{tot}^2}{2E} \in [T_-; T_+]$, the entropy is maximized for a solution from the continuum. The value of $h^\star$ and $\beta^\star$ are not uniquely determined by the value $\frac{X_{tot}^2}{2E}$ and the selected solution is the one that corresponds to $|\beta^\star| \leq 6\kappa'$. As $\frac{X_{tot}^2}{2E} \to T_-^+$, the vertical jet gets thinner.
- For $\frac{X_{tot}^2}{2E} \leq T_-$, the entropy is maximized by a mixed solution, associated to the eigenvalue κ'. As $\frac{X_{tot}^2}{2E} \to 0$, the vertical jet gets transformed into a dipolar flow. The dipoles are vertical for wide cylinders and horizontal for thin cylinders.

Those results and the equilibrium poloidal fields $\langle \xi(\mathbf{x}) \rangle^{pol}$ are summarized on the phase diagram shown on Figure 4. Note, that the entropy of the equilibrium state is

$$\mathcal{S}_M[p_M^{\star,E}] \underset{M\to\infty}{=} \log 2M + \frac{1}{2|\mathcal{D}|M^2}(\beta^\star E - h^\star X_{tot}) + o\left(\frac{1}{M^2}\right), \tag{63}$$

where for each value of the energy and of the poloidal circulation, the corresponding values of $\beta^\star$ and $h^\star$ are the ones described above.

3.4 Statistical mechanics of the simplified problem

As explained in Paragraph 3.1.3, we will now couple the toroidal and the poloidal degrees of freedom in order to solve the non-helical problem and describe the non-helical axi-symmetric measure. The total entropy is then

$$S_M(E) = \sup_{E_{tor}} \{ S_M^{pol}(E - E_{tor}) + S^{tor}(E_{tor}) \}, \tag{64}$$

where E_{tor} is the toroidal energy, $E - E_{tor}$ the poloidal one. Recall that the toroidal entropy S^{tor} is depicted in Figure 3, and the poloidal entropy is given by Equation (63). The extrema condition leads to the equality of the poloidal and toroidal inverse temperatures

$$\beta_M^{pol} = \left.\frac{\partial S_M^{pol}(E_{pol}, X_{tot})}{\partial E_{pol}}\right|_{X_{tot}} = \beta^{tor} = \left.\frac{\partial S^{tor}(E_{tor}, \{A_k\})}{\partial E_{tor}})\right|_{\{A_k\}} .Weno \tag{65}$$

The fundamental remark is that in the limit $M \to \infty$, the number of poloidal degrees of freedom scales with M. Hence, the inverse poloidal temperature is equal to zero whenever the poloidal energy is non zero – see Equation (63) – and use that $\beta^\star \to \infty$ for $E_{pol} \to 0$. When the inverse poloidal temperature is zero, so is the inverse toroidal temperature. This prescribes that the toroidal energy reaches its extremal value $E^\star$ – see Figure 3. We are therefore left with two alternatives:

- $E < E^\star$ then $E_{pol} = 0$ and $E_{tor} = E$.
- $E > E^\star$ then $E_{pol} = E - E^\star$ and $E_{tor} = E^\star$.

The phase diagram corresponding to the non-helical problem is then quite simple, although also quite "extreme". It is shown on Figure 5, and we can describe the two kinds of equilibria it exhibits.

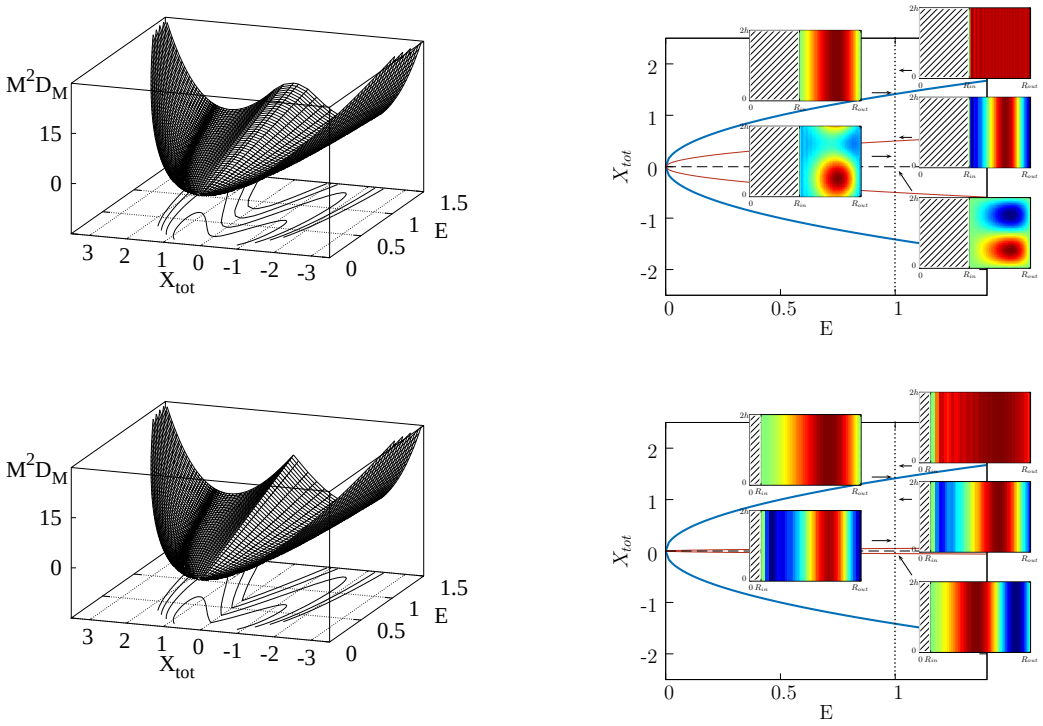

Figure 4: Left : Minus the poloidal entropy $M^2\mathcal{D}_M = 2\left|\mathcal{D}\right| M^2(\log 2M - \mathcal{S}_M)$ as a function of the circulation X_{tot} and of the poloidal energy E. The entropy was numerically estimated for a domain with height $2h = 1$, outer radius $R_{out} = \sqrt{2}$ and inner radius $R_{out} = 0.63$ (up) and $R_{in} = 0.14$ (down) . X_{tot} is rescaled by a factor $c_1 = \sqrt{\frac{|\mathcal{D}|}{32h}}$ and the entropy by a factor $c_2 = \left(\frac{|\mathcal{D}|}{2h\pi}\right)^2$ so that the value of T_+ is 1. Right: The corresponding poloidal phase diagrams. The typical poloidal fields $\langle\xi\left(\mathbf{x}\right)\rangle^{pol,E}$ are shown $E = 1$ and various values of X_{tot}. Those fields are renormalized by a factor $\sup_{\mathcal{D}}\left|\langle\xi\left(\mathbf{x}\right)\rangle^{pol,E}\right|$ so that the colormap ranks from -1 (blue) to 1 (red). With our choice of units the blue parabola has equation $X_{tot}^2 = 2E$. The red parabola separates the solutions from the continuum from the mixed solutions (see text and Appendix C for details).

For small energies, ($e.g$ $E < E^{\star}_{tor}$), there is a large scale organization of the toroidal flow. In this region, the microcanonical temperature ${\beta_{tor}}^{-1}$ is positive. The smaller E is, the smaller the toroidal temperature is and the less the toroidal energy fluctuates. As for the poloidal flow, it is vanishing. In the case where X_{tot} is non-zero, the limit $E_{pol} \to 0$ exists but yields a singular distribution for the poloidal field, since it corresponds to a typical poloidal field having a non-zero momentum while having a vanishing energy.

For high energies, ($e.g$ $E > E^{\star}_{tor}$), the equilibria describe toroidal fields that are uniform, the levels of $\mathfrak{S}_K$ being completely intertwined. The poloidal fields have infinite fluctuations. This is a consequence of the microcanonical temperature being infinite. When the poloidal energy is small, typically $E_{pol} \ll \frac{1}{2}X_{tot}^2$, the typical poloidal field is uniform over the domain. For larger poloidal energies, the typical poloidal field gets organized into a single vertical jet ($E_{pol} \simeq \frac{1}{2}X_{tot}^2$) or a large-scale dipole ($E_{pol} \gg \frac{1}{2}X_{tot}^2$).

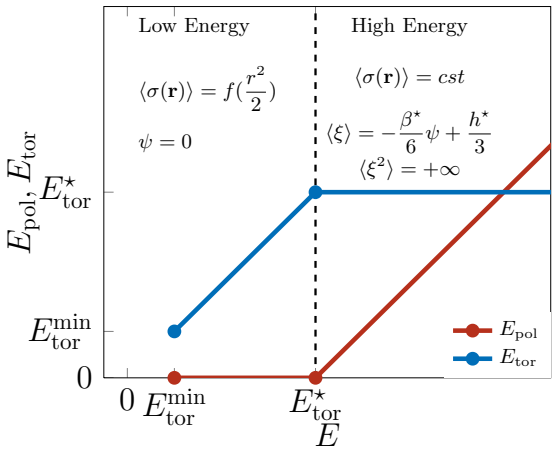

Figure 5: Phase diagram for the non-helical problem.

4 Statistical mechanics of the full problem

We now consider the full problem, in which the constraints induced by the presence of the Helical Casimirs are no longer ignored. The construction explicitly carried out in the simplified non-helical case is easily extended to the general case. A long but straightforward calculation needs to be done to describe the limit microcanonical measure, by letting $N \to \infty$ and $M \to \infty$ subsequently. In the present section, we shall not describe the calculation in full details, but rather put an emphasis on the main theoretical results. Quite surprisingly, we find out that the energy phase diagram described in the non-helical case is also relevant for the helical case. In particular, in the high-energy regime, we find out that the correlations play no role in the large scale organization of both fields. This is quite a striking result which is due to the temperature being infinite whenever the poloidal energy is non vanishing. As a result, the correlations average themselves out at every point of the domain, so that the coarse-grained equilibria only depend on the poloidal circulation and on the total energy. Some mathematical developments related to the full problem are presented in the next three subsections. The axi-symmetric equilibria are described in (4.4).

4.1 Construction of the (helical) axi-symmetric microcanonical measure

Unlike in the previously described non-helical toy problem of Section 3 , the poloidal and the toroidal fields are now coupled not only trough their respective energies, but also through the K partial circulations $\{X_k\}$. In this case, there is no obvious need to separate the configuration space into a toroidal space and a poloidal space. We therefore cut through this step and directly define the space of bounded Beltrami-spin configurations $\mathcal{G}_{M,N}(E,\{A_k\},\{X_k\})$ together with the phase space volume $\Omega_{M,N}(E,\{A_k\},\{X_k\})$ as

$$\begin{aligned}\mathcal{G}_{M,N}(E,\{A_k\},\{X_k\}) = \Big\{(\sigma_N,\xi_N) \in (\mathfrak{S}_K \times [-M;M])^{N^2} \;|\; \mathcal{E}(\sigma_N,\xi_N) = E \\ \text{and } \forall k \in [\![1;K]\!],\, \mathcal{A}_k[\sigma_N] = A_k \text{ and } \mathcal{X}_k[\sigma_N,\xi_N] = X_k\Big\}, \\ \text{and } \Omega_{M,N}(E,\{A_k\},\{X_k\}) = \sum_{\sigma_N \in \mathfrak{S}_K^{N^2}} \prod_{(i,j)\in[\![1;N]\!]^2} \int_{-\infty}^{+\infty} \mathrm{d}\xi_{N,ij} \mathbf{1}_{(\sigma_N,\xi_N)\in\mathcal{G}_{M,N}(E,\{A_k\},\{X_k\}}.\end{aligned} \tag{66}$$

A straightforward extension of Equations (19) and (21) is used to define the microcanonical weight $\mathrm{d}\mathcal{P}_{M,N}$ of a configuration $\mathcal{C} = (\sigma_N, \xi_N) \in \mathcal{G}_{M,N}(E, \{A_k\}, \{X_k\})$, together with the M, N-dependent microcanonical averages $<>_{M,N}$. The microcanonical averages $<>_M$ and $<>$ are then defined by letting successively $N \to \infty$ and $M \to \infty$, accordingly to Equation (22).

4.2 Estimate of $<>_M$

To describe the limit $N \to \infty$, the central object that we need to investigate is the asymptotic estimate of the phase space volume $\Omega_{M,N}(E, \{A_k\}, \{X_k\})$. As in the toy problem, we can use a large deviation analysis to relate it to a macrostate entropy.

Randomly and independently assigning on each node of the lattice a random value of ξ from the uniform distribution over the interval $[-M; M]$ together with a random value of σ_k drawn from the uniform distribution over $\mathfrak{S}_K$, we then define through a coarse-graining procedure the local probability $p_{k,M}(\xi, \mathbf{x})$ that a Beltrami spin takes a toroidal value σ_k together with a poloidal value between ξ and $\xi + \mathrm{d}\xi$ in an infinitesimal area $\mathbf{dx}$ around a point $(\mathbf{x})$. The distributions $p_M = \{p_{k,M}(\xi, \cdot)\}_{\substack{k \in [\![1;K]\!] \\ \xi \in [-M;M]}}$ define a poloidal macrostate, whose entire set we denote as $\mathcal{Q}$. The macrostates satisfy the local normalization constraint :

$$\forall \mathbf{x} \ \in \mathcal{D}, \sum_{k=1}^{K} \int_{-M}^{M} \mathrm{d}\xi \, p_{k,M}(\xi, \mathbf{x}) = 1. \tag{67}$$

The macrostate entropy is given by

$$\mathcal{S}_M[p_M] = -\frac{1}{|\mathcal{D}|} \int_{\mathcal{D}} \mathbf{dx} \sum_{k=1}^{K} \int_{-M}^{M} \mathrm{d}\xi \, p_{k,M}(\xi, \mathbf{x}) \log p_M(\xi, \mathbf{x}) \, / \tag{68}$$

The constraints on the configurations of Beltrami spins can be mapped to constraints on the macrostates through :

$$\begin{aligned} &\mathcal{A}_k[p_M] = \int_{\mathcal{D}} \mathbf{dx} \int_{-M}^{M} \mathrm{d}\xi \, p_{k,M}(\xi, \mathbf{x}) \,, \quad \mathcal{X}_k[p_M] = \int_{\mathcal{D}} \mathbf{dx} \int_{-M}^{M} \mathrm{d}\xi \, \xi p_{k,M}(\xi, \mathbf{x}) \,, \\ &\text{and } \mathcal{E}[p_M] = \frac{1}{2} \int_{\mathcal{D}} \mathbf{dx} \sum_{k=1}^{K} \int_{-M}^{M} \mathrm{d}\xi \, \{\frac{\sigma_k^2}{2y} + \psi(\mathbf{x}) \, \xi\} p_{k,M}(\xi, \mathbf{x}) \,. \end{aligned} \tag{69}$$

The total entropy is then given by the entropy of the most probable poloidal macrostate which satisfies the constraints. Therefore,

$$\begin{aligned} S(E, \{A_k\}, \{X_k\}) = \sup_{p_M \in \mathcal{Q}} \{\mathcal{S}_M[p_M] \mid \forall k \in [\![1; K]\!] \, \mathcal{A}_k[p_M] = A_k, \\ \mathcal{X}_k[p_M] = X_k \ \text{ and } \mathcal{E}[p_M] = E\} \,. \end{aligned} \tag{70}$$

The critical distributions $p_M^\star(\xi, \mathbf{x})$ of the optimization problem (70) can be written using $2K + 1$ Lagrange multipliers as

$$\begin{aligned} p_{M,k}^\star(\xi, \mathbf{x}) &= \frac{1}{M Z_M^\star(\mathbf{x})} \exp\{\alpha_k^{(M)} - \frac{\beta^{(M)} \sigma_k^2}{4y} + \left(h_k^{(M)} - \frac{\beta^{(M)} \psi(\mathbf{x})}{2}\right) \xi\}, \\ \text{with } \ Z_M^\star(\mathbf{x}) &= \sum_{k=1}^{K} \int_{-1}^{1} d\xi \exp\{\alpha_k^{(M)} - \frac{\beta^{(M)} \sigma_k^2}{4y} + \left(h_k^{(M)} - \frac{\beta^{(M)} \psi(\mathbf{x})}{2}\right) M\xi\}, \end{aligned} \tag{71}$$

where the Lagrange multipliers $\alpha_k^{(M)}$, $h_k^{(M)}$, $\beta^{(M)}$ are determined through

$$A_k = \int_{\mathcal{D}} \mathbf{dx}\, \frac{\partial \log Z_M^\star(\mathbf{x})}{\partial \alpha_k^{(M)}},\ X_k = \int_{\mathcal{D}} \mathbf{dx}\, \frac{\partial \log Z_M^\star(\mathbf{x})}{\partial h_k^{(M)}}, \\ \text{and } E = -\int_{\mathcal{D}} \mathbf{dx}\, \frac{\partial \log Z_M^\star(\mathbf{x})}{\partial \beta^{(M)}}. \tag{72}$$

From (72), we can compute the one-point moments as

$$\langle \sigma^p(\mathbf{x})\rangle_M = \sum_{k=1}^K \int_{-M}^M \mathrm{d}\xi\, \sigma_k^p\, p_{M,k}^\star(\xi,\mathbf{x}) \text{ and } \langle \xi^p(\mathbf{x})\rangle_M = \sum_{k=1}^K \int_{-M}^M \mathrm{d}\xi\, \xi^p p_{M,k}^\star(\xi,\mathbf{x}). \tag{73}$$

In particular, the stream function solves

$$\Delta_\star \psi(\mathbf{x}) = -\langle \xi(\mathbf{x})\rangle_M = -\sum_{k=1}^K \frac{\partial \log Z_M^\star(\mathbf{x})}{\partial h_k^{(M)}}. \tag{74}$$

Finally, note that the average one-point helicities read :

$$\langle \sigma(\mathbf{x})\,\xi(\mathbf{x})\rangle_M = \sum_{k=1}^K \int_{-M}^M \mathrm{d}\xi\, \xi\sigma_k\, p_{M,k}^\star(\xi,\mathbf{x}). \tag{75}$$

4.3 Estimate of <>, and mean-field closure equation

In order to obtain a microcanonical limit $M \to \infty$ from Equations (73) and (74), one has to find the correct scaling for the Lagrange multipliers, as derived in the purely poloidal case. We need to consider two cases, depending on whether or not the poloidal energy E_{pol} is vanishing .

The case $E_{pol} \neq 0$. With an argument similar to the one previously exposed in Section 3.3.2, we find out that the correct microcanonical scaling for the Lagrange multipliers is

$$\alpha_k = \lim_{M\to\infty} M^0 \alpha_k^{(M)},\quad h_k^\star = \lim_{M\to\infty} M^2 h_k^{(M)},\quad \text{and}\quad \beta^\star = \lim_{M\to\infty} M^2 \beta^{(M)}. \tag{76}$$

Using those latter scalings to take the limit $M \to \infty$ in Equations (74) and (73), one obtains

$$\forall p \geq 1\ \langle \sigma^p(\mathbf{x})\rangle = \overline{\sigma_k^p}, \tag{77}$$

$$\text{together with}\ \ \langle \xi(\mathbf{x})\rangle = -\frac{\beta^\star}{6}\psi(\mathbf{x}) + \frac{1}{3}\overline{h_k^\star},\ \ \text{and}\ \ \forall p \geq 2\ |\langle \xi^p(\mathbf{x})\rangle| = +\infty, \tag{78}$$

where for any $\{\mathcal{O}_k\}_{1\leq k\leq K}$, $\overline{\mathcal{O}_k}$ is defined by $\overline{\mathcal{O}_k} \equiv \sum_{k=1}^K \frac{A_k}{|\mathcal{D}|}\mathcal{O}_k$. The closure equation is similar to Equation (62) obtained for the non-helical toy poloidal problem. It reads :

$$\Delta_\star \psi = \frac{\beta^\star}{6}\psi - \frac{1}{3}\overline{h_k^\star}. \tag{79}$$

The one-point helicities are obtained from Equation (75). They read

$$\langle \sigma(\mathbf{x})\,\xi(\mathbf{x})\rangle = \frac{\overline{\sigma_k h_k^\star}}{6} + \langle \sigma(\mathbf{x})\rangle\langle \xi(\mathbf{x})\rangle. \tag{80}$$

Hence, the toroidal and the poloidal fields remain correlated in the limit $M \to \infty$. The first term of the r.h.s can be interpreted as an extra small-scale contribution to the total helicity.

Now, the distributions $p^\star_M$ are critical points of the macrostate entropy (68) but do not necessarily maximize it. We still need to determine which values of $\overline{h^\star_k}$ and $\beta^\star$ actually solve the optimization problem (73), at least for the case under consideration here, that is to say for large values of M. It turns out, that the asymptotic expansions of the critical values of the macrostate entropy read

$$\mathcal{S}_M[p^\star_M] \underset{M\to\infty}{=} \log 2M - \sum_{k=1}^{K} \frac{A_k}{|\mathcal{D}|}\log\frac{A_k}{|\mathcal{D}|} + \frac{1}{2\,|\mathcal{D}|\,M^2}\left(\beta^\star E_{pol} - \overline{h^\star_k} X_{tot}\right) + \frac{3}{2M^2}\overline{\left(\frac{X_k}{A_k} - \frac{X_{tot}}{|\mathcal{D}|}\right)^2} + o\left(\frac{1}{M^2}\right). \tag{81}$$

Some technical details about the derivation can be found in Appendix B.2. The crucial observation here is that Equation (81) compares with the *non-helical* poloidal macrostate entropy given by Equation (63). We conclude that the selection of the most probable poloidal state only depends on the value of E_{pol} and X_{tot}. In other words, given a value of E_{pol} and X_{tot}, the most probable macrostates are the same in the non-helical problem as in the full helical problem, whatever the specific values of the X_k are.

The case $E_{pol} = 0$. In this case, the stream function ψ is necessarily vanishing. The correct scaling for the Lagrange multipliers is then :

$$\alpha_k = \lim_{M\to\infty} M^0 \alpha_k^{(M)}, \quad h^\star_k = \lim_{M\to\infty} M^2 h_k^{(M)}, \quad \text{and} \quad \beta^\star = \lim_{M\to\infty} M^0 \beta^{(M)}., \tag{82}$$

For the toroidal field, such a scaling yields :

$$\langle \sigma^p(\mathbf{x})\rangle = \frac{\sum_{k=1}^K \sigma_k^p e^{\alpha^\star_k - \beta\sigma_k^2/4y}}{\sum_{k=1}^K e^{\alpha^\star_k - \beta\sigma_k^2/4y}}. \tag{83}$$

For the poloidal field, it yields

$$\langle \xi(\mathbf{x})\rangle = \frac{\sum_{k=1}^K h^\star_k e^{\alpha^\star_k - \beta\sigma_k^2/4y}}{3\sum_{k=1}^K e^{\alpha^\star_k - \beta\sigma_k^2/4y}}, \text{ and } \langle \xi^p(\mathbf{x})\rangle = +\infty \ \text{ for } p>1\ . \tag{84}$$

.

Just like in the toroidal problem which was treated in the non-helical case described in Section 3.2, the Lagrange multipliers $\alpha^\star_k$ and $\beta^\star$ are then uniquely determined by inverting the system made of the $K+1$ equations

$$\begin{aligned} E &= \int_{\mathcal{D}} \frac{\sum_{k=1}^K (\sigma_k^2/4y) e^{\alpha_k - \beta^\star\sigma_k^2/4y}}{\sum_{k=1}^K e^{\alpha_k - \beta^\star\sigma_k^2/4y}}, \\ \text{and } \frac{A_k}{|\mathcal{D}|} &= \int_{\mathcal{D}} \frac{e^{\alpha_k - \beta^\star\sigma_k^2/4y}}{\sum_{k=1}^K e^{\alpha_k - \beta^\star\sigma_k^2/4y}} \ \text{ for all } 1\le k\le K. \end{aligned} \tag{85}$$

It is not difficult to check that the reduced Lagrange multipliers $h^\star_k$ satisfy $h^\star_k = 3\dfrac{X_k\,|\mathcal{D}|}{A_k}$.

Therefore, in the case where the poloidal energy is vanishing, the helical correlations do not affect the typical toroidal states: the toroidal equilibria are exactly those described in Section 3.2 and depicted in a simplified two-level case on Figure 3. The poloidal field is however "enslaved" to the toroidal field. It does not contribute to the total energy.

4.4 Phase diagram of the full problem

In the last section, we have obtained that in the case where the poloidal energy is non-vanishing that the toroidal levels σ_k are completely mixed – Equation (77). As a consequence, $E_{tor} = E^\star$. We thus deduce the same alternative as in the reduced problem:

- If $E \geq E^\star_{tor}$, then $E_{tor} = E^\star_{tor}$ and $E_{pol} = E - E^\star_{tor}$.
- If $E < E^\star_{tor}$, then $E_{tor} = E$ and $E_{pol} = 0$.

$E^\star_{tor}$ is computed from Equation (77) as $E^\star_{tor} = \sum_{k=1}^K \frac{A_k \sigma_k^2}{2\,|\mathcal{D}|} \log \frac{R_{out}}{R_{in}}$, just as in the non-helical case. Therefore, the phase diagram describing the splitting of the total kinetic energy between the toroidal and the poloidal degrees of freedom is exactly the same as the one described in the simplified problem of Section 3. It is therefore shown on Figure 5. It displays a high energy ($E \geq E^\star$) and a low energy regime ($E < E^\star$). In each of those energy regime, the axi-symmetric equilibria are very much akin to the non-helical equilibria described in Section 3.4, with just a small alteration for the typical poloidal field in the low energy regime. To make this result stand more clearly, we summarize below the characteristics of both regimes.

In the low energy regime ($E < E^\star$)**,** the typical fields are characterized through

$$\begin{aligned} &\langle \sigma(\mathbf{x}) \rangle = \frac{\sum_{k=1}^K \sigma_k e^{\alpha_k^\star - \beta\sigma_k^2/4y}}{\sum_{k=1}^K e^{\alpha_k^\star - \beta\sigma_k^2/4y}},\ \langle \xi(\mathbf{x}) \rangle = \frac{\sum_{k=1}^K h_k^\star e^{\alpha_k^\star - \beta\sigma_k^2/4y}}{\sum_{k=1}^K e^{\alpha_k^\star - \beta\sigma_k^2/4y}}(y), \\ &\text{and } \psi = 0. \end{aligned} \tag{86}$$

The Lagrange multipliers are determined through Equation (85). The poloidal fluctuations are infinite. Qualitatively, the flow (poloidal and toroidal) is stratified along the radial direction. In the limit of a very low energy ($E \gtrsim E^{\min}_{tor}$) the toroidal patches are completely segregated, and sorted by increasing toroidal values from the inner to the outer wall. When the energy gets close to $E^\star_{tor}$, it becomes uniform – see Figure 3.

In the high energy regime ($E \geq E^\star$)**,** the typical fields are characterized through

$$\begin{aligned} &\langle \sigma(\mathbf{x}) \rangle = \sum_{k=1}^K \frac{A_k}{|\mathcal{D}|}\sigma_k,\ \langle \xi(\mathbf{x}) \rangle = -\frac{\beta^\star}{6}\psi(\mathbf{x}) + \frac{1}{3}\sum_{k=1}^K \frac{A_k}{|\mathcal{D}|} h_k^\star, \\ &\text{with } \Delta_\star \psi = \frac{\beta^\star}{6}\psi(\mathbf{x}) - \frac{1}{3}\sum_{k=1}^K \frac{A_k}{|\mathcal{D}|} h_k^\star. \end{aligned} \tag{87}$$

The Lagrange multipliers $\beta^\star$ and $h_k^\star$ can be completely determined – see Appendix B.2. The poloidal energy is prescribed as $E_{pol} = E - E^\star_{tor}$. Qualitatively, the toroidal field is uniform. This corresponds to the toroidal patches being completely intertwined, regardless of their position in the domain $\mathcal{D}$. The poloidal field exhibits infinitely large fluctuations around a large scale organization. The latter is completely prescribed by the values of the poloidal energy and of the poloidal circulation and does not depend on the specific choice of the partial poloidal circulations X_k.

For prescribed values of the constraints, the entropy of the full problem as given by Equation (81) matches the non-helical poloidal entropy (63) up to some constants terms. Therefore, the large scale organization of the poloidal field is exactly the one depicted on Figure 4.

4.5 Further Comments

4.5.1 Stationarity and formal stability of the equilibria

We can observe that the axi-symmetric statistical equilibria described in the previous Section 4.4 describe average fields which are stationary states of the Euler axi-symmetric equations (3). In the low energy regime, this is due to the stream function ψ being vanishing and to the typical toroidal field being a function of the radial coordinate only. In the high energy regime, this is due to the typical toroidal field being constant, and to the poloidal field being a function of the stream function ψ. Note that this is in itself a result, and not an input of the theory.

Besides, we can also note that not only are those typical fields stationary, they are also formally stable with respect to any axi-symmetric perturbation. For infinite dimensional systems, formal stability is a pre-requisite for non-linear stability [Holm et al., 1985]. In the case of axi-symmetric flows, a sufficient criterion for formal stability based on the general Energy-Casimir method can be found in [Szeri and Holmes, 1988, Eq 3.15]. With the notation at use in the present paper, and with an "e" subscript to denote an axi-symmetric stationary solution, this criterion reads

$$\frac{\partial \xi_e}{\partial \sigma_e}\frac{\mathrm{d}\psi_e}{\mathrm{d}\sigma_e} + \frac{\sigma_e}{2y^2}\frac{\partial y}{\partial \sigma_e} - \frac{1}{-\Delta_\star^{-1}}\left(\frac{\mathrm{d}\psi_e}{\mathrm{d}\sigma_e}\right)^2 \geq 0. \tag{88}$$

The notation $1/(-\Delta_\star^{-1})$ can be liberally replaced by any $1/\kappa_i^2$ with κ_i^2 either one of the eigenvalue of $-\Delta_\star^{-1}$, which are real and non-negative – see Appendix A. As noticed by Szeri and Holmes, "the inequality cannot be expected to hold in general, for the simple reason that the eigenvalues of the operator $[1/\Delta_\star^{-1}]$ have no upper bound". However, the criterion is fulfilled for the very limited set of equilibria obtained from our statistical mechanics approach. In the low energy regime, only the term $\dfrac{\langle\sigma\rangle}{2y^2}\dfrac{\partial y}{\partial\langle\sigma\rangle}$ is non-vanishing. It is however positive, as the stratification causes the values of $\langle\sigma\rangle$ to increase from the inner to the outer cylinder. Hence the criterion is fulfilled. In the high energy regime, every term involved in Equation (88) vanishes. Therefore, the stability criterion is also – trivially – fulfilled.

4.5.2 Link to previous work

The axi-symmetric equilibria (87) and (87) which we obtained in the present paper substantially differ from the ones described in previous works about the statistical mechanics of axi-symmetric swirling flows. We can note that an attempt to bound the poloidal fluctuations with an extraneous cutoff can be found in [Leprovost et al., 2006, Appendix E]. In this appendix, a set of canonical equilibria are derived and the authors assume that a physical interpretation can be given to the extraneous cutoff. Those canonical equilibria are however "dramatic" : they depend exponentially on the extraneous cutoff. The authors note that the average fields which are described by this statistical mechanics approach are *not* steady solutions of the axi-symmetric Euler equations.

For this reason, [Leprovost et al., 2006,Naso et al., 2010a] rather prefer to work out the statistical mechanics of the axi-symmetric Euler equations by analogy with the 2D Euler equations, setingthe poloidal fluctuations 0, and considering a toroidal mixing subject to a "robust" set of three constraints, namely the energy, the helicity and the toroidal momentum. In [Naso et al., 2010a, Eq (36-37)], it is found that the typical fields correspond

to large scale Beltrami flows, such that $\langle \sigma(\mathbf{x}) \rangle = B\psi(\mathbf{x})$ and $\langle \xi(\mathbf{x}) \rangle = B\langle \sigma \rangle / 2y + C$, where B and C are related to the Lagrange multipliers associated to the constraints of energy, helicity and angular momentum. From a physical point of view, and as far as the axi-symmetric Euler equations are concerned, those equilibria have in a sense two "drawbacks" : i) they predict a multi-stability of solutions and do not predict the emergence of large scale structure as maximal entropy structures and ii) they predict that the average fields are steady states of the Euler axi-symmetric equations, yet of an unstable kind. More explicitly, for the Beltrami flows just described, the presence of a large scale helicity creates a dependence between the typical toroidal field and the stream function. This makes the term $\left(\frac{\mathrm{d}\psi}{\mathrm{d}\sigma}\right)^2$ in the criterion (88) be non vanishing and hereby prevents the steady states from being stable.

In our statistical approach, both of the issues have been fixed, although their outcome was not *a priori* known. The main ideas were to consider infinitely large poloidal fluctuations, and to work exclusively in the microcanonical ensemble so as to find out a good scaling for the Lagrange multipliers at stake. Besides, we managed to take into account all the invariants. The price to pay is that the equilibria that we get within our approach are in a sense more extreme and more limited than the ones previously found. They are however more natural.

5 Discussion

Some additional technical comments.

It was not obvious from the beginning that the construction of microcanonical measures *à la* Robert-Miller-Sommeria for the axi-symmetric Euler equations could be carried out extensively, nor that it would yield non trivial insights to understand the physics of axi-symmetric flows. What can be considered as the key point here is the accurate renormalization of the inverse temperature and associated Lagrange multipliers with respect to the phase space volume. This allowed us to build an asymptotic limit consistent with the physical constraints and prevented us from encountering an avatar of the Jeans paradox. The renormalization was not carried out in the previous works concerning axi-symmetric equilibria. Here, it is crucial in order to take into account the invariants related to the poloidal degrees of freedom that live in an infinite phase space.

Other choices could have been made to renormalize the phase space. Instead of a cut-off M, it is also possible to make the divergent integrals converge by integrating over the ν dependent measures $e^{-\nu\xi^2}\mathrm{d}\xi$ – rather than over the M dependent measures $\mathbf{1}_{[-M;M]}\mathrm{d}\xi$ – . This is tantamount to restricting the set of macrostates on which the suprema of the entropy are taken, to those whose poloidal fluctuations are bounded. To work out the microcanonical limit, one then needs to introduce some ν-dependent Lagrange multipliers $\beta^\nu = \nu\beta^\star$, $h^\nu = \nu h^\star$ and let $\nu \to 0$ subsequently. The limit measures obtained with the latter renormalization are completely consistent with the ones we described in this paper. They are also in a sense more general as they allow to retrieve the previously found Beltrami states by considering the other limit $\nu \to 0$.

Note also that in order to carry out our analysis, we have restricted ourselves to the case where the inner cylinder has a non-vanishing radius R_{in}, so that we worked

in the framework of a "Tayor-Couette geometry". It is yet not so clear how to extend the analysis to the limit case $R_{in} \to 0$, which can be thought of as a "von Kármán geometry". The problem comes from the blow up of the equilibrium toroidal energy $E^\star_{tor} = \sum_{k=1}^{K} \frac{A_k \sigma_k^2}{2\,|\mathcal{D}|} \log \frac{R_{out}}{R_{in}}$ if we simply let $R_{in} \to 0$. [4]

Physical insights about axi-symmetric turbulence

The physics described by the micrononical measure is interesting. Let us first comment about the role of the invariants. We may have built a measure by taking into account every kind of inviscid invariant of the axi-symmetric Euler equations, it turns out that most of the physics comes from a reduced set of invariants, namely the energy, the toroidal Casimirs and the total circulation. In particular, our result shows that the helicity – which relates to the correlation between the toroidal and the poloidal degrees of freedom – plays no role in the description of large scale structure at the level of the macrostates when the energy is high enough. This is consistent with the traditional picture of a downward helicity cascade in $3D$ turbulence. This may also explain why previous attempts to find axi-symmetric equilibria by neglecting the fluctuations of the poloidal field while keeping a constraint on the helicity would only lead to unstable equilibria, likely to be destabilized by small-scaled perturbations.

The axi-symmetric equilibria are very different from those obtained in the 2D case. In the low temperature, low energy regime, the large scale stripes come from the interaction of the toroidal degrees of freedom with the position field – the interaction being inhomogeneous and invariant with respect to vertical translations. As for the infinite temperature, high energy regime, the Toroidal Casimirs play no role in it. The linear relationship between the poloidal field and the stream function may be seen as the axi-symmetric analogue of the low energy limit of the sinh-Poisson relation in 2D turbulence. Yet, the infinite fluctuations related to the poloidal field may be heuristically interpreted as a very 3D turbulent feature and may be related to the tendency of vortices to leak towards the smallest scales available in 3D turbulence. Therefore, neither regimes have strict analogues in 2D.

Some perspectives.

Extensions to closely related flows. Let us mention the close analogy between axi-symmetric flows and other flows of geophysical and astrophysical interests such as two-dimensional stratified flows in the Boussinesq approximation (Boussinesq flows) [Szeri and Holmes, 1988, Abarbanel et al., 1986] and two-dimensional magnetohydrodynamics (2D MHD). In the former case, it almost suffices to replace the word "poloidal" by the word "vorticity" and the word "toroidal" by the word "density " in the present paper to obtain *mutatis mutandi* a statistical theory for ideal Boussinesq flows. The case of 2D MHD

[4] One naive way to cope with this issue and obtain a specific class of equilibria for the von Kármán geometry is to renormalize each toroidal level σ_k^2 in $\mathfrak{S}_K$ as $\sigma_k^2 \to \frac{\sigma_k^2}{\log \frac{R_{out}}{R_{in}}}$. Another possibility is to impose a local smoothing condition near the center of the cylinder that could be enforced at the level of the macrostates. It would suffice for instance to prescribe $< \sigma(\mathbf{x}) >_M \underset{r\to 0}{=} O(r^\epsilon)$ with ϵ being non negative in order to avoid a blow up of the equilibrium toroidal energy. A third alternative is to rule out the existence of infinite temperature states in this geometry.

is slightly more subtle. The Casimir invariants of ideal 2D MHD are similar to the axi-symmetric Casimir invariants but the energies slightly differ. It would therefore be very interesting to generalize the method described in the present paper to the 2D MHD case, which is more documented than the axi-symmetric case, and for which inviscid statistical theories have recently been reinvestigated [Weichman, 2012].

Are microcanical measures relevant for real turbulence ? It is finally tempting to ask whether some of the axi-symmetric equilibrium features can be recognized in real turbulent experiments. Examples of a turbulent flows likely to be modeled by the axi-symmetric Navier-Stokes are von Kármán turbulence [Herbert et al., 2012, Saint-Michel et al., 2013] or Taylor-Couette turbulence [Smith and Townsend, 1982,Dong, 2007]. There however exist many caveats concerning a thorough investigation of the link between axi-symmetric ideal measures and turbulent experiments, examples of which include requirements on a "separation of scales", the relevance of fragile invariants in the presence of forcing and dissipation, the intrinsic "3Dness" of a turbulent experiment. We therefore postpone the discussion to a forthcoming paper.

Acknowledgements. We thank J. Barré, P-H. Chavanis, B. Turkington, A. Venaille and an anonymous referee for their careful proof reading and their useful comments that helped improve the presentation of the arguments discussed in the present paper.

A Solutions of the mean-field equation

We show here how to solve the closure equations (62) and (79) in terms of the eigenmodes of the operator $\Delta^\star$, for fields that are $2h$-periodic along the z direction and are vanishing on both the inner and the outer cylinders. Recall that those equations both read

$$\Delta_\star \psi = \frac{\beta^\star}{6}\psi - \frac{h^\star}{3} \quad \text{with} \quad \Delta_\star = \frac{1}{2y}\partial_{zz} + \partial_{yy}. \tag{89}$$

A.1 Explicit computation of the eigenmodes of the operator $\Delta^\star$

The eigenmodes of $\Delta_\star$ are solutions to the eigenvalue problem $\Delta_\star \phi_\kappa = -\kappa^2 \phi_\kappa$ – with the prescribed boundary conditions. Let ϕ_κ be such an eigenmode. We can Fourier decompose ϕ_K and write $\phi_K(y,z) = \sum_{k\in\mathbb{Z}} f_k(y) \exp \frac{ik\pi z}{h}$. ϕ_K is a solution to the eigenvalue probleme *iff* each one of the functions f_k satisfies

$$\begin{gathered} f_k''(y) + \left(\kappa^2 - \frac{k^2\pi^2}{2h^2 y}\right) f_k(y) = 0, \\ \text{or equivalently } \tilde{f}_k''(\tilde{y}) + \left(1 - \frac{k^2\pi^2}{2h^2\kappa\tilde{y}}\right)\tilde{f}_k(\tilde{y}) = 0 \text{ putting } \tilde{y} = \kappa y \text{ and } \tilde{f}_k(\tilde{y}) = f_k(y). \end{gathered} \tag{90}$$

The latter equation is known as a "Coulomb Wave equation" [Abramowitz and Stegun, 1965].

If $k = 0$, then $f_0(y) = A\sin\kappa(y - Y_{in}) + B\cos\kappa(y - Y_{in})$. $f_0(Y_{in}) = 0$ gives $B = 0$. $f_0(Y_{out}) = 0$ gives $\kappa = \kappa_{0l} = \frac{l\pi}{Y_{out} - Y_{in}}$. For each value of $l \geq 0$, we write $\phi_{0l} = \frac{\sin[\kappa_{0l}(y - Y_{in})]}{\sqrt{h(Y_{out} - Y_{in})}}$. ϕ_{0l} is an eigenmode of $\Delta^\star$, such that $\Delta_\star \phi_{0l} = -\kappa_{0l}^2 \phi_{0l}$. The normalization factor is chosen so that $\int_{Y_{in}}^{Y_{out}} dy \int_0^{2h} dz \phi_{0l}^2 = 1$.

If $k \neq 0$, $\tilde{f}_k(\tilde{y}) = C_1 F_0(\eta_k, \tilde{y}) + C_2 G_0(\eta_k, \tilde{y})$ where F_0 and G_0 are respectively the regular and singular Coulomb Wave functions associated to the parameter $\eta_k = \frac{k^2\pi^2}{4h^2\kappa}$. The non trivial solutions are determined using the vanishing boundary condition for ψ on the walls. For each value of k, the horizontal eigen modes correspond to the values κ_{kl} for wich the quantity

$$W(\kappa) = \begin{vmatrix} F_0\left(\frac{k^2\pi^2}{4h^2\kappa}, \kappa Y_{in}\right) & G_0\left(\frac{k^2\pi^2}{4h^2\kappa}, \kappa Y_{in}\right) \\ F_0\left(\frac{k^2\pi^2}{4h^2\kappa}, \kappa Y_{out}\right) & G_0\left(\frac{k^2\pi^2}{4h^2\kappa}, \kappa Y_{out}\right) \end{vmatrix} \text{ is vanishing.} \tag{91}$$

Each mode κ_{kl} is therefore related to two eigenmodes $\phi_{kl}^\pm = A_{kl} \exp\left(\pm i \frac{k\pi z}{h}\right) f_k(\kappa_{kl} y)$, such that $\Delta_\star \phi_{kl} = -\kappa_{kl}^2 \phi_{kl}$. The normalization factor is taken such as to enforce $\int_{Y_{in}}^{Y_{out}} dy \int_0^{2h} dz \phi_{Kl}^2 = 1$.

The Fourier decomposition of ϕ_K can now be rewritten as $\phi_K(y,z) = \sum_{k,l\in\mathbb{Z}} a_{kl}\phi_{kl}(y,z)$. Two modes corresponding to two different eigenvalues are orthogonal for the scalar product $(f|g) \equiv \int_{\mathcal{D}} dydz\bar{f}g$. Hence, ϕ_K is a solution of $\Delta^\star\psi = -\kappa^2\phi_K$ *iff* there exists (k,l) such that $\kappa_{kl}^2 = \kappa^2$.

As an illustration, a numerical estimation for different domain shapes of the first eigenvalues of $\Delta^\star$ together with their corresponding eigenmode is provided on Figure 6.

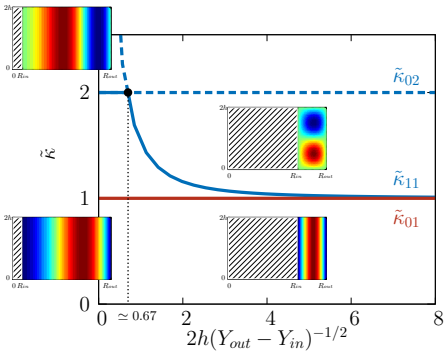

Figure 6: Numerical estimation of the first eigenvalues of $\Delta^\star$ as functions of the domain size. The eigenvalues κ are adimensionnalised and $\tilde{\kappa} = \dfrac{\kappa}{\pi(Y_{out} - Y_{in})}$. The estimation was made with a fixed height $2h = 1$ and fixed outer radius $R_{out} = \sqrt{2}$. The inserted pictures represent maps of the corresponding eigenmodes.

A.2 Types of solutions for equation (89).

Let ψ be a solution of equation (89) and let us decompose ψ as $\psi = \sum_{k,l} p_{kl}\phi_{kl}$. Then necessarily,

$$\forall (k,l) \in \mathbb{Z}^2 \quad p_{kl}\left(\kappa_{kl}^2 + \frac{\beta^\star}{6}\right) = \frac{h^\star}{3}(1|\phi_{kl}). \tag{92}$$

Let us note that the only modes with a non vanishing integral over the domain, – namely such that $(1|\phi_{kl}) \neq 0$ – are the modes obtained for $k = 0$ and l odd. To describe the solutions of equation (92) we now need to consider the three following different cases. We hereby follow an existing terminology, as found for example in [Chavanis and Sommeria, 1996, Naso et al., 2010a].

i) Continuum solutions. If $\forall (k,l), \beta^\star \neq -6\kappa_{kl}^2$, then necessarily

$$\forall (k,l) \quad p_{kl} = \frac{h^\star(1|\phi_{kl})}{3\left(\kappa_{kl}^2 + \dfrac{\beta^\star}{6}\right)}. \tag{93}$$

In this case, ψ can be written as

$$\psi = \frac{h^\star}{3}\sum_{k,l}\frac{(1|\phi_{kl})}{\left(\kappa_{kl}^2 + \dfrac{\beta^\star}{6}\right)}\phi_{kl} = \frac{h^\star}{3}\sum_{l\,odd}\frac{(1|\phi_{0l})}{\left(\kappa_{0l}^2 + \dfrac{\beta^\star}{6}\right)}\phi_{0l} \tag{94}$$

For any odd value of l, this family of solution is continuous for values of $-\beta^\star/6$ between two eigenvalues κ^2_{0l} and κ^2_{0l+2} , and diverge for $-\beta^\star/6$ close to κ^2_{0l}. In particular, it is continuous for values of $-\beta^\star/6 = \kappa^2_{mn}$ such that $(1|\phi_{mn}) = 0$.

ii) Mixed solutions and eigenmodes. Otherwise there exists (k_0, l_0) such that $\beta^\star = -6\kappa^2_{k_0l_0}$. Then necessarily $\forall (k,l) \neq (k_0,l_0)$ $p_{kl} = \dfrac{h^\star (1|\phi_{kl})}{3\left(\kappa^2_{kl} - \kappa^2_{0l_0}\right)}$.

ii.a) Mixed Solutions. If $(1|\phi_{k_0l_0}) = 0$, – *e.g* if $k_0 \neq 0$ or l_0 is even –, then ψ can be written as $\psi = p_{k_0l_0}\phi_{k_0l_0} + \dfrac{h^\star}{3}\sum_{l\,odd} \dfrac{(1|\phi_{0l})}{\left(\kappa^2_{0l} - \kappa^2_{k_0l_0}\right)}\phi_{0l}$. The coefficient $p_{k_0l_0}$ can take any value. ψ can be seen as a superposition of a solution from the continuum with the eigenmode $\phi_{k_0l_0}$, and we therefore call these solutions "mixed solutions".

ii.b) Odd eigenmodes. Otherwise, $(1|\phi_{k_0l_0}) \neq 0$ – *e.g* $k_0 = 0$ and l_0 is odd. Equation (92) considered for $(k,l) = (0,l_0)$ implies $h^\star = 0$. In this case ψ is proportionnal to the odd eigenmode ϕ_{0l_0}, namely $\psi = A\phi_{0l_0}$.

B Explicit derivation of the macrostate entropies

We hereafter show how to derive the expressions (63) and (81), which correspond to the critical macrostate poloidal entropy of the simplified problem, and the critical macrostate entropy of the full problem in the high energy regime.

B.1 Deriving the non-helical poloidal critical macrostate entropies.

Recall that the critical distributions $p^{\star,E}_M$ related to the non-helical poloidal problem are described by Equations (54) and (55). Recall that their macrostate entropy reads – Equation (48) – :

$$\begin{aligned}
\mathcal{S}^{pol}_M[p^{\star,E}_M] &= -\frac{1}{|\mathcal{D}|}\int_{\mathcal{D}} \mathbf{dx} \int_{-M}^{M} \mathrm{d}\xi\, p^{\star,E}_M(\xi,\mathbf{x}) \log p^{\star,E}_M(\xi,\mathbf{x}) \\
&= -\frac{1}{|\mathcal{D}|}\int_{\mathcal{D}} \mathbf{dx} \int_{-M}^{M} d\xi\, p^{\star,E}_M(\xi,\mathbf{x}) \left\{ \left(h^{(M)} - \beta^{(M)} \frac{\psi(\mathbf{x})}{2} \right) \xi - \log M - \log Z^\star_M(\mathbf{x}) \right\} \\
&= \log M - \frac{1}{|\mathcal{D}|}\left(h^{(M)} X_{tot} - \beta^{(M)} E \right) + \frac{1}{|\mathcal{D}|}\int_{\mathcal{D}} \log Z^\star_M(\mathbf{x})\,.
\end{aligned}$$

The last equality is obtained using $\int_{-M}^{M} \mathrm{d}\,\xi\, p^{\star,E}_M(\xi,\mathbf{x}) = 1$ on one hand, and remembering that

$$\int_{\mathcal{D}} \mathbf{dx} \int_{-M}^{M} \mathrm{d}\xi\, p^{\star,E}_M(\xi,\mathbf{x}) = X_{tot} \text{ and } \int_{\mathcal{D}} \mathbf{dx} \int_{-M}^{M} \mathrm{d}\xi\, \frac{\psi}{2}\xi\, p^{\star,E}_M(\xi,\mathbf{x}) = E \text{ on the other hand.}$$

The asymptotic development of $\log Z^\star_M(\mathbf{x})$ for large M now yields

$$\log Z^\star_M(\mathbf{x}) \underset{M\to\infty}{=} \log\{2+\int_{-1}^{1} d\xi \frac{\xi^2}{2M^2}\left(h^\star-\beta^\star\frac{\psi(\mathbf{x})}{2}\right)^2+o\left(\frac{1}{M^2}\right)\}$$
$$\underset{M\to\infty}{=} \log 2+\frac{1}{6M^2}\left(h^\star-\beta^\star\frac{\psi(\mathbf{x})}{2}\right)^2+o\left(\frac{1}{M^2}\right). \quad (95)$$

Therefore,

$$\int_{\mathcal{D}}\mathbf{dx}\,\log Z^\star_M(\mathbf{x}) \underset{M\to\infty}{=} |\mathcal{D}|\log 2+\frac{1}{2M^2}\left(h^\star X_{tot}-\beta^\star E\right)+o\left(\frac{1}{M^2}\right). \quad (96)$$

From Equation (95) and Equation (96), we finally obtain (63).

B.2 Deriving the (helical) critical macrostate entropies in the high energy regime.

For the full problem in the case of a non-vanishing poloidal energy, recall that the critical distributions $p^\star_M$ are given by Equation (72) and the scaling of the Lagrange multipliers by Equation (82). In addition to the reduced Lagrange multipliers defined in (82), we also define $\alpha^\star_k=\lim_{M\to\infty}M^2(\alpha^{(M)}_k-\alpha_k)$.

It is useful to express the Lagrange multipliers $h^\star_k$ and α_k in terms of the constraints. It is easily obtained from Equation (69) and Equation (72) that

$$A_k=|\mathcal{D}|\frac{\exp\alpha_k}{\sum_{k'=1}^K\exp\alpha_{k'}} \quad\text{and}\quad X_k=\frac{A_k h^\star_k}{3}-\frac{\beta A_k}{6|\mathcal{D}|}\int_{\mathcal{D}}\mathbf{dx}\,\psi(\mathbf{x}), \quad (97)$$

from which it follows that $\alpha_k=\log\frac{A_k}{|\mathcal{D}|}$ – up to an unphysical constant that can be absorbed in the partition function – and $\frac{X_{tot}}{|\mathcal{D}|}-\frac{X_k}{A_k}=\frac{1}{3}\left(\overline{h^\star_k}-h^\star_k\right)$.

The critical points of the macrostate entropy then read

$$\mathcal{S}_M[p^\star_M]=-\frac{1}{|\mathcal{D}|}\int_{\mathcal{D}}\mathbf{dx}\sum_{k=1}^K\int_{-M}^{M}\mathrm{d}\xi\,p^\star_{M,k}(\xi,\mathbf{x})\log p^\star_{M,k}(\xi,\mathbf{x})$$
$$=-\frac{1}{|\mathcal{D}|}\int_{\mathcal{D}}\mathbf{dx}\sum_{k=1}^K\int_{-M}^{M}d\xi\,p^\star_{M,k}(\xi,\mathbf{x})\left\{\alpha^{(M)}_k-\beta^{(M)}\frac{\sigma_k^2}{4y}\right. \quad (98)$$
$$\left.+\left(h^{(M)}_k-\beta^{(M)}\frac{\psi(\mathbf{x})}{2}\right)\xi-\log M-\log Z^\star_M(\mathbf{x})\right\}$$
$$=\log M-\frac{1}{|\mathcal{D}|}\left(\sum_{k=1}^K\alpha^{(M)}_k A_k+\sum_{k=1}^K h^{(M)}_k X_k-\beta^{(M)}E\right)+\frac{1}{|\mathcal{D}|}\int_{\mathcal{D}}\log Z^\star_M(\mathbf{x}). \quad (99)$$

The last equality is obtained using $\int_{-M}^{M}\mathrm{d}\,\xi\,p^{\star,E}_M(\xi,\mathbf{x})=1$ on one hand, and using Equation (69) to compute A_k, X_k, and E on the other hand. The asymptotic development of $Z^\star_M(\mathbf{x})$ for large M then yields

$$Z^\star_M(\mathbf{x}) \underset{M\to\infty}{=} 2\sum_{k=1}^K e^{\alpha_k}\{1+\frac{1}{M^2}\left[\alpha^\star_k-\beta^\star\frac{\sigma_k^2}{4y}+\frac{1}{6}\left(h^\star_k-\beta^\star\frac{\psi(\mathbf{x})}{2}\right)^2\right]+o\left(\frac{1}{M^2}\right)\}. \quad (100)$$

Hence,

$$\int_{\mathcal{D}} \mathbf{dx}\, \log Z^\star_M(\mathbf{x}) \underset{M\to\infty}{=} |\mathcal{D}| \log 2 + \frac{1}{M^2}\left\{ |\mathcal{D}|\, \overline{\alpha^\star_k} - \beta^\star E^\star_{tor} + \frac{1}{2}\sum_{k=1}^{K} h^\star_k X_k - \frac{\beta^\star}{2} E_{pol} \right\} + o\left(\frac{1}{M^2}\right). \quad (101)$$

From (101) and (99), we finally obtain

$$\mathcal{S}_M[p^\star_M] \underset{M\to\infty}{=} \log 2M - \sum_{k=1}^{K} \frac{A_k}{|\mathcal{D}|} \log \frac{A_k}{|\mathcal{D}|} + \frac{1}{2\,|\mathcal{D}|\,M^2}\left(\beta^\star E_{pol} - \sum_{k=1}^{K} h^\star_k X_k\right) + o\left(\frac{1}{M^2}\right), \quad (102)$$

and equivalently the expression (81).

C Maximizers of the macrostate entropy for the non-helical poloidal problem.

The constraints E and X_{tot} being prescribed, we want to determine the values of $h^\star$ and $\beta^\star$ which minimize the poloidal macrostate entropy (48). We start from Equation (63). We want to determine which among the critical distributions achieve the maximum of the macrostate entropy, when M is large. In the next paragraphs, we will rather work with the reduced "neg-entropy" $D(\beta^\star, h^\star)$, whose minima are the maxima of the macrostate entropy :

$$D(\beta^\star, h^\star) \underset{\text{def}}{=} \lim_{M\to\infty} \{-2M^2\,|\mathcal{D}|\,\mathcal{S}^{pol}_M[p^\star_M] + \log 2M\} = (h^\star X_{tot} - \beta^\star E). \quad (103)$$

It is convenient to define some auxiliary functions :

$$f(z) = \sum_{l\ odd} \frac{(1|\phi_{0l})^2 \kappa^2_{0l}}{(\kappa^2_{0l} - z)}, \text{ and } \mathcal{F} = \frac{f^2}{f'}. \quad (104)$$

f is defined on $\mathbb{R} - \{\kappa^2_{0(2l+1)}, l \in \mathbb{N}\}$. $\mathcal{F}$ is defined continuously over $\mathbb{R}$ by taking $\mathcal{F}(\kappa_{0l}) = (1|\phi_{0l})^2\kappa^2_{0l} = 16\pi/|\mathcal{D}|$ for every odd value of l. Those functions are sketched on Figure 7. We can now relate $h^\star$ and $\beta^\star$ to E and X_{tot} for each kind of solutions, in terms of f and F

For a continuum solution,

$$X_{tot} = \frac{h^\star}{3} f\left(\frac{-\beta^\star}{6}\right), \quad 2E = \frac{h^{\star 2}}{9} f'\left(\frac{-\beta^\star}{6}\right), \text{ and } X^2_{tot} = 2E\mathcal{F}\left(\frac{-\beta^\star}{6}\right). \quad (105)$$

For a mixed solution,

$$X_{tot} = \frac{h^\star}{3} f\left(\kappa^2_{k_0 l_0}\right), \quad 2E = p^2_{k_0 l_0}\kappa^2_{k_0 l_0} + \frac{h^{\star 2}}{9} f'\left(\kappa^2_{k_0 l_0}\right), \text{ and } X^2_{tot} \le 2E\mathcal{F}\left(\kappa^2_{k_0 l_0}\right). \quad (106)$$

For an odd eigenmode,

$$X^2_{tot} = 2E_0\kappa^2_{0l_0}(1|\phi_{0l_0})^2 = 2E_0\mathcal{F}\left(\kappa^2_{0l_0}\right). \quad (107)$$

It is clear from Figure 7 and Equations (105), (106) and (107) that we need to make a distinction between the cases $\frac{X^2_{tot}}{2E} > \mathcal{F}(\kappa^2_{01})$, $\frac{X^2_{tot}}{2E} = \mathcal{F}(\kappa^2_{01})$, and $\frac{X^2_{tot}}{2E} < \mathcal{F}(\kappa^2_{01})$.

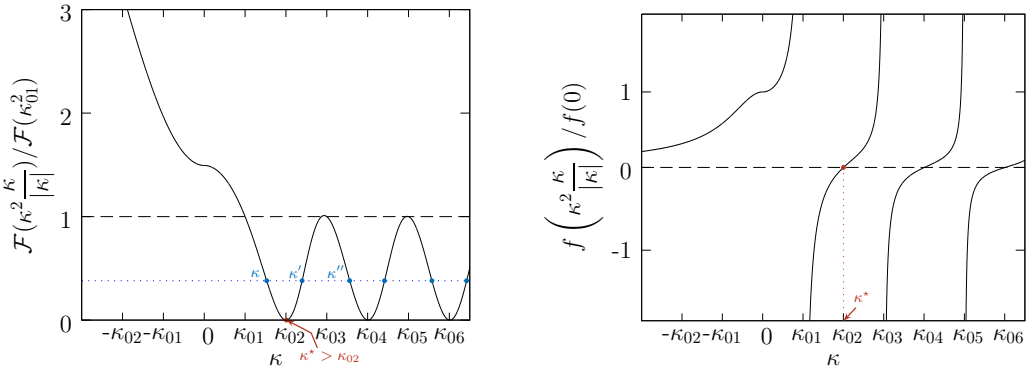

Figure 7: $\mathcal{F}$ and f as functions of κ. The minimum value $\kappa^\star$ for which both $\mathcal{F}$ and f are zero is greater than κ_{02}.

Case $\dfrac{X_{tot}^2}{2E} > \mathcal{F}(\kappa_{01}^2)$

In this case, the Lagrange multipliers $(h^\star, \beta^\star)$ are uniquely determined from the constraints. They describe a solution from the continuum, which is therefore the maximal entropy solution. From a practical point of view, there is a one to one correspondance between the value of $\beta^\star$ and the value of $\dfrac{X_{tot}^2}{2E}$ – see Figure 7. We can therefore write without ambiguity $\beta^\star = -6\mathcal{F}^{-1}\left(\dfrac{X_{tot}^2}{2E}\right)$.

If $\dfrac{X_{tot}^2}{2E} < \mathcal{F}(0)$, then $\beta^\star < 0$ and we define $\kappa(\beta^\star) = \sqrt{-\beta^\star/6}$. Otherwise, $\dfrac{X_{tot}^2}{2E} \geq \mathcal{F}(0)$, and $\beta^\star \geq 0$. We then define $\kappa(\beta^\star) = -\sqrt{\beta^\star/6}$. In both cases, $\kappa(\beta^\star) < \kappa_{01}$ and the other Lagrange multiplier is uniquely determined as $h^\star = \dfrac{3X_{tot}}{f\left(-\beta^\star/6\right)} = \dfrac{3X_{tot}}{f\left(\kappa^3/|\kappa|\right)}$.

Case $\dfrac{X_{tot}^2}{2E} < \mathcal{F}(\kappa_{01}^2)$

This case seems at first sight more intricated. First, there exist an infinite number of solutions from the continuum for which the constraints are satisfied. Indeed, for any odd value of l, there exist two values for the inverse temperature $\sqrt{-\beta^\star/6}$ in the interval $[\kappa_{0l}; [\kappa_{0l+2}[$ – denoted by κ and κ' on Figure 7. Second, there can exist an eigenvalue $\kappa_{k_0 l_0}^2$ associated to an eigenmode $\phi_{k_0 l_0}$ with $(1|\phi_{k_0 l_0}) = 0$ such that $\mathcal{F}(\kappa_{k_0 l_0}) > X_{tot}^2/2E$. In this case, there also exists a mixed solution associated to the eigenvalue $\kappa_{k_0 l_0}^2$ for which the constraints are satisfied.

The situation is however easily settled because the following result holds true. It is a non-trivial but fairly standard result [Chavanis and Sommeria, 1996].

Result C.1 *Between two solutions that satisfy the same constraints, the one associated with the lower value of $|\beta^\star|$ has the lower reduced neg-entropy – and hence achieves the higher macrostate entropy.*

From the latter result, we deduce that if $\kappa_{\min}$ denotes the smallest eigenvalue whose associated eigenfunction has a vanishing mean on the domain, then

- if $\mathcal{F}(\kappa^2_{\min}) \leq \dfrac{X^2_{tot}}{2E} < \mathcal{F}(\kappa^2_{01})$, the selected solution is the solution from the continuum with inverse temperature $-6\beta^\star = \kappa^2 < \kappa^2_{\min}$ and $h^\star = 3X_{tot}/f(\kappa^2)$ uniquely determined from (105).

- if $\dfrac{X^2_{tot}}{2E} \leq \mathcal{F}(\kappa^2_{\min})$, the selected solution is the mixed solution, with inverse temperature satisfying $-6\beta^\star = \kappa^2_{\min}$ and $h^\star = 3X_{tot}/f(\kappa^2_{\min})$ uniquely determined from (106).

What remains to show is that (C.1) actually holds true. This is what the next two paragraphs are devoted to.

Maxima of the macrostate entropy achieved by the continuum solutions. Let us first focus on the continuum solutions. Those solutions are uniquely determined by the value of the inverse temperature $\beta^\star$. Indeed, from Equation (105), and given a value $\beta^\star$ such that $\mathcal{F}\left(-\beta^\star/6\right) = \dfrac{X^2_{tot}}{2E}$, then $h^\star$ is uniquely determined as $h^\star = 3X_{tot}/f(-\beta^\star/6)$. Defining $\kappa(\beta^\star) = \sqrt{-\beta^\star/6}$, we can write the reduced neg-entropy of such a continuum solution as

$$D^{(c)}(\kappa(\beta^\star)) = 6\kappa(\beta^\star)^2 E + \frac{3X^2_{tot}}{f\left(\kappa(\beta^\star)^2\right)}. \tag{108}$$

Let us now define

$$\kappa = \min\{\kappa' \,\Big|\, \mathcal{F}\left(\kappa'^2\right) = \frac{X^2_{tot}}{2E}\}. \tag{109}$$

It is clear from Figure 7 that $\kappa \in [\kappa_{01}; \kappa^\star[$ where $\kappa^\star$ is the first zero of $\mathcal{F}$.
Then, κ also achieves the minimal value of the reduced entropy (108), namely

$$D^c\left(\kappa\right) = \min\{D^c\left(\kappa'\right) \,\Big|\, \mathcal{F}\left(\kappa'^2\right) = \frac{X^2_{tot}}{2E}\}. \tag{110}$$

To see this, let $\kappa'' > \kappa$ be such that $\mathcal{F}(\kappa''^2) = \mathcal{F}(\kappa^2) = \dfrac{X^2_{tot}}{2E}$.

- If $f(\kappa''^2) > 0$, then

$$D^{(c)}(\kappa) - D^{(c)}(\kappa'') = 6E\overbrace{\left(\kappa^2 - \kappa''^2\right)}^{<0} + 3X^2_{tot}\overbrace{\left(\frac{1}{f(\kappa^2)} - \frac{1}{f(\kappa''^2)}\right)}^{<0} < 0. \tag{111}$$

- Otherwise, let $\kappa' = \sup\{\kappa | \kappa < \kappa'' \text{ and } \mathcal{F}(\kappa^2) = \mathcal{F}(\kappa''^2)\}$. Then $f(\kappa'^2) > 0$ (see Figure 7), and

$$D^{(c)}(\kappa') - D^{(c)}(\kappa'') < 6E\Big(\kappa'^2 - \kappa''^2\Big) + 3X^2_{tot}\frac{\kappa''^2 - \kappa'^2}{\mathcal{F}(\kappa'^2)} \leq 0. \tag{112}$$

The first inequality of equation (112) is obtained by using Tayor inequality at first order and by noticing that $(1/f)' = -1/\mathcal{F}$, while the second inequality stems froms the fact that $X^2_{tot} = 2E\mathcal{F}(\kappa'^2) = 2E\mathcal{F}(\kappa''^2)$. Therefore,

$$D^{(c)}(\kappa) - D^{(c)}(\kappa'') = D^{(c)}(\kappa) - D^{(c)}(\kappa') + D^{(c)}(\kappa') - D^{(c)}(\kappa'') < 0. \tag{113}$$

Maxima of the macrostate entropy for continuum and mixed solutions. Let us now determine whether mixed solutions can achieve a higher macrostate entropy than solutions from the continuum for the same prescribed contraints. Consider for instance a mixed solution associated to the eigenvalue $\kappa_0^2 = \kappa_{k_0 l_0}^2$. Equation (106) tells that this solution exists provided $X_{tot}^2 \leq 2E\mathcal{F}(\kappa_0^2)$. Let us suppose this is the case. For this solution, the Lagrange multipliers are then uniquely determined as $\beta^\star = -6\kappa_0^2$, and $h^\star = \dfrac{3X_{tot}}{f\left(\kappa_0^2\right)}$. The corresponding reduced neg-entropy reads

$$D^{(m)}(\kappa_0) = 6\kappa_0^2 E + 3\frac{X_{tot}^2}{f(\kappa_0^2)}. \tag{114}$$

We know from the previous paragraph, that the minimum of $D^{(c)}(\kappa')$ is achieved for some $\kappa \in [\kappa_{01}; \kappa_\star[$ which is uniquely determined. We therefore need to compare $D^{(c)}(\kappa)$ and $D^{(m)}(\kappa_0)$.

- If $\kappa_0 > \kappa_\star$, then inequalities similar to the inequalities (111) and (112) yield $D^{(c)}(\kappa) < D^{(m)}(\kappa_0)$, so that the continuum solution f has a lower reduced neg-entropy and hence a higher macrostate entropy than the mixed solution.
- Otherwise, we need to have $\kappa_0 < \kappa < \kappa^\star$ in order for both solutions to exist. Then,

$$D^{(m)}(\kappa_0) - D^{(c)}(\kappa) \leq 6E\left(\kappa_0^2 - \kappa^2\right) + 3X_{tot}^2\frac{\kappa^2 - \kappa_0^2}{\mathcal{F}(\kappa^2)} < 0, \tag{115}$$

  and the mixed solution has a lower reduced neg-entropy than any solution from the continuum that correspond to the same values of E and X_{tot}.

Similar inequalities show that when two mixed solutions can coexist, it is the one associated with the lower value of κ that also achieves the higher macrostate entropy.

This concludes the proof of (C.1).

Case $\dfrac{X_{tot}^2}{2E} = \mathcal{F}(\kappa_{01}^2)$

On this parabola, the only solutions that can exist are mixed solutions and pure odd mode solutions. For the odd eigenmodes, $h^\star = 0$, the reduced entropy simply reads $D^{(o)}(\kappa_{0l}) = 6E\kappa_{0l}^2$. It is then clear, that the eigenmode with the lowest value of $D^{(o)}$ is the gravest mode κ_{01}.

One can also notice that $D^{(c)}(\kappa_{01}+\epsilon) \underset{\epsilon\to 0}{\to} D^{(o)}(\kappa_{01})$. We can then extend by continuity Inequality (115), so that if there also exists a mixed solution on the parabola $\dfrac{X_{tot}^2}{2E} = \mathcal{F}(\kappa_{01}^2)$, it is the gravest odd mode that solves the extremization problem.

Conclusion

We can now conclude the discussion. Recall that $\kappa_{\min}$ denotes the smallest eigenvalue with vanishing mean on the domain. Note that $\kappa_{\min}$ is lower than the first zero of $\mathcal{F}$ (see Figure 7).

- For $X_{tot}^2 > 2E\mathcal{F}(\kappa_{01}^2)$, the selected solution is a continuum solution, with $\kappa < \kappa_{01}$ uniquely determined by E and X_{tot}.
- For $X_{tot}^2 = 2E\mathcal{F}(\kappa_{01}^2)$, the selected solution is the gravest eigenmode κ_{01}^2.

- For $2E\mathcal{F}(\kappa^2_{01}) > X^2_{tot} \geq 2E\mathcal{F}(\kappa^2_{\min})$, the selected solution is the one from the continuum associated to the value $\kappa^2_{01} < \kappa^2 \leq \kappa^{\star 2}$.
- For $2E\mathcal{F}(\kappa^2_{\min}) \geq X^2_{tot}$ the selected solution is the mixed solution associated to the eigenvalue $\kappa^2_{\min}$.

References

[Abarbanel et al., 1986] Abarbanel, H. D., Holm, D. D., Marsden, J. E., and Ratiu, T. S. (1986). Nonlinear stability analysis of stratified fluid equilibria. *Philosophical Transactions of the Royal Society of London. Series A, Mathematical and Physical Sciences*, 318(1543):349–409.

[Abramowitz and Stegun, 1965] Abramowitz, M. and Stegun, I. A. (1965). Handbook of Mathematical Functions with Formulas, Graph, and Mathematical tables. *Applied Mathematics Series*, 55:1046.

[Bouchet and Corvellec, 2010] Bouchet, F. and Corvellec, M. (2010). Invariant measures of the 2D Euler and Vlasov equations. *Journal of Statistical Mechanics: Theory and Experiment*, 2010:P08021.

[Bouchet and Venaille, 2011] Bouchet, F. and Venaille, A. (2011). Statistical mechanics of two-dimensional and geophysical flows. *Arxiv preprint arXiv:1110.6245*.

[Chavanis and Sommeria, 1996] Chavanis, P. and Sommeria, J. (1996). Classification of self-organized vortices in two-dimensional turbulence: the case of a bounded domain. *Journal of Fluid Mechanics*, 314:267–298.

[Chavanis and Sommeria, 1998] Chavanis, P. and Sommeria, J. (1998). Classification of robust isolated vortices in two-dimensional hydrodynamics. *Journal of Fluid Mechanics*, 356:259–296.

[Cover et al., 1994] Cover, T. M., Thomas, J. A., and Kieffer, J. (1994). Elements of information theory. *SIAM Review*, 36(3):509–510.

[Dong, 2007] Dong, S. (2007). Direct numerical simulation of turbulent taylor-couette flow. *Journal of Fluid Mechanics*, 587:373.

[Ellis et al., 2004] Ellis, R., Jordan, R., Otto, P., and Turkington, B. (2004). A statistical approach to the asymptotic behavior of a class of generalized nonlinear Schrödinger equations. *Communications in mathematical physics*, 244(1):187–208.

[Ellis, 1984] Ellis, R. S. (1984). Large deviations for a general class of random vectors. *The Annals of Probability*, 12(1):1–12.

[Ellis et al., 2000] Ellis, R. S., Haven, K., and Turkington, B. (2000). Large deviation principles and complete equivalence and nonequivalence results for pure and mixed ensembles. *Journal of Statistical Physics*, 101(5-6):999–1064.

[Eyink and Sreenivasan, 2006] Eyink, G. and Sreenivasan, K. (2006). Onsager and the theory of hydrodynamic turbulence. *Reviews of modern physics*, 78(1):87.

[Herbert et al., 2012] Herbert, E., Daviaud, F., Dubrulle, B., Nazarenko, S., and Naso, A. (2012). Dual local and non-local cascades in 3D turbulent Beltrami flows. *arXiv preprint arXiv:1206.5613*.

4.3 Addendum : a brief description of the two-dimensional inviscid equilibria from the Robert-Miller-Sommeria perspective.

For thoroughness, a brief and pedagogic description of the two-dimensional Euler inviscid equilibria from the Robert-Miller-Sommeria could be insightful. This description provides the opportunity to add a few words about microstates and macrostates, and make the discretization process alluded to in equation (P52) more precise and more visual. It is largely inspired from the original papers of Miller [Miller, 1990, Miller et al., 1992] and the more recent and pedagogical description of [Potters et al., 2013].

Inviscid Invariants in physical space. For simplicity, let us consider a two-dimensional rectangular domain $\mathcal{D}$, with size (L_x, L_z). We assume no-slip boundary conditions. We work with cartesian coordinates $\mathbf{r} = (x, z)$. The Casimir invariants in the two-dimensional case are then well known : any function of the vorticity field integrated over the domain $\mathcal{D}$ is conserved by the dynamics. Those invariants are akin to the toroidal Casimirs described in the axisymmetric case. In the special case where only a finite number of vorticity levels, say $\omega_1, .., \omega_K$ account for the initial vorticity distribution, the inviscid conservation of the Casimir invariants for two-dimensional flows is equivalent to the conservation of each one of the K areas $\mathcal{A}_k = \frac{1}{\mathcal{D}} \int_{\mathcal{D}} \mathrm{d}\mathbf{r} \mathbf{1}_{\omega(\mathbf{r})=\omega_k}$. As for the two-dimensional kinetic energy, which the inviscid dynamics also preserves, it can be written in terms of the Green-function G associated to the two-dimensional Laplacian $-\Delta$ as

$$\mathcal{E}[\omega] = \frac{1}{2} \int_{\mathcal{D}} \mathrm{d}\mathbf{r} \int_{\mathcal{D}} \mathrm{d}\mathbf{r}' \omega(\mathbf{r}) G(\mathbf{r}, \mathbf{r}') \omega(\mathbf{r}'). \tag{4.7}$$

Away from the boundary, $G(\mathbf{r}, \mathbf{r}') \propto \log |\mathbf{r} - \mathbf{r}'|/R_0$, with R_0 a prescribed length.

Discretization and microcanonical ensemble. To build a microcanonical measure, we proceed exactly as described in paragraph §2.3 of the paper. We discretize the physical domain $\mathcal{D}$ onto a $N \times N$ lattice, with mesh L_x/N and L_z/Nalong the x and z direction, and consider a discretization of the vorticity field $\omega_N = \omega_{N,ij}$ over the lattice. We then define the discrete areas $\mathcal{A}_k$ and the energy $\mathcal{E}$ as

$$\mathcal{A}_k[\omega_N] = \frac{|\mathcal{D}|}{N^2} \sum_{(i,j)\in[\![1;N]\!]^2} \mathbf{1}_{\omega_{N,ij}=\omega_k} \quad \text{and} \quad \mathcal{E}[\omega_N] = \frac{|\mathcal{D}|}{2N^4} \sum_{\substack{(i,j)\in[\![1;N]\!]^2 \\ (i',j')\in[\![1;N]\!]^2}} \omega_{N,ij}\omega_{N,i'j'} G_{iji'j'}. \tag{4.8}$$

$G_{iji'j'}$ is a discretized version of $G(\mathbf{r}, \mathbf{r}')$. For prescribed values of the areas and the energy, a N-dependent microcanonical measure is then easily built. It is defined as the uniform measure over the (finite) set of lattice configurations ω_N, such that (i) the number of lattice sites occupied by each vorticity level ω_k is exactly $N_k = N^2 A_K/\mathcal{D}$, and (ii) the discretized energy $\mathcal{E}[\omega_N]$ takes a value between E and $E + \Delta E$. The number of such configurations defines a microcanonical "volume", $\Omega_N(E, \{A_k\})$. The microcanonical measure is then defined by taking the large $N \to \infty$ limit of the N-dependent micro-

canonical averages, as described in equation (P22) – but without the need to introduce a cutoff M. To describe this limit, we basically need to estimate the large N limit of the microcanonical volume $\Omega_N(E, \{A_k\})$.

Coarse-graining and macrostates. How do we estimate $\Omega_N(E, \{A_k\})$? One way to answer this is to straightforwardly generalize equations (P43), (P52) and (P53). Let us, however try to be more pedagogic and do some elementary counting. As explained in the paper, a fundamental concept to estimate ω_N is the concept of macrostate distribution, which is defined through a coarse-graining procedure. Let us make the coarse-graining process explicit. It is obtained by grouping together assemblies of contiguous $n \times n$ lattice sites into N_b^2 blocks, so that $n \times N_b = N$ [(a)]. The process is made visually explicit on Figure 4.4.
Let us write $\mathbf{r}_B$ the central position of a given block B. Each one of the block B is made of n^2 lattice sites. We now uniformly randomly and independently assign one of the K vorticity value $\omega_1 ... \ \omega_K$ to each one of the N^2 lattice site, and write n_K^B the number of lattice sites belonging to the block B on which the vorticity is equal to ω_K. The K empirical frequencies $(n_1^B/n^2, ..., n_K^B/n^2)$ define an empirical probability distribution p_{n,N_b}^B for the block B. The collection of those N_b^2 probability distribution define an empirical macrostate p_{n,N_b}. It is "visually" clear, that if we let $n \to \infty$ at fixed N_b and subsequently let $N_b \to \infty$, one can define a local probability $p_k(\mathbf{r})\mathrm{d}\mathbf{r}$ that the vorticity takes value ω_k in an infinitesimal area $\mathrm{d}\mathbf{r}$ around the position $\mathbf{r}$, anywhere on the domain. The collection of those local probability functions $(p_1 ... p_K)$ defines one –continous– macrostate p – see Figure 4.4.

Entropy of a macrostate. For each block B, the number of microscopic configurations that corresponds to an empirical probability distribution $p_{n,N_b}^B = (n_1^B/n^2, ..., n_K^B/n^2)$ is given by the ratio $\dfrac{n^2!}{\prod_{k=1}^K n_k^B!}$. Hence, the number of microscopic configurations which share a same prescribed empirical macrostate p_{n,N_b} is then simply

$$\sharp_{n,N_b}^p = \prod_{B=1}^{N_b^2} \frac{n^2!}{\prod_{k=1}^K n_k^B!}. \tag{4.9}$$

We take the logarithm of this number and divide it by $N^2 = N_b^2 n^2$ to define the entropy $S_{n,N_b}[p]$ of the empirical macrostate p_{n,N_b} : [(b)]

$$S_{n,N_b}[p] = \frac{1}{N^2} \log \sharp_{n,N_b}^p = -\frac{1}{N_b^2} \sum_{B=1}^{N_b^2} \sum_{k=1}^{K} \frac{n_K^B}{n^2} \log \frac{n_K^B}{n^2}. \tag{4.10}$$

We then define the entropy $S[p]$ of a macrostate p as $S[p] = \lim_{N_b \to \infty} \lim_{n \to \infty} S_{n,N_b}[p]$. Taking the limit $n \to \infty$ (with N_b kept fixed) allows us to liberally substitute the ratios $\dfrac{n_K^B}{n^2}$

[(a)] Without loss of generality, and to avoid blocks composed of solitary cells, we can restrict ourselves to the case where both N, n and N_b are powers, and only consider say dyadic or triadic discrete lattices.

[(b)] The empirical macrostate entropy can be alternatively thought of as an "entropy per spin". This explains why the definition involves a factor $1/N^2$.

by the distributions $p_K(\mathbf{r}_B)$. The limit N_b is carried out by replacing the (2D) Riemann sum $\frac{1}{N_b^2}\sum_{B=1}^{N_b^2}$ by the integral $|\mathcal{D}|^{-1}\int_{\mathcal{D}}\mathbf{dr}$.

The computation of those two limits yields the following expression

$$S[p] = -\frac{1}{|\mathcal{D}|}\int_{\mathcal{D}}\sum_{k=1}^{K}\mathbf{dr}\, p_k(\mathbf{r})\log p_k(\mathbf{r}), \tag{4.11}$$

that we interpret as the entropy of a macrostate. We have therefore pedagogically justified the use of equation (P40).

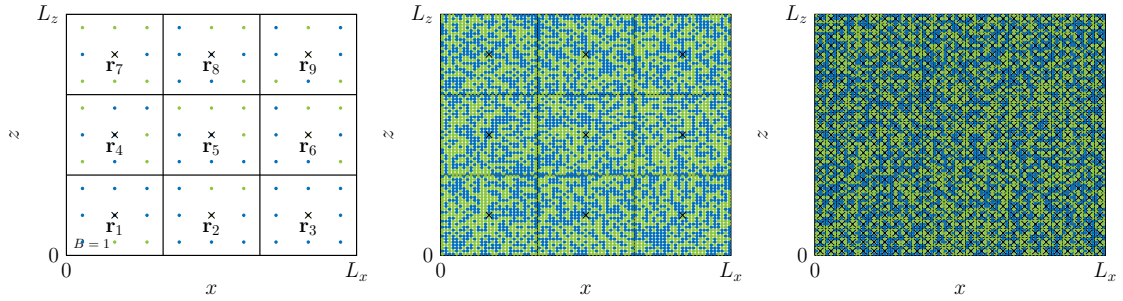

(a) $N_b = 3, n = 9$ **(b)** $N_b = 3$, "$n \to \infty$" **(c)** "$N_b \to \infty$", "$n \to \infty$"

Figure 4.4: An illustration of the coarse-graining procedure, for the case where the vorticity value can only take two values, say -1 (•) and +1 (•). We can illustrate some notations with figure (a) . It contains $N_b^2 = 9$ boxes, labelled from $B = 1$ to $B = 9$, whose central positions r_i are indicated. If we count the number of blue and green dots in the box $B = 1$, one finds $n_{\bullet}^1 = 7$ and $n_{\bullet}^1 = 2$. We therefore compute $p_{3,3}^1 = (7/9, 2/9)$.

Energy and areas of a macrostate. We define the area and the energy of a macrostate p accordingly to equations (P41) and (P50) :

$$\begin{aligned}\mathcal{A}_k[p] = \frac{1}{|\mathcal{D}|}\int_{\mathcal{D}}\mathbf{dr}\, p_k(\mathbf{r}), \quad \text{and} \quad \mathcal{E}[p] = \frac{1}{2}\int_{\mathcal{D}}\mathbf{dr}\,\psi(\mathbf{r})\sum_{k=1}^{K}\omega_k p_k(\mathbf{r}) \\ \text{where} \quad \psi(\mathbf{r}) = \int_{\mathcal{D}}\mathbf{dr}' G(\mathbf{r},\mathbf{r}')\sum_{k=1}^{K} p_k(\mathbf{r}')\omega_k.\end{aligned} \tag{4.12}$$

As noticed in (P52), while the areas associated to a corresponding a microscopic configuration and the areas associated to a macrostate do coincide, such is not exactly the case for the energy but we can show that $\mathcal{E}[\omega_N] = \mathcal{E}[p] + O\left(\frac{1}{N_b^2}\right)$. A rather technical justification of this claim can be found in the last paragraph of the section.

Most probable macrostate. From these two observations, we can now estimate the phase space volume $\Omega_N(E, \{A_k\})$. The latter is dominated by the microscopic configurations whose corresponding macrostate achieves the highest macrostate entropy under

the constraints of prescribed macrostate energy and macrostates areas, namely

$$\frac{1}{N^2}\log \Omega_N E, \{A_k\} = \sup_p \{S[p] | \mathcal{E}[p] = E \text{ and } \forall k\, \mathcal{A}_k[p] = A_k\}. \tag{4.13}$$

The critical points of the macrostate entropy are reached by the macrostates $p^\star$ such that

$$\begin{aligned} p_k^\star(\mathbf{r}) &= \mathcal{Z}(\mathbf{r})^{-1} \exp\left\{-\frac{\beta}{2}\psi\omega_k + \alpha_k\right\}, \quad \text{with} \quad \mathcal{Z}(\mathbf{r}) = \sum_{k=1}^{K} \exp\left\{-\frac{\beta}{2}\psi\omega_k + \alpha_k\right\}, \\ E &= -\frac{\partial \log \mathcal{Z}}{\partial \beta}, \quad \text{and} \quad A_k = \frac{\partial \log \mathcal{Z}}{\partial \alpha_k}. \end{aligned} \tag{4.14}$$

The mean-field equation is more complicated than its axisymmetric counterpart. It reads

$$-\Delta\psi = \langle\omega\rangle = \frac{\sum_{k=1}^{K} \omega_k \exp\left\{-\frac{\beta}{2}\psi\omega_k + \alpha_k\right\}}{\sum_{k=1}^{K} \exp\left\{-\frac{\beta}{2}\psi\omega_k + \alpha_k\right\}}. \tag{4.15}$$

This differential equation has been studied quite extensively since the initial work of Miller and Robert and Sommeria, [Miller, 1990, Robert and Sommeria, 1991, Miller et al., 1992]. Its solutions are highly non-trivial. The low-energy limit ($\psi \to 0$), also known as a strong mixing limit, was considered for instance in [Chavanis and Sommeria, 1996]. In this limit, the equation becomes linear. β is then prescribed by the value of the smallest eigenvalue of minus the Laplacian the domain. If the latter eigenvalue is non-degenerate, the typical state is then a large scale jet. When considering higher energies, or when additional invariants such as the momentum or the total circulation are not zero non trivial thermodynamic transitions towards jets or dipolar flows can occur. Such transitions have been investigated both theoretically [Chavanis and Sommeria, 1996, Chavanis and Sommeria, 1998, Bouchet and Barre, 2005] and numerically [Whitaker and Turkington, 1994, Turkington and Whitaker, 1996, Potters et al., 2013].

A technical justification that $\mathcal{E}[\omega_N] = \mathcal{E}[p] + O\left(\frac{1}{N_b^2}\right)$.

Proof : We start from the expression of the microscopic energy as given by equation (4.8). Let us write $J_{BB'}$ a discretization of the Laplacian over the $N_b \times N_b$ lattice obtained by considering the central positions $\mathbf{r}_B$ of each box B. Let us first relabel each site of the lattice, as (B, i, j) where the two coordinates (i, j) from 1 to n and the label B of the box the lattice belongs to run from 1 to N_b^2. The value of the vorticity field at position (B, i, j) is now written $\omega^B_{N,i,j}$. The discretization of the Green function on the microscopic lattice is now written as $G^{BB'}_{iji'j'}$. It is just a change of labels to recast the microscopic energy (4.8) as

$$\mathcal{E}[\omega_N] = \frac{|\mathcal{D}|}{2N^4} \sum_{(B,B')\in[\![1;N_b]\!]^2} \sum_{\substack{(i,j)\in[\![1;n]\!]^2 \\ (i',j')\in[\![1;n]\!]^2}} G^{BB'}_{iji'j'} \omega^B_{N,ij} \omega^B_{N,i'j'}. \tag{4.16}$$

Let us first identify the energy of the empirical macrostate energy as

$$\mathcal{E}[p_{n,N_b}] = \frac{|\mathcal{D}|}{2N_b^4} \sum_{B \neq B'} G^{BB'} \frac{1}{n^4} \sum_{i,j,i',j'} \omega^B_{N,ij} \omega^B_{N,i'j'}. \tag{4.17}$$

The coefficients i, j, i', j' run from 1 to N; B and B' run from 1 to N_b^2. Upon taking the two limits $n \to \infty$ and $N_b \to \infty$ subsequently, glibly identifying the sums $n^{-2} \sum_{i,j} \omega^B_{N,i'j'}$ with the coarse grained field $\langle \omega(\mathbf{r}_B) \rangle = \sum_{k=1}^K p_k(\mathbf{r}) \omega_k$, and generously substituting the Riemann sum $N_b^{-4} \sum_{B \neq B'}$ by the integral $\frac{1}{|\mathcal{D}|^2} \int_{\mathcal{D}^2} \mathbf{d}\mathbf{r}\mathbf{d}\mathbf{r}'$, one can remark that the empirical macrostate energy gives the correct macrostate energy (4.12).

Let us now show how to bound the quantity $\Delta_{n,N_b} = \mathcal{E}[\omega_N] - \mathcal{E}[p_{n,N_b}]$. We compute Δ_{n,N_b} as

$$\Delta_{n,N_b} = \underbrace{\frac{|\mathcal{D}|}{2N_b^4} \sum_B \frac{1}{n^4} \sum_{i,j,i',j'} G^{BB}_{iji'j'} \omega^B_{N,ij} \omega^B_{N,i'j'}}_{①} + \underbrace{\frac{|\mathcal{D}|}{2N_b^4} \sum_{B \neq B'} \frac{1}{n^4} \sum_{i,j,i',j'} \omega^B_{N,ij} \omega^{B'}_{N,i'j'} \left\{ G^{BB'}_{iji'j'} - G^{BB'} \right\}}_{②}. \tag{4.18}$$

.

The term ① can be bounded as $|①| \leq \frac{|\mathcal{D}| \sup_{k \in [\![1;K]\!]} |\omega_k|^2}{2N_b^4} \sum_B \frac{1}{n^4} \sum_{i,j,i',j'} |G^{BB}_{iji'j'}|$. If N_b is chosen to be large enough, we can bound $\frac{1}{n^4} \sum_{i,j,i',j'} |G^{BB}_{iji'j'}|$ by a term of the kind $\int_{\mathcal{D}_\epsilon} \mathbf{d}\mathbf{r}\mathbf{d}\mathbf{r}' |G_{\mathbf{r},\mathbf{r}'}|$. The latter integration runs over a disk $\mathcal{D}_\epsilon$ whose radius can be chosen as small as wanted, provided that N_b is large enough. Switching to polar coordinates, one observes that the integral converges. Hence, the first term is at most of order $1/N_b^2$. Assuming the discrete Green functions to depend only on the distances between the grid lattice sites, and upon using a triangular inequality, one can bound ② in a similar way. We conclude, that $|\Delta_{n,N_b}| \leq A \sup_{k \in [\![1;K]\!]} |\omega_k|^2 / N_b^2$, as was claimed. [(a)] ■

[(a)] The present justification implies that one should rather replace the term $O(N_b^{-2})$ by a term $O(M^2 N_b^{-2})$ add a M^2 term in equation (P52). This doesn't change much, though, as in the axisymmetric case, the limit $M \to \infty$ is taken only after the mean field arguments are advocated.

Chapter 5

Magnetohydro and axisymmetric Monte Carlo dynamics.

In the present chapter, a Microcanonical "Creutz" Monte-Carlo algorithm is devised and used, which highlights the axisymmetric equilibria described in the previous chapter, and allows for further comments on the limit $M \to \infty$ of infinitely fluctuating poloidal fields. The discussion is then extended to two-dimensional magneto-hydro fluids. From a lattice-model point of view, the magneto-hydro equilibria are more complicated than the axisymmetric equilibria as they involve an interplay between a long-range Energy (the kinetic energy) and a short-range one (the magnetic energy). A simplified two-level "MHD Ising model" is used to illustrate this interplay, and discuss the properties of the relevant statistical magneto-hydro equilibria from a completely microcanonical perspective. The equilibrium regimes which we find are consistent with those previously obtained in [Jordan and Turkington, 1997] and [Weichman, 2012].

Contents

5.1 Introduction.

Issues. It is not so clear whether the axisymmetric microcanonical measures which we described in the previous chapter can account for "real life" dynamics. Numerical simulations of ideal fluids typically only conserve quadratic invariants ; real flows are rarely axisymmetric and even more rarely ideal. From this perspective, both axisymmetric flows and their associated microcanonical measures involving all the axisymmetric ideal invariants seem to be at best purely conceptual issues. We can however reverse the issue and consider specific dynamics built in to be described by axisymmetric micronanonical measures. Examples of such dynamics can be provided by random Metropolis-Creutz flows – defined below. The use of such random flows will allow us to check the accuracy of the theoretical construction of the previous chapter and get more practical. Such random dynamics were recently used to sample numerically the microcanonical measures of inviscid two-dimensional flows [Potters et al., 2013].

Another pending question of Chapter 4 was whether our construction of axisymmetric measures could be extended to the less confidential case of two-dimensional magneto-fluids. If no cross-helicity is included, the generalization is straightforward. In the general case, it is not so clear. Metropolis flows will allow us to comment on the similarities and differences between the axisymmetric and the magneto-hydro equilibrium regimes from a purely microcanonical point of view.

Layout. The chapter is organized as follows. First, we intuitively describe the Creutz algorithm. The description is illustrated by results from Monte-Carlo simulations of the well-known Ising model. We then use the Creutz algorithm to sample the microcanonical ensembles of a two-level "Axisymmetric Ising model", which allows us to highlight the axisymmetric microcanonical equilibrium regimes. Finally, we use the Creutz algorithm to investigate the properties of a helical two-level " MHD Ising Model", and discuss the statistical equilibria of two-dimensional ideal magneto-fluids from a microcanonical perspective.

5.2 The Creutz algorithm explained on an Ising Model.

In this section, I explain what the Creutz algorithm consists of, and illustrate its use with the landmark example of the two-dimensional (2D) Ising-model. I explain how the algorithm can be used to sample microcanonical measures, and estimate quantities such as microcanonical averages, microcanonical temperatures and so on. I illustrate the description with microcanonical Monte-Carlo simulations of the (2D) Ising-model using a Glauber dynamics. I compare those to standard canonical simulations of the 2D Ising model.

5.2.1 The Ising Model.

Description. "Ising-model" is almost a common noun in contemporary condensed-matter physics. However, to set some ideas, and also set some notations, let me first briefly describe the model.In its most simple, bidimensional, square-lattice version, the Ising model describes an assembly of N^2 "spins", dispatched on a regular $N \times N$ square lattice. Each lattice site contains a spin $\sigma_{\mathbf{i}}$, whose value is either -1 or $+1$. Each one of the 2^{N^2} spin configurations σ_N, has an energy $\tilde{\mathcal{E}}[\sigma_N] = -\sum_{\langle \mathbf{i},\mathbf{j} \rangle} \sigma_{\mathbf{i}}\sigma_{\mathbf{j}}$. The latter sum runs over the $2N^2$ lattice edges, so that only nearest neighboring spins directly interact with each other. In order to have a more hydrodynamical vision of the energy, we will rather normalize the energy of a configuration as $\mathcal{E}[\sigma_N] = 1 - \frac{1}{2N^2}\sum_{\langle \mathbf{i},\mathbf{j} \rangle} \sigma_{\mathbf{i}}\sigma_{\mathbf{j}}$. The energy now runs from 0 to 2. With this definition, $\mathcal{E}[\sigma_N]$ can naturally be interpreted as an energy per site, but it can also be interpreted as a discrete hydrodynamical energy in a domain $\mathcal{D} = [0;1]^2$, akin for instance to the two-dimensional kinetic energy described by Equation (4.8) in the previous chapter.

Ensembles. Let us write $\mathcal{G}_N$ the set of all 2^{N^2} lattice configurations – regardless of their energies – , and assign a probability weight to each one of the 2^{N^2} configurations in $\mathcal{G}_N$. Specific choices for the weighting yield different statistical ensembles.
The canonical ensemble corresponds to the choice

$$p_{N,\beta}(\sigma_N) = \frac{e^{-\beta N^2 \mathcal{E}[\sigma_N]}}{\mathcal{Z}_N(\beta)} \quad \text{with} \quad \mathcal{Z}_N(\beta) = \sum_{\sigma_N \in \mathcal{G}_N} e^{-\beta N^2 \mathcal{E}[\sigma_N]} \quad . \tag{5.1}$$

The microcanonical ensemble corresponds to the choice

$$p_{N,E}(\sigma_N) = \begin{cases} \dfrac{1}{\Omega_N(E)} & \text{if } E \leq \mathcal{E}[\sigma_N] \leq E + \delta E \\ 0 \quad \text{otherwise} \end{cases} \quad . \tag{5.2}$$

$\Omega_N(E)$ is here simply the number of lattice configurations whose energies lie between E and $E + \delta E$. Microcanonical and canonical averages $\langle\rangle_{N,E}$ and $\langle\rangle_{N,\beta}$ of observables $\mathcal{O}[\sigma_N]$ are then defined using the standard definitions of statistical mechanics [Khinchin, 1949, Tolman, 1938] as

$$\langle \mathcal{O} \rangle_{N,E} = \sum_{\sigma_N \in \mathcal{G}_N} \mathcal{O}[\sigma_N] p_{N,E}(\sigma_N). \quad \text{and} \quad \langle \mathcal{O} \rangle_{N,\beta} = \sum_{\sigma_N \in \mathcal{G}_N} \mathcal{O}[\sigma_N] p_{N,\beta}(\sigma_N). \tag{5.3}$$

Much work has been devoted to give exact expressions for those averages since Onsager's incidental remark at a 1948 conference at Cornell university that the mean magnetization per site had an exact expression [Montroll et al., 1963]. It is now well known, that in the canonical ensemble, the 2D square Ising model is exactly soluble [Baxter, 1982,Mussardo, 2010]. In the microcanonical ensemble, fewer analytical results exist, but the phase diagram of the Ising model is pretty much understood [Kastner, 2002]. Here, we want to compute those averages numerically.

5.2.2 Canonical Monte-Carlo sampling : the Metropolis algorithm.

Markov Chains. An other informal survey performed at the coffee room of the SPHYNX laboratory gives rise to another Pavlovian answer concerning canonical sampling : "So, you want to estimate canonical averages on your laptop, huh ? Well, this is something you learn at school ! You should use Markov Chains. And Monte Carlo methods. And check for the Metropolis algorithm," an anonymous SPHYNX head scientist would typically reply. Once again, the answer makes it clear. Canonical sampling is pretty conventional. It involves the use of Markov Chain Monte-Carlo (MCMC) methods. The basic idea is to implement a biased random walk in the space of configurations $\mathcal{G}_N$, say $\mathcal{C}_0 \to \mathcal{C}_1 \to \mathcal{C}_2 \to ...\mathcal{C}_i \to ...$ [(a)] trough a Markov Chain, whose stationary probability exists, is unique and precisely matches the canonical measure we want to sample. Canonical averages are then estimated by replacing the sum $\sum_{\sigma_N \in \mathcal{G}_N} \mathcal{O}[\sigma_N] p_{N,\beta}(\sigma_N)$ by a more manageable quantity of the kind $\dfrac{1}{n_{it}} \sum_{i=1}^{n_{it}} \mathcal{O}[\mathcal{C}_i]$, where n_{it} is the number of iterations of the Markov Chain.

Metropolis algorithms. To find such a Markov chain, it suffices to choose some transition probabilities $P\left(\mathcal{C}_i \to \mathcal{C}_{i+1}\right)$ which (i) make the Markov Chain irreducible [(b)] and (ii) satisfy the detailed balance condition :

$$p_{N,\beta}(\mathcal{C}_i) P\left(\mathcal{C}_i \to \mathcal{C}_{i+1}\right) = p_{N,\beta}(\mathcal{C}_{i+1}) P\left(\mathcal{C}_{i+1} \to \mathcal{C}_i\right). \tag{5.4}$$

Condition (ii) ensures the canonical distribution to be a stationary measure for the Markov Chain. Condition (i) ensures that it is the only one (see for instance [Landau and Binder, 2009] and references therein or [Wikipedia, 2013b]). Numerical implementations of such Markov Chains are now called Metropolis algorithms, an early implementation of which can be found in [Metropolis et al., 1953]. Algorithm 5.1 is a standard Metropolis algorithm that can be used to sample the canonical ensemble of an Ising model at positive temperature $1/\beta$.

[(a)] Here, "$\mathcal{C}_i$" denotes a configuration in $\mathcal{G}_N$

[(b)] This means that for any configurations $\mathcal{C}$ and $\mathcal{C}'$ the probability to obtain $\mathcal{C}'$ if you iterate the Markov Chain from $\mathcal{C}$ sufficiently long is non zero

Algorithm 5.1 (*Metropolis dynamics for the Ising model*)

(1) *(i)* *Pick any configuration* $\mathcal{C}_0$ *in* $\mathcal{G}_N$*.*

(ii) *Initialize* $i \leftarrow 0$

(2) *While* $i < n_{it}$

(i) *Pick a random configuration* $\mathcal{C}' \in \mathcal{G}_N$*.*

(ii) *Compute* $\delta E = \mathcal{E}[\mathcal{C}'] - \mathcal{E}[\mathcal{C}_i]$*.*

(iii) *- If* $\delta E < 0$*, then* $\mathcal{C}_{i+1} \leftarrow \mathcal{C}'$

- Else

- Pick a random number η *uniformly between 0 and 1.*

- - If $\eta < e^{-N^2 \beta \delta E}$*, then* $\mathcal{C}_{i+1} \leftarrow \mathcal{C}'$

- Else $\mathcal{C}_{i+1} \leftarrow \mathcal{C}_i$*.*

(iv) $i \leftarrow i + 1$

To fully specify the algorithm, it remains to choose how we pick at random the new configuration $\mathcal{C}'$ in step 2.i. A basic and simple choice is to consider so called "Glauber moves" [Landau and Binder, 2009]. The new configuration $\mathcal{C}'$ is then obtained from configuration $\mathcal{C}_i$ by picking at random a site (k, l) on the lattice, and switching $\sigma_{k,l}$ into $-\sigma_{k,l}$. More subtle choices are possible, but the discussion of their comparative advantages is clearly not the subject of the present chapter. Note, that in order to sample canonical ensembles at negative inverse temperatures $1/\beta$, step 2.iii of Algorithm 5.1 needs to be slightly altered. This yields Algorithm 5.2 – the step that has changed is step (iii) .

Algorithm 5.2 (*Metropolis dynamics for the Ising model at negative* β*.*)

(1) *(i)* *Pick any configuration* $\mathcal{C}_0$ *in* $\mathcal{G}_N$*.*

(ii) *Initialize* $i \leftarrow 0$

(2) *While* $i < n_{it}$

(i) *Pick a random configuration* $\mathcal{C}' \in \mathcal{G}_N$*.*

(ii) *Compute* $\delta E = \mathcal{E}[\mathcal{C}'] - \mathcal{E}[\mathcal{C}_i]$*.*

(iii) *- If* $\delta E > 0$*, then* $\mathcal{C}_{i+1} \leftarrow \mathcal{C}'$

- Else

- Pick a random number η *uniformly between 0 and 1.*

- - If $\eta < e^{-N^2 \beta \delta E}$*, then* $\mathcal{C}_{i+1} \leftarrow \mathcal{C}'$

- Else $\mathcal{C}_{i+1} \leftarrow \mathcal{C}_i$*.*

(iv) $i \leftarrow i + 1$

Numerical Illustration. For each one of the algorithms 5.1 and 5.2, we define one Monte-Carlo time $\tau_{m.c.}$ as N^2 iterations of step (2). On average, after one Monte-Carlo time, each

spin on the lattice has been considered once for a flipping. The use of algorithms 5.1 and 5.2 is illustrated on Figure 5.1 for a 64^2 Ising model in a doubly- periodic domain, sampled at three different temperatures. The initial configuration is taken to be the configuration where all the spins are $+1$.

5.2.3 Microcanonical Monte-Carlo sampling : the Creutz algorithm.

Creutz algorithm. To sample the microcanonical averages defined in equation (5.3), we remain in the MCMC framework. All we need to find is a way to implement a random walk on the set of configurations which samples the microcanonical measure $<>_{N,E}$. This means that we need to find "suitable" transition probabilities $P(\mathcal{C}_i \rightarrow \mathcal{C}_{i+1})$. We shall then need to alter step $(2).(iii)$ and possibly $(2).(ii)$ of the Metropolis algorithms to fit our needs.

A way to achieve such a sampling could be to prescribe a dynamics which automatically conserve E [Landau and Binder, 2009]. In the case of the Ising model, where the energy can only take discrete values, such a choice could be possible, although possibly slightly cumbersome to prescribe at a numerical level. Let us keep the possibility in mind for the future sections though. Another way to achieve the sampling is to allow for small fluctuations in the energy, and perform a random walk in the space of configurations whose energies $\mathcal{E}[\sigma_N]$ lie between, say E^- and E^+ with $E^- \leq E \leq E^+$. Such samplings were originally discussed by Michael Creutz back in the 1980's [Creutz, 1983, Creutz, 1985, Creutz, 1986]. The Metropolis algorithms are then easily adapted to yield Algorithm 5.3.

Algorithm 5.3 (*Creutz dynamics for the Ising model*)

(1) *(i)* *Pick a configuration $\mathcal{C}_0$ in $\mathcal{G}_N$ such that $E^- \leq \mathcal{E}[\mathcal{C}_0] \leq E^+$*

(ii) *Initialize $i \leftarrow 0$*

(2) *While $i < n_{it}$*

(i) *Pick a random configuration $\mathcal{C}' \in \mathcal{G}_N$.*

(ii) *Compute $\mathcal{E}[\mathcal{C}']$.*

(iii) *- If $E^- \leq \mathcal{E}[\mathcal{C}'] \leq E^+$, then $\mathcal{C}_{i+1} \leftarrow \mathcal{C}'$*

- Else $\mathcal{C}_{i+1} \leftarrow \mathcal{C}_i$

(iv) $i \leftarrow i + 1$

Just as in the canonical case, a standard low-level programing choice for step $(2).(i)$ is to consider Glauber moves in the space of lattice configurations. [(a)]

[(a)] In his original papers, Creutz advocates use of additional degrees of freedom to allow for fluctuations of the lattice energy. Those additional degrees of freedom are picturesquely interpreted as small "demons" or even "whole battalions" of demons, which carry with them little "sacks of energy". The demons hop from sites to sites on the lattice either deterministically or stochastically. They have the ability to allow the switch from one configuration to another by either giving some energy to the lattice if they carry enough in their bags, or storing some excess energy from the lattice if their bags are large enough. The whole process is done in such a way that the system {spins + bags of energy} is kept at constant energy. Creutz

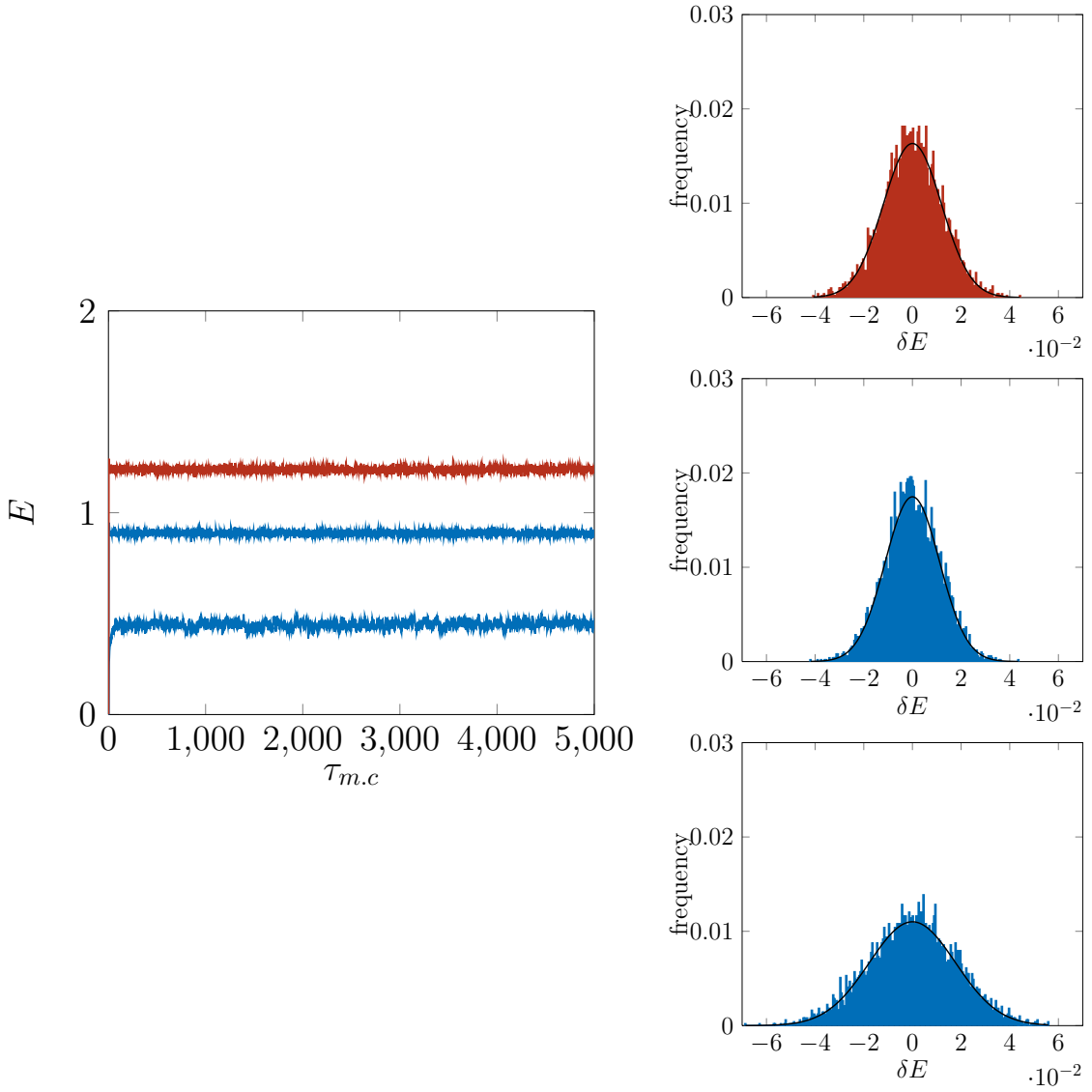

Figure 5.1: Left: evolution of the energy as a function of the Monte-Carlo time $\tau_{m.c.}$ for three Metropolis runs of the Ising model, with $N^2 = 64$ and $\beta = 0.40$, 0.10 – and -0.20 (–), from bottom to top. Right: the corresponding time distribution of the energy $\delta E = E - \langle E \rangle$. The histograms include the value of the energy samples every Monte-Carlo step from $\tau_{m.c} = 100$ to $\tau_{m.c} = 1000$. Negative β samplings are obtained with Algorithm5.2. Positive β samplings are obtained with Algorithm 5.1.

Stationary measures and microcanonical averages for the Creutz dynamics. At this stage questions that could legitimately be asked are : Does the Markov chain induced by Algorithm 5.3 converge towards a stationary measure? If yes, how must we choose E^- and E^+ so that averages computed using the Markov Chain match the averages computed within the true microcanonical ensemble ?
Quite clearly, Algorithm 5.3 is designed to sample a measure which weights equally all the configurations in $\mathcal{G}_N$ whose energies lie between E^- and E^+. Let us write p_{N,E^-,E^+} such a measure. It is quite obvious that the Markov Chain which the Algorithm 5.3 simulates satisfies a condition of detailed balance for the measure p_{N,E^-,E^+}. At any step i, both $\mathcal{E}[\mathcal{C}_i]$ and $\mathcal{E}[\mathcal{C}_{i+1}]$ lie between E^- and E^+. Hence, the transition probabilities satisfy $P(\mathcal{C}_i \to \mathcal{C}_{i+1}) = P(\mathcal{C}_{i+1} \to \mathcal{C}_i)$. Hence, p_{N,E^-,E^+} is a stationary measure of the Markov Chain.
A drawback of the algorithm is that p_{N,E^-,E^+} may not be the only stationary measure consistent with the detailed balance condition. In other words, it might very well be that the dynamics that we choose make the Creutz Markov Chain not irreducible. [(a)] It has to be considered as a working hypothesis, that the Creutz algorithm correctly samples p_{N,E^-,E^+}. This is probably the major drawback of the algorithm.

Link between p_{N,E^-,E^+} and $p_{N,E}$. Choice of E^- and E^+. We assume from now on that the Creutz dynamics correctly samples the measure p_{N,E^-,E^+}. How should E^- and E^+ be chosen so that averages computed through the Creutz dynamics are good estimators of the microcanonical averages $<>_{N,E}$? The answer turns out to depend on the local behavior of the Boltzmann entropy per site $S(E) = \lim_{N\to\infty} \frac{\log \Omega_N(E)}{N^2}$, and hence on the sign of the microcanonical inverse temperature $\beta(E)$, defined as

$$\beta(E) = \frac{\mathrm{d}S(E)}{\mathrm{d}E}. \tag{5.5}$$

Let us for instance consider the case a strictly positive β. In this case, the entropy S is locally an increasing function of the energy. This means that if N is large enough, most of the configurations whose energies are between E^- and E^+ have in fact an energy E^+. This is simply a consequence of Laplace method of steepest descent to estimate the number of configurations $\sharp(E^-, E^+)$ with energy between E^- and E^+ as

$$\sharp(E^-, E^+) = \int_{E^-}^{E^+} \mathrm{d}E\, \Omega_N(E) \underset{N\to\infty}{\simeq} (E^+ - E^-) e^{N^2 S(E^+)}. \tag{5.6}$$

In this case, it we take E^- small enough and $E^+ = E$, then computing averages from the Creutz dynamics allows to estimate the microcanonical averages. In practice, a small

argues that the fluctuations of energies within the sacks of the Demons then allows the measurement of the microcanonical temperature $\beta(E)$ – to be defined more explicitly in the next paragraphs. As noted in [Potters et al., 2013], the use of such demons is not really needed, and may lead to misleading interpretations, when the microcanonical temperatures are negative. In our use of Creutz algorithms, the demons are therefore exorcized .

[(a)] An easy way to see this, is to run the Creutz dynamics on a space of configuration made of three states $\mathcal{C}_1$, $\mathcal{C}_2$,$\mathcal{C}_3$ with $\mathcal{E}[\mathcal{C}_1] = \mathcal{E}[\mathcal{C}_3] = E$ $\mathcal{E}[\mathcal{C}_2] \neq E$ and only consider moves that allow to go from $\mathcal{C}_1$ to $\mathcal{C}_3$ only by transiting through $\mathcal{C}_2$. Then, if E^- and E^+ are chosen such that $\mathcal{E}[\mathcal{C}_2]$ is not within $[E^-; E^+]$, then the probability to reach $\mathcal{C}_2$ from $\mathcal{C}_1$ is 0. Hence, the Markov chain is not irreducible.

enough E^- means that we can crudely take $E^- = 0$. The case of a negative β is similar : in this case, the choice $E^- = E$ and $E^+ = +\infty$ ensures that averages computed through a Creutz dynamics yield an estimate of the microcanonical averages.

The practical morality is therefore the following : if you expect to sample a negative temperature state, set $E^- = E$ and $E^+ = +\infty$. On the contrary, if you expect to sample a positive temperature state, set $E^- = 0$ and $E^+ = E$. The next paragraph – combined with Figure 5.2 – explains how to measure the temperature $\beta(E)$.

Temperature Measurements The Creutz algorithm provides a ready-to-use microcanonical thermometer. It is very easy to measure microanonical temperatures from the time series of the energy. Let me explain this at a heuristic level. Let us suppose for instance that the sampled energy level E_0 has a positive microcanonical temperature, and that the values E^+ and E^- have been chosen as prescribed in the previous paragraph. If N is large enough, then the empirical frequency of observing a prescribed level of energy $E \lesssim E_0$ close to E_0, within a narrow band of energy $\mathrm{d}E$ should be close to the quantity [(a)] :

$$p_{E^+,E^-}(E)\mathrm{d}E = \frac{\Omega_N(E)\mathrm{d}E}{\int_0^E \Omega_N(\tilde{E})\mathrm{d}\tilde{E}} \simeq \frac{1}{E} e^{N^2(S(E)-S(E_0))}\mathrm{d}E \propto e^{-N^2\beta(E_0)(E_0-E)}\mathrm{d}E. \qquad (5.7)$$

Hence, the histogram of the quantity $\delta\mathcal{E}[\mathcal{C}_i] = E_0 - \mathcal{E}[\mathcal{C}_i]$ sampled say at every Monte Carlo step, should – for small $|\delta\mathcal{E}[\mathcal{C}_i]|$ – follow an exponential distribution with parameter $N^2\beta(E_0)$. In practice, the whole distribution is generally well fitted by an exponential distribution – see Figure 5.2 and subsequent examples. Hence, it suffices to measure the empirical average $\langle\delta E\rangle_{\text{emp}}$ of the time series of δE to deduce the inverse temperature $\beta(E_0)^{-1}$. In the case of the Ising model simulated with Glauber moves, the quantity $N^2\delta E$ can only take a discrete set of values $0, 1, 2, 3....$ Hence, the empirical frequency that $N^2\delta E$ takes the value k should be well approximated by the probability :

$$p(k) = \begin{cases} \left(1 - e^{-\beta(E_0)}\right) e^{-\beta(E_0)k} & \text{if } k \geq 0 \\ 0 \quad \text{otherwise} \quad . \end{cases} \qquad (5.8)$$

We conclude that $\beta(E_0) \simeq \log\left(1 + \dfrac{1}{N^2\langle\delta\mathcal{E}\rangle_{\text{emp}}}\right)$. If we take $\delta E = \mathcal{E}[\mathcal{C}_i] - E_0$, the same formula accounts for negative values of β.

Therefore, the Creutz algorithms for the Ising model allows to "measure" the inverse microcanonical temperature β as

$$\beta(E_0) = \log\left(1 + \frac{1}{N^2\langle\delta\mathcal{E}\rangle_{\text{emp}}}\right) \quad \text{with} \quad \delta\mathcal{E}[\mathcal{C}] = \begin{cases} E_0 - \mathcal{E}[\mathcal{C}] & \text{if } E^+ = E_0 \\ \mathcal{E}[\mathcal{C}] - E_0 & \text{otherwise} \end{cases} . \qquad (5.9)$$

Finally, let us remark that if the values of the energy span a continuous range, then the empirical probability that $N^2\delta E$ lies between x and $x + \mathrm{d}x$ follows an exponential law

[(a)]– obtained from the Taylor approximation $S(E) \simeq S(E_0) + \beta(E_0)(E - E_0)$ –

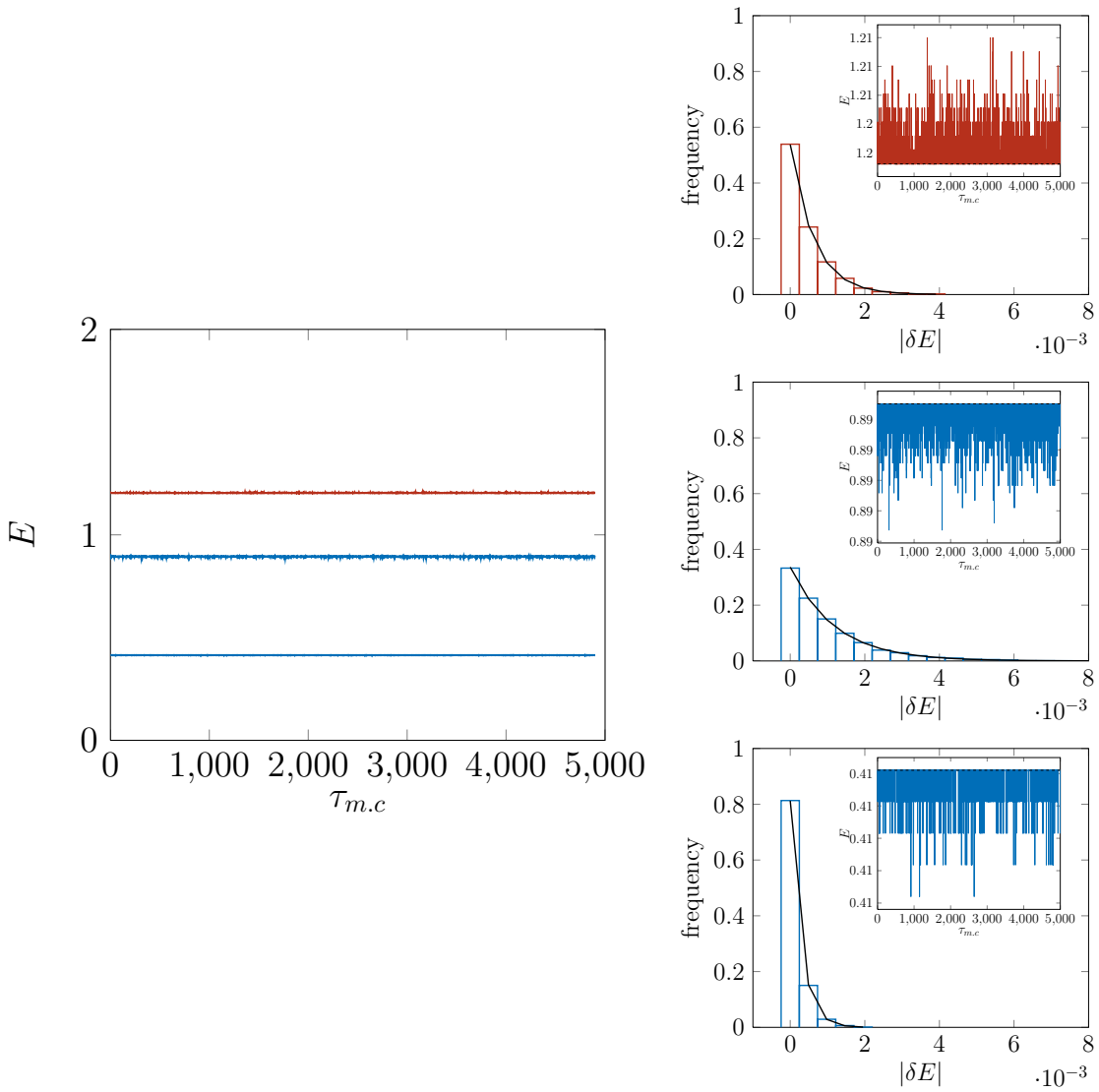

Figure 5.2: Left: evolution of the energy as a function of the Monte-Carlo time $\tau_{m.c.}$ for three Creutz samplings of the Ising model, with $N^2 = 64$ and $E_0 = 0.41$, 0.90 – and 1.20 (–), from bottom to top. Right: the corresponding time distribution of the energy $|\delta\mathcal{E}| = |\mathcal{E}[\mathcal{C}_i] - E_0|$, built from the value of the energy taken at each Monte-Carlo step, from $\tau_{m.c.} = 100$ to $\tau_{m.c.} = 5000$. The distributions are fit by an exponential fit, whose parameter β is measured on the time series of $|\delta E|$ displayed on the insets, as explained in the body of the text. Each run is initialized with the last configurations of the Metropolis runs displayed on Figure 5.1.

with parameter $\beta(E_0)$. $\beta(E_0)$ can therefore be measured as

$$\beta(E_0) = \frac{1}{N^2 \langle \delta\mathcal{E} \rangle_{\text{emp}}} \quad \text{with} \quad \delta\mathcal{E}[\mathcal{C}] = \begin{cases} E_0 - \mathcal{E}[\mathcal{C}] & \text{if } E^+ = E_0 \\ \mathcal{E}[\mathcal{C}] - E_0 & \text{otherwise} \end{cases}. \tag{5.10}$$

5.2.4 Numerical illustration of the Creutz Algorithm.

To check the accuracy of the "Creutz thermometer", let me show what the Metropolis dynamics and the Creutz dynamics typically yield when used on Ising models.

Description of the simulations.

1. Lattices of size $N^2 = 32^2, 64^2, 128^2, 256^2$ with doubly periodic boundary conditions are considered.
2. At time $\tau_{m.c.} = 0$ [(a)], all the spins are set to $+1$ at time 0.
3. The Metropolis algorithms 5.1 and 5.2 are iterated for 5000 Monte-Carlo steps. A wide range of inverse temperatures is considered , from $\beta = 0$ to $\beta = 1$ with increments of 0.02 or 0.01. For $N^2 = 64^2$, we also span the negative temperature regime, and perform a hundred runs from $\beta = 0$ to $\beta = -1$.
4. For each Metropolis run, the final configuration $\mathcal{C}_f$ is used to initialize the Creutz algorithm 5.3. The Creutz algorithm is then also run for 5000 Monte-Carlo steps to sample the energy level $\mathcal{E}[\mathcal{C}_f]$.
5. Averages are then typically computed by using the configurations obtained at each Monte-Carlo step, over the last 4900 Monte-Carlo steps. A similar process is used to measure the microcanonical temperatures.

Comments on the results. The results are shown on Figures 5.1, 5.2 and 5.3.

We note that the two kinds of dynamics (Creutz and metropolis) have a very different behavior – see Figures 5.1, 5.2. The Metropolis algorithms allow for way more fluctuations in the energy than the Creutz algorithm. For the latter, the distributions of the increments of the energies are very well described by an exponential distribution whose parameter is measured as prescribed by Equation (5.9) – see Figure 5.2.

The values of the microcanonical temperatures measured from the Creutz dynamics at a prescribed energy are in excellent agreement with the values of the average energies measured from the Metropolis dynamics at a prescribed inverse temperature – see Figure 5.3. Both the plots $\beta - < E >_{\text{cano}}$ and $\beta_{\text{micro}} - E$ show an inflection point around $\beta \simeq 0.45$, *i.e* $T \simeq 2.2$, compatible with the theoretical value of the critical temperature for the 2D square Ising model : $T_c = \left[\tanh^{-1}(\sqrt{2} - 1)\right]^{-1} \simeq 2.26$ – see for example [Baxter, 1982, Mussardo, 2010].

[(a)] Recall that one Monte-Carlo step or Monte-Carlo unit time $\tau_{m.c.}$ corresponds to N^2 iterations within the algorithms in use.

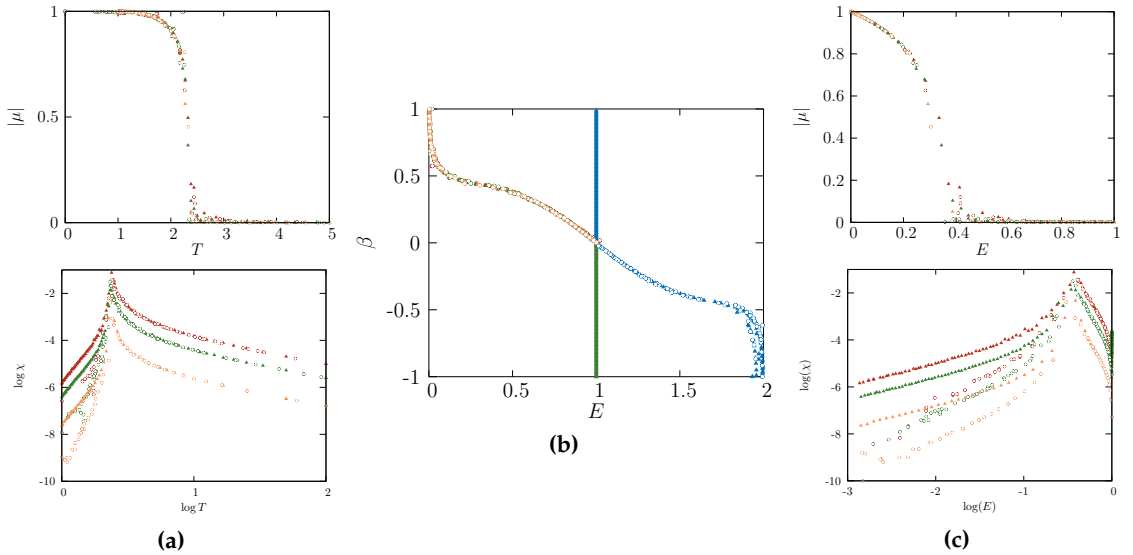

Figure 5.3: (a) The magnetization and the susceptibility plotted as functions of the temperatures (measured or prescribed). (b) The inverse temperatures plotted in regards of the energies (measured or prescribed). (c) The magnetization and the susceptibility plotted as functions of the energies. In each plot, the results are shown for $N^2 = 32$ (Metropolis : ▲, Creutz : ○), $N^2 = 64^2$ (Metropolis : ▲, Creutz : ○), $N^2 = 256$ (Metropolis : ▲, Creutz : ○). In the negative temperature regime, ($E > 1$), we show the case $N^2 = 64^2$ (Metropolis : ▲, Creutz :○). Note that the vertical line in plot (b) is obtained by misusing the Metropolis algorithms. For example, its part comes from the sampling of negative β with Algorithm 5.1 instead of Algorithm 5.2. A misuse of Creutz algorithm would have led to a horizontal line.

There is no substantial difference between the averages of the magnetization per site $\mu[\sigma_N] = \frac{1}{N^2}\sum_{\mathbf{i}\in[\![1;N]\!]^2}\sigma_{N,\mathbf{i}}$ computed with the Creutz algorithm or with the Metropolis algorithms – see Figure 5.3.

One can however spot some differences within the two dynamics when one looks for example at the susceptibility $\xi = \beta\left(\langle\mu^2\rangle - \langle\mu\rangle^2\right)$ below the critical temperature. I don't have a clear explanation for this behavior.

A final word. At an empirical level, the heuristic argument yielding the estimates of the inverse temperature seem to work very well even when the number of degrees of freedom is moderate. This is a consequence of the very low level of fluctuations of the energy that can be observed numerically. This low level of fluctuations has however a dynamical drawback, which is mentioned in Creutz' 1983 paper and that may be worth keeping in mind when we consider more subtle microcanonical measures : "Finite size effects differ from those in the canonical approach ; on small systems, trapping in metastable states is potentially more serious" [Creutz, 1983]. One could finally pleasantly remark, that both Metropolis and Creutz algorithms could be sorted into the same refined rubric of "MCMCMC" algorithms, the additional "MC" either standing for "Metropolis Canonical" or "Microcanonical Creutz" !

5.3 The Axisymmetric statistical equilibria from a Creutz perpective.

In the previous chapter, we have argued that the microcanonical Axisymmetric inviscid equilibria could be built using an analogy with a well-defined lattice-spin model. We have argued that a well-defined thermodynamic limit within the microcanonical ensemble for this model which could be given a hydrodynamical meaning and could be analytically computed. The purpose of the present section is not so much to discuss the analogy further, but rather to confirm the analytical results discussed in [Thalabard et al., 2013] and gain some physical and intuitive insights about the limit "$M \to \infty$" of infinitely large poloidal fluctuations. To do that, a Creutz Algorithm is used.

5.3.1 The "Axisymmetric Ising model".

Definition. To avoid any ambiguity and recall some notations, let me briefly redefine the lattice model which we used to build the "stationary microcanonical measures for the axisymmetric Euler equations". In the previous chapter, the construction was pretty general. For the sake of clarity and simplicity, I here simply discuss the case where the toroidal spins can take only two values, say ± 1.

The lattice model that we consider describes an assembly of N^2 "Beltrami spins", dispatched on a regular $N \times N$ lattice. Each lattice site (i,j) corresponds to a position in physical space (y_i, z_j). It contains a Beltrami spin (σ_{ij}, ξ_{ij}) with two degrees of freedom, one named "toroidal", the other one named "poloidal". The toroidal degrees of freedom σ_{ij} can take only the two values ± 1 . The poloidal degrees of freedom ξ_{ij} can take any real value. An assembly of N^2 Beltrami spins defines a configuration $\mathcal{C}_N = (\sigma_N, \xi_N)$, to which is associated a toroidal energy $\mathcal{E}^{\text{tor}}[\mathcal{C}_N]$, a poloidal energy $\mathcal{E}^{\text{pol}}[\mathcal{C}_N]$, a total energy $\mathcal{E}[\mathcal{C}_N]$, together with two toroidal areas $\mathcal{A}_\pm[\mathcal{C}_N]$ and two partial poloidal circulations $\mathcal{X}_\pm[\mathcal{C}_N]$, defined as

$$\begin{aligned}
&\mathcal{X}_\pm = \frac{1}{N^2} \sum_{\substack{(i,j)\in[\![1;N]\!]^2 \\ \text{and } \sigma_{ij}=\pm 1}} \xi_{ij}, \qquad \mathcal{A}_\pm = \frac{1}{N^2} \sum_{\substack{(i,j)\in[\![1;N]\!]^2 \\ \text{and } \sigma_{ij}=\pm 1}} 1, \\
&\quad \text{and} \quad \mathcal{E}[\mathcal{C}_N] = \mathcal{E}^{\text{tor}}[\mathcal{C}_N] + \mathcal{E}^{\text{pol}}[\mathcal{C}_N], \\
\text{with} \quad &\mathcal{E}^{\text{tor}}[\mathcal{C}_N] = \frac{1}{N^2} \sum_{(i,j)\in[\![1;N]\!]^2} \frac{\sigma_{ij}^2}{4y_i} \quad \text{and} \quad \mathcal{E}^{\text{pol}}[\mathcal{C}_N] = \frac{1}{2N^4} \sum_{(i,j,k,l)\in[\![1;N]\!]^4} J_{kl}^{ij} \xi_{ij} \xi_{kl}.
\end{aligned} \tag{5.11}$$

J_{kl}^{ij} denotes a discrete Green function for the differential operator $-\Delta_\star = -\frac{1}{2y}\partial_{zz}^2 - \partial_{yy}^2$ with vanishing boundary conditions along the y-axis (radial direction), at $y = Y_{in}$ and $y = Y_{out}$, and $2h$-periodic boundary conditions along the z-axis (vertical direction). Here, J_{kl}^{ij} is naively defined by inverting a discrete version of $\Delta_\star$ defined on the lattice through a standard five-point stencil approximation [Wikipedia, 2013a]. I will slightly abusively refer to such a lattice model as an "Axisymmetric Ising Model".

Microcanonical measure. As described in the previous chapter, it is convenient to define a truncated microcanonical measure $p_{M,N}$ as the uniform measure on the set $\mathcal{G}_{M,N}(E, A_\pm, X_\pm)$ of every configuration $\mathcal{C}_N$ that satisfy $\mathcal{X}_\pm[\mathcal{C}] = X_\pm$, $\mathcal{A}_\pm[\mathcal{C}] = A_\pm$, and $\mathcal{E}[\mathcal{C}] \in [E; E + \delta E]$. Axisymmetric absolute equilibria are then obtained by taking the "thermodynamic limit" of $p_{M,N}$ by letting $N \to \infty$ first and $M \to \infty$ then . We want to use a Creutz algorithm to sample $p_{M,N}$, make the latter limit visual and confirm the analytical results previously described. In particular, the expected M^{-2} behavior of the energy inverse temperature requires some kind of numerical confirmation.

5.3.2 The Axisymmetric Creutz dynamics.

"Built-in" *vs* "fluctuating" treatment of the invariants. To sample the axisymmetric microcanonical measure $p_{M;N}$, we consider a Creutz algorithm which allows for some fluctuations in the energy – just as the algorithm 5.3 – but in which the additional conservation laws $\mathcal{X}_\pm[\mathcal{C}] = X_\pm$ and $\mathcal{A}_\pm[\mathcal{C}] = A_\pm$ are directly encoded within the random moves. Such a dynamics will allow a very simple measurement of the inverse energy temperature as was the case for the Ising Model. [(a)]

We replace the Glauber moves at use for the Ising model by a set of smarter moves in the space of configurations. Those moves are described by Algorithm 5.4, in which (i, j) and (k, l) denote two distinct pairs of indices, and M the prescribed poloidal cutoff:

Algorithm 5.4 (*"Axisymmetric M-moves"*)

(1) Pick $(i, j) \in [\![1; N]\!]^2$ *and* $(k, l) \in [\![1; N]\!]^2$ *uniformly at random.*

(2) (i) If $\sigma_{ij} = \sigma_{kl}$*, then*

- *Pick uniformly at random* $d\xi \in [-M, M]$.
- $\xi_{ij} \leftarrow \xi_{ij} + d\xi$
- $\xi_{kl} \leftarrow \xi_{kl} - d\xi$

(ii) Else

- *Switch* ξ_{ij} *and* ξ_{kl}
- *Switch* σ_{ij} *and* σ_{kl}

Move $(2).(i)$ aims at sampling the poloidal degrees of freedom. Move $(2).(ii)$ = is designed to provide some mixing for the toroidal degrees of freedom. Starting from a configuration $\mathcal{C}$, the configuration $\mathcal{C}'$ that we get after either move $(2).(i)$ or $(2).(ii)$ does clearly have the same number of plus and minus toroidal spins as the initial configuration, $\mathcal{A}_\pm[\mathcal{C}'] = \mathcal{A}_\pm[\mathcal{C}]$. The same holds true for the poloidal partial circulations : $\mathcal{X}_\pm[\mathcal{C}] = \mathcal{X}_\pm[\mathcal{C}']$. In this sense, $A_\pm$ and $X_\pm$ are "built-in invariants", embedded in the dynamics. This is not the case for the energy, which is allowed to fluctuate slightly . We can note that move $(2).(ii)$ is very reminiscent of the Kawasaki dynamics sometimes used in Monte-Carlo simulations of Ising-like models.

[(a)] Note that the obvious drawbacks of such a choice are (i) that the Creutz algorithm won't allow for a measurement of the "areas" or the "helicity" temperatures, and (ii) that it will allow for less fluctuations in the space of configurations, and thus might enhance the chance of an unwanted "dynamical trapping".

Creutz dynamics Anyhow, it is now easy to define a Creutz dynamics to sample the microcanonical measure $p_{M,N}$. Such a dynamics is for example given by Algorithm 5.5.

Algorithm 5.5 (*"Axisymmetric Creutz dynamics"*)

(1) *(i)* *Initialize* $i \leftarrow 0$

(ii) *Pick a configuration* $\mathcal{C}_0$ *in* $\mathcal{G}_N(E, A_\pm, X_\pm)$ *such that* $E^- \leq \mathcal{E}[X_0] \leq E^+$

(2) *While* $i < n_{it}$

(i) *Pick at random a new configuration* $\mathcal{C}' = (\sigma', \xi')$ *as prescribed by Algorithm 5.4.*

(ii) *Compute* $\mathcal{E}[\mathcal{C}']$

(iii) *Compute* $M' = \sup_{(i,j)\in[\![1;N]\!]^2} |\xi'_{ij}|$

(iv) - *If* $E^- \leq \mathcal{E}[X'] \leq E^+$ *and* $M' \leq M$, *then* $\mathcal{C}_{i+1} \leftarrow \mathcal{C}'$

- *Else* $\mathcal{C}_{i+1} \leftarrow \mathcal{C}_i$

(v) $i \leftarrow i + 1$

Note the additional step $(2).(iii)$ and the additional condition $(2).(iv)$ that we need to impose in order to enforce the cutoff prescription. As explained in the previous section, with a convenient choice of E^- and E^+, the algorithm should allow to sample the microcanonical averages $p_{M,N}(E)$. At a numerical level, note that step $(2).(ii)$ can be quite time-consuming. In our naive implementation, the discrete Green function has size $N^2 \times N^2$. Hence, step $(2).(ii)$ requires N^2 operations. [(a)] Let us however move forward, and accommodate ourselves with our gullibility.

Initialization of the algorithm. In order to be able to sample some energy levels with the Creutz algorithm, it remains to specify a way to initialize it.
Let us suppose that we want to sample the energy level E, at fixed $A_\pm$ and $X_\pm$. Let us assume that we have strong hints that its microcanonical temperature is negative.
We can start by disregarding the energy constraint and create a configuration from scratch with the good areas and helicities. One way to do that is to pick $N_+ = N^2 A_+$ Beltrami spins at random on the lattice and set their toroidal degrees of freedom to $+1$. The toroidal degrees of freedom of the remaining ones are then set to -1. Then, we assign to each poloidal degree of freedom the values $\xi_\pm = \dfrac{X_\pm}{A_\pm}$ accordingly to the sign of their corresponding toroidal degree of freedom. We now have in our hand a configuration $\mathcal{C}_0$ such that $\mathcal{A}_\pm[\mathcal{C}_0] = A_\pm$ and $\mathcal{X}_\pm[\mathcal{C}_0] = X_\pm$ – this is simply checked using the definition (5.11). What about the energy ? It has no reason to be close to the value E that we want to target at. If the energy E is say higher than the energy $\mathcal{E}[\mathcal{C}_0]$, one can however run the " exploring Algorithm" 5.7 until a configuration with energy higher than E is reached. It is also convenient to define a "Frozen Creutz algorithm" [(b)]. Both algorithms are defined

[(a)] It consists in updating each one of the N^2 values of the stream function. Each of those updates takes $O(1)$ operations. Hence, the step $(2).(ii)$ indeed requires N^2 and not N^4 operations.

[(b)] When run at $M = 0$, the "Frozen Creutz algorithm" is simply a Creutz dynamics where new configurations are obtained from shuffles of the Beltrami spins already on the lattice.

below.

Algorithm 5.6 (*Axisymmetric Frozen Creutz dynamics*)

(1) *(i)* *Initialize* $i \leftarrow 0$

(ii) *Pick a configuration* $\mathcal{C}_0$ *in* $\mathcal{G}_N(E, A_\pm, X_\pm)$ *such that* $E^- \leq \mathcal{E}[X_0] \leq E^+$

(2) *While* $i < n_{it}$

(i) *Pick at random a new configuration* $\mathcal{C}' = (\sigma', \xi')$ *as prescribed by Algorithm 5.4.*

(ii) *Compute* $\mathcal{E}[\mathcal{C}']$

(iii) - *If* $E^- \leq \mathcal{E}[X'] \leq E^+$, *then* $\mathcal{C}_{i+1} \leftarrow \mathcal{C}'$
- *Else* $\mathcal{C}_{i+1} \leftarrow \mathcal{C}_i$

(iv) $i \leftarrow i + 1$

Algorithm 5.7 (*Axisymmetric exploring dynamics*)

(1) *(i)* *Initialize* $i \leftarrow 0$

(ii) *Pick the configuration* $\mathcal{C}_0$ *with* $\mathcal{A}_\pm[\mathcal{C}_0] = A_\pm$ *and* $\mathcal{X}_\pm[\mathcal{C}_0] = X_\pm$.

(iii) $E_+ \leftarrow +\infty$.

(2) *While* $i < n_{it}$

(i) $E_- \leftarrow \mathcal{E}[\mathcal{C}_i]$

(ii) *Run Algorithm 5.6 during 1 Monte-Carlo Step taking* $\mathcal{C}_i$ *as the initial configuration. Keep the last configuration* $\mathcal{C}_f$.

(iii) $\mathcal{C}_{i+1} \leftarrow \mathcal{C}_f$

We now know how to initialize the Axisymmetric Creutz dynamics *ab nihilo* !

5.3.3 Description of the simulations.

I present some numerical results obtained with the axisymmetric Creutz algorithms run on assemblies of 32^2 and 64^2 Beltrami spins, sampled at three energy different levels $E_1 < E_2 < E_3$, for the choice $X_\pm = \pm 0.1$ and various values of M and $A_\pm$ reported on Table 5.1. The reader may have already noticed that since the toroidal spins σ can only be ± 1, the toroidal energy is constant, whatever the choice of $X_\pm$, $A_\pm$. We can therefore identify the energy to the poloidal energy. With such a choice, we loose the interplay between E^{tor} and E^{pol}, but we can take a closer look at the infinite temperature regime described for instance in the previous chapter.

The runs are initialized with the exploring algorithm 5.7 at "M=0", which we use to obtain specific configurations at $E_1 \simeq 2.0 \cdot 10^{-5}$, $E_2 =\simeq 1.1 \cdot 10^{-4}$ and $E_3 \simeq 2.0 \cdot 10^{-4}$. Figure 5.4 typically shows the range of energy that is spanned by the algorithm. For each

N^2	32^2	64^2
Geometry	$Y_{in} = 0 \quad Y_{out} = 1 \quad 2h = 1$	
X_+, X_-	$\pm 0.1 \quad \mp 0.1$	
Final time	$1200\,\tau_{m.c}$	
A_+	$0.1 \quad 0.3 \quad 0.5 \quad 0.7 \quad 0.9$	0.5
M	$0, \quad 0.1 \quad 0.2 \quad 0.3 \quad 0.5 \quad 1 \quad 2 \quad 3 \quad 5$	$0 \quad 0.7 \quad 1 \quad 3 \quad 5 \quad 7 \quad 10$
Energies	$E_1 \simeq 2.0 \cdot 10^{-5}$, $E_2 \simeq 1.1 \cdot 10^{-4}$, $E_3 \simeq 2.0 \cdot 10^{-4}$	$E_3 \simeq 2.0 \cdot 10^{-4}$

Table 5.1: Parameters for the Axisymmetric Creutz dynamics simulations reported in section 5.3.3.

of those levels we then increase the value of M. We run Algorithm 5.6 if $M < \max_{\pm} \frac{|X_\pm|}{A_\pm}$ and Algorithm 5.5 otherwise.

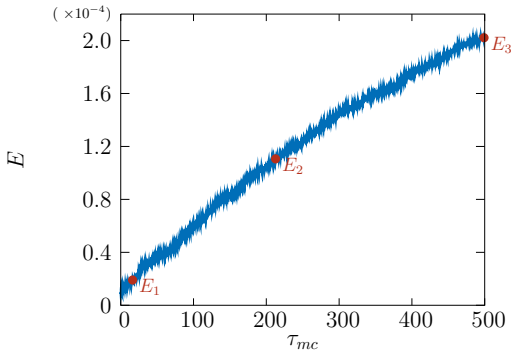

Figure 5.4: A typical use of the exploring algorithm 5.7 showing the energies of the configurations as a function of the number of iterations –in Monte Carlo time. In the present case $N = 32$, $A_\pm = 0.5$,$X_\pm = \pm 0.1$ and $M = 0$. E_1, E_2 and E_3 are as indicated in the body of the text.

As explained in section 5.2, we can very easily measure the inverse microcanonical temperature using Equation (5.10) for each run – see for instance Figure 5.5. The statistical averages involve the last 1100 Monte-Carlo steps. To measure β, we use the time series $\delta\mathcal{E} = \mathcal{E}[\mathcal{C}] - E$ sampled every $\tau_{m.c}/10$.

5.3.4 Results

The main results obtained from the Algorithm are summarized on Figures 5.6, 5.7, 5.8 and 5.9. Figures 5.10 and 5.11 show the typical fields which the Creutz dynamics may yield.

Large M behavior. Although the spin assemblies that we consider are quite small, let us try to spot a "large M limit" in our simulations. First, we observe numerically, that if we try to increase M at fixed $A_\pm$, $X_\pm$, E and fixed N, there exists a critical value M_c, which seems to depend on those six parameters, and above which the Creutz algorithm measures only positive temperature. For M lower than this critical value, the Creutz algorithm yields negative temperatures. In this negative temperature regime, we can

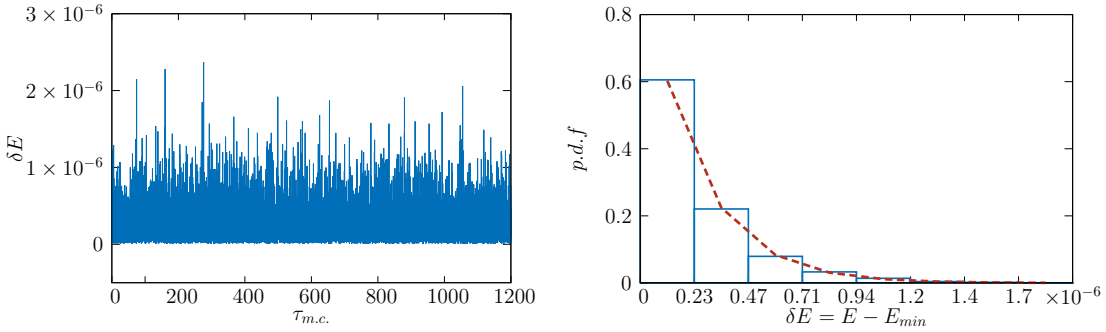

Figure 5.5: The typical time series (left) and distributions (right) of the energy increments $\delta E = \mathcal{E}[\mathcal{C}] - E_3$ obtained with the Creutz Algorithm 5.6. In the present case, $N^2 = 32$, $M = 0$, $X_\pm = \pm 0.1$, $A_\pm = 0.5$, and $E = E_3$. The red dotted line is an exponential law with parameter $\beta = \dfrac{1}{N^2 \langle \delta E \rangle}$ measured on the times series on the energy.

observe that the inverse temperature scales with M^{-2}; and that the average poloidal fluctuation per site scales with M^2, which is in remarkable agreement with the theoretical limit $M \to \infty N \to \infty$, as shown on Figure 5.6. At a heuristic level, we can understand that when the fluctuations of M are small enough ($M/N \ll 1$), the contribution of each poloidal spin to the total energy is small. Hence, high energy states can be obtained using the long range interactions between the spins, and are substantially mean field states. Such is however not the case when M is large ($M/N \gtrsim 1$). In this case, the fluctuations of the energy per site are of the order of the energy level that we want to sample. The most probable states are states where the energy are almost entirely contained in a small number of poloidal degrees of freedom.

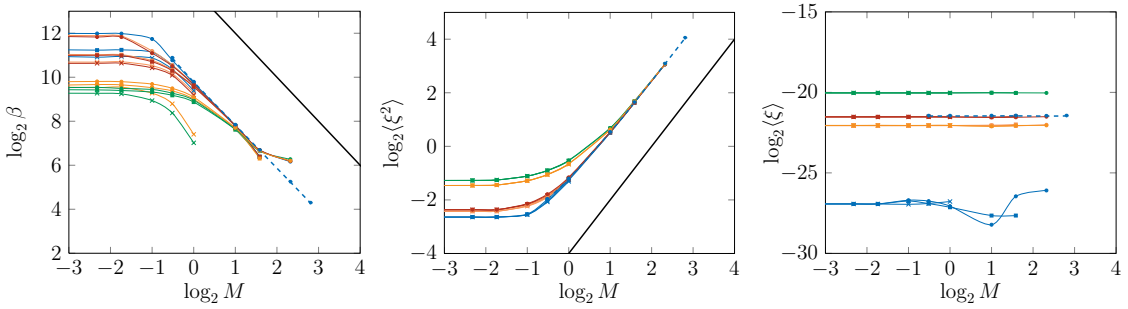

Figure 5.6: Scaling laws in the negative temperature region. As a function of M are plotted (minus) the inverse temperature (a), the microcanonical averages $< \xi^2 >$ (b) and $< \xi >$ (c) both integrated over the domain. Data are shown for $N^2 = 32^2$, $X_\pm = \pm 0.1$, $A_+ = 0.9$ (–), 0.7 (–), 0.5 (–), 0.3 (–), 0.1 (–), and $E_1(\times)$, $E_2(\blacksquare)$, and $E_3(\bullet)$. The $N^2 = 64^2$ run corresponds to the dotted line. The scaling laws that we expect to see in the limit $M \to \infty N \to \infty$ are shown in solid black.

Vanishing cutoff and Frozen behavior. Let us focus on the negative temperature regions. In this region, the scaling laws agree with the theoretical prediction. Is it the case for the mean field relations which relate the typical toroidal field to the typical stream

function ? In the case of a vanishing poloidal cutoff ($M = 0$), the poloidal field cannot fluctuate independently from the toroidal field. Each Beltrami spin has therefore a "frozen" poloidal degree of freedom. Hence, in this case, as in the 2D case, both the typical toroidal fields and the typical poloidal field should be related to the stream function through the 2D mean field equations (4.15). In the visual case of symmetric toroidal levels ($A_\pm = 0.5$), we therefore expect to see $\langle\sigma\rangle = \sigma_+ \tanh B_+\psi$ and $\langle\xi\rangle = \xi_+ \tanh B_+\psi$ with $B_+ = -\beta\xi_+$ –see Appendix E for more details. This is pretty much what we get, as shown on Figure 5.7. Note that there is no "fitting parameter", as the temperature is independently measured on the time series of the energy.

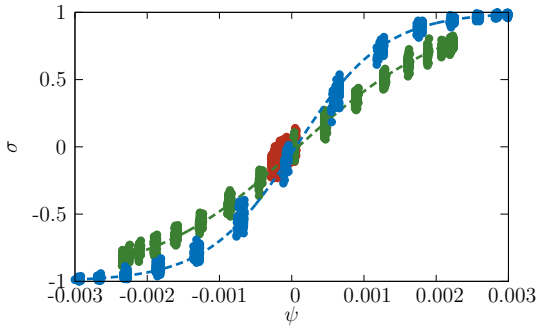

Figure 5.7: The mean field relation $\langle\sigma\rangle - \psi$ obtained for $N^2 = 32^2$, $X_\pm = \pm 0.1$, $A_\pm = 0.5$ and $E = E_1$ (•), E_2 (•), E_3 (•). The dotted lines indicate the theoretical prediction with the temperature measured independently from the time series of the energy.

Large cutoff and strong - mixing behavior. By contrast, if we let M increase within the negative temperature region, the typical toroidal field becomes uniform and the $\tanh$ relation disappears. Similarly the typical poloidal field becomes a linear function of the stream function. As M becomes larger, the empirical averages exhibit more and more fluctuations. Those behaviors are shown on Figures 5.8 and 5.9.

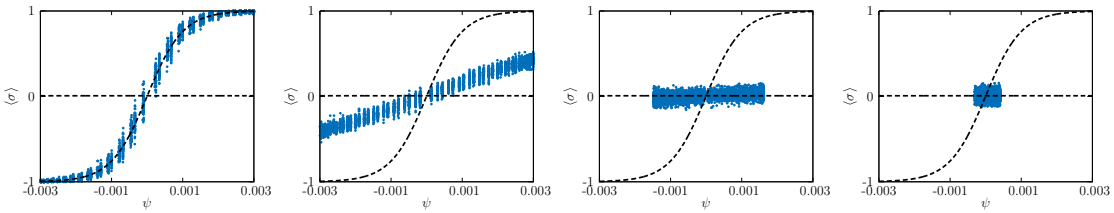

(a) $M = 0$ **(b)** $M = 1$ **(c)** $M = 3$ **(d)** $M = 5$

Figure 5.8: The average toroidal field $\langle\sigma\rangle$ plotted as a function of the average stream function ψ for various values of M . Here, $N^2 = 64^2$, $A\pm = 0.5$, $X_\pm = \pm 0.1$ and $E = E_3$. The dotted lines indicate the theoretical predictions for the case $M = 0$($\tanh law$) and $M = \infty$ (horizontal line). They use the value of the inverse temperature measured on the time series of the energy for the run $M = 3$.

As a final illustration on the axisymmetric case, Figures 5.10 and Figures 5.11 show the average toroidal and poloidal fields obtained for the various values of the parameters $A_\pm$ and $X_\pm$ that were used. As M increases, the equilibrium state given by the Creutz algorithm is either a negative temperature state for which the poloidal field is a vertical

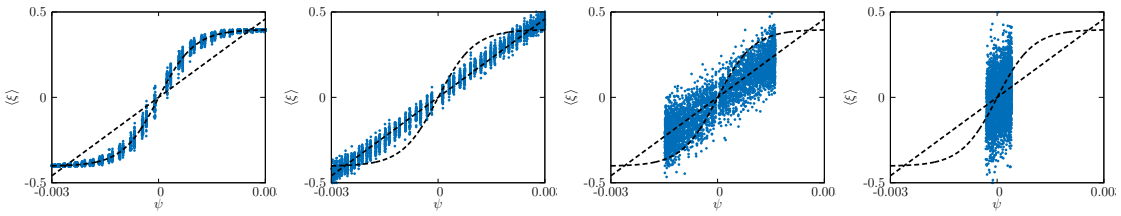

(a) $M = 0$ **(b)** $M = 1$ **(c)** $M = 3$ **(d)** $M = 5$

Figure 5.9: The average poloidal field $\langle \xi \rangle$ plotted as a function of the average stream function ψ for various values of M . Here, $N^2 = 64^2$, $A\pm = 0.5$, $X_\pm = \pm 0.1$ and $E = E_3$. The dotted lines indicate the theoretical predictions for the case $M = 0$ ($\tanh$) and $M = \infty$ (linear behavior). They use the value of the inverse temperature measured on the time series of the energy for the run $M = 3$.

jet, or a positive temperature state in which no structure is apparent.

5.3.5 Conclusion

It is remarkable that some predictions made by taking two limits at ∞ are pretty well illustrated by even fairly small assemblies of spins. The Creutz simulations and the limit discussed in the previous chapter are therefore self-consistent. One could complain though, that no big surprise came out of the axisymmetric MCMCMC dynamics. We pretty much seek and looked for the scalings that we wanted to see. One could further complain, that we have not studied the interplay between the poloidal and the toroidal energies, because the symmetries of the toroidal levels made us focus on the "high energy" regime. The case of two-dimensional magento-hydrodynamics will allow us to make up for such a default.

5.4 2D MHD Equilibria from the microcanonical perspective.

It is quite tempting to see whether magneto-hydro measures can be defined in the same spirit. We expect the physics of magneto-hydro measures to be different. Recall from Chapter 3 that Kraichnan's absolute equilibria yielded basically two-regimes. Depending on the sign of the negative magnetic potential squared temperature ("α"), the absolute equilibrium regime either describes a condensation of magnetic energy on the smallest wavelength ($\alpha < 0$), or a spread out of kinetic energy over the largest wavelengths($\alpha > 0$). No thermodynamic limit was found for the positive α regime. In the lattice model approach, it will turn out, that both regimes can be given a thermodynamic description. The "positive α" magneto-hydro regime is given a more refined description, and found to be closely related to the axisymmetric high energy microcanonical regime. The magneto-hydro ensembles are only explicitly computed in the non-helical case. Comments on the helical case are illustrated by the use of an appropriate Creutz dynamics. Note that inviscid equilibria for magneto fluids from the Robert-Miller-Sommeria perspective have been described in [Turkington and Jordan, 1995, Jordan and Turkington, 1997], and more recently in [Weichman, 2012]. In both papers the "lattice model" point of view is present. I will comment on those works at the end of the section.

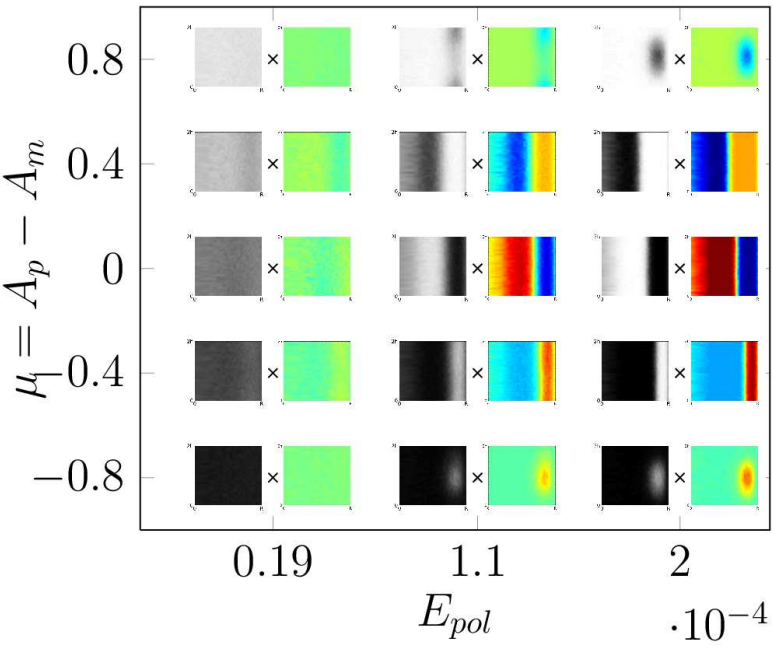

(a) M=0

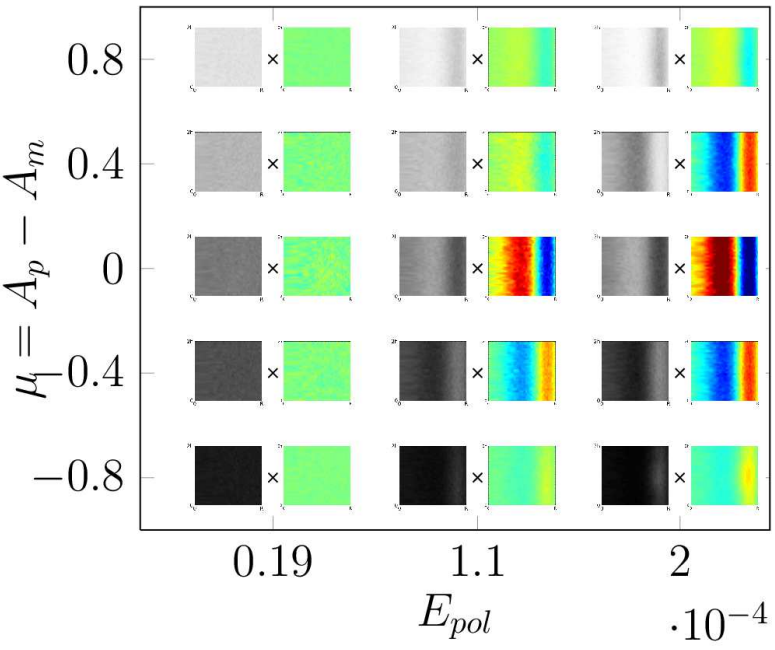

(b) M=1

Figure 5.10: For $N^2 = 32^2$ and $X_\pm = \pm 0.1$, we show for each value of the magnetization $\mu = A_+ - A_-$ and of the energy E_{pol} both the average toroidal field – grayscale – and the average poloidal field. The toroidal gray scale ranges from -1 (black) to +1(white). The poloidal color scale is normalized and ranges from -1 (blue) to +1 (red).

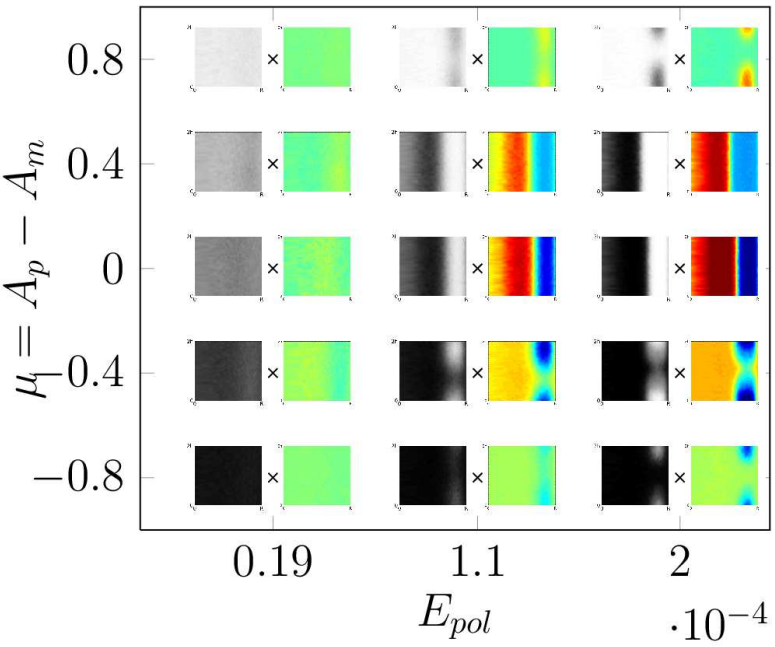

(a) M=0

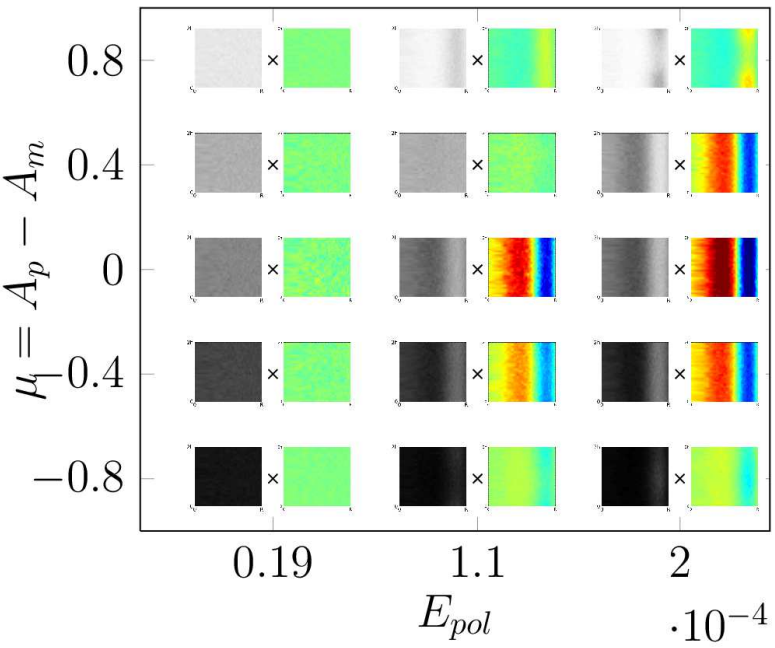

(b) M=1

Figure 5.11: Same as Figure 5.10 except that $X_{\pm} = \mp 0.1$

5.4.1 The"MHD Ising model"

Definition. Recall from Chapter 3 and Table 1.1 that except for the magnetic part of the energy, the invariants of the two-dimensional magneto-hydro ideal equations are in a one-to-one mapping with the axisymmetric ideal invariants. The "Axisymmetric Ising Model" described in section 5.3.1 can therefore be readily modified to yield a companion "2D MHD Ising model" . The correspondence between the two models is given by Table 5.2. In the MHD lattice model, the Beltrami spins have a magnetic degree of freedom A_{ij} that can take only two values $\pm a_0$, and a continuous kinetic degree of freedom ω_{ij}.

	Axisymmetric Ising Model	2D MHD Ising Model
Beltrami spin	$\sigma_{ij} = \pm 1, \xi_{ij} \in \mathbb{R}$	$A_{ij} = \pm a_0, \omega_{ij} \in \mathbb{R}$
Configurations	$\mathcal{C}_N = \{(\sigma_{ij}, \xi_{ij})\}_{ij}$	$\mathcal{C}_N = \{(A_{ij}, \omega_{ij})\}_{ij}$
Generalized Helicities	$\mathcal{X}_\pm[\mathcal{C}_N] = \frac{1}{N^2} \sum_{\sigma_{ij}=\pm 1} \xi_{ij}$	$\mathcal{X}_\pm[\mathcal{C}_N] = \frac{1}{N^2} \sum_{A_{ij}=\pm a_0} \omega_{ij}$
Areas	$\mathcal{A}_\pm[\mathcal{C}_N] = \frac{\sharp\{\sigma_{ij} = \pm 1\}}{N^2}$	$\mathcal{A}_\pm[\mathcal{C}_N] = \frac{\sharp\{A_{ij} = \pm a_0\}}{N^2}$
Total energy	$\mathcal{E}[\mathcal{C}_N] = \mathcal{E}^{\text{tor}}[\mathcal{C}_N] + \mathcal{E}^{\text{pol}}[\mathcal{C}_N]$	$\mathcal{E}[\mathcal{C}_N] = \mathcal{E}^{\text{mag}}[\mathcal{C}_N] + \mathcal{E}^{\text{kin}}[\mathcal{C}_N]$
Poloidal/Kinetic Energy	$\mathcal{E}^{\text{pol}}[\mathcal{C}_N] = \frac{1}{2N^4} \sum_{(i,j,k,l)} G^{ij}_{kl} \xi_{ij} \xi_{kl}$	$\mathcal{E}^{\text{kin}}[\mathcal{C}_N] = \frac{1}{2N^4} \sum_{(i,j,k,l)} G^{ij}_{kl} \omega_{ij} \omega_{kl}.$
Toroidal/Magnetic Energy	$\mathcal{E}^{\text{tor}}[\mathcal{C}_N] = \frac{1}{N^2} \sum_{i,j} \frac{\sigma_{ij}^2}{4y_i}$	$\mathcal{E}^{\text{mag}}[\mathcal{C}_N] = \frac{1}{2N^2} \sum_{i,j,k,l} J^{ij}_{kl} A_{ij} A_{kl}$
Discrete Stream function	$\psi_{ij} = \frac{1}{N^2} \sum_{kl} G^{ij}_{kl} \xi_{kl}$	$\psi_{ij} = \frac{1}{N^2} \sum_{kl} G^{ij}_{kl} \omega_{kl}$

Table 5.2: From the "Axisymmetric Ising model" to the "2D MHD model". The sums run from 1 to N for each index.

Some additional comments are needed :

The values allowed for the levels of the magnetic toroidal are chosen to be symmetric and are denoted $\pm a_0$, yet non-precribed.

To avoid a possible misinterpretation of the magnetic areas "$\mathcal{A}_\pm$" in terms of the magnetic degrees of freedom "A_{ij}", let us rather work with the "magnetization" of a configuration $\mu[\mathcal{C}_N] = \mathcal{A}_+[\mathcal{C}_N] - \mathcal{A}_-[\mathcal{C}_N]$. The sum of the magnetic areas is one. Therefore, The magnetization of a configuration fully specifies its magnetic areas.

In the present case, the MHD Ising model is considered on a doubly periodic domain $\mathcal{D}$, of size $2\pi \times 2\pi\delta$, described by cartesian coordinates (x, y). The lattice has therefore a mesh $2\pi/N$ in the x-direction and $2\pi\delta/N$ in the y-direction.

The tensor G is a discrete Green function for the Laplacian $-\Delta$ on the doubly periodic domain $\mathcal{D}$, computed for instance with a Discrete Fourier transform.

The tensor J is minus a discrete Laplacian over the lattice. It depends on N. An explicit expression for J can be given through a five-point stencil estimate of (minus) the Laplacian as

$$J^{ij}_{kl} = \begin{cases} -\dfrac{N^2}{4\pi^2\delta^2} & \text{if } i = k \text{ and } j - l = \pm 1 \\ -\dfrac{N^2}{4\pi^2} & \text{if } i - k = \pm 1 \text{ and } j = l \\ \dfrac{N^2}{2\pi^2}(1 + \delta^{-2}) & \text{if } i = k \text{ and } j = l \end{cases} . \tag{5.12}$$

Hydrodynamic limit. In the hydrodynamic limit ($N \to \infty$) the quantities $\mathcal{A}_\pm$, $\mathcal{X}_\pm$ and $\mathcal{E}_\pm$ match the invariants of inviscid two-dimensional magnetohydrodynamics , expressed using the vorticity and the magnetic potential variables. [(a)] If one takes for granted the Formal Theorem of Liouville described in Chapter 2 – which in the case of the 2D MHD equations precisely involves the magnetic potential field A and the vorticity field ω – , one can easily get convinced, that well-defined statistical ensembles of the MHD lattice model can be used to define measures of possible relevance to inviscid magneto-fluids. Note that we could consider a more general model, – more akin to a Potts model – and take K levels or even a compact distribution for the levels of the magnetic potentials. For the sake of simplicity, those cases are not considered here.

Microcanonical ensemble. We can remark that just as in the axisymmetric case, the kinetic degrees of freedom are not bounded. To define a microcanonical measure, we need to normalize the finite dimensional measures appropriately, for example with the use of a kinetic cutoff M. The microcanonical measure $\mu^{E,m,H_\pm}_{M,N}$, [(b)] is then given the standard definition of a uniform measure over the set of configurations $\mathcal{C}_N$ satisfying $\mu[\mathcal{C}_N] = \mu$, $\mathcal{X}_\pm[\mathcal{C}_N] = X_\pm$ and $\mathcal{E}[\mathcal{C}_N] = E$ and whose kinetic degrees of freedom are bounded by M. We then follow the construction of the microcanonical ensemble prescribed in the previous chapter – and recalled in paragraph 5.3.1 – by taking the two limits $N \to \infty$ and $M \to \infty$ successively.

5.4.2 Condensation and "weak-A" equilibria.

Condensation Regime. $A \in [\![-1; 1]\!]$ In the magneto-hydro case, the physics described by the microcanonical statistics equations turns out to depend on what we choose to consider for the levels of magnetic potential A. A natural and obvious choice is to consider a distribution with compact support, and allow the magnetic degrees of freedom to take only the two values -1 and $+1$. For such a choice, the "thermodynamic" limit "$M \to \infty N \to \infty$" yields a condensation regime, akin to the magnetic squared potential negative temperature states that we obtained from a Kraichnan-type of argument. Here,

[(a)] In particular, the discrete magnetic energy correctly yields $E^{\text{mag}} = \dfrac{1}{2|\mathcal{D}|}\int_{\mathcal{D}} dx\,(-\Delta A)A = \dfrac{1}{2|\mathcal{D}|}\int_{\mathcal{D}} \mathbf{dr}\,|\nabla A|^2$ in the hydrodynamic limit.

[(b)] whose averages are written $<>_{M,N}$ for short

the statistical explanation of the condensation regime relies on a fairly simple argument : the conservation of the magnetic areas makes the magnetic energy an extensive quantity, as opposed to the kinetic energy, which is akin to a thermodynamic energy per spin, and therefore intensive. The argument is explained more extensively in Appendix D.

Weak magnetic potential. $A \in [\![-1/N; 1/N]\!]$ One can make other choices for A. To induce a non-trivial balance between the magnetic energy E^{mag} and the kinetic fluctuations – prescribed by M –, one can choose to consider an initial very weak – but non zero – magnetic distribution, whose discrete gradients are non zero. To do that, one can simply take $A \in [\![-1/N; 1/N]\!]$. Such a choice has no consequence on the helical invariants or on the magnetic areas : those invariants only depend on the number of levels of A. However, it changes the balance between the magnetic energy and the kinetic energy [(a)]. Such a choice might seem arbitrary. It makes the link between the statistical ensembles and the stationary measure of the magneto-hydro equations shaky. However, it will turn out that the equilibrium regimes that arise from such a choice can be interpreted as the microcanonical counterparts of the magneto-hydro absolute equilibria. It will also turn out, that those regimes can be be put in perspective with the previous descriptions of the magneto-hydro relaxed states [Jordan and Turkington, 1997, Weichman, 2012].

5.4.3 Description of the "weak-A" equilibria.

5.4.3.1 Brief theoretical considerations.

A comment on the Magnetic Energy. With the choice of $A \in [\![-1/N; 1/N]\!]$, the magnetic energy is bounded. Up to a constant multiplicative geometric factor $1/4\pi^2$ that we consciously omit, it takes its values between 0 and $4(1 + 1/\delta)$, whatever the mesh size. The most probable energy level is $E^\star = 2(1 + 1/\delta)$. The physical origin of the energy then lies in the gradients of A, which , unlike the field A, take finite but non necessarily vanishing values as $N \to \infty$. The magnetic potential is vanishing in the limit $N \to \infty$. Such is however not necessarily the case for the magnetic field $\mathbf{B} = (\partial_y A, -\partial_x A)$, nor for the more convenient scalar current $J = -\nabla A$.

Analogy with the axisymmetric case. The "weak-A Ising MHD model" describes an interplay between magnetic degrees of freedom whose total energy is bounded and kinetic degrees of freedom whose potentially large fluctuations may make the kinetic energy become very large compared to the magnetic energy. This feature is very reminiscent of the axisymmetric equilibria. Besides, once again, except for the magnetic energy, it is only a matter a vocabulary to pass from the Axisymmetric Ising model to the present MHD model. So, are those MHD equilibria akin to the axisymmetric equilibria ? At a technical level, note that the magnetic energy involves only nearest neighbor interaction. Up to a factor $1/2$, it is very similar to the hydrodynamical energy "E"of the Ising configurations defined in the first paragraph of the present chapter – and at use for example in Figure

[(a)] We can observe that other scalings $a_0 \propto \frac{1}{N^a}$ are in principle possible. If $a > 1$, the result is a favoring of the kinetic energy. If$a < 1$, the magnetic energy is favored. Only in the case $a = 1$ are the two energies on the same "footage".

5.3. More generally, it corresponds to the energy per site of a short-range ferromagnet. In general, the magnetic energy cannot be mapped onto a macrostate constraint. Such a mapping could be made using a Braggs-Williams type of approximation, but in the general case, one cannot rely on the asymptotic counting of microstates provided by Sanov theorem. However, because one pretty much knows what the entropy of a 2D ferromagnet is supposed to be, one can understand the phase diagram for the MHD model, at least in the case of weak helical correlations.

Unhelical Phase diagram. In the simplified case where the helical correlations are not taken into account, and rather replaced by a constraint on the total circulation $\mathcal{X} = \mathcal{X}_+ + \mathcal{X}_-$ – which we require to be zero for doubly periodic domains –, the kinetic degrees of freedom and the magnetic degrees of freedom are only coupled through the energy constraint. Therefore, just as in the axisymmetric case, the ratio of kinetic energy over magnetic energy for a typical configuration is prescribed by the equality between an inverse magnetic microcanonical temperature with an inverse kinetic microcanonical temperature. For the magnetic degrees of freedom, the evolution of the temperature as a function of the energy is typically as shown on Figure 5.3. As for the kinetic part, it suffices to remember Figure P4 of the previous chapter, to see that if the kinetic energy is to be non vanishing, then the inverse temperature needs to be zero in the limit of a large kinetic cutoff M. Therefore, we conclude the same alternative as in the axisymmetric case : one has two make a first distinction between a high energy regime ($E > E^\star = 2(1+1/\delta)$), and a low energy regime ($E < E^\star$).

In the high energy regime, the stream function ψ is necessarily non-vanishing. The most probable M-dependent macrostate distribution of the kinetic field is simply obtained from equation (P54) (Chapter 4) as

$$p^\star_M(\omega, \mathbf{r}) = \frac{e^{-\beta^{(M)}\omega\psi(\mathbf{r})+h^{(M)}\omega}}{Z^\star_M(\mathbf{r})} \quad \text{with} \quad Z^\star_M(\mathbf{r}) = \int_{-M}^{M} \mathrm{d}\omega e^{-\beta^{(M)}\omega\psi(\mathbf{r})+h^{(M)}\omega}. \tag{5.13}$$

For the doubly periodic boundary conditions, the vanishing total circulation makes the Lagrange multiplier $h^{(M)}$ be zero. The limit $M \to \infty$, is then computed using the scalings (P58). At the end, one obtains an expression for the average kinetic vorticity field in terms of the reduced inverse temperature $\beta^\star = M^2\beta^{(M)}$. It reads :

$$\langle\omega(\mathbf{r})\rangle = -\frac{\beta^\star}{6}\psi \quad \text{and} \quad \langle|\omega(\mathbf{r})|^p\rangle = +\infty \quad \text{if } p > 1 \tag{5.14}$$

The most probable macrostate is obtained when $\beta^\star/6$ is equal to the smallest eigenmode of $-\Delta$. Due to the choice $a_0 \propto 1/N$, $\langle A\rangle_N$ vanishes as $N \to \infty$. There however exists a counterpart to the axisymmetric toroidal field being completely intertwined. It is given by the statistics of the sign of the magnetic potential. Equation (P75) can therefore be translated into

$$\langle \mathrm{sign}(A)^p\rangle = \sum_{\pm} (\pm 1)^p \frac{1 \pm \mu}{2}. \tag{5.15}$$

Since $\langle A\rangle = 0$, one could think that the average of the electric current $\langle j\rangle$ should also

be vanishing. This is however not the case. The choice $a_0 \propto 1/N$ yields finite dimensional magnetic potentials whose gradients are continuous in the hydrodynamic limit, but whose second variations may diverge with N. Therefore, in general $\lim_{N\to\infty}\langle \Delta A\rangle_{M,N} \neq \Delta\langle A\rangle_M$. The correct definition of the average current is $\langle j\rangle = \lim_{M\to\infty}\lim_{N\to\infty} = \langle j\rangle_{M,N}$. It is therefore not necessarily vanishing.

In the lower-energy regimes ($E < E^\star$), the stream function ψ is necessarily vanishing. The energy is then strictly magnetic. Because of the short-range nature of the interactions, there exists a critical energy E^c and one needs to make a further distinction as to the values of the total energy.
The intermediate energy regime $E_c \leq E \leq E^\star$ can be thought of as a paramagnetic regime : the signs of the magnetic potential A are intertwined, and no spontaneous islands of same sign magnetic potential emerge. Therefore, the average electric currents are strong, but they are not organized at large scale. This intermediate energy is somehow analogous to the axisymmetric low-energy regime.
If the energy is lower than E_c, then there exists a ferromagnetic self-organization of the signs of the magnetic potential A into macroscopic islands. This yields a vanishing current J except at the interfaces of these islands, where it gets infinite.

To sum up, the unhelical, "weak A" MHD Ising model therefore admits three regimes, (i) a high energy (HE) regime $E \geq E^\star = 2(1 + 1/\delta)$, characterized by a large scale organization of the vorticity field, and strong fluctuations, (ii) an intermediate energy (IE) regime $E_c \leq E \leq E^\star$ with a vanishing kinetic energy and no obvious large scale organization, and (iii) a low energy (LE) regime $E < E_c$, characterized by the presence of macroscopic strong electric currents. Those regimes are highlighted on Figure 5.12.

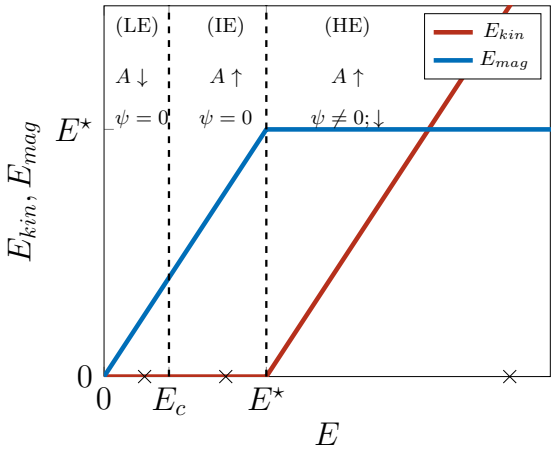

Figure 5.12: Non-Helical, "weak A" regimes for the MHD Ising model – see the text. The arrows indicate a large (↓) or a small (↑) scale organization. The crosses show the values of the energies for the which Creutz simulations are performed.

5.4.3.2 An illustrated description of the (helical) equilibria.

In the general case with cross-helicity, the equilibria for the MHD Ising model are not so easily derived, although the counting argument could probably be used for $E < E_c$ – see Appendix D. However, one can sample the helical microcanonical measures using the Creutz dynamics (5.5). The presence of helical correlations does not alter the interplay between the magnetic and kinetic energies. It however creates a helical alignment between the velocity and the magnetic fields, which is visible at the level of the kinetic vorticity and of the electric density current fields.

Creutz helical and unhelical dynamics. To sample the helical microcanonical measure of the MHD Ising model, the Algorithm 5.5 is used, initiated by the exploring Algorithm 5.7. In those two algorithms, the label "σ" is just replaced by the label "ω" and the label "ξ" by the label "ω". In order to sample the non-helical ensembles, the moves in the space of configurations were taken slightly differently. Instead of the "Axisymmetric M-moves" of Algorithm 5.4, I have used the "Non-helical M-moves" described by Algorithm 5.8. In both cases, an attempt to rotate the system by $\pm\pi/2$ at each Monte-Carlo step was also added. If the attempt was successful, the next attempt to rotate the system could only rotate it back to its initial state.

Algorithm 5.8 (*"Non-helical M-moves"*)

(1) Pick $(i,j) \in [\![1;N]\!]^2$ *and* $(k,l) \in [\![1;N]\!]^2$ *uniformly at random.*

(2) Pick a random number η *between* 0 *and* 1*.*

(3) (i) If $\eta > 0.5$*, then*

- *Pick uniformly at random* $d\omega \in [-M, M]$*.*
- $\omega_{ij} \leftarrow \omega_{ij} + d\omega$
- $\omega_{kl} \leftarrow \omega_{kl} - d\omega$

(ii) Else

- *Switch* ω_{ij} *and* ω_{kl}

Runs and Parameters. We run the Creutz dynamics at three different energies, $E_1 = 1$, $E_2 = 3$, $E_3 = 10$, in order to respectively investigate the low-energy, the intermediate and the high energy regime for a square domain $(\delta = 1)$ –see Figure 5.12. The magnetization was taken to be zero. The initial correlations $X_\pm$ were taken as 0, $0.25\cdot$ or 1.25, and M was typically ranging from 1 to 10. The resolutions were pretty modest : from 32^2 to 128^2. The runs were performed over $400\tau_{m.c}$ and the averages performed over the last 300 steps.

The high energy regime : $E \geq E^\star$. The presence of helical correlations does not seem to alter the interplay between E^{mag} and E^{kin}, as shown on Figures 5.13 and 5.14. In both cases (helical and non-helical), the presence of a large poloidal cutoff forces the magnetic energy to be equal to $E^\star$. At fixed M, increasing N makes the kinetic fluctuations decrease. At a fixed "large" N, increasing M enhances the kinetic fluctuations. The inverse

temperature measured on the times series of the energy display the correct "axisymmetric scaling law" in M^{-2} whether or not the correlations are present – see Figure 5.15.

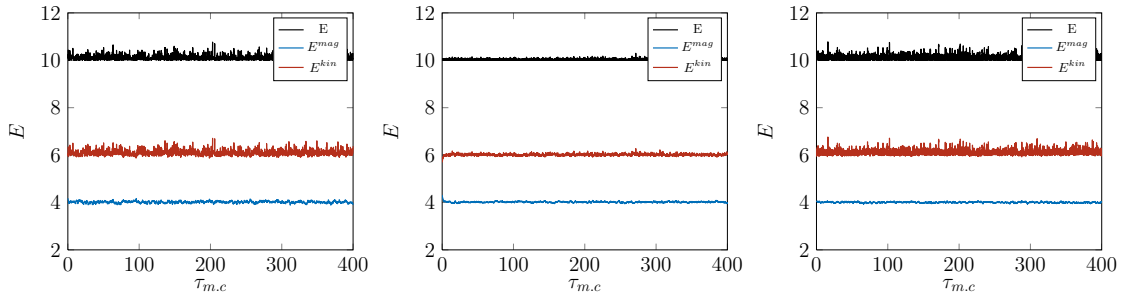

(a) $N^2 = 64^2$, $M = 4$ **(b)** $N^2 = 128^2$, $M = 4$ **(c)** $N^2 = 128^2$, $M = 8$

Figure 5.13: Evolution of the kinetic and magnetic energy in the high energy regime $(E = 10)$, using the non-helical Creutz dynamics for various values of N and M.

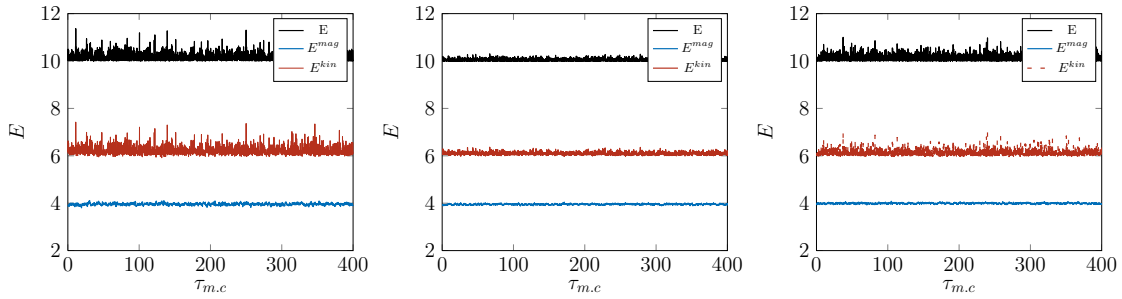

(a) $N^2 = 64^2$, $M = 4$ **(b)** $N^2 = 128^2$, $M = 4$ **(c)** $N^2 = 128^2$, $M = 8$

Figure 5.14: Same as Figure 5.13 but this time in the presence of helicity ($X_{\pm} \simeq 1.25$).

The instantaneous vorticity fields are highly fluctuating, both with and without cross-helicity. In both cases, a clear mean field relation $\langle\omega\rangle - \langle\psi\rangle$ emerges out of a monte-carlo time averaging. The relation is in accordance with Equation 5.14 : it is linear and the slope is $-\beta^\star/6 = 1$, which corresponds to the smallest eigenvalue of the $2\pi \times 2\pi$ domain – see Figures 5.25 and 5.26 at the end of the chapter. Note, that in order to make those relations emerge more clearly, a local averaging of the time-averaged fields was performed, yielding coarse-grained, time-averaged fields. The coarse-graining process consists in computing a local average over contiguous blocks of 2×2 spins. As an example, Figure 5.16 shows the result of such an averaging process on the vorticity field, in the non-helical case.

The magnetic potential is also very fluctuating. In the helical case, one can however spot an emerging, vanishing structure after both a time averaging and a coarse-graining. However, because of the high level of fluctuations, no such structures are visible for the current $j = -\nabla^2 A$. There is however a hint of a linear relation between the average current and the average vorticity in the helical case – see Figure 5.13 and 5.14. One could therefore expect, that a non-uniform average current would emerge out of a longer averaging process.

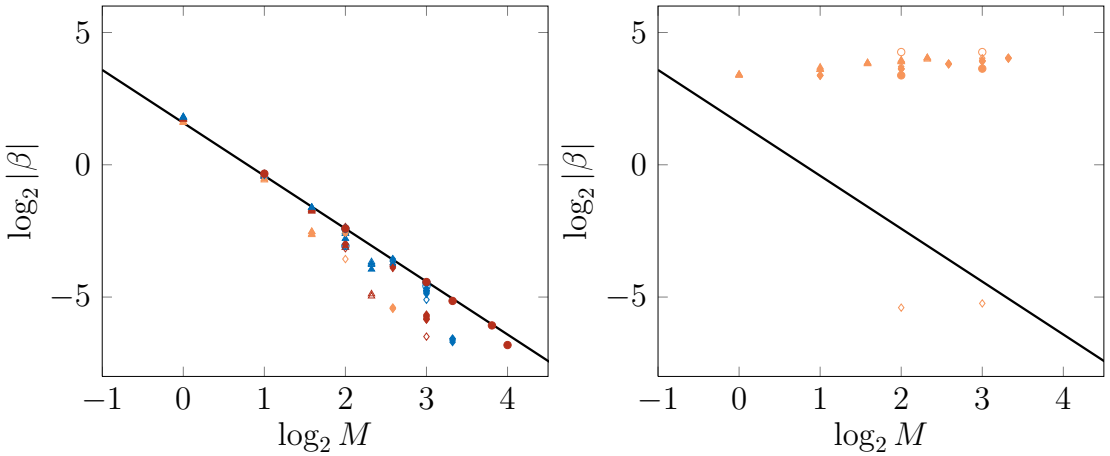

(a) $E \geq 4$ **(b)** $E = 3$

Figure 5.15: Evolution of the measured inverse temperature as a function of the vorticity cutoff M. Open (filled) symbols indicate a helical (non helical) run. Their shapes indicate the resolution ; 32^2 (△),64^2 (⋄),128^2(○). For the high energy regime $E \geq 4$, thee color indicate the value of the energies : $E = 6$ (–) , 8 (–), 10(–). The solid lines indicate a M^{-2} behavior.

Finally note the very strong non-uniform distribution of the instantaneous vorticity fields, shown on Figures 5.19 and 5.20.

Intermediate energy regime. In the intermediate energy regime, no substantial difference between the correlated and the uncorrelated dynamics are either visible at the level of the interplay between the kinetic and the magnetic energies – see Figure 5.17. The microcanonical temperature obtained from the time series of the energy is independent of M – see Figure 5.15. The helical distributions of the instantaneous vorticity fields, are also strongly non uniform, and are peaked for the extreme values of the vorticity – see Figures 5.19 and 5.20.

The inverse temperature as measured on the times series of the energy does not display any longer a M^{-2} behavior. It is a consequence of the stream function being zero – see Figure 5.15. The two "weird points" that can be observed in Figure 5.15 correspond to two 64^2 runs. In those two runs, the helical correlations are high : $X_\pm/A_\pm \lesssim M$. The time distribution of the energy was found not to be exponential, yielding a wrong estimate for the inverse temperature.

Scatter plots and coarse grained fields are shown on Figures 5.24 and 5.23. In both the helical and the non-helical case, the consequence of the vanishing kinetic energy is the vanishing of the stream function ψ. The dispersion of the vorticity is lower in the the non-helical case than in the helical-case. This behavior is compatible with the non-helical prediction of a vanishingly uniform vorticity field. In the helical case, the vorticity is not uniform any longer. It is clearly proportional to the average current $\langle J \rangle$. The linear relation between the current and the vorticity is a signature of the alignment between the average magnetic field and the average velocity field. The alignment emerges even though no large scale structure is present. It is due to the presence of cross-helical corre-

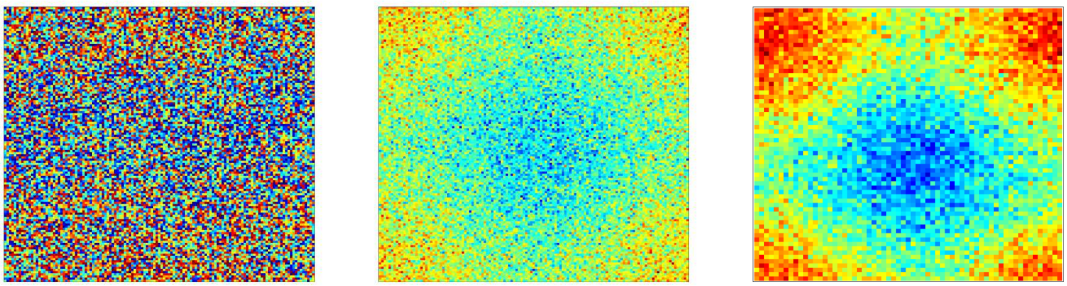

(a) ω (instantaneous) **(b)** $<\omega>$ **(c)** $<\omega>$, after one coarse graining

Figure 5.16: Illustration of the averaging process for the vorticity field in the high energy regime (E=10), $N^2 = 128^2$ and $M = 4$ in the non helical case. The colormap is scaled to the maximal value of each field.

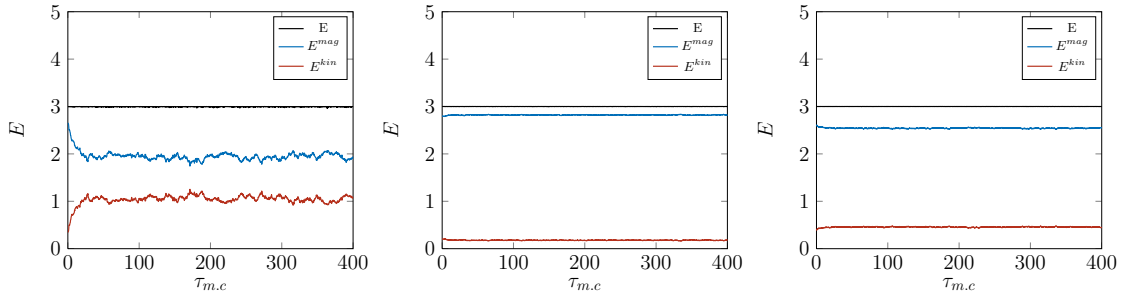

(a) $N^2 = 32^2$, $M = 4$ **(b)** $N^2 = 128^2$, $M = 4$ **(c)** $N^2 = 128^2$, $M = 4$, helical

Figure 5.17: Evolution of the kinetic and magnetic energy in the intermediate energy regime ($E = 3$) , in non-helical (a,b) and helical (c) situations.

lations.

Low Energy Regime. In the low energy regime, the helical runs have been made for a lower value of the helicity. As in the two other regimes, the presence of helicity does not alter the interplay between the kinetic and the magnetic energies (Figure 5.18). As expected, there exists a ferromagnetic large-scale organization for the (signs of) the magnetic potential, which yields the emergence of a large-scale current : the latter is vanishing everywhere except at the frontier of the same-sign clusters of the magnetic potential. In the helical case, the proportionality between the current and the vorticity translates into the emergence of "large scale" vorticity filaments to appear – see 5.22 and 5.21. Note that the "chess game" look of the average magnetic potential and (sign of the) stream function in Figures 5.22 and 5.21 owes to the time averaging taking into account both non-rotated and $+\pi/2$ -rotated fields – as for the two other regimes.

Conclusion : In both three regimes, the presence of helicity does not alter the balance between the kinetic and the magnetic energies. In the high energy regime, it is not clear whether a mean non vanishing current does indeed emerge whenever some helicity is

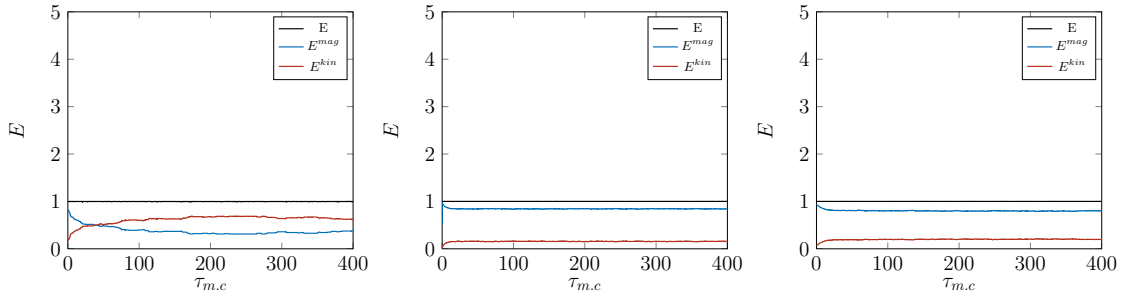

(a) $N^2 = 32^2$, $M = 4$ **(b)** $N^2 = 128^2$, $M = 4$ **(c)** $N^2 = 128^2$, $M = 4$, helical

Figure 5.18: Evolution of the kinetic and magnetic energy in the low energy regime $(E = 1)$, in non-helical (a,b) and helical (c) situations.

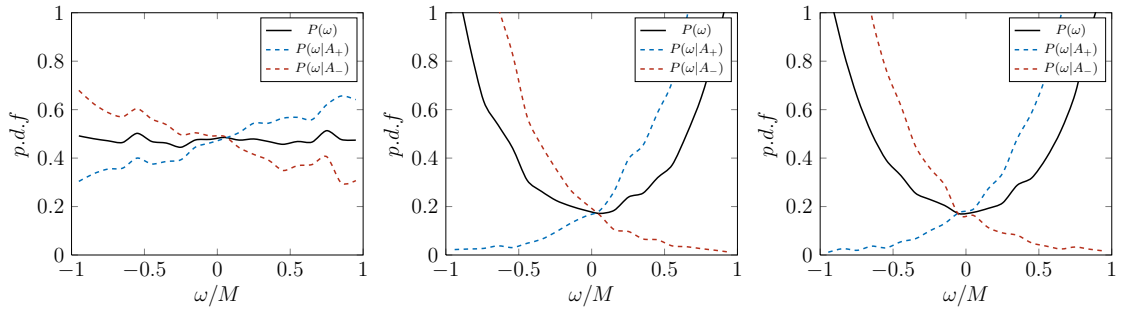

(a) $E = 1$ **(b)** $E = 3$ **(c)** $E = 10$

Figure 5.19: Density of probability of the instantaneous vorticity field. Helical case. $M = 4$. $N^2 = 128^2$

incorporated in the model. It is anyhow blurred by the high level of fluctuations. If such was the case though, the helicity has here the role to enslave the current to the vorticity field. In the low energy regime, the situation is somehow reversed. Without helicity, it is the electric current which spontaneously emerges as a large-scale quantity. With helicity, the vorticity field is proportional to the current : the helicity therefore enslaves the vorticity to the current. The same might be said for the intermediate energy regimes, except that no coherent organization for the electric current is visible.

5.4.4 Conclusion and link to previous works.

In a nutshell. The microcanonical equilibria of the MHD Ising model that we have investigated share similarities with those obtained for the axisymmetric Ising model. They however exhibit a richer phenomenology. This is due to the competition between the long range kinetic energies and the short range magnetic energy and non trivial interactions due to the presence of helical correlations. In the non-helical case, four regimes can be distinguished. The first regime corresponds to the condensation regime described within the framework of absolute equilibria. It is obtained when the gradients of the magnetic potential are far greater than the fluctuations of the kinetic energy. The three other regimes are obtained in the case of a vanishing average magnetic potential. In this case three regions of energies can be distinguished : (i) a large energy regime with a large

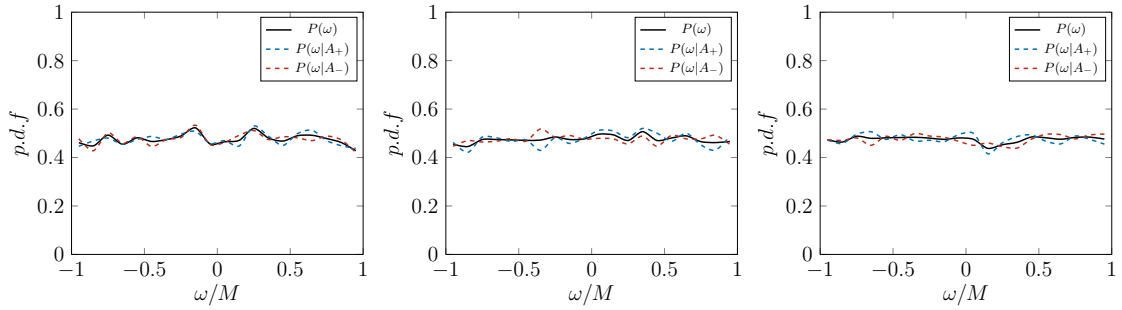

(a) $E = 1$ **(b)** $E = 3$ **(c)** $E = 10$

Figure 5.20: Density of probability of the instantaneous vorticity field. Non-helical case. $M = 4$. $N^2 = 128^2$

scale mean kinetic flow (ii) an intermediate energy regime in which the current and the vorticity are proportional to each other but where no large scale organization emerges, (iii) a low energy regime, in which filaments of current should emerge. In both three regimes, the distribution of the vorticity fields is peaked towards it extrema. We remark that the high energy regime may be seen as the analogue of the the magnetic squared potential positive temperature regime discussed in Chapter 3 in the context of absolute equilibria. Whether this thermodynamic regime is of physical relevance and not only an artifact remains to be discussed. Anyhow the phase diagram is now considerably refined.

We note that other choices of magnetic levels could have been considered. Had we wanted to describe non-infinite hydrodynamics current, we would have considered the case $a_0 \propto 1/N^2$. However, in this case, the magnetic energy would have become negligible with respect to the kinetic energy in the limit of large N. Among all the choices $a_0 \propto 1/N^a$, only $a = 1$ allows for a balanced interplay between the two-kinds of energies. The price to pay is the existence of infinitely large, localized currents. This is a consequence of the Casimirs acting on a large-scale variable (A) – contrarily to the two-dimensional hydrodynamical case.

Link with [Jordan and Turkington, 1997, Weichman, 2012]. The picture that we get from our low level MHD lattice model is very related to the global picture given in [Jordan and Turkington, 1997]. Using a separation of scale hypothesis, which is tantamount to assume that the equilibria can be described in terms of a Gibbsian macrostate probability, it is found in [Jordan and Turkington, 1997] that for low values of the macrostate energy the fluctuation are low, while for high values of the macrostate energy the fluctuations "obliterate the coherent structures". The states that we get in our model are qualitatively similar. In the low energy regime, the microcanonical temperature is low: hence the fluctuations of the energy are small. In the high energy regime, the temperature is formally infinite. However, taking the two limits M and N to ∞ one after another allows us to "zoom" on the high energy regime and find out that the statistics of the fluctuations are not Gaussian in this regime. The zoom yields a ratio of $E^{\text{mag}}/E^{\text{kin}}$ being not necessarily greater than 1 in our model, as opposed to [Jordan and Turkington, 1997]. Note, that

in the present model, the separation of scale hypothesis is not always valid : this is due to the Liouville variables A_{ij} being already large scale, "coarse-grained" variables.

In the more recent and quite compact work of Weichman [Weichman, 2012], the MHD equilibria are derived within a grand canonical ensemble, using the "spin variables" A_{ij} and ψ_{ij}. Within those variables the problem of the unboundedness of the vorticity is circumvented by the assumption that the fields A and ψ have Gaussian fluctuations around their typical state. The balance between the kinetic and magnetic energies is then non trivial. The equilibria are found to describe an alignment of the mean velocity field with the mean magnetic field. Those equilibria also depend on a microscale energy ϵ, which may be related to the kinetic cutoff M of our model. The author observes that "for a spatially irregular initial condition with comparatively large energy, one will have $\epsilon \gg |v_0|^2, |B_0|^2$ and the physical equilibrium fields will be masked by fluctuations". One could make the same observation for the model discussed in the present chapter.

5.5 Conclusion.

The use of Monte-Carlo dynamics allowed us to check the plausibility of the analytical developments related to the axisymmetric microcanonical measures. It led to a practical visualization of those equilibria and made the analogy between stationary measures and lattice models quite vivid. At a yet more heuristic level, it allowed us to comment on the analogy between magnetic ideal flows and axisymmetric flows, using a very simple MHD Ising model and simple physical considerations. In the case where the kinetic fluctuations are disregarded, one retrieves the magnetic condensation regime. In the case where the fluctuations of the kinetic field are taken so as to induce a non trivial balance between the short range magnetic energy and the long-range kinetic energy, one can identify three different regimes, depending on the initial value of the input energy. The high energy and the intermediate energy regime share a striking resemblance to the axisymmetric equilibria. In the present chapter, the algorithms that were discussed were quite naively implemented. Therefore, the presence of long range interactions made it difficult to make finely tuned new predictions. This is an indirect consequence of the velocity field and magnetic field being incompressible. In the case, where the calculation of the energies could be implemented locally, one could however hint that the Creutz algorithm can be a very powerful tool to investigate non trivial hydrodynamical measures. Such an observation could be speculatively of interest for Shallow-water flows.

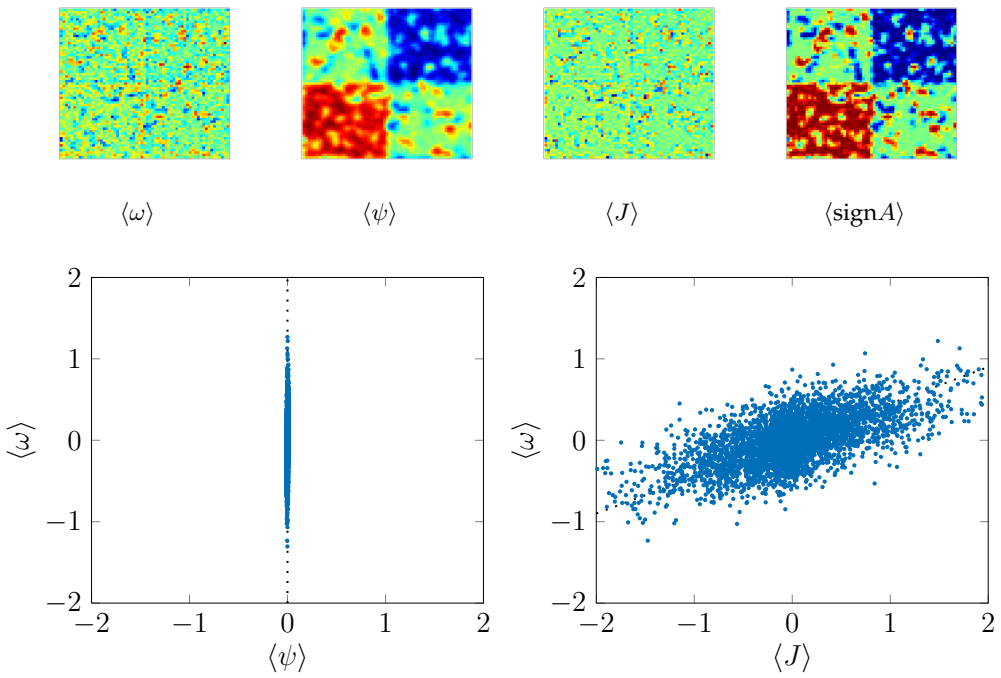

Figure 5.21: $E = 1$. Low energy regime. Helical. Scatter plots of $\langle\omega\rangle$ against $\langle\psi\rangle$ (a) and $\langle J\rangle$ (b). The insets show the corresponding average fields.

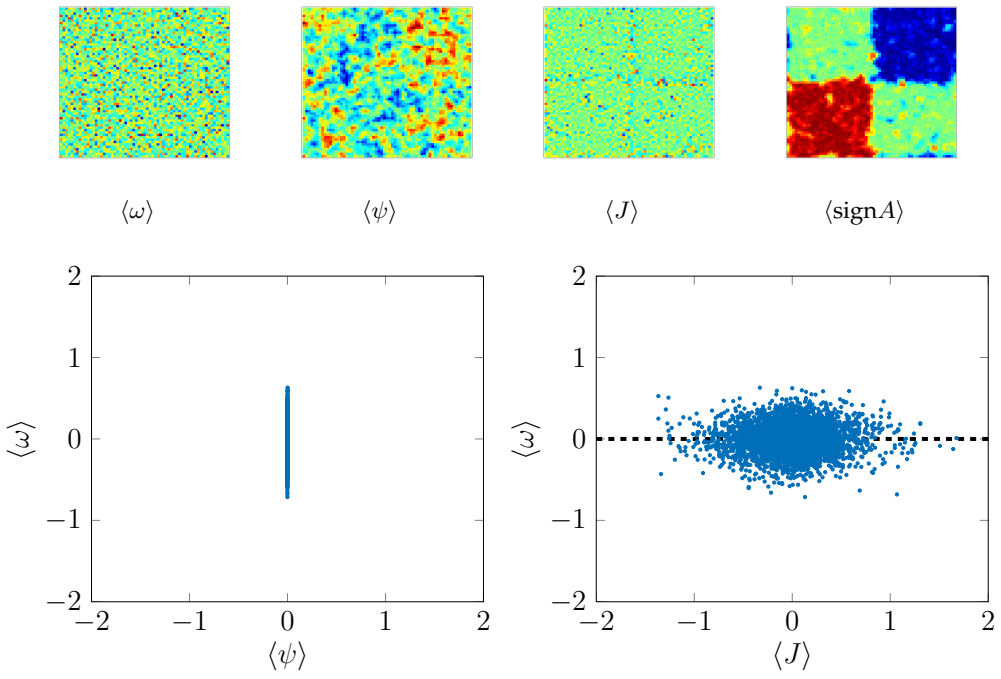

Figure 5.22: $E = 1$. Low energy regime. Non-helical.

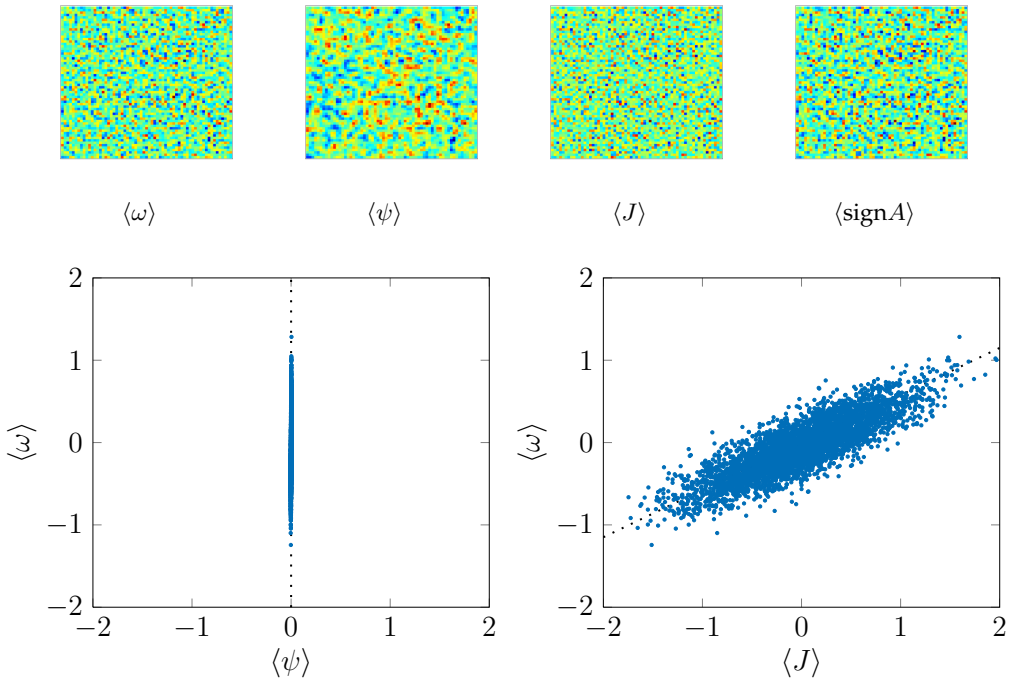

Figure 5.23: $E = 3$. Intermediate energy regime. Helical.

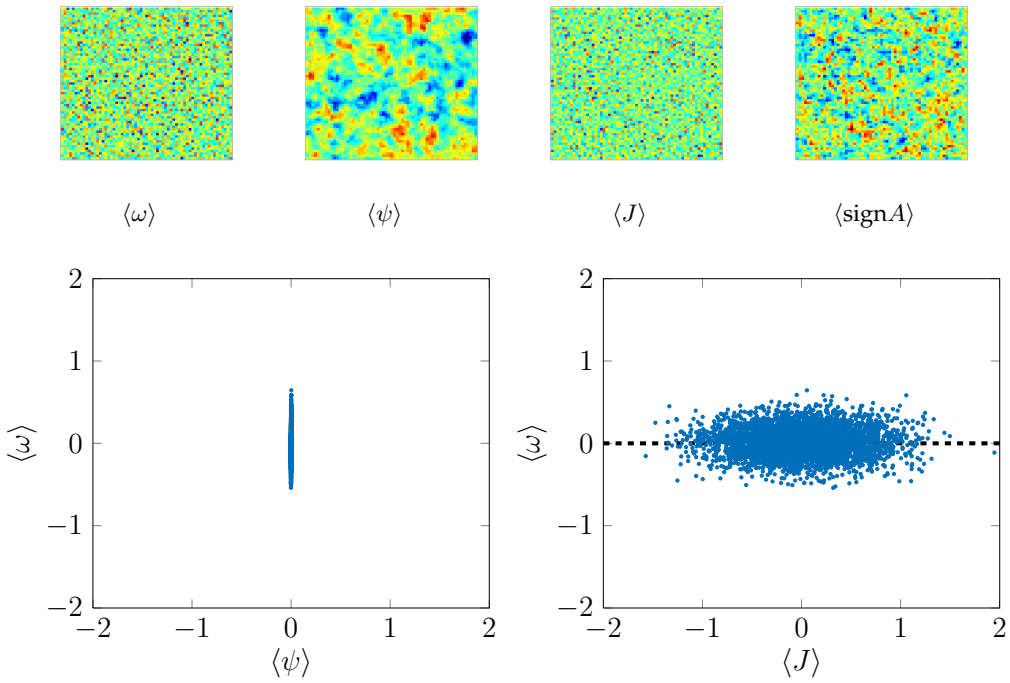

Figure 5.24: $E = 3$. Intermediate energy regime. Non-helical.

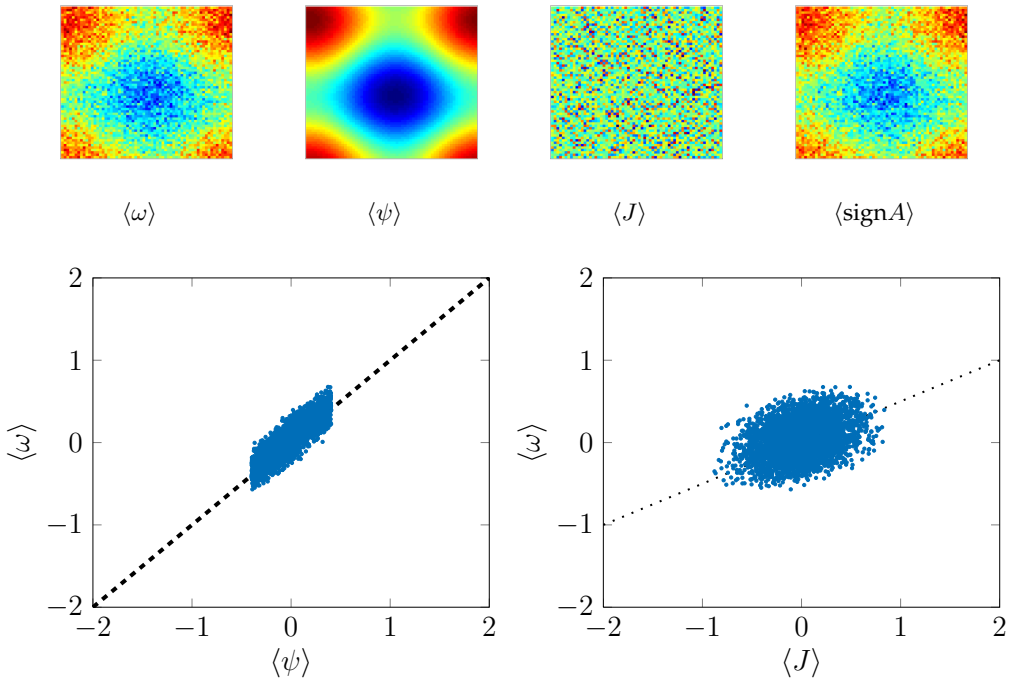

Figure 5.25: $E = 10$. High energy regime. Helical.

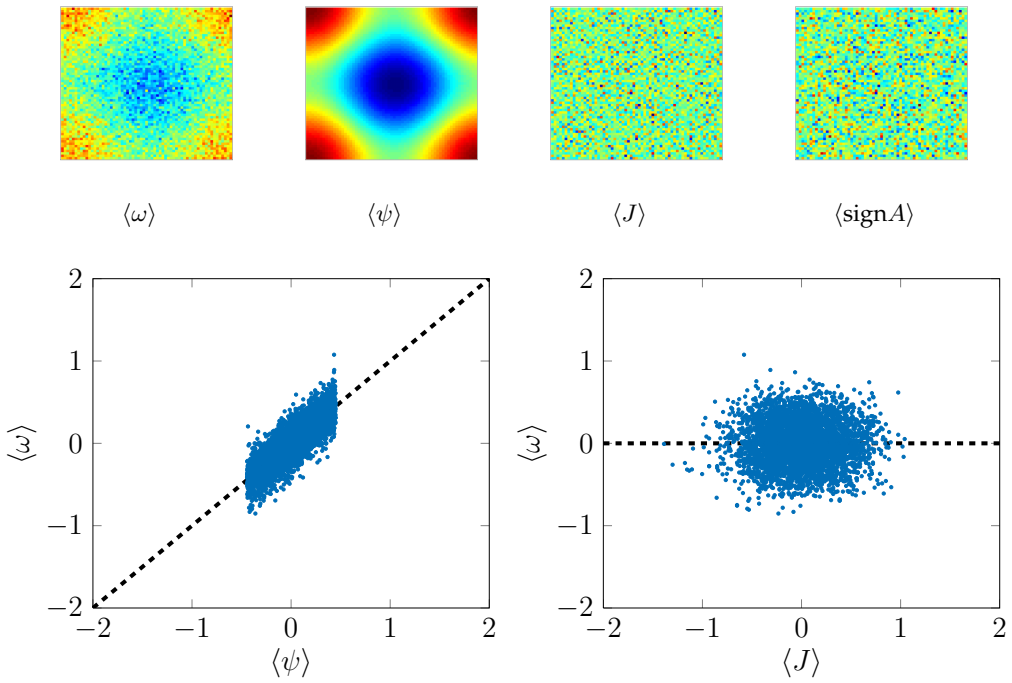

Figure 5.26: $E = 10$. High energy regime. Non-helical.

Part II

Wet use of dry statistical mechanics

Chapter 6

Application : stationary states of a Von Kármán flow.

I hereby discuss whether the highly turbulent coherent states that are observed in experimental Von Kármán turbulent flows can be explained from an equilibrium inviscid statistical mechanics perspective. I argue that there should be no reason to expect that. I then show some experimental evidence that inviscid theories may account for the properties of the Von Kármán steady states. They also give insights about their physics.

Contents

6.1 Introduction

Von Kármán setups. The experimental Von Kármán setup, in which a fluid inside a cylindrical tank is stirred by two propellers located at both ends, has been very popular over the last thirty years. The literature is abundant – see [Ravelet, 2005] for a concise review up to the year 2000. The setup allows to generate a highly turbulent flow using a human size apparatus. The class of flows generated by Von Kármán setups is both fundamental and practical. At a practical level, Von Kármán flows are laboratory models of

geophysical flows, the most emblematic example of which being perhaps the "VKS" experiment – in which the propelled fluid is sodium –, which provides a laboratory model of the turbulent geodynamo [Berhanu et al., 2007,Monchaux et al., 2007]. At a fundamental level, the Von Kármán setup has been used to explore both standard characterizations of swirling turbulence, such as spectra, intermittency, structure functions [Moisy et al., 1999, Moisy et al., 2001, Herbert et al., 2012], and less standard out-of-equilibrium phenomena, such as pressure and power fluctuations [Fauve et al., 1993, Labbé et al., 1996]. More recently, studies have focused on the dynamical properties of the large-scale average structures which exist in highly turbulent Von Kármán flows. Many intriguing physical mechanisms have emerged, among which hysteretic cycles [Ravelet, 2005,Monchaux, 2007], spontaneous "momentizations" and symmetry breaking [de la Torre and Burguete, 2007, Cortet et al., 2010, Cortet et al., 2011], zero-mode mechanisms [Saint-Michel et al., 2013a]... Those phenomena have very strong statistical mechanics connotations, but their study is mostly out of scope of the present chapter. Fresh developments about the dynamics and the out-of-equilibrium properties of Von Kármán flows were recently carried out by Brice Saint Michel, in a thesis [Saint-Michel, 2013] companion to the present one.

Aims. We shall be quite modest here, and focus on the description of the steady states of a Von Kármán setup filled with water. Those steady states are "well-known" : if the forcing is symmetric, one typically observes the appearance of four large scale recirculation cells each filling a fourth of the tank. If the symmetry of the forcing is sufficiently broken, the recirculation cells merge into two cells, which each fills one half of the tank. In the symmetric case, the presence of the cells has a clear mechanical explanation : "The fluid is ejected radially from the disks by centrifugal force and loops back towards the axis in the mid-plane between the impellers. A strong differential rotation is superimposed on this poloidal flow, which generates a high shear in the mid-plane" [Berhanu et al., 2007]. We shall adopt a slightly different point of view here, and discuss whether those large circulation cells are close to a statistical equilibrium. We clearly have in mind to discuss the use of axisymmetric inviscid theories described in the previous chapter to account for the presence of such states. There is no reason why it should be the case. A preliminary connection of Von Kármán steady states with inviscid axisymmetric equilibria was however observed during the PhD thesis of Romain Monchaux, and is reported in [Monchaux et al., 2006].

Organization of the chapter. The chapter is organized as follows. We first present the Von Kármán experimental setup currently at use at the SPHYNX laboratory, and from which the data that we analyze stem from. We then argue about the reasons which make more than dubious the use of axisymmetric inviscid theories to describe the large-scale steady states observed in such a Von Kármán experiment. We finally show that in practice, two inviscid theories, Leprovost's mixing theory and a "frozen axisymmetric" theory, can be used to describe the Von Kármán steady states. The insights provided by both theories are different.

6.2 The "VK" experiments.

I give a rough description of the Von Kármán experiments performed at the SPHYNX laboratory. Such a basic description is partial but is sufficient for our concerns. A thorough description of the present Von Kármán setup at the SPHYNX can be found in Romain Monchaux's or Brice Saint-Michel's thesis papers [Monchaux, 2007, Saint-Michel, 2013]. Older versions of the experiments are described in Louis Marié's and Florent Ravelet's [Marié, 2003, Ravelet, 2005].

6.2.1 Experimental setup

Loose description. In a Von Kármán experiment, a fluid confined in a cylindrical tank is stirred by two counter rotating propellers located at both extremities of the tank. The Von Kármán experiments that have been built and studied at the former GIT and now SPHYNX laboratory are human size Von Kármán experiments. The latest version of the experiment –from which the data of the present chapter come from – is for example $2H = 270mm$ tall, and has a radius $R = 200$ mm. The propellers are separated by a distance $2h = 180$ mm. Their radius rank from 0.5 to 0.925 times the radius of the cylinder. This version of the experiment goes by the code name of "VK2"[(a)]. It was built during the PhD thesis of Romain Monchaux [Monchaux, 2007]. Sketches and photographs of the VK2 experiment are shown on Figures 6.1 and 6.2.

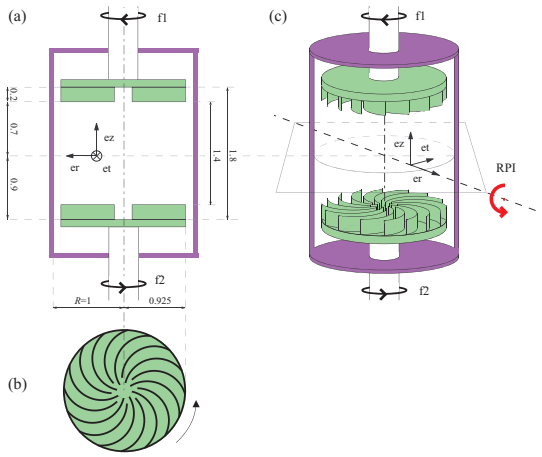

Figure 6.1: Sketch of the VK2 experiment. Taken from [Dubrulle and the VKEteam, 2013].

Intuitive control parameters. One can intuitively expect two parameters to play a significant role in the physics of VK flows. The first one is the (macroscale) Reynolds number Re, estimated as [Ravelet, 2005]

$$Re = 2\pi f R^2 \nu^{-1}. \tag{6.1}$$

The Reynolds number is built on (i) the injection scale, estimated as the radius of

[(a)]Older versions are the "VKE", and "VKR" experiments. I will refer to the flows obtained within all those experiments as "VK" flows.

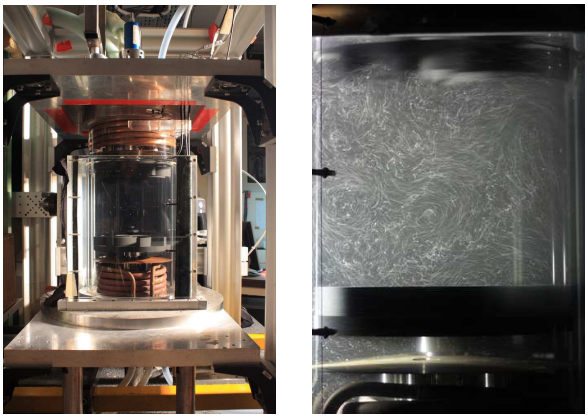

Figure 6.2: The VK2 experiment at rest (a) and in activity (b). Courtesy of Brice Saint-Michel.

the tank R, (ii) the time scale $f = \dfrac{f_1 + f_2}{2}$ with f_1 and f_2 the rotation frequencies of the propellers, and (iii) the viscosity of the fluid which can be tuned by considering appropriate mixture of water and glycerol. In the VK2 experiment, it is possible to explore four decades of Reynolds number from 10^2 to 10^6, upon playing both with the rotating frequency of propellers and/or the dynamical viscosity of the fluid stirred inside the tank.

The second intuitive control parameter is given by the rotation number

$$\theta = \frac{f_1 - f_2}{f_1 + f_2}, \tag{6.2}$$

which measures the relative influence of global rotation over a typical turbulent shear frequency. The exact counter rotating regime corresponds to $\theta = 0$. When θ is non zero, the experimental system is similar, within lateral boundary conditions to an exact counter rotating experiment at frequency $f = \dfrac{f_1 + f_2}{2}$ with an overall global rotation at frequency $\dfrac{f_1 - f_2}{2}$ [Marié, 2003].

There exist however less obvious, hidden parameters that may deeply alter the physics observed in the Von Kármán tank, and on which we shall say a word at the end of the section.

Measures. To characterize the flows obtained in the VK experiments, one has access to two kinds of time series measurements. The first kinds of measurements are made at the level of the propellers. They provide quantities such as the frequencies of the propellers $f_{1,2}$, and also the torques K_{12} exerted by the propellers on the fluid. Those quantities are important to monitor the forcing. The second kinds of measurements are time series of the coarse-grained three components of the velocity field measured on a prescribed meridional plane (e_r, e_z). In the VK2 experiment this information is provided trough PIV and SPIV measurements [(a)]. The PIV and SPIV techniques give access to time series of the three components of the velocity fields measured on a two-dimensional meridional plane

[(a)] "PIV" stands for Particle Image Velocimetry and "SPIV" for Stereoscopic Particle Image Velocimetry

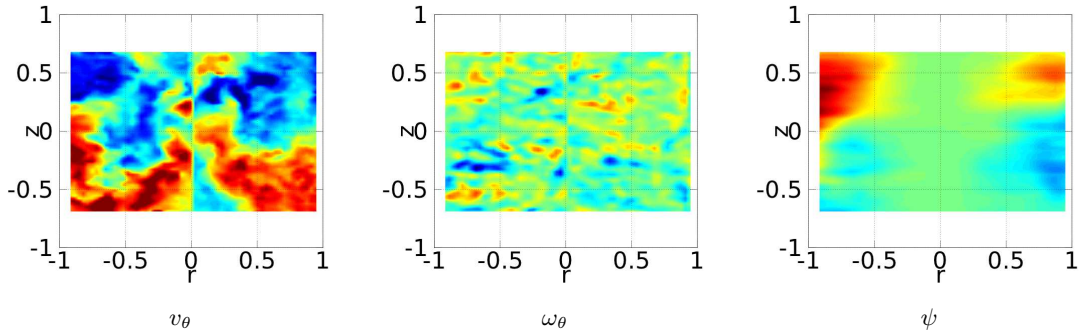

Figure 6.3: Instantaneous fields reconstructed from a SPIV measurements at $Re \simeq 3 \times 10^5$ and $\theta = 0$. Details in text.

$v_r(r,z), v_\theta(r,z), v_z(r,z)$ and sampled on a 58×63 mesh grid. The spatial resolution is approximately 1 cm [Herbert et al., 2012]. The samplings typically vary from 1.7 to 15 Hz , so that one typically gets one velocity map every 1 to 10 rotations of the impellers. Again, a detailed description of those techniques as used for the VK experiments can be found in Romain Monchaux' thesis paper [Monchaux, 2007].

The take-to-the-next-paragraph message is simply the following : the SPIV measurements map a three-dimensional continuous time (fine grained) Von Kármán flow onto a discrete-time, coarse-grained 2D3C flow, defined by the time series of the three components of $v_r(r,z)$, $v_\theta(r,z)$, $v_z(r,z)$ on a prescribed meridional plane. As an example, Figure 6.3 shows three components of such a 2D3C flows, namely an instantaneous toroidal velocity v_θ, a poloidal vorticity $\omega_\theta = \partial_z v_r - \partial_r v_z$ and a stream function ψ reconstructed from the PIV measurements of a three-dimensional turbulent Von Kármán flow at Reynolds approximately 3×10^5 – such as the one depicted on Figure 6.2. One could observe that the toroidal and poloidal fields seem discontinuous at $r = 0$. Such a discontinuity is however not physical : it comes from the discrete nature of the Eulerian grid which is used to reconstruct the fields from the PIV measurements.

It is crucial to emphasize that the instantaneous vorticity and velocity fields are *not* axially symmetric. This can be seen on Figure 6.3 : neither of the fields are symmetric with respect to the transformation $r \to -r$ [(a)] as it should be the case, if the flow was indeed axially symmetric.

Coarse-Grained quantities. From the instantaneous PIV fields v_r, v_θ, v_z, coarse -grained quantities such as coarse-grained energies, helicities and so on can be computed. Note that the coarse-grained quantities computed from the instantaneous fields may be very different from their fine-grained analogues (i) as a result of the coarse-graining and (ii) because the PIV window does not cover the entire meridional plane, but only a small region $\mathcal{D}_{\text{piv}}$ of it. To make things unambiguous when needed, I will write $\bar{X}$ the value

[(a)] or rather $\theta \to \theta + \pi$

of the observable X computed from the instantaneous fields. The energies, meridional helicities, toroidal momenta computed from the instantaneous field will for instance be computed as :

$$\bar{E} = \frac{\int_{\mathcal{D}_{\text{piv}}} r\mathrm{d}r\mathrm{d}z\,(v_r^2 + v_z^2 + v_\theta^2)}{2\int_{\mathcal{D}_{\text{piv}}} r\mathrm{d}r\mathrm{d}z}, \qquad \bar{H} = \frac{\int_{\mathcal{D}_{\text{piv}}} r\mathrm{d}r\mathrm{d}z\,\omega_\theta v_\theta}{\int_{\mathcal{D}_p} r\mathrm{d}r\mathrm{d}z}, \bar{I} = \frac{\int_{\mathcal{D}_{\text{piv}}} r\mathrm{d}r\mathrm{d}z r v_\theta}{\int_{\mathcal{D}_{\text{piv}}} r\mathrm{d}r\mathrm{d}z}, \tag{6.3}$$

and so on for the other observables.

6.2.2 What do we see in a Von Kármán flow ?

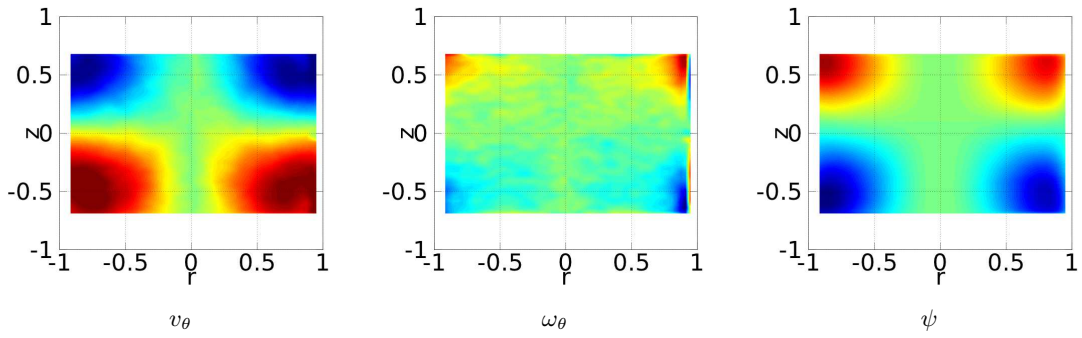

Figure 6.4: The fields of Figure 6.4 averaged over 600 snapshots.

Axisymmetric time averages. It is natural thing to compute "ensemble averages" using the time series of the PIV instantaneous fields. We will write $\langle \bar{X} \rangle$ the ensemble average of the quantity $\bar{X}$. With respect to the true dynamics, the averages $\langle\rangle$ are not really time averages, though : the sampling frequency is not synchronized with the rotating frequencies of the propellers. Therefore, averages made on the times series of the PIV measurements are both time averages and azimuthal averages. The notation "$\langle\rangle$" therefore hides an operation of the kind "$\frac{1}{2\pi T}\int_0^T \int_0^{2\pi} \mathrm{d}\theta$". Hence, it is natural to expect and to assume that the average flow defined by the three quantities $\langle v_r \rangle$,$\langle v_\theta \rangle$, $\langle v_z \rangle$ is axisymmetric. The symmetry $r \to -r$ which emerges on Figure 6.4 shows that this assumption is more than reasonable.

Since the average flow is axisymmetric, it is natural to compute an axisymmetric stream function ψ, obtained from the poloidal velocity fields v_r and v_z as

$$v_r = -\frac{1}{r}\partial_z \psi \quad , \quad v_z = \frac{1}{r}\partial_r \psi \quad \text{and} \quad \psi(r=0,z) \equiv 0. \tag{6.4}$$

For the instantaneous PIV flow, the incompressibility condition $\nabla \cdot \mathbf{v} = 0$ involves a non-vanishing term $\frac{1}{r}\partial_\theta v_\theta$. The instantaneous stream function is therefore ill-defined. It is a way to encode the poloidal velocity field rather than a physical quantity. It is only after the averaging operation $\langle\rangle$ takes place, that ψ can be thought of as a genuine axisymmetric stream function.

What do VK flows look like ? At a dynamical level, the phenomenology of Von Kármán turbulence is both complicated, rich and potentially complex. It exhibits many intriguing physical phenomena : zero modes mechanisms, hysteretic cycles, phase transitions, spontaneous toroidal magnetization, chaotic dynamics... The description of those phenomena is mostly out the scope of the present chapter. The average stationary states of the VK flows are more simple to describe. This is what we do here.

Mean flows. What does a stationary flow typically look like ? The most obvious feature of Von Kármán flows is the presence of a large scale average Beltrami flow : the average large scale vorticity is proportional to the average large scale velocity. In the exact counter rotating regime ($\theta = 0$), and provided that the Reynolds number is large enough ($Re \gtrsim 10^3$), the standard mean flow is divided into two toric recirculation cells, separated by an azimuthal shear layer, as shown on Figure 6.4 [(a)]. If θ is driven away from zero, a change of topology occurs at a critical value θ_c : the mean flow bifurcates from the two-counter rotating recirculation cells to a single cell [Ravelet, 2005]. The critical value θ_c and the sharpness of the transition depend on the geometry of the propellers, the forcing, and so on.

Transitions. The transition between the two-recirculation cells towards the single cell has a very strong statistical mechanics flavor when put in perspective with the Reynolds number. The susceptibility of the flow $\chi = \dfrac{\mathrm{d}\langle \bar{I} \rangle}{\mathrm{d}\theta}$ to symmetry breaking is found to be possibly divergent near $Re = 10^5$ [Cortet et al., 2010, Cortet et al., 2011]. If one replaces the words "toroidal momentum" ($\langle \bar{I} \rangle$) by the word "magnetization" , the word "rotation number " by the word "external magnetic field", and thinks of the (logarithm of the) Reynolds number as an inverse temperature – $T \propto 1/\log Re$ as proposed in [Castaing, 1996] – , the analogy between this transition and a paramagnetic-ferromagnetic phase transition is striking. We shall say later a few more words about this analogy.

Spectra. At $\theta = 0$, the turbulence inside the tank is very anisotropic. The energy spectra is steeper than Kolmogorov's, with an exponent varying between -2 and -2.4, depending on the Reynolds number [Herbert et al., 2012]. The exponent can be obtained using a phenomenological reasoning *à la* Kolmogorov, under the three assumptions (i) of a downward cascade of helicity, (ii) local or non-local interactions between the modes, and (iii) a "maximal helicity", "Betrami" working assumption that the velocity is proportional to the vorticity – not only at large scale.

Forcing dependent turbulence. At a finer level of description, one finds out that the turbulence inside the tank may strongly depend on hidden, or at least no so obvious parameters. Von Kármán turbulence is forcing-dependent in at least two aspects. First, different propellers produce different kinds of turbulence. The radius of the turbines, the presence of blades, their height, their curvature, their number are as many parameters that change the properties of the turbulence within the tank [Ravelet, 2005]. For instance,

[(a)] From now on, we describe the structures in the half-meridional plane $r \geq 0$.

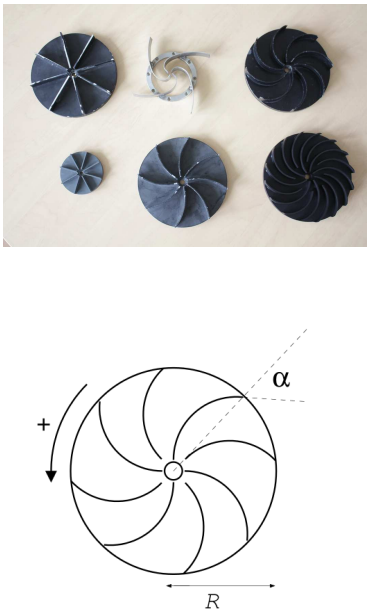

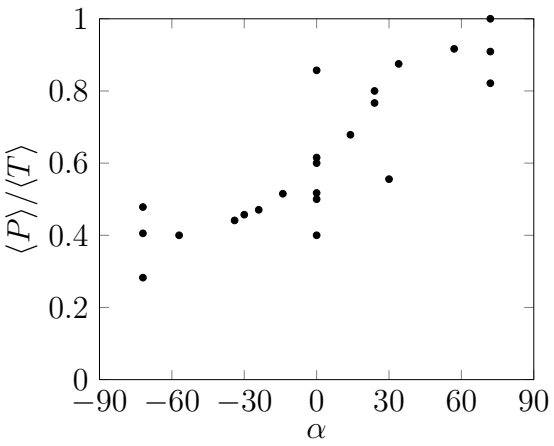

Figure 6.5: (a) Partial zoology of the propellers currently at use in the VK experiments. A "TM60" propeller is visible at the bottom right of the picture; a "TM73" propeller at the bottom center. (c) shows the influence of the curvature (b) of the blades on the ratio between the large scale poloidal component of the velocity field $< P >$ and the large scale toroidal component $< T >$ for reynolds numbers $Re \sim 10^5$ and a vanishing rotation number. Taken from [Ravelet, 2005].

at a qualitative level, the higher the blades, the more helical is the forcing of the experiment; the curvier the blades the more poloidal is the large scale flow – see Figure 6.5. In the present chapter, the turbulence is obtained with either "TM60" propellers, with 16 blades and a curvature $\alpha = 72°$ or "TM73" propellers with 8 blades and $\alpha = 24°$.

Secondly, different stirrings produce different steady states. If one monitors the injected power inside the experiment by controlling the torques that the turbulence exerts at each propeller, one obtains a richer phase diagram than if one monitors the rotation frequencies f_{12} of the propellers [Saint-Michel et al., 2013b].

6.3 Inviscid Statistical mechanics and Von Kármán experiments: general considerations.

Compared to the rich variety of dynamical and out-of-equilibrium properties of VK flows, the aim of inviscid statistical mechanics is quite modest. What do we expect for it ? Basically, we could want the inviscid theory to provide a good qualitative description of the stationary states, correctly predicting the presence of a mean large scale Beltrami flow, giving some hints about the distribution of vorticity and velocity fluctuations and about the interplay between the different kinds of energy at stake (poloidal/toroidal). There are however not too many reasons to expect that. One can think of many reasons why it should not be the case.

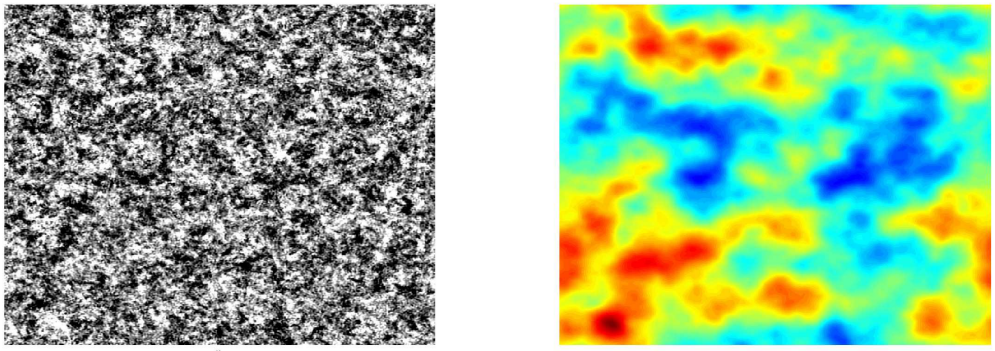

$\langle \omega_z \rangle_z$ $\langle \psi \rangle_z$

Figure 6.6: The averaging along the z direction in a 512^3 Taylor Green Direct Numerical Simulation, forced at $k = 4$ in a triply periodic box, at a late time ($\tau \simeq 15$ turn-over time). Courtesy of Duane Rosenberg.

7 Reasons which make the use of an axisymmetric inviscid theory dubious for Von Kármán flows.

(i) We have in mind to use some results obtained for the axisymmetric Euler Equations to account for the properties of forced-stirred VK flows. But as already remarked, it is only at the level of the mean flows that such a comparison is legitimate. The dynamics of the flows inside the tank is not axisymmetric. It would not preserve the axisymmetric invariants even if the forcing and the dissipation were weak ! There is either no reason why the dynamics of the average flow should described by the axisymmetric Euler equations. For example, let us take for granted the argument that the average $\langle\rangle$ is an azimuthal averaging $\frac{1}{2\pi}\int_0^{2\pi} \mathrm{d}\theta$. Let us also assume that the forcing is weak. It is then well known that the dynamics of the velocity $\langle \mathbf{v} \rangle$ involve interactions of the kind $\langle (\langle \mathbf{v}_i \rangle - \mathbf{v}_i)(\langle \mathbf{v}_j \rangle - \mathbf{v}_j) \rangle$ that will add a turbulent viscosity – through a Reynolds stress – to the dynamics. There is no reason to expect that the 2D3C average flow which is measured will be close to a non-trivial axisymmetric stationary state. If one looks at the vorticity field obtained in a numerical simulation of 3D turbulence forced at large scale with a Taylor Green flow and average the vorticity on one direction, one does not find an obvious large-scale self-organization of the average vorticity field, as predicted by two-dimensional inviscid statistical theories – see Figure 6.6.

(ii) The presence of forcing and dissipation puts the system clearly out of equilibrium. This is confirmed by the presence of an energy spectra consistent with the assumption of an upward (from large to small scale) helicity cascade [Herbert et al., 2012].

(iii) The presence of a forcing does not automatically rule out the use of inviscid theories. In the limit of weak forcing and weak dissipation, computer simulations of the stochastic two-dimensional Navier-Stokes equations have shown that the stationary states were close to inviscid equilibrium states [Bouchet and Simonnet, 2009].

The presence of a *Large-Scale* forcing might however be more of a problem. In particular, one can hardly invoke a separation of scale working hypothesis : the structures that we want to describe are at the same scale than the injection scale.

(iv) The presence of a viscosity, even small, might be problematic in the intrinsically three-dimensional Von Kármán flows. The limit $Re \to \infty$ might very well be a singular limit.

(v) What kind of statistical mechanics description should we use : microcanonical ? canonical ? Grand Canonical ? The relevance of the canonical description to account for the properties of small scaled stirred turbulence have been suggested in [Turkington et al., 2001, Chavanis, 2005, Salmon, 2012]. In the presence of a Large scale forcing, this is less clear. At a very qualitative level, if one reminds himself of the Kraichnan's mock equilibria for axisymmetric turbulence described in Chapter 3, the ratio of the poloidal to the toroidal energy was found to be given by the ratio of two Lagrange multipliers [(a)]. In the experiment, this ratio depends on the curvature of the propellers – see Figure 6.5. This suggests that canonical temperatures could be used to measure the properties of a forcing. However, we can anticipate that the statistics of the fields will turn out to be strongly non-Gaussian. Hence, rugged invariants would need to be supplemented by other invariants.

(vi) In the present case, it is hard to see how to make a good use of a fully microcanonical statistical theory to account for the properties of Von Kármán turbulence. For example, we do not know what the total kinetic energy of the flow (E or $\langle E \rangle$) is. All we have access to are coarse grained quantities $\langle \bar{E} \rangle$, $\langle \bar{H} \rangle$, and coarse-grained distributions. This suggests that an inviscid theory can at best describe Von Kármán flows *a posteriori*. If one measures $\langle \bar{E} \rangle$, $\langle \bar{H} \rangle$, and relevant coarse grained distributions, one may make relevant predictions. However, one cannot predict those quantities from scratch, knowing say only the properties of the forcing or the power injected in the apparatus.

(vii) How many invariants should we take into account ? Only a finite set of them, as in Leprovost's theory ? Or potentially many ?

Conclusion. It is not so clear whether one could counter argue those objections one by one. But it may be good to have them in mind. Let us however move forward. We will show, that in spite of those a priori considerations, the stationary states obtained in Von Kármán are very reminiscent of the axisymmetric ideal equilibria, and can be interpreted as quenched axisymmetric equilibria.

6.4 Inviscid Statistical mechanics and Von Kármán experiments: practical considerations.

We discuss the stationary states obtained in the Von Kármán experiments, when the flow is stirred by TM60 or TM73 propellers.

[(a)] Recall "$\langle E_{\text{tor}} \rangle / \langle E_{\text{pol}} \rangle = \beta/(\beta + \epsilon)$."

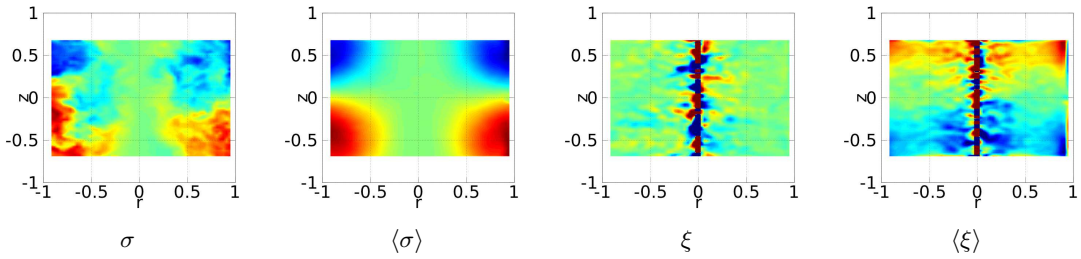

Figure 6.7: Instantaneous and average toroidal and poloidal fields obtained with "TM60" propellers at $\theta = 0$ and $Re \simeq 3 \times 10^5$.

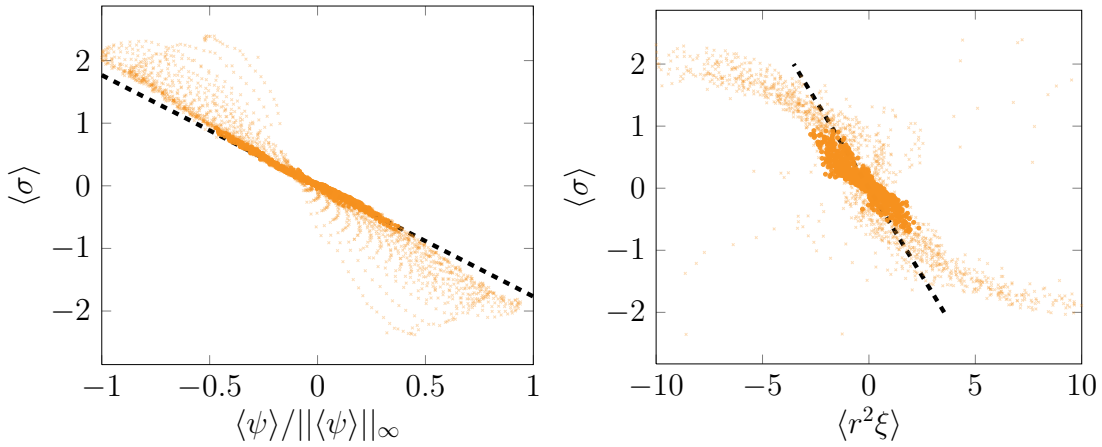

Figure 6.8: characterization of Von Kármán stationary solutions "TM60" propellers at $\theta = 0$ and $Re \simeq 3 \times 10^5$. $||\langle\psi\rangle||_\infty = \max_{\mathcal{D}_p}\langle|\psi|\rangle$. Opaque points are the points measured far from the propellers. The dotted lines show $\langle\sigma\rangle = B\psi$ and $\langle\sigma\rangle = \langle r^2\xi\rangle/B$. B is obtained from (a).

6.4.1 Von Kármán average flows vs ideal axisymmetric flows

Von Kármán Stationary states are close to inviscid axisymmetric stationary states. To begin with, let us put the statistical mechanics considerations aside, and observe that the Von Kármán average states are reasonably close to inviscid axisymmetric stationary states. The ideal axisymmetric stationary flows were already mentioned in passing in chapter 4 – Equation (4.2). We recall that those flows are many : they can be any flow satisfying

$$\sigma = F(\psi), \qquad \xi(\mathbf{r}) = r^{-2}F(\psi)F'(\psi) + G(\psi), \quad \text{and} \quad \xi = -\Delta_\star\psi, \tag{6.5}$$

with F and G any sufficiently regular functions.

Empirically, it was observed that the average toroidal and poloidal fields $\langle\sigma\rangle$ and $\langle\psi\rangle$ do satisfy the relations (6.5). Let us look for example at the central region of the tank, far from the propellers. On the PIV fields, a bulk region can be defined as $|z| \leq 0.5$ and $r \leq 0.5$. Within those bounds, one finds out that a linear F ($F(x) = Bx$) and a constant G

($G = C$) reasonably fit the data, as shown on Figures 6.7 and 6.8. Hence, it is reasonable to assert that the average states of the Von Kármán flows are close to inviscid axisymmetric steady states, almost entirely described by two parameters, B and C :

$$\langle \sigma(\mathbf{r}) \rangle = B \langle \psi(\mathbf{r}) \rangle, \qquad \langle \xi(\mathbf{r}) \rangle = r^{-2} B^2 \psi(\mathbf{r}) + C, \quad \text{and} \quad \xi = -\Delta_\star \psi, . \tag{6.6}$$

The observation is not new. It was made during the PhD thesis of Romain Monchaux [Monchaux, 2007] : in spite of the three-dimensionality of the experiments, the averages of Von Kármán steady flows are somehow close to some steady axisymmetric inviscid flows.

6.4.2 Practical description of the steady states using Leprovost's statistical theory.

Reminder of the theory. Based on the observation of Monchaux, Nicolas Leprovost, with the help of Pierre-Henri Chavanis and Bérengère Dubrulle proposed a "practical use" of the maximum entropy principle, as accounted for in Chapter 4. They found that extremizing a mixing toroidal entropy under the constraints of prescribed macrostate energies, helicities and toroidal momenta, precisely yields the set of equations (6.6). The reader can check that there is no magic trick : the set of equations (4.5) of Chapter 4 is exactly the same as the set of equations (6.6) of the present chapter. The theory provides a very elegant and fruitful interpretation of the equilibria. The coefficients B and C can be expressed as functions of the prescribed macrostate quantities. It happens that the macrostate quantities are precisely related to the quantities that can be measured from the PIV average fields. The macrostate energies, helicities and toroidal momenta introduced in Chapter 4 were the axisymmetric quantities :

$$H_\odot = \frac{1}{\mathcal{D}} \int_{\mathcal{D}} \bar{\xi}\bar{\sigma}, \qquad E^{c.g}_\odot = \frac{1}{2|\mathcal{D}|} \int_{\mathcal{D}} \frac{\bar{\sigma}^2}{r^2} + \bar{\xi}\bar{\psi} \quad \text{and} \quad I_\odot = \frac{1}{|\mathcal{D}|} \int_{\mathcal{D}} \bar{\sigma}, \tag{6.7}$$

with the "$\bar{.}$" denoting a local averaging. The coefficients B and C are then prescribed as $B = B(I_\odot^2/H_\odot)$ and $C = C(I_\odot, B_\odot)$ – see [Naso et al., 2010b] or Figure 4.3 of Chapter 4.

Inside the tank. The counterparts of the latter quantities in the experiment need to be measured directly on axisymmetric quantities, that is to say on the averages of the PIV fields :

$$H_\odot = \frac{1}{\mathcal{D}} \int_{\mathcal{D}} \langle\bar{\xi}\rangle\langle\bar{\sigma}\rangle, \qquad E^{c.g}_\odot = \frac{1}{2|\mathcal{D}|} \int_{\mathcal{D}} \frac{\langle\bar{\sigma}\rangle^2}{r^2} + \langle\bar{\xi}\rangle\langle\bar{\psi}\rangle \quad \text{and} \quad I_\odot = \frac{1}{|\mathcal{D}|} \int_{\mathcal{D}} \langle\bar{\sigma}\rangle. \tag{6.8}$$

Recall that the PIV window does not cover the entire tank, so the integrals estimated from the PIV are rather $\int_{\mathcal{D}_{\text{piv}}}$ instead of $\int_{\mathcal{D}}$. To fix this, one needs to normalize the theoretical curb by putting an effective height $h^\star$ and an effective radius $R^\star$ instead of the true dimensions of the tank. But then, if one measures B, $I_\odot$ and $H_\odot$ independently from the PIV fields, and plot B as a function of $I_\odot^2/H_\odot$, it is found out that the measurements agree extremely well with the theoretical prediction – see for instance Figure 6.9, as the preliminary work of Monchaux et al suggested [Monchaux et al., 2006].

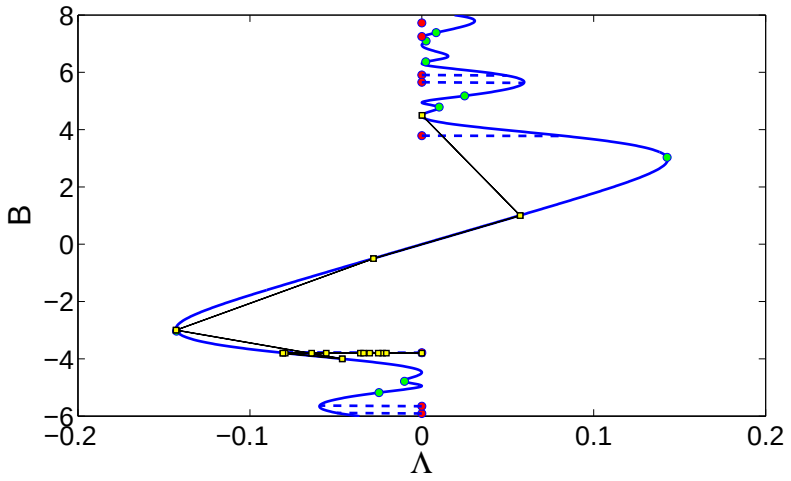

Figure 6.9: B as a function of Λ for TM73 propellers at $Re = 10^6$. The blue line is the theoretical prediction, the yellow squares are the points corresponding to the experiments.

What we do learn ...and do not learn from Leprovost's theory. Looking at Figure 6.9, it seems pretty hard to do better than Leprovost's mixing theory. The data fits well, and the theory is linear – therefore not too complicated. The latter provides a compact framework to interpret and classify the Von Kármán steady states. It highlights the role of the toroidal mixing and shows that an inviscid theory can account for forced steady turbulence. This was by no mean obvious. In spite of this successful description, there remain some issues, that may be significant to address :

(a) When one looks closely at Figure 6.9, one can remark that although many 'B' are compatible with the same value of Λ, the experiment selects a "small" B, which corresponds to a single cell or a dipole – in the half cylinder. The mixing theory does not tell why this particular "B" is selected: it simply accounts for it.

(b) It does not explain the role of the invariants that are singled out. It is mostly a data driven choice : to obtain linear fits, one hast to plug in the maximization of the entropy some quadratic invariants. We don't know whether the data that are not fitted by the linear fit (the points closer to the propellers) are close to a more complex equilibrium or if the theory only works in the bulk of the tank.

(c) The mixing which is invoked in the theory is mostly conceptual. We have already mentioned that the instantaneous 2D3C flow as obtained from the PIV measurements was not axisymmetric, and that the 2D3C axisymmetric averages flow had no reason to be described by an axisymmetric ideal dynamics. Since the quantities that control the parameters B and C are computed directly from the axisymmetric static state, it is not clear whether the use of a mixing entropy accounts for an underlying physical mixing process. From the coarse grained point of view, it rather resembles to an inference theory (*à la* Jaynes).

In the next section, we will adopt a slightly different point of view, that may shed some light about those three issues and about the nature of the steady states in the Von Kármán flows.

6.4.3 Steady Von Kármán flows from a frozen, helical perspective.

We focus on the case of a vanishing rotation number $\theta \simeq 0$, and discuss the statistics of the signs of the poloidal and fields, in the spirit of the analogy with an axisymmetric long range lattice model. We study the influence of the Reynolds number on the stationary states. The analysis shows that the Von Kármán steady states can be interpreted as experimental analogues of the $M = 0$ frozen axisymmetric equilibria mentioned in the previous chapters and described in Appendix E.

Statistics of the signs of the fields. Instead of trying to describe the average fields, let us here only focus on the statistics of the signs of those fields. As explained in the first section, a Von Kármán acquisition yields a discrete time series of instantaneous PIV fields. Instead of studying the full statistics, we restrict ourselves to the time series of the signs of the toroidal and poloidal field. In order words, we play the following game : we deteriorate each instantaneous field σ by mapping them onto the two-value fields $\text{sign}(\sigma)$ defined as

$$\text{sign}(\sigma)(\mathbf{r}) = \begin{cases} +1 & \text{if } \sigma(\mathbf{r}) > 0 \\ -1 & \text{otherwise} \end{cases}, \tag{6.9}$$

We perform a similar operation for the toroidal fields ξ. We then compute the averages of those binary fields, $\langle \text{sign}(\sigma) \rangle$, $\langle \text{sign}(\xi) \rangle$ – see Figure 6.10.

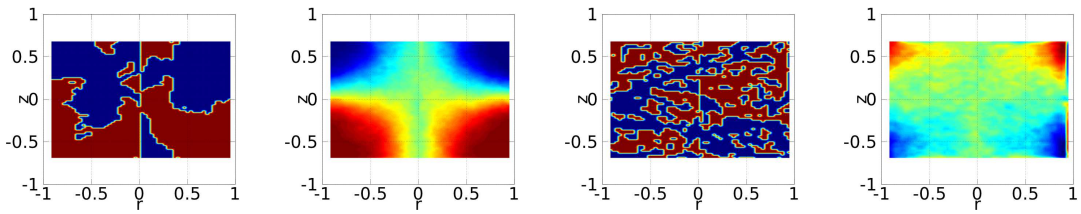

(a) signσ **(b)** $\langle \text{sign}\sigma \rangle$ **(c)** signξ **(d)** $\langle \text{sign}\xi \rangle$

Figure 6.10: The instantaneous and average signs of the toroidal and poloidal fields, using TM60 propellers at $\theta = 0$, $Re = 3 \times 10^4$.

Toroidal areas and generalized helicities. With the axisymmetric Beltrami-Ising model analogy in mind, it is quite natural to look at the temporal evolution of those quantities that play a key role in the inviscid theory :

$$\begin{aligned} \mathcal{A}_\pm(\tau) &= \int_{\mathcal{D}_{\text{piv}}} r\mathrm{d}r\mathrm{d}z\mathbf{1}_{\text{sign}(\sigma)=\pm 1}, \qquad \mathcal{X}_\pm(t) = \int_{\mathcal{D}_{\text{piv}}} r\mathrm{d}r\mathrm{d}z\xi\mathbf{1}_{\text{sign}(\sigma)=\pm 1}, \\ \text{and} \quad \mathcal{E}_{\text{pol}}(\tau) &= \int_{\mathcal{D}_{\text{piv}}} r\mathrm{d}r\mathrm{d}z\xi\psi. \end{aligned} \tag{6.10}$$

We also write $\mu(\tau) = \dfrac{\mathcal{A}_+(\tau) - \mathcal{A}_-(\tau)}{\mathcal{A}_+(\tau) + \mathcal{A}_-(\tau)}$ and $\mathcal{X}(\tau) = \mathcal{X}_+(\tau) + \mathcal{X}_-(\tau)$. As can be expected, those quantities are not constant throughout time – see Figure 6.11. We can remark that there is no substantial difference between the behavior of the poloidal energy $\mathcal{E}_{\rm pol}(\tau)$ – which is not an ideal invariant– and the behavior of the toroidal areas $\mathcal{A}_\pm(\tau)$ or the generalized helicities/parital cicrulations $\mathcal{X}_\pm(\tau)$. Thoses quantities fluctuate around a mean value. The fluctuations are rather mild. Their distributions are not displayed here but are essentially Gaussian.

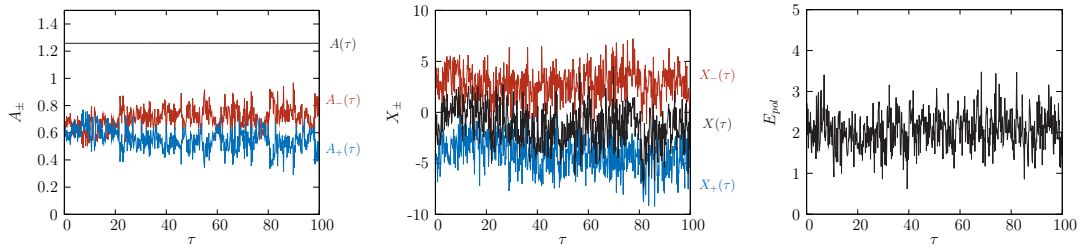

(a) **(b)** **(c)**

Figure 6.11: (a,b,c) : Time evolution of the inviscid toroidal invariants $A_\pm$, $X_\pm$, and of the poloidal energy $\bar{E}_{\rm pol}$, $\theta = 0$, at $Re = 3\times10^4$ and using TM 60 propellers. The time is in seconds.

It is interesting to observe that the mean values $\langle \mathcal{X}_\pm \rangle$ of the generalized helicities are very distinct from one another. The two time series of $\mathcal{X}_\pm(\tau)$ remain distinct throughout time.

This feature is significant. If we now look at the distribution of the toroidal field, built from the 600 instantaneous fields, we find out that the distributions $P(\xi|\text{sign}(\sigma) = \pm 1)$ (conditional probabilities) and $P(\xi)$ distinct from one another. The most probable values $\xi_\pm$ of $P(\xi|\text{sign}(\sigma) = \pm 1)$ are very reasonably approximated by the quantity $\langle \dfrac{\mathcal{X}_\pm}{\mathcal{A}_\pm} \rangle$ – see Figure 6.12(a).

Besides, the three distributions are strongly non Gaussian. Their tails are fatter. This is not a spurious effect due to a bad numerical reconstitution of the poloidal field near the central vertical axis of the cylindrical tank – see Figure 6.12(b).

These observations call for two comments. (i) The non-Gaussian behavior of the poloidal field is reminiscent of the non-Gaussian statistics that was predicted by the inviscid axisymmetric microcanonical theory of Chapter 4. (ii) The existence of distinct maxima is an indication of a tendency of the poloidal field to get aligned or anti-aligned with the toroidal field. The values $\xi_\pm$ are finer indicators of the presence of vorticity velocity correlations than the total average axisymmetric helicity given by equation (6.8), which in the present case is close to zero.

"$\tanh$" laws and "frozen" equilibria. The next natural step to take is to see what kind of mean-field relation – if any – the averages of the toroidal and poloidal signs do satisfy. Scatter plots at $Re = 3 \cdot 10^5$ are shown on Figure 6.13.

The scatter plot of $\langle \text{sign}(\xi) \rangle$ against $\langle \psi \rangle$ indicates the presence of a linear relation between both quantities : this is very reminiscent of the axisymmetric equilibria described in Chapter 4. The scatter plot of $\langle \text{sign}(\sigma) \rangle$ against $\langle \psi \rangle$ is however not so reminiscent of

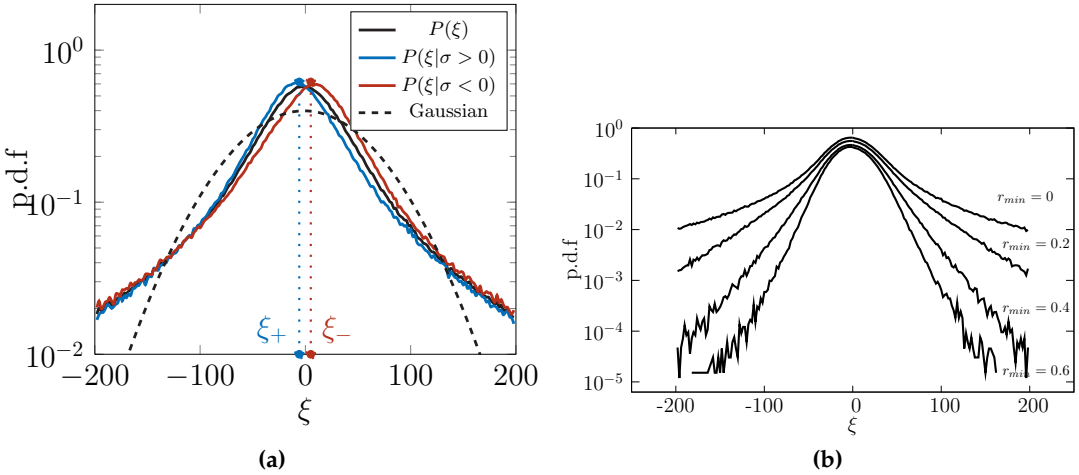

Figure 6.12: (a) : probability density function for the toroidal field ξ, computed from the time series of the fields (involving $56 \times 61 \times 600 \simeq 2 \cdot 10^6 points$). (b) Probability functions computed without considering the points below a treshold radius $r_{\min}$.

those. Instead, a "tanh " law emerges. A "tanh" for the toroidal field is not prescribed by the full inviscid theory, which prescribes that the stream function and the toroidal field be independent. One way to see things is to conclude is that the Von Kármán steady states are not inviscid axisymmetric equilibria. We did not really expect them to be anyway. This makes the story end here. Another way to see things is to observe that the toroidal scatter plot has a very "two-dimensional" connotation. As explained in Chapter 4, tanh laws emerge naturally when one works out a mean-field statistical mechanics for the 2D Euler equations with only two levels (or two signs) of vorticity. Closer to the present chapter, one can remind that a similar toroidal law was obtained from a Monte-Carlo dynamics in Chapter 5 – see Figure 5.7. This was the case when the poloidal cutoff was not high enough to mix the poloidal degrees of freedom independently from the toroidal degrees of freedom ("$M = 0$"). We had casually described this regime as a "frozen" or "quenched" regime, in which not only the conditional poloidal averages but the full conditional poloidal probability distributions are prescribed. Those equilibrium regimes emerge naturally from the maximization of a macrostate entropy and a detailed derivation of those equilibria can be found in Appendix E. For now, it suffices to say that in the present case, where we can assume from experimental facts that the conditional distributions are symmetric $P(\xi|\sigma > 0) = P(-\xi|\sigma < 0)$ (Figure 6.12), those equilibria yield the following mean field frozen equilibria :

$$\langle \text{sign}(\sigma) \rangle(\mathbf{r}) = \tanh(B\psi(\mathbf{r})), \quad \text{and} \quad \langle \text{sign}(\xi) \rangle(\mathbf{r}) = \text{sign}(\xi)_+ \tanh(B\psi(\mathbf{r})), \\ \text{with} \quad B = -\frac{\beta(\xi_+ - \xi_-)}{2}. \tag{6.11}$$

In the latter formula, β is a microcanonical inverse temperature. $\xi_\pm$ are the most probable values of the conditional probabilities, as defined on Figure 6.12. In the present case, we approximate those quantities as $\xi_\pm = \langle X_\pm / A_\pm \rangle$. Those formula are the ones at use to fit the scatter plots of Figure 6.13. The toroidal scatter plots points are quite accurately

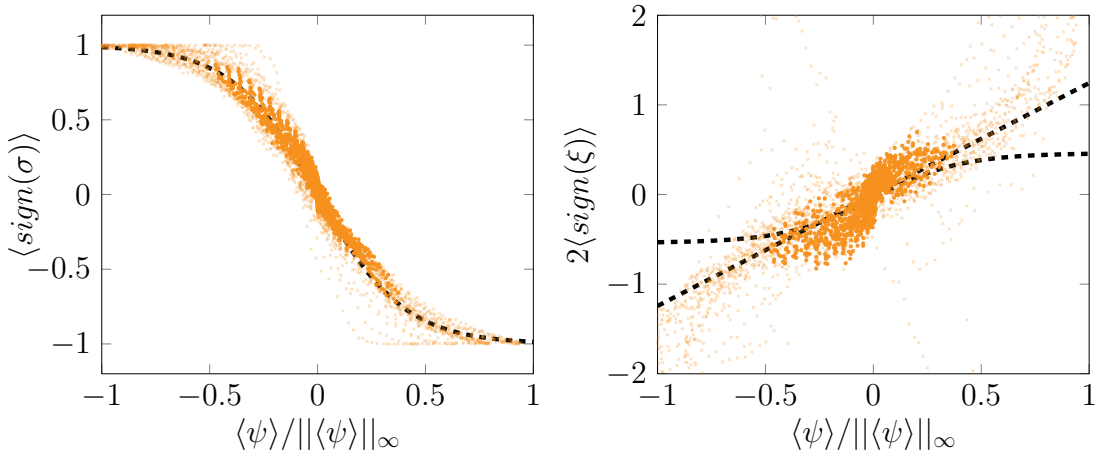

(a) $\langle \text{sign}(\sigma)\rangle - \psi$ **(b)** $\langle \text{sign}(\xi)\rangle - \psi$

Figure 6.13: Scatter plots of the averages of the toroidal and poloidal signs against the stream function ($\theta = 0$,$Re = 3 \times 10^4$). The opaque dots are the dots located in the restricted window described in Figure 6.8. The black "sinh" dotted lines are the quenched equilibria predictions, with the coefficient "B" measured on the toroidal data. On Figure (b), an additional linear fit of the data is shown, which maps the sinh law for low values of the stream function. to the More details in the text.

fitted. For the poloidal scatter plots, the fit only works for small values of the stream functions, indicating that a more refined description might be in need. We however stick to the two-level description.

Influence of the Reynolds number. We use the frozen approach to study a set of 70 Von Kármán experiments obtained at $\theta = 0 \pm 2.5 \cdot 10^{-3}$, with TM60 propellers and a Reynolds number going from 10^2 to 10^6. Averages are typically computed using sequences of 600 instantaneous fields.

We have gathered the scatter plots of the average fields obtained for each one of the experiments on two plots, displayed on Figure 6.14. Whatever the Reynolds number, the tanh law remain visible for the toroidal field. This provides a fair validation of the frozen equilibrium scenario. It is less evident to interpret the poloidal scattering laws. The frozen predictions provide an accurate picture of the scattering for low values of the stream function. This is not the case when ψ is larger. The poloidal scatter plots seem however to be better described by the two-level prediction for the higher Reynolds numbers (blue points).

Technical *aparté*: units and normalization We want to put the frozen scatter plots in perspective with comments on the energies and of the fluctuations measured in the experiments. Prior to doing that, a technical *aparté* is here needed. As explained in Section 6.2.1, knowledge about the flow inside the Von Kármán setup is obtained both from PIV measurements and analogical measurements. Both kinds of measures generate date with units. Frequencies are measured in hertz, the velocities in meter per second, the

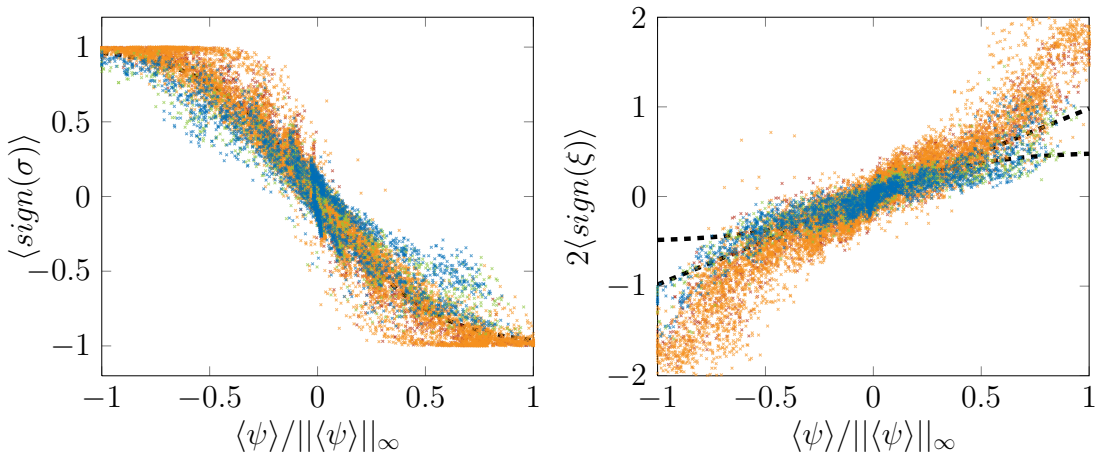

(a) **(b)**

Figure 6.14: Collapse of Scatter plots obtained at $\theta = 0$ for the 70 experiments taken into account. Different colors indicate different ranges of Reynolds number : $Re < 10^4$, $10^4 \leq Re < 5 \times 10^5$, $5 \cdot 10^5 \leq Re < 10^6$, $10^6 \leq Re$. The same color code is used throughout the chapter.

energies in joules, and so on. Now, in order to look at the influence of the Reynolds number on the steady states profile, we need to make all the measures non-dimensional. Indeed, to generate a flow at high Reynolds number 6.1, one may either play on the flow viscosity or play on the frequency $f = (f_1 + f_2)/2$. Figure 6.15(a) shows the values of the rotation frequency of the impellers for the flows at stake in the present chapter. In particular, note that low values of f were used to generate very high Reynolds number experiments at $Re \simeq 10^5$. Therefore, in order to compare the different experiments with each other, it is crucial to make the fields and the coarse-grained quantities under scrutiny non-dimensional. This ensures that we investigate not only the effects of the forcing, but also the effects of the viscosity, hereby analysing the effects of the turbulence. Figure 6.15(a) shows that if we do not consider non-dimensional quantities, then false or weird insights about the Reynolds number dependence can be obtained, however only related to the forcing frequencies.

In the remainder of the chapter, we therefore deal with non-dimensional quantities. A typical length scale is given by the radius of the propeller R, a typical time is given by $1/f$. A typical energy is therefore given by $|\mathcal{D}|(Rf)^2$, a typical vorticity is given by f, a typical velocity is given by Rf. We here discuss only "TM60" propellers. We can therefore work in units in which the radius R is 1. To It is however crucial to divide the quantities that we consider by f (for the velocity or the vorticity fields) or f^2 (for the energies, the helicities, and so on).

Energies and fluctuations. Let us now investigate how the energies and the poloidal fluctuations depend on the Reynolds number.

The total energy does not depend on the Reynolds number, as long as the Reynolds number is large enough (here $Re \gtrsim 10^3$). The energy for the non-turbulent case ($Re \simeq 10^2$) is smaller than the energy observed for $Re \gtrsim 10^3$ – see Figure 6.16(a).

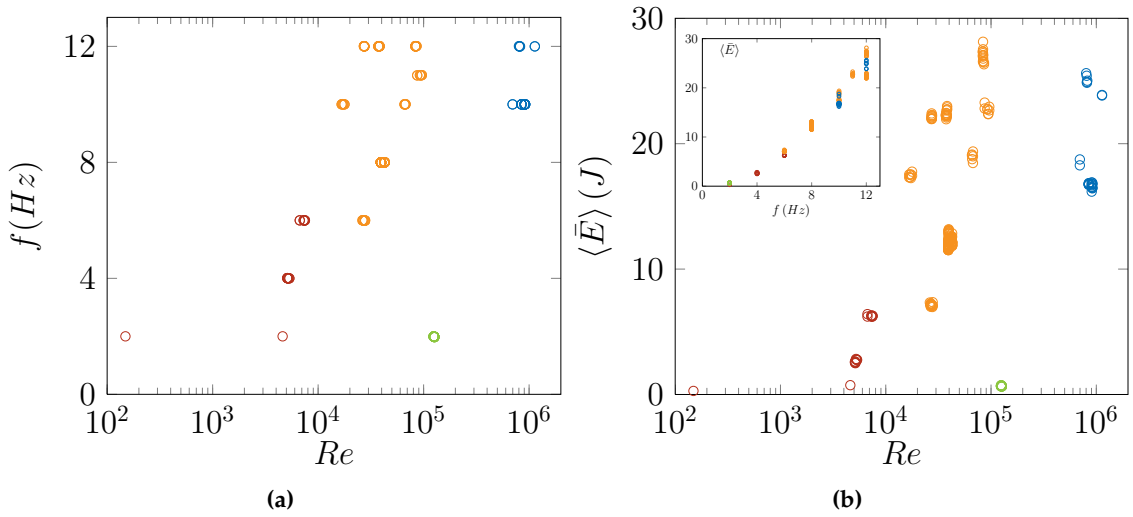

(a) **(b)**

Figure 6.15: (a) The rotation frequency as a function of the Reynolds number for the 70 experiments discussed in the present chapter. (b) The non-normalized energy as a function of the Reynolds number. The inset shows the dependence of the non-normalized energy with the rotation frequency. The color code is the same as in Figure 6.14. The data come from 70 experiments, but there are 242 and not 70 points on those two pictures : for some of the experiments several time series of 600 PIV fields were recorded.

Whatever the Reynolds number, the toroidal energy measured at large scale is commensurate with the poloidal energy measured on the instantaneous fields, even though it is systematically higher – see Figure 6.16(b). This feature corroborates the frozen scenario, in which contrarily to the strong mixing scenario, where the poloidal degrees of freedom can freely vary, the poloidal and toroidal energies are coupled.

The most probable values $\xi_{\pm}$ show only little variation with the Reynolds number – see Figure 6.16(b).

Intuitively, we could think that the relevance of the frozen equilibria should be only restricted to low Reynolds regimes, where the poloidal fluctuations would be very low. This is not the case. For the particular Von Kármán steady flows studied here, the fluctuations of the poloidal field are far greater than the most probable poloidal values (Figure 6.17(a)), whatever the Reynolds number that is considered. The level of poloidal fluctuations is approximately constant for $Re \gtrsim 10^3$, but peaks of fluctuations are measured around $Re \simeq 3 \times 10^4$.

Insights from the frozen axisymmetric theory. The scatter plots of the average signs of the fields show a fairly good agreement between the predictions of the frozen equilibria and the Von Kármán data.This provides some physical insights about the turbulence created within the tank and allow us to partly address the three comments made about the axisymmetric mixing theory.

(a) The frozen theory describes why the selected structures are large scale dipoles[(a)],

[(a)] We consider the structures obtained in the half meridional plane $r \geq 0$.

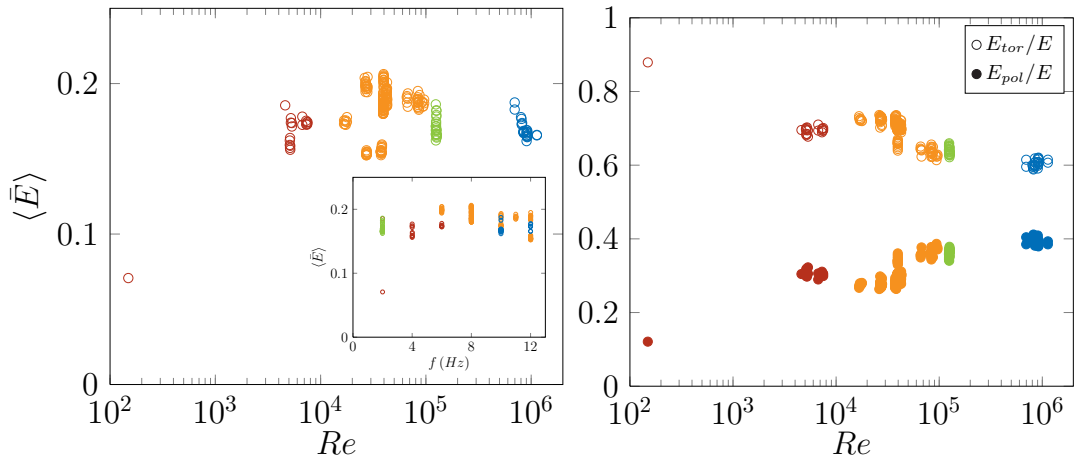

(a) **(b)**

Figure 6.16: (a) The total coarse-grained energy as a function of the Reynolds number, as measured in the experiments and normalized by f^2. The inset shows the dependence of the (non-dimensional) energy with the rotation frequency. (b) The toroidal and poloidal fraction of energy plotted against the Reynolds number. The color code is the same as in Figure 6.14.

and not for instance octopoles or dodecapoles, the maximal frozen entropy structures being related to the smallest modes of the domain.

(b) As far as only the signs of the fields are taken into account, the toroidal scatter plot needs not to be considered only in the region far from the propellers. This implies that the region where a statistical description holds extends to the entire PIV window. The price to pay is that only rough observables are here taken into account. In a sense, the frozen theory has more invariants than the mixing theory, since it requires the prescription of the conditional poloidal distributions – see Appendix E. In practice however, in the case of a symmetric forcing, the only control parameters are the most probable conditional poloidal values ($\xi_\pm$), the magnetization μ, and the poloidal energy.

(c) The $\tanh$ laws give insight about the nature of the steady states observed in the tanks. The Von Kármán average steady states are not strictly speaking inviscid axisymmetric maximal entropy equilibria. However, they can be interpreted as the average states obtained from the physical/dynamical mixing of microscopic toroidal degrees of freedom (here taken as ± 1), whose mutual long-range interactions is prescribed by some frozen-in poloidal degrees of freedom.

Catches of the frozen axisymmetric theory. Clearly, as in Leprovost's theory, there are a couple of catches in the present theory.

(a) The frozen axisymmetric theory is a data driven theory. From the observation that the areas, the helicities, the coarse-grained energy do not vary too much, we can derive a prediction (the "$\tanh$" law), but the theory does not explain why the dis-

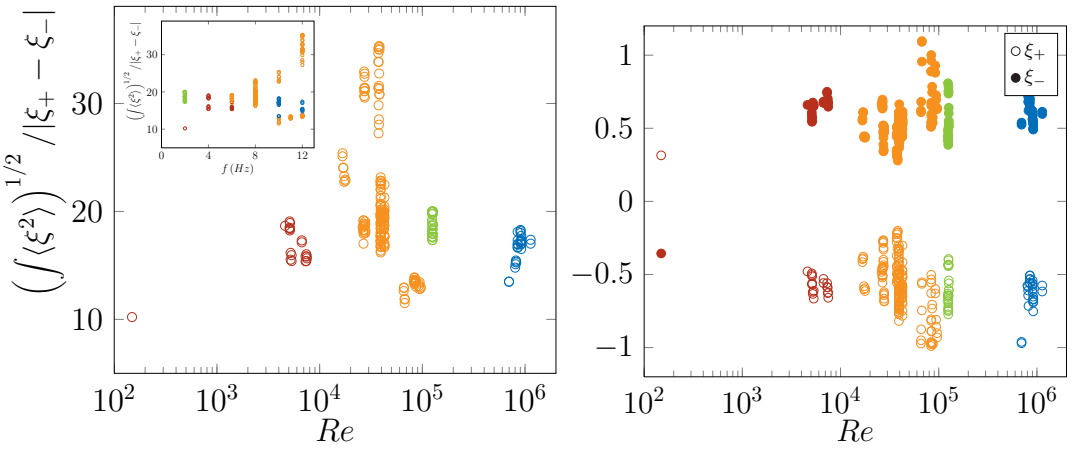

(a) (b)

Figure 6.17: (a) The coarse-grained poloidal fluctuations as a function of the Reynolds number. The inset shows the dependence of the poloidal fluctuations with the rotation frequency. (b) The most probable conditioned poloidal values $\xi_\pm$ against the Reynolds number. The poloidal values are normalized by f. The color code is the same as in Figure 6.14.

tributions of the poloidal signs needs to be frozen. It is therefore only an *a posteriori* description.

(b) The instantaneous fields are not axisymmetric. Hence, the instantaneous poloidal energy used in the theory should not be called that name before it has been azimuthally averaged. Indeed, while it is true that the instantaneous pseudo stream function satisfies $\bar{\xi} = -\Delta_\star \bar{\psi}$, it is wrong that multiplying the quantity $\int_{\mathcal{D}} r\mathrm{d}r\mathrm{d}z\bar{\xi}\bar{\psi}$ by 2π gives the coarse-grained energy of the flow within the tank, unless one assumes that the instantaneous flows are axisymmetric – which is not the case.

The temperature of Von Kármán turbulence. At a qualitative level, the global shape of the scatter plots is quite independent of the Reynolds number, if properly scaled. The toroidal scatter plots can therefore be used to associate to each of the time series, a microcanonical temperature $1/|\beta|$, hereby obtaining a temperature of turbulence, rooted in statistical mechanics. For each experiment, the (frozen) microcanonical inverse temperature β is given by the "B" of Equation (6.11) [(a)], as measured from the scatter plots, divided by the quantity $(\xi_+ - \xi_-)$, as obtained from the *time series* of the 2D3C PIV flows. In the light of the frozen equilibrium theory, the temperature is truly a microcanonical temperature. The dependence on $\xi_\pm$ with the Reynolds number is displayed on Figure 6.17(b), the dependence on the inverse temperature with the Reynolds number on Figure 6.18.

This " Von Kármán temperature" β^{-1} is vanishing in the non-turbulent case but not in the turbulent regimes ($Re \gtrsim 10^3$). In the latter regimes, whether the temperature slightly increases or is essentially constant with the Reynolds number is not clearly determined.

[(a)] Note that this "B" is numerically akin to the "B" of the mixing theory, at stake in Figure 6.9.

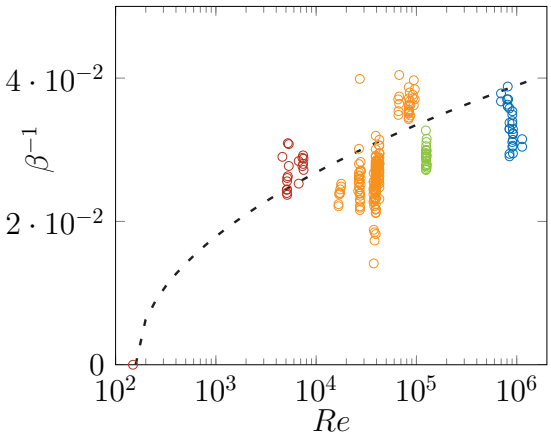

Figure 6.18: The temperature against the Reynolds number. The dashed line is only a guide for the eye.

The fluctuations of the temperature are quite high. This plot however suggests that high Reynolds turbulent states correspond to finite temperature "warm" states.

More iconoclastically, one can decide to forget about the Reynolds number and take the temperature β^{-1} as the driving parameter, hereby obtaining a thermal vision of Von Kármán turbulence. This thermal vision of Von Kármán turbulence is displayed on Figure 6.19. We observe, that the variations of the poloidal energies, the poloidal fluctuations and the poloidal most probable values were not obviously when the Reynolds number was taken into account. The temperature however provides a good collapse parameter, which highlights those variations.

We note, that the temperature β^{-1} seems to behave linearly with the poloidal energy – see 6.19(b). Quite interestingly, we see that the peaks of the poloidal fluctations at $Re \simeq 3 \cdot 10^4$ observed on Figure 6.17 translates into a low-temperature peak at $1/\beta \simeq 2 \times 10^{-2}$. This peak may be seen as a $\theta = 0$ mark of the high Reynolds number divergence of the toroidal susceptibility $\chi = \dfrac{\mathrm{d}\bar{I}}{\mathrm{d}\theta}$ previously observed in the present Von Kármán experiment, and reported in [Cortet et al., 2010, Cortet et al., 2011]. This divergence is highlighted on Figure 6.20.

6.5 Conclusions

Insights from the inviscid theories. In spite of their intrinsic out-of-equilibrium character, the steady-states obtained within the VK setups can be interpreted, at least partially, in the light of inviscid equilibrium theories. On the one hand, Leprovost's mixing theory achieves a remarkable description and classification of those averages Beltrami flows, in terms of two coarse-grained, axisymmetric parameters : the coarse-grained axisymmetric energy, and the ratio of a coarse-grained axisymmetric toroidal momentum squared over a axisymmetric coarse-grained helicity. The theory however predicts the existence of quadrupoles, octopoles and other "n-poles" that are not observed within the experi-

ment. It fails to account for the non-Gaussian behavior of the poloidal and the toroidal fields. On the other hand, the axisymmetric frozen theory makes clearer the fact that the Von Kármán steady states are *not* ideal axisymmetric equilibra states, but can still be interpreted as the maximizers of a macrostate entropy. This may explain why the "(large) n-poles" flows are absent from the experiment. The theory does not predict anything about the shapes of the poloidal distributions, as it uses the latter as inputs. In both cases, some insights about the role of the forcing are given. In the light of the mixing theory, the forcing provides a stabilization of the metastable states of the axisymmetric Euler equations. In the light of the frozen theory, the forcing provides extra-correlations between the toroidal and poloidal fields. It emphasizes the role of the helical correlations in the formation of the large scale Beltrami cells.

Openings. If those two theories do apply more generally than in the case studied here, than some qualitative predictions can be made. For example, there should exist a geometrical transition : for "flat" geometries ($h < R$), a vanishing rotation number should yield vertical dipoles rather than the horizontal ones observed in the experiment.

A more exciting but speculative use of the statistical theories is to provide new eyes to look at turbulent flows. Here, a steady-state temperature of turbulence was defined, in analogy with the frozen equilibrium case. The (frozen) turbulent temperature gives the vision of very high Reynolds number corresponding to a "warm" but finite-temperature turbulence. We note that the "frozen" temperature somehow conflicts with the phenomenological temperature of turbulence proposed by Castaing [Castaing, 1996] $T \propto 1/\log Re$, which implies that a High-Reynolds number yields a "cold" turbulence. The situation is not conflictory as the two-temperatures are distinct from another. The frozen temperature is based on equilibrium considerations and dynamical invariant. Castaing's turbulent temperature is derived from a "scale invariant" and a dynamical cascade argument. It is therefore intrinsically an "out-of-equilibrium" temperature.

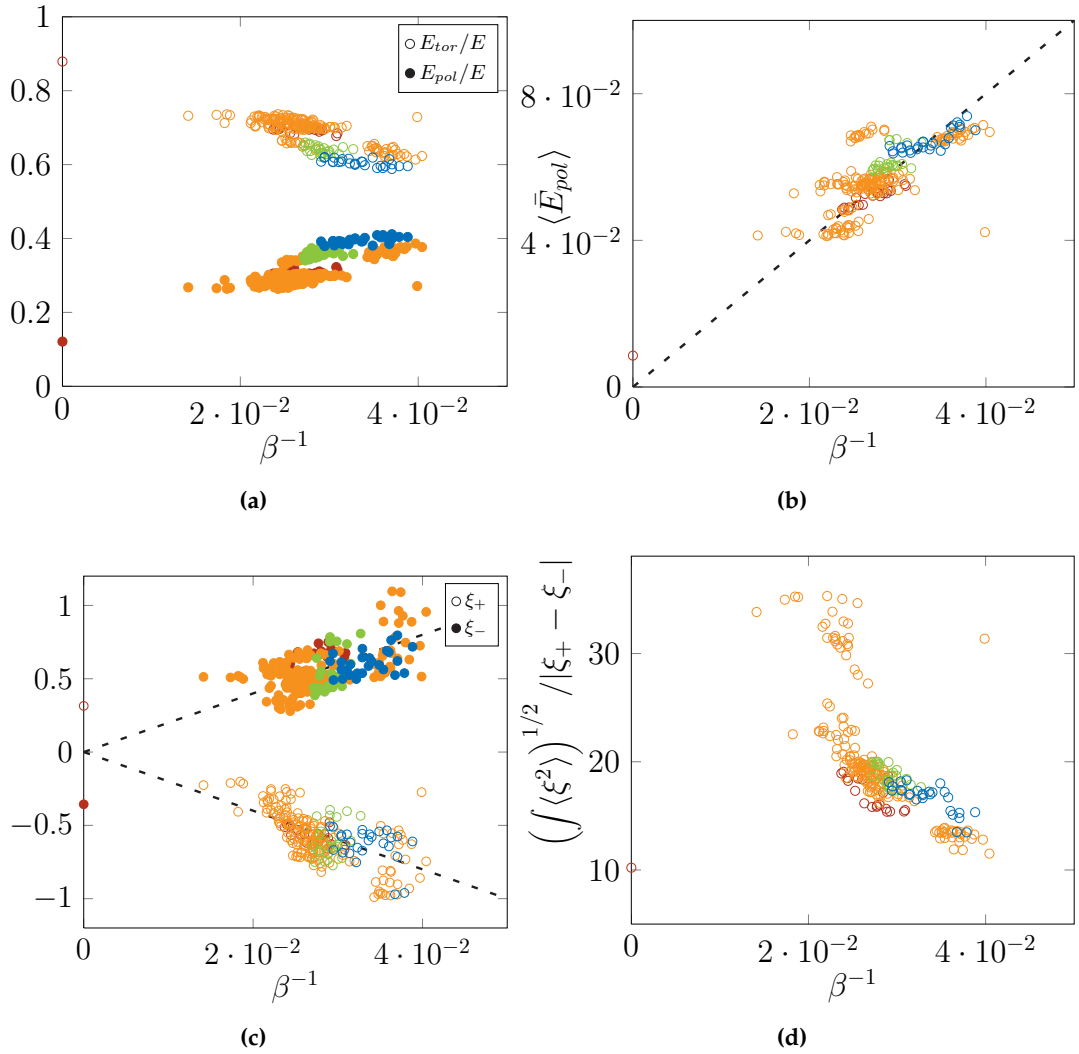

Figure 6.19: The average fractions of poloidal and toroidal energies (a), the (non-dimensional) poloidal energy (b), the conditional most probable poloidal values (c) and the poloidal fluctuations (d) plotted against the temperature $|\beta|^{-1}$. The color code for the Reynolds number is still the same as in Figure 6.14. The dotted lines are guide-lines for the eyes. They indicate a linear behavior with a $+2$ slope (b), and ± 20 slope (c).

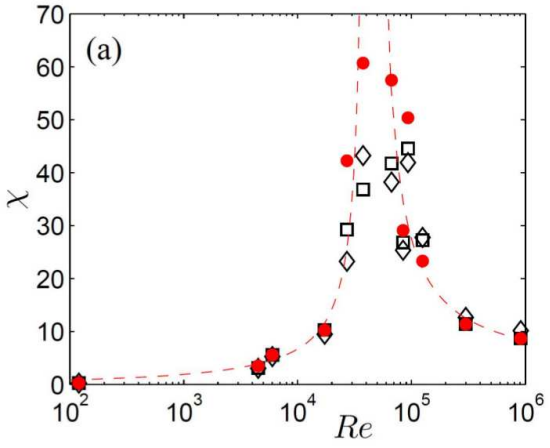

Figure 6.20: The finite-Reynolds divergence of the axisymmetric susceptibility $\chi = \left.\frac{\mathrm{d}I_\odot}{\mathrm{d}\theta}\right|_{\theta=0}$. Taken from [Cortet et al., 2011].

Chapter 7

Is quasi-2D Turbulence critical ?

The present chapter might seem slightly disconnected from the previous ones. We forget about the ideal world of purely 2D3C flows and we also partly forget about the largest scales of Turbulence. Instead, we relate the existence of possible hints of a weak form of conformal symmetry in terms of "Schramm-Löwner traces", in two quasi-two dimensional turbulent regimes. This form of conformal invariance has recently been discovered in the inverse cascades of two-dimensional turbulent flows [Bernard et al., 2006, Bernard et al., 2007], and is more commonly found in the continuum limit of many *short range* lattice models. It is here also possibly found in a laboratory soap film experiment of two-dimensional turbulence, as well as in a self-similar regime of three dimensional turbulence with rotation and helicity. If correct, the observation may suggest unsuspected further analogies between quasi-2D turbulence and (short-range) lattice models at criticality. The chapter is composed of two papers, obtained from a collaboration with Annick Pouquet, Pablo Mininni, and Duane Rosenberg. The chapter is supplemented by two addenda. The first briefly explains what the inertial ranges in rotating helical turbulence can be expected to be. The second gives transparency to the "Schramm-Löwner" analysis presented in both papers.

Contents

7.1 arXiv paper : Experimental evidence of conformal invariance in soap film turbulent flows

Experimental evidence of conformal invariance in soap film turbulent flows

S. Thalabard[1], M.I. Auliel[2], G. Artana[2], P.D. Mininni[3,1], and A. Pouquet[1]
[1] *Computational and Information Systems Laboratory, NCAR, P.O. Box 3000, Boulder, Colorado 80307-3000, USA.*
[2] *Laboratory of Fluid Dynamics, Facultad de Ingeniería, Universidad de Buenos Aires and CONICET, Paseo Colón 850, C1063ACV Buenos Aires, Argentina.*
[3] *Departamento de Física, Facultad de Ciencias Exactas y Naturales, Universidad de Buenos Aires and IFIBA, CONICET, Ciudad Universitaria, 1428 Buenos Aires, Argentina.*

(Dated: December 9, 2010)

We present experimental evidence of statistical conformal invariance in isocontours of fluid thickness in experiments of two-dimensional turbulence using soap films. A Schlieren technique is used to visualize regions of the flow with constant film thickness, and association of isocontours with Schramm-Löwner evolution (SLE) is used to identify conformal invariance. In experiments where an inverse energy cascade develops, statistical evidence is consistent with such an association. The diffusivity of the associated one-dimensional Brownian process is close to 8/3, a value previously identified in isocontours of vorticity in high-resolution numerical simulations of two-dimensional turbulence (D. Bernard et al., Nature Phys. 2, 124, 2006). In experiments where the inverse energy cascade is not sufficiently developed, no statistical evidence of conformal invariance is found.

PACS numbers: 47.27.-i, 92.60.hk, 68.15.+e, 11.25.Hf

Two-dimensional (2D) turbulence displays important differences with the three-dimensional (3D) case [1]. While turbulent flows in 3D tend to create smaller scales and disorder, flows in 2D tend to self-organize and create long-living coherent structures [2]. These differences are not just of academic interest, as many flows in nature are quasi-2D. This is often the result of volume forces that impose a preferred direction, as e.g., rotation and/or stratification in the atmosphere, and magnetic fields in the interplanetary medium. In particular, the atmosphere can be considered to a good degree of approximation as a shallow layer of fluid, as most of the weather takes place in a thin layer (the troposphere) of approximately 10 km depth, while the larger horizontal scales are of the order of thousand kilometers [3].

2D turbulence is far from being completely understood. If injected at intermediate scales, enstrophy (the squared vorticity) is transferred towards smaller scales, in a so-called *direct cascade*, while energy is transferred towards larger scales in an *inverse cascade* [1, 2]. Besides the direction of the cascade, and unlike its 3D counterpart, the energy cascade is scale invariant: while in 3D turbulence strong intermittent events develop that make the flow multi-fractal, 2D flows are absent of such intermittency at large scale [4, 5].

An even stronger form of symmetry was identified in recent years: that of conformal invariance [6]. While scale-invariance is a global property, often quantified using two-point correlation functions, conformal invariance is a local property involving invariance under conformal (angle-preserving) transformations. Conformal invariance is used in quantum field theories, including applications in condensed matter [7]. In fluid dynamics, it is often used to solve Laplace equation for ideal incompressible and irrotational flows in 2D domains. That 2D turbulence (a much harder problem where non-linear effects are dominant) may be conformal invariant was originally proposed in [8]. Its confirmation requires measurement of multi-point correlation functions. Instead, in a recent work [6], evidence of conformal invariance in numerical simulations of 2D turbulence was shown using Schramm-Löwner evolution (SLE) [9]. SLE applies to a special set of random curves without self-intersections in a 2D space, and it was shown that if the conformal transformation that maps curves in the 2D space into the real axis gives a one-dimensional (1D) Brownian process (BP), then the original curves are statistically conformal invariant. This result was used to show that isocontours of zero vorticity in simulations of 2D turbulence are conformal invariant (and moreover, they are generated by an SLE process) [6]. The analysis also allowed identification of the class of universality to which these curves belonged, identified by the diffusivity κ of the BP, and noted SLE_κ. These classes share common statistical properties, such as critical exponents. More recently, the result was used to show that isocontours of temperature in a quasi-geostrophic model also were SLE, with a different κ [10].

It is unclear however how these results can be extended to more realistic configurations. Under favorable conditions, flows in nature can be considered as quasi-2D at best. They are not exactly 2D as they may have small (but finite) thickness, or translation symmetry in the out-of-plane direction. As a consequence, motions outside the plane of interest can develop. Are conformal invariant properties still relevant in such cases? Moreover, the method used to detect conformal invariance in 2D turbulence relies on the vorticity, a quantity which is hard to measure with small uncertainties in experiments or observations. In many cases, vorticity is obtained after applying a curl to particle image velocimetry (PIV) measurements. This results in a loss of spatial resolution (PIV gives, as a rule, the velocity field every six or more

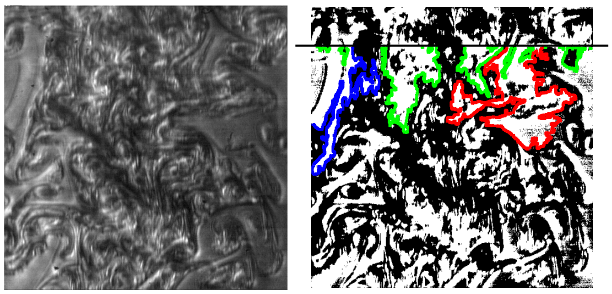

FIG. 1: (Color online) *Left:* Typical raw Schlieren image of the soap film for configuration A. *Right:* Extraction of paths with constant thickness. The shortest paths in light gray (green), whose lengths are below $l_{\rm tr}$, are eliminated.

image pixels, per virtue of the interrogation window used for the correlation), and in an increase of error per virtue of the numerical derivatives required to compute the curl. In some cases, spatial resolution of the correlation technique can be improved by using flow optic approaches with PIV images. However, an artificial smoothing of the results may still take place as a consequence of the regularization employed.

In this letter, we show evidence of conformal invariance in experiments of turbulence in soap films [11–13]. Such experiments approximate 2D turbulence, although deviations arise from variations in the soap film thickness, and also because of the friction in the presence of rough boundaries [14]. Indirect vorticity measurements have been done [12, 13] and despite these effects, its dynamic is in some cases consistent with predictions for 2D turbulence. Also, to lowest order in the film thickness, thickness is advected as a passive scalar, and a strong correlation between thickness fluctuations and vorticity has been reported [13]. However, both weak and strong intermittency effects have also been observed, in the direct and the inverse cascade, attributed to finite thickness effects [15]. The experiments we present here share these properties; a detailed description of PIV measurements is left for the future.

Given these similarities and differences, it is interesting to know whether conformal invariance can be identified in the system at hand. In the experiment, grid turbulence is generated using grids with different spacing of wires, while the fluid flows through a vertical channel as a result of gravity. To avoid indirect vorticity measurements and loss of resolution associated with PIV, we rely for the analysis on raw images of film thickness variation. The thickness variation in the film is visualized using a Schlieren technique [16]. When employing this technique, gradients of film thickness act on light rays as density gradients do in volumetric flows. Changes in the thickness act as changes in the refraction index, and the deviation of the light rays can be used to obtain an intensity image proportional to thickness variations. The use of this method allows us to have images with high contrast and resolution. Conformal invariance is then examined studying isolevels of constant film thickness. As an illustration, we present two experimental configurations: one with a grid size such that a wide inverse cascade of energy develops, and another with a grid size such that only a short range of inverse cascade is available. In the former case, evidence of conformal invariance is found, while in the latter conformal invariance is not observed.

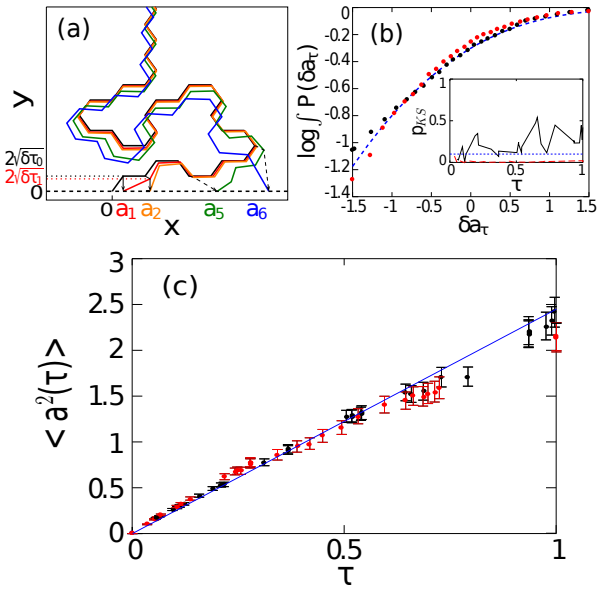

FIG. 2: (Color online) (a) The zipper algorithm: the original path (black) is gradually conformally squeezed down onto the x-axis (indicated by the gray paths and the dashed arrows). This defines a 1D path $a_n(\tau_n)$ (see [17]). (b) Cumulative PDF of the increments δa_τ, displayed here for $L = 800$ pixels for configurations A (black dots) and B (gray or red dots); the dashed (blue) line corresponds to a cumulative (normalized) Gaussian distribution. The inset shows the Kolmogorov-Smirnov probability p_{KS}, testing the null hypothesis that the increments fall into a Gaussian distribution. Black lines are for dataset A and long-dashed gray (red) lines for dataset B; the dashed (blue) line indicates a conventional threshold at 0.1. (d) Scaling with error bars of the variance of a with driving time τ; the best fit for configuration A (black dots) yields $\kappa = 2.5 \pm 0.3$ (solid blue line). Configuration B (gray or red dots) has a less clear scaling and does not pass the Gaussianity test.

The experimental setup is as follows. We use a z-type Schlieren configuration with two mirrors of 50 cm in diameter and 3.0 m focal length. Two razor blades perpendicularly disposed at the sagital and meridional focal planes enable us to obstruct the deviated light rays and to improve the contrast of the otherwise shadowgraph image that would form at the CCD of a monochromatic high-speed video camera (3000 fps with a resolution of 512×512 pixels). Images are captured at a rate of 2500 fps, with one pixel corresponding to 0.161 mm (corresponding to an area of 82.4×82.4 mm^2 centered in the

middle of the channel width). The vertical soap film channel has a width of 160 mm, and a length of 0.6 m in the region of constant width (the expansion and the contraction of the tunnel have the same length). In the first configuration (configuration A), a grid with a separation between wires of 5.1 mm and a width of 65 mm is used to create turbulence downstream. The mean flow velocity is 1400 mm/s, the mean film thickness is 5.6 μm, and the Reynolds number (based on the injection scale) is $Re \approx 870$. When the third order structure function is computed from PIV data, a range with negative energy flux (corresponding to an inverse cascade) can be identified for scales between ≈ 30 and 110 mm. In the second configuration (configuration B), a grid with a separation between wires of 0.3 mm and a width of 45 mm is used instead. The mean flow velocity is 1930 mm/s, the channel width is 160 mm, the mean film thicknes is 4.1 μm, and the Reynolds number is $Re \approx 70$. Configuration B has an estimated inverse cascade range (from third order structure functions) between ≈ 25 and 45 mm.

Figure 1 shows a Schlieren image of the soap film. In each analysis, 2000 snapshots of the film are used. An average of all snapshots is used as the background image, that we remove to undertake the analysis. The resulting image corresponds to thickness gradients, with zero value associated to constant thickness. For each image we then look at its four possible orientations, and for each one of those we set up an arbitrary x-axis (see the right panel in Fig 1). From each axis, we then explore all curves with no thickness variation until the curve goes out of the image or it returns to the x-axis. When the paths are not self-avoiding, we erase the loops similarly to how the loops are erased in loop erased random walks (LERWs) [9]. Finally, only the paths whose length are above a given threshold $l_{\rm tr}$ are kept. Here we consider $l_{\rm tr} = 500$ pixels. We thus obtain a collection of paths which are correlated. In order to avoid redundancies (as the flow has a typical time-correlation given by its turnover time), we impose that the paths coming from two different snapshots have to be separated by a certain number of snapshots $n_{\rm fil}$. The results given below are obtained with $n_{\rm fil} = 8$, but we checked that $n_{\rm fil} = 4$, 8, 12, 16, and 20 give the same results. For $n_{\rm fil} > 20$, similar results are obtained although with worse statistical accuracy as less curves are preserved ($n_{\rm fil} = 20$ roughly corresponds to the turnover time of the eddies at the injection scale in configuration A). With $n_{\rm fil} = 8$, the number of paths above 500 pixels is 1934 for configuration A, and 2216 for configuration B.

These curves are projected with a conformal map into 1D paths (the *driving functions*, which we will label $a(\tau)$), as done in [6]. The zipper algorithm is used to obtain the 1D paths; see [17] and Fig. 2(a). The parametric variable τ (the "time") here only labels the successive points of the 1D paths, and should not be confused with the actual time corresponding to the different snapshots in the experiment. For increasing τ, all curves in the 2D plane are generated in the direction that keeps positive vorticity to the right. Following Schramm's results [9], in order to check whether the measure of these curves is conformal invariant, we have to test whether these driving functions are likely to be seen as Brownian 1D paths. In other words, the paths must be of the form $a(\tau) = \sqrt{\kappa} B(\tau)$, where κ is a diffusion coefficient, and $B(\tau)$ is a standard Brownian motion. To test this, we first perform a Kolmogorov-Smirnov test, testing the null hypothesis that the increments of the driving functions fall into a Gaussian distribution (whose mean and variance are data driven). To compute the increments, a length L is picked, and all driving functions with length larger than L are selected. Then, the minimum driving time τ for which L is reached in all these functions is found, and the increments are defined as $\delta a_\tau = a(\tau)$ with τ the minimum driving time for the given L. As an example, the cumulative probability density function (PDF) of the increments for datasets A and B and for $L = 800$ pixels is shown in Fig. 2(b). The p_{KS} values of the Kolmogorov-Smirnov test for different minimum driving times τ (i.e., different lengths L) are shown in the inset of Fig. 2(b). For configuration A the null hypothesis is rejected. Finally, we study the dependence of the variance of a as a function of the driving time τ for datasets A and B to evaluate κ; see Fig. 2(c). For configuration A we obtain $\kappa \approx 2.6$; configuration B presents slightly larger deviations from the linear behavior and does not pass the Gaussianity test.

The procedure described above was also tested on synthetic 2D paths generated from LERWs, and from self avoiding walks (SAWs). The former are generated with a 2D Brownian motion in the upper plane whose loops are successively erased, while the latter are generated with a Markov chain Monte Carlo algorithm (the "pivot algorithm" [18]). In each case, 1000 paths are used. Both synthetic datasets pass the Gaussianity test and have

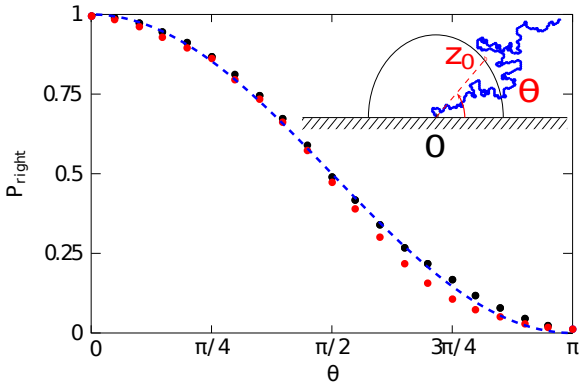

FIG. 3: (Color online) Probability that a path keeps a given point z_0 to its right. The dashed (blue) line indicates the SLE prediction given by Eq. (1) with $\kappa = 8/3$. Black dots are for dataset A and gray (red) dots for dataset B. In the latter a larger departure is observed from the predicted behavior. The inset shows a sketch of a 2D path that keeps the given point z_0 to its left, and indicates how the angle $\theta = arg(z_0)$ is defined.

variance $\kappa = 2.0 \pm 0.2$ (LERWs) and 2.9 ± 0.3 (SAWs).

The driving functions for configuration A show good p_{KS} values as well as good scaling of the variance with τ. The analysis thus indicates that the isolines used are good SLE candidates. The value found is compatible with $\kappa = 8/3$, reported previously in numerical simulations [6], under the hypothesis that we are measuring here the properties of the envelope of the paths, thus accessing to the dual. This value corresponds to the continuum limit of SAWs. Configuration B, with a smaller Reynolds number and a narrower inverse energy cascade range, may not be sufficiently turbulent for conformal invariance to develop and be identified.

To confirm these findings, we now consider two properties that isocontours should exhibit if they are conformal invariant. First, we calculate the fractal dimension d_f of each of the paths, and study the distribution of $\tilde{\kappa} = 1 + d_f/8$. For the two synthetic datasets mentioned before, the distributions of $\tilde{\kappa}$ based on the fractality of the 2D paths have mean 1.9 and variance 0.3 in the LERWs, and 2.4 ± 0.5 in the SAWs. For dataset A, $\tilde{\kappa} = 2.4 \pm 0.4$, while for dataset B, $\tilde{\kappa} = 2.3 \pm 0.6$. In other words, fractality (as given by a measure of d_f) obtains in both cases A and B, and we observe good agreement between κ and the value derived from the distribution of the fractal dimensions of the 2D paths.

Second, we verify a non-trivial result predicted by the SLE theory. If the curves are conformal invariant, then the probability that a path keeps a given point z_0 to its right depends only on κ and $\theta = \arg(z_0)$, namely [17]

$$p_{\text{right}} = \frac{1}{2} + \frac{\Gamma(\frac{4}{\kappa})}{\sqrt{\pi}\Gamma(\frac{8-\kappa}{2\kappa})} {}_2F_1\left(\frac{1}{2}, \frac{4}{\kappa}, \frac{3}{2}, -\cot^2\theta\right)\cot\theta \quad (1)$$

where Γ is the Gamma function, and ${}_2F_1$ is the Gauss hypergeometric function. This is a good example of non-trivial exact predictions that can be obtained if 2D or quasi-2D turbulence is conformal invariant (see [6] for other examples). Results are shown in Fig. 3. Although both configurations show good agreement with the prediction, the agreement is better for dataset A.

The results indicate that the soap film flows studied here exhibit a behavior consistent with conformal invariance when an inverse energy cascade is sufficiently developed, at least to the point that SLE predictions are in good agreement with the experimental results. Note that an experimental result for SLE in a different context, that of the rugosity of tungsten oxide surfaces, has been reported recently [19], identified in their case with the Ising model ($\kappa = 3$). Given the role played by 2D and quasi-2D flows as simple (although incomplete) models of atmospheric an oceanic turbulence, it is to be hoped that studies which bring together fluid dynamics and critical phenomena, together with the link to conformal field theory, will shed new light on the statistical properties of such flows.

NCAR is sponsored by the National Science Foundation. PDM & MIA acknowledge support from grants UBACYT 20020090200692 and PICT 2007-02211, GA & MIA from grants PIP 3003, UBACYTI017, and PICT 12-9482, and AP and PDM from grant nsf-cmg 1025166DMS.

[1] R.H. Kraichnan and D. Montgomery, *Rep. Prog. Phys.* **43**, 547 (1980).
[2] R.H. Kraichnan, *Phys. Fluids* **10**, 1417 (1967); G.K. Batchelor, *Phys. Fluids* **12**, 233 (1969).
[3] J. Pedlosky, "Geophysical fluid dynamics" (Springer, Berlin, 1986).
[4] E. Siggia and H. Aref, *Phys. Fluids* **24**, 171 (1981); L. Smith and V. Yakhot, *Phys. Rev. Lett.* **71**, 352 (1993); G. Boffetta, A. Celani, and M. Vergassola, *Phys. Rev. E* **61**, R29 (2000).
[5] J. Paret and P. Tabeling, *Phys. Fluids* **10**, 3126 (1998).
[6] D. Bernard, G. Boffetta, A. Celani, and G. Falkovich, *Nature Physics* **2**, 124 (2006).
[7] A.A. Belavin, A.M. Polyakov, A.B. Zamolodchikov, *Nucl. Phys. B* **241**, 333 (1984).
[8] A.M. Polyakov, *Nucl. Phys. B* **396**, 2 (1993).
[9] K. Löwner, *Math. Ann.* **89**, 103 (1923); O. Schramm, *Israel J. Math.* **118**, 221 (2000); J. Cardy, *Ann. Physics* **318**, 81 (2005).
[10] D. Bernard, G. Boffetta, A. Celani, and G. Falkovich, *Phys. Rev. Lett.* **98**, 024501 (2007).
[11] Y. Couder, *J. Phys. (France) Lett.* **45**, 353 (1984); Y. Couder, J.-M. Chomaz, and M. Rabaud, *Physica D* **37**, 384 (1989); M. Gharib and P. Derango, *Physica D* **37**, 406 (1989); H. Kellay, X.L. Wu, and W.I. Goldburg, *Phys. Rev. Lett.* **74**, 3975 (1995); H. Kellay and W.I. Goldburg, *Rep. Prog. Phys.* **65**, 845 (2002).
[12] H. Kellay, X.L. Wu, and W.I. Goldburg, *Phys. Rev. Lett.* **80**, 277 (1998).
[13] M. Rivera, P. Vorobieff, and R.E. Ecke, *Phys. Rev. Lett.* **81**, 1417 (1998); P. Vorobieff, M. Rivera, and R.E. Ecke, *Phys. Fluids* **11**, 2167 (1999).
[14] N. Guttenberg and N. Goldenfeld, *Phys. Rev. E* **79**, 065306(R) (2009); note that a friction term is included in the 2D numerical simulations reported in [6].
[15] A. Belmonte, W.I. Goldburg, H. Kellay, M.A. Rutgers, B. Martin, and X.L. Wu, *Phys. Fluids* **11**, 1196 (1999); W.B. Daniel and M.A. Rutgers, *Phys. Rev. Lett.* **89**, 134502 (2002); Y. Jun and X.L. Wu , *Phys. Rev. E* **72**, 035302(R) (2005).
[16] G.S. Settles, "Schlieren and shadowgraph techniques: visualizing phenomena in transparent media" (Springer-Verlag, Berlin, 2001).
[17] W. Kager and B. Nienhuis, *J. Stat. Phys.* **115**, 1149 (2004); J.L. Cardy, *Annals Phys.* **318**, 81 (2005); T. Kennedy, *J. Stat. Phys.* **131**, 803 (2008).
[18] M. Lal, *Molec. Phys.* **17**, 57 (1969).
[19] A.A. Saberi *et al.*, *Phys. Rev. Lett.* **100**, 044504 (2008).

7.2 PRL paper : Conformal invariance in three-dimensional rotating turbulence

The letter was published in *Physical Review Letters* in 2011.

Conformal invariance in three-dimensional rotating turbulence

S. Thalabard[1,2], D. Rosenberg[1], A. Pouquet[1] and P.D. Mininni[1,3]
[1] *Computational and Information Systems Laboratory, NCAR, P.O. Box 3000, Boulder CO 80307, USA.* [2] *CEA Saclay, l'Orme les Merisiers, France.*
[3] *Departamento de Física, Facultad de Ciencias Exactas y Naturales, UBA & IFIBA, CONICET, Ciudad Universitaria, 1428 Buenos Aires, Argentina.*

(Dated: April 12, 2011)

We examine three–dimensional turbulent flows in the presence of solid-body rotation and helical forcing in the framework of stochastic Schramm-Löwner evolution curves (SLE). The data stems from a run on a grid of 1536^3 points, with Reynolds and Rossby numbers of respectively 5100 and 0.06. We average the parallel component of the vorticity in the direction parallel to that of rotation, and examine the resulting $\langle\omega_z\rangle_z$ field for scaling properties of its zero-value contours. We find for the first time for three-dimensional fluid turbulence evidence of nodal curves being conformal invariant, belonging to a SLE class with associated Brownian diffusivity $\kappa = 3.6 \pm 0.1$. SLE behavior is related to the self-similarity of the direct cascade of energy to small scales in this flow, and to the partial bi-dimensionalization of the flow because of rotation. We recover the value of κ with a heuristic argument and show that this value is consistent with several non-trivial SLE predictions.

PACS numbers: 47.32-y,05.40.-a,47.27.-i,47.53.+n

Self-similarity in physics is a common phenomenon, with identical properties of a system when considered at different scales. Rugged coast lines, fractals, traffic in computer networks, growth processes, geometrical properties of interfaces, phase transitions in critical phenomena such as in the Ising model for spontaneous magnetization, classical and quantum field theory, often display power-law scaling of some variable and such scaling exponents have been the object of intense investigations resulting in the finding of broad classes of universality.

A property stronger than scale invariance is conformal invariance, under transformations that preserve angles with rescaling that depends on position; it is difficult to test, since it implies the need to investigate the scaling of multi-point high-order correlation functions. However, recent developments by Schramm in particular (see e.g. [1] and references therein) allow in some cases for a statistical characterisation of conformal invariance. Such scaling laws can be related to Brownian motion (which is scale invariant, and conformal in two dimensions) in what is now named Schramm-Löwner evolution (SLE), with as sole parameter the diffusivity κ associated with this Brownian motion. In this approach, the driving of the Löwner equation (Eq. 2 below) is stochastic, with a conformal map allowing to go from static (fixed time) two-dimensional (2D) paths in the complex plane $\mathbb{C}$ to "dynamic" one-dimensional (1D) motions. In other words, it allows one to describe paths in $\mathbb{C}$ by a succession (convolution) of conformal maps obeying a differential equation. Schramm's theorem (see, e.g., [1]) states that if and only if the driving is Brownian is the measure of the 2D paths conformally invariant.

Two-dimensional turbulence differs in many ways from the three-dimensional (3D) case because of the presence of an extra invariant in the absence of viscosity, the enstrophy $S = \left\langle |\nabla \times \mathbf{u}|^2/2 \right\rangle$, leading to an inverse cascade of energy $E = \left\langle |\mathbf{u}|^2/2 \right\rangle$ to large scales [2], with $\mathbf{u}$ the velocity field. It was shown in [3] that this inverse cascade, which is known to lack intermittency and is self-similar, can be viewed in the framework of conformal invariance when examining zero-vorticity lines; it belongs to the universality class with $\kappa = 8/3$ (the enstrophy cascade to small scales, however, is not SLE [3]). These results stem from direct numerical simulations (DNS) on grids of up to $16,384^2$ points, with forcing at intermediate wavenumber, $k_F/k_{min} \approx 100$, with $k_{min} = 2\pi/L_0$, L_0 being the size of the vessel.

In the case of 3D Navier-Stokes (NS) incompressible flows at high Reynolds numbers, the cascade of energy to small scales is not self-similar, because of the presence of strong vorticity gradients. Only one time scale is present, the eddy turn-over time $\tau_{\rm NL} \sim \ell/u_\ell$, with u_ℓ the velocity at scale ℓ, and dimensional analysis gives an energy spectrum $E(k) \propto k^{-5/3}$ that is quite close to observed spectra in the atmosphere or in laboratory experiments. However, when introducing solid body rotation Ω with inertial time $\tau_\Omega \sim 1/\Omega$, $E(k)$ steepens and its spectral index can be recovered by taking into account the weakening of nonlinear interactions due to the inertial waves [4]. In this case, self-similarity and Gaussianity in the 3D direct energy cascade was found recently both in the laboratory [5, 6] and in DNS [7, 8], more clearly so in the presence of helicity, i.e., velocity-vorticity correlations [9].

Since rotating flows tend to become quasi-2D (but not strictly 2D, as our results will confirm) when strong rotation is imposed, the question thus arises as to whether SLE can be identified in such flows. To this end, we examine the large data set produced in a run of rotating helical turbulence on a grid of 1536^3 points, with $L_0 = 2\pi$ and forcing at k_F=7; an inverse cascade of energy to large scales (with constant negative flux) is observed, but with too little extent in wavenumber to allow for a SLE analysis similar to that performed in [3] for the 2D NS inverse cascade. We concentrate instead on the direct energy

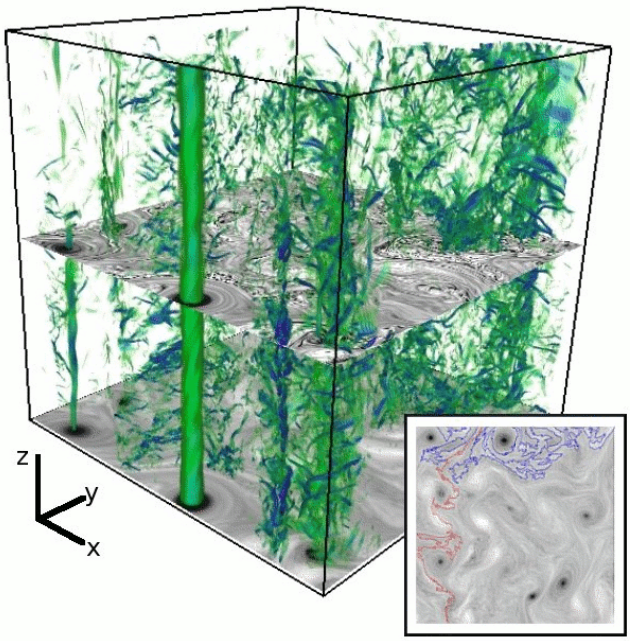

FIG. 1: (*Color online*) Perspective volume rendering of vorticity intensity in a snapshot of the flow. The slice in the middle of the box shows a 2D cut of ω_z, while the slice at the bottom shows the same field averaged vertically. The inset is $\langle\omega_z\rangle_z$, with super-imposed nodal paths, the traversing ones (top to bottom, red online) being discarded from the analysis.

cascade to small scales (with constant and positive flux, see Fig. 9 in [8]), and analyzed for its classical statistical properties and structures in [9]. A pseudo-spectral code with periodic boundary conditions was used, with at the onset of the inverse cascade a Reynolds number $Re = U_0 2\pi/[\nu k_F] \approx 5100$ (with ν the viscosity), and the Rossby number $Ro = U_0 k_F/[2\pi\Omega] \approx 0.06$; $U_0 \approx 1$ is the *r.m.s.* velocity. We integrated the 3D NS equations in the rotating frame for an incompressible flow ($\nabla\cdot\mathbf{u} = 0$); with $\boldsymbol{\omega} = \nabla\times\mathbf{u}$ the vorticity, they read:

$$\frac{\partial\mathbf{u}}{\partial t} + \boldsymbol{\omega}\times\mathbf{u} + 2\boldsymbol{\Omega}\times\mathbf{u} = -\nabla\mathcal{P} + \nu\nabla^2\mathbf{u} + \mathbf{F}\ ; \qquad (1)$$

$\mathcal{P}$ is the total pressure modified by the centrifugal term, and $\mathbf{F}$ is a helical Arn'old-Beltrami-Childress forcing [7, 8]. The rotation is imposed in the vertical (z) direction, with $\boldsymbol{\Omega} = 9\hat{\mathrm{z}}$. The code is fully parallelized, uses the 2/3 de-aliasing rule, and the temporal scheme is a second-order Runge-Kutta. Note that in 3D, besides energy, total helicity $H = \langle\mathbf{u}\cdot\boldsymbol{\omega}\rangle$ is also an ideal invariant [11].

The procedure: Considering the symmetries of Eq. (1), we construct a 2D field by averaging in the vertical direction the parallel component of vorticity, which we denote hereafter $\langle\omega_z\rangle_z$; we also compute a transverse average $\langle\omega_z\rangle_y$ to compare with. Starting from an arbitrary line, say the x-axis, we explore iso-contours of zero field as trajectories in the 2D plane that keep positive field to their right. The direction along the trajectories is parametrized by a "driving time" τ. The path is stopped whenever it returns to the initial axis. The end-point is then sent to infinity through a holomorphic (Möbius) transformation as in [3], with a cut-off Δ chosen to be such that the tip of the curve is within a small arbitrary distance of the chosen axis; results are insensitive to the choice of Δ in a range of 1 to 10 pixels, and agree as well with a procedure in which the Möbius conformal mapping is not applied. Note that, because of periodicity, the procedure is not affected by the boundaries, and that all trajectories are renormalized to $\tau_{max} = 1$.

We have shown numerically for this flow the existence of scale invariance for the direct energy cascade and the Gaussianity of the velocity in [9] (see Figs. 7 and 8), also examining anisotropy at different times using a $SO(2)\times\mathbb{R}$ decomposition (see Figs. 2 and 3 in [9] for the actual scaling ranges). We now probe the conformal invariance of these 2D curves viewed as paths in the upper complex plane; the paths are encoded in a "driving function" $\xi(\tau)$ obtained through the chordal Löwner equation below, with $g_\tau(\zeta)$ ($\zeta\in\mathbb{C}$) a conformal map (see, e.g., [12]):

$$\partial_\tau g_\tau(\zeta) = \frac{2}{g_\tau(\zeta) - \xi(\tau)}\ ; \qquad (2)$$

$\xi(\tau)$ is the unknown 1D real continuous stochastic driving function for the path. In order to estimate $\xi(\tau)$ numerically, we use the zipper algorithm (ZA) with vertical slits [14]. Then $g_{a,\delta\tau}(\zeta) = a + \sqrt{[(\zeta-a)^2 + 4\delta\tau]}$ conformally maps the upper plane minus the vertical slit in $\mathbb{C}$, $[(a,0);(a,2\sqrt{\tau})]$, into the upper plane: ZA gradually zips the whole path onto the x-axis using the composition of functions $g_{a,\delta\tau}(\zeta)$ for different $\delta\tau$. We thus transform the erratic nodal line in the plane (inset in Fig. 1, described below) into an unknown motion along the real axis, $\xi(\tau)$.

To test for conformal invariance, we therefore must ask: Is $\xi(\tau)$ a Gaussian process? Does it correspond to a Brownian motion? And if so, what is its diffusivity? To answer the first question, one can use the classical Kolmogorov-Smirnov (KS) test, and check (i) whether its p_{KS} value is above a given threshold for a wide range of driving times τ, and (ii) whether the steps in this motion are independent. When both tests are favorable, we then consider the scaling of the variance of $\xi(\tau)$. If the scaling is reasonably linear with τ, we will conclude that the set of driving functions likely stems from a Brownian process, and hence that the vorticity isolines obtained as indicated above are likely to be conformally invariant. The linear scaling also gives us the diffusivity κ which describes entirely the statistics of the SLE process.

Results: We now apply the procedure to the 1536^3 DNS data. After performing the average (either in z or in y), fifteen temporal snapshots are analyzed, separated by approximately one eddy turn-over time. The resulting dataset has in excess of 3.5×10^7 points for each averaging direction. In Fig. 1 is given a snapshot of $|\boldsymbol{\omega}(\mathbf{x})|$ in 3D, a 2D slice of $\omega_z(\mathbf{x})$ (in the middle of the box), and the same field component when vertically averaged, $\langle\omega_z\rangle_z$ (bottom slice). The flow displays features of both

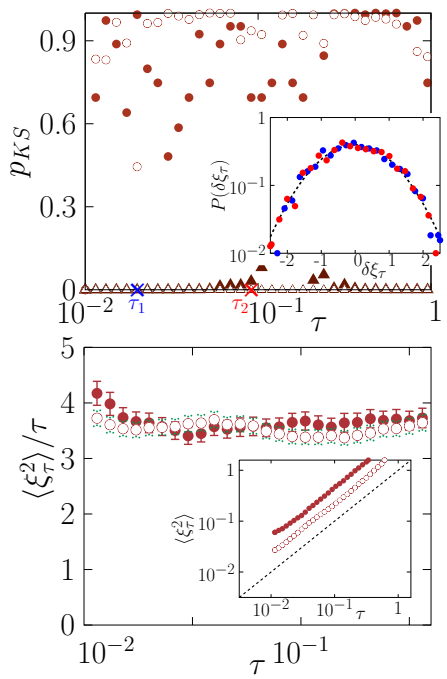

FIG. 2: (*Color online*) SLE analysis for $\langle\omega_z\rangle_z$ (circles) and $\langle\omega_z\rangle_y$ (triangles). Filled symbols comprise the full data, and open symbols correspond to paths in the dataset filtered at $\ell < 2\pi/10$. Driving time τ is in log coordinates. *Top:* KS test; inset: PDFs of driving function increments for $\langle\omega_z\rangle_z$ for τ_1 and τ_2 as marked on the τ–axis; the dashed line indicates a Gaussian. *Bottom:* Diffusivity κ for $\langle\omega_z\rangle_z$ with error bars; inset: scaling of variance for $\langle\omega_z\rangle_z$, with dash line indicating linear variation with τ.

2D and 3D behavior [7, 9]; prominent are tangles of vortex filaments loosely organized parallel to $\Omega\hat{z}$, and Beltrami core vortices, smooth long-lived helical columns. The inset shows $\langle\omega_z\rangle_z$ face-on with a few examples of superimposed paths that are analyzed below, noting that we discard the traversing paths, only keeping returning paths (loops at the top, blue online), as done in [3, 10].

Figure 2 summarizes the analysis, for ω_z averaged either parallel (full circle) or transverse (y, full triangle) to $\Omega\hat{z}$. Since a barely-resolved inverse cascade of energy develops in the DNS between the forcing scale and the box size, we also performed the analysis in a dataset in which ω_z was filtered so as to only preserve scales smaller than the driving scale: for $\ell < 2\pi/10$, the results are now displayed with open symbols. Figure 2 (top) gives the p_{KS} values of the KS test with abscissa τ in log scale. The value $p_{KS} \approx 10^{-5}$ for $\langle\omega_z\rangle_y$ (triangles) shows that the transverse y-averaged field is not Gaussian, and we shall not analyze further such y-averaged data. On the other hand, $p_{KS} \geq 0.6$ for most values of τ for $\langle\omega_z\rangle_z$ (circles). These opposite results imply that our test can eliminate non-Gaussian behavior, and that, due to the anisotropy of the flow, only parallel z-averaging may lead to conformal invariance. To confirm the Gaussianity of the process with *parallel* averaging, we show in the inset the probability distribution functions (PDFs) for two driving times τ_1 and τ_2; the dotted line is a Gaussian with zero mean and unit variance [13]. Note that Gaussianity also implies independence of increments (we show the evolution of the PDFs for different τ in Fig. 2).

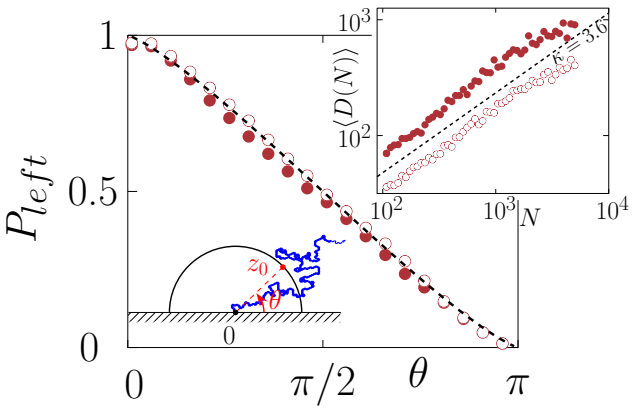

FIG. 3: (*Color online*) Winding angle probability P_{left} as a function of the angle θ, as illustrated by the sketch at the bottom. *Inset:* Mean gyration radius D of nodal lines as a function of the number of pixels N. Dashed lines: theoretical predictions for $\kappa_S = 3.6$; open and filled circles as in Fig. 2.

Figure 2 (bottom) gives the variance of the motion normalized by τ with error bars for the datasets that are not discarded by the KS test. The resulting diffusivity for the associated Brownian motion is $\langle\xi_\tau^2\rangle/\tau = \kappa = 3.6 \pm 0.1$ for the full data set (full circles), and $\kappa = 3.5 \pm 0.2$ for the data in which the scales comparable to or larger than the forcing have been filtered out (open circles). The inset shows the actual scaling of variance with driving time, in log-log coordinates, with the dashed line for linear variation. Note that, within error bars, the results are insensitive to whether or not we filter the numerical data (keeping only Fourier modes $k > 10$, thereby making sure we restrict the data to the direct cascade of energy).

Finally, we confirm the scaling we found for κ by examining some of the predictions on statistical properties of nodal lines of $\langle\omega_z\rangle_z$ that can be made using the SLE framework (see [1]). A classical one concerns the fractal dimension of the nodal lines, but less trivial features predicted by SLE include for instance the so-called "winding angle" or the gyration radius. The winding angle prediction states that the probability P_{left} of a SLE line to leave a point $z_0 = \rho e^{i\theta}$ in $\mathbb{C}$ to its left depends only on κ and θ following a known expression [1]. Figure 3 shows the results obtained from our datasets as a function of θ, as well as the mean gyration radius of the nodal lines as a function of their length in pixels in the top-right inset. In both cases, the SLE predictions for $\kappa = 3.6$, given with the dashed lines, appears convincing.

We thus conclude that our analysis identifies conformal invariance for nodal lines of the vertical component of the vorticity field when averaging parallel to the direction of rotation, and fails to identify such invariance

in its transverse average. For the parallel-averaged vertical vorticity, the associated diffusivity is $\kappa \approx 3.6 \pm 0.1$. Moreover, SLE predictions for this value of κ agree well with our results. It is also important to remark that our analysis could fail to reject the hypothesis of Gaussianity if data were insufficiently resolved; this is not surprising since it is hard to distinguish SLE behavior from something close to SLE [14]. In spite of these limitations, the data analyzed here up to the spatial resolution considered is found to be consistent with SLE behavior.

Discussion: Rotating helical turbulence may be perhaps the first documented case presenting SLE scaling for three-dimensional flows undergoing a direct cascade of energy and of helicity to small scales, when properly averaged in the direction of rotation. Conformal invariance is a strong local property and allows determination of a series of scaling laws, as exemplified in [3, 10] for 2D NS and other related 2D cases such as surface quasi-geostrophic (SQG) flows, and as found here as well. SLE obtains convincingly for the vertical component of the vorticity averaged along the direction of rotation, with $\kappa \approx 3.6$, close (but not identical) to the value identified in [10] for SQG flows for an inverse cascade. Note that anisotropy of this 3D rotating flow must play an essential role, since the direct cascade of enstrophy in strictly 2D NS is not SLE as shown in [3].

The fractal dimension $\mathrm{D}_F \leq 2$ of SLE curves can be related to κ [3], as well as to the cancellation exponent κ_C which measures how fast a field changes sign [15]. With d the dimension of space, we have $D_F = 1+\kappa/8 = d-2\kappa_C$. It is straightforward to relate the diffusivity of the SLE process κ and the exponent e of the energy spectrum, $E(k) \sim k^{-e}$, under the assumption of self-similarity, $\zeta_p = a_S p$; ζ_p are the exponents of the pth-order longitudinal structure functions of the velocity field, $\langle \delta u_L(r)^p \rangle \sim r^{\zeta_p}$, where δu_L is the variation of the velocity projected along the direction of the spatial increment $\mathbf{r}$. We use that $\kappa_C = \zeta_1 = a_S$, $\zeta_2 = e-1$ for $1 < e \leq 3$, and that dimensional analysis for a given dynamics gives a_S. Then,

$$\frac{\kappa}{8} = d - e = d - 1 - 2a_S \ . \qquad (3)$$

Hence, the value of κ is quite sensitive to e or a_S [16]. For 2D NS, a_S=1/3 and κ=8/3, as found in [3] (with dual value $\kappa^* = 6$). For rotating helical turbulence, a_S=3/4, using a phenomenological model based on three assumptions [7, 9]: wave-modulated energy spectrum; domination of the helicity cascade to small scales; and maximal helicity. The first hypothesis allows to write that the transfer of energy to small scale is slowed down in the proportion $\tau_{\mathrm{NL}}/\tau_\Omega$; the second one stems from the fact that the energy undergoing an inverse cascade to large scale, little energy is left to feed the small scales, whereas helicity only possesses a small-scale cascade and thus is the determining factor in this direct cascade. These two concepts lead to $e + h = 4$, with helicity spectrum $H(k) \sim k^{-h}$. The third assumption gives $h = e - 1$ and thus $\zeta_p = 3p/4$, a value reported experimentally as well [6, 16]. From Eq. (3), we then obtain $\kappa = 4$, close to the value we find given the statistics.

The connection between SLE and statistical properties of turbulence allows one to look at such flows with a new eye, and to build bridges between fluid dynamics and other research areas in mathematics, condensed matter, percolation, and quantum field theory. Other three-dimensional flows may be studied with the same tools when the flow is self-similar and symmetries allow for a reduction of dimensionality. As an example, we leave for future work an investigation of SLE properties in the inverse cascade of rotating turbulence.

Computer time was provided by NCAR, which is sponsored by NSF; partial support was given by grants nsf-cmg 1025188, and for PDM by UBACYT 20020090200692, PICT 2007-02211, and PIP 11220090100825.

[1] J. Zinn-Justin, "Quantum Field Theory and Critical Phenomena" (Oxford Univ. Press., 2002); W. Werner, Saint-Flour summer school, arxiv:math/0303354 (2003); I.A. Gruzberg and L.P. Kadanoff, *J. Stat. Phys.* **114**, 1183 (2004); J.L. Cardy, *Annals Phys.* **318**, 81 (2005).
[2] R.H. Kraichnan and D. Montgomery, *Rep. Prog. Phys.* **43**, 547 (1980).
[3] D. Bernard *et al. Nature Phys.* **2**, 124 (2006).
[4] F. Bellet *et al.*, *J. Fluid Mech.* **562**, 83 (2006).
[5] C. Simand, Thèse, "Etude de la turbulence au voisinage d'un vortex," Ecole Normale Supérieure de Lyon (2002).
[6] L. J. van Bokhoven *et al.*, *Phys. Fluids* **21**, 096601 (2009).
[7] P.D. Mininni and A. Pouquet, *Phys. Rev. E* **79**, 026304 (2009).
[8] P.D. Mininni and A. Pouquet, *Phys. Fluids* **22**, 035105 (2010).
[9] P.D. Mininni and A. Pouquet, *Phys. Fluids* **22**, 035106 (2010).
[10] D. Bernard *et al.*, *Phys. Rev. Lett.* **98**, 024501 (2007); G. Falkovich and S. Musacchio, arXiv:1012.3868 (2010).
[11] H.K. Moffatt, *J. Fluid Mech.* **35**, 117(1969).
[12] T. Kennedy, *J. Stat. Phys.* **131**, 803 (2008).
[13] A similar test for $\langle \omega_z \rangle_y$ gives strong departures from a Gaussian for its driving function increments (not shown).
[14] D.D. Marshall and S. Rohde, *SIAM J. Num. Ana.* **45**, 2577 (2007).
[15] E. Ott *et al.*, *Phys. Rev. Lett.* **69**, 2654 (1992).
[16] Different problems with the same inertial index e can lead to the same diffusivity κ; conversely, a set of rotating fluids with different energy indices ($e+h=4, e \neq h$) can lead to different diffusivities, provided they are SLE.

7.3 Addendum : Phenomenology of 3D turbulence with rotation.

Inertial Ranges. It may seem strange to look for a conformal invariance property in a " direct cascade of energy" of a 3D turbulent run, where it is not clear if even scale invariance should hold. It happens that the inertial regime studied in the PRL paper is very specific to 3D turbulence with rotation. It is a wave regime, which is "sufficiently large scale" to be affected by the presence of rotation. The existence of this meso-scale regime can be understood through phenomenological arguments, a plausible example of which we relate here. The arguments are taken from [Pouquet and Mininni, 2010], in which a way more detailed *état de l'art* can be found. The plausible phenomenology of forced 3D turbulence with rotation and helicity which is described in the next paragraphs is summarized on Figure 7.1.

In forced 3D non-rotating helical turbulence, a well-accepted scenario is that of a dual direct cascade : one cascade of energy, in which the energy cascades from large to small scales at a constant energy rate $\epsilon_E \sim kE(k)/\tau_E$, and one cascade of helicity with its own transfer rate $\epsilon_H \sim kH(k)/\tau_H$. If the typical times are taken to be the usual turn-over times, $\tau_E = \tau_H = l/u_l$, one obtains -5/3 laws for both the spectrum of energy and the spectrum of helicity [Pouquet and Mininni, 2010].

When rotation is added, the phenomenology of turbulence changes. For scales larger than the injection scale, the Taylor-Proudman theorem may be used to argue about the existence of a 2D-like inverse cascade energy regime, and thus of a $-5/3$ spectrum of perpendicular energy. For scales smaller than the energy injection rate, one expect to see cascades of energies and of helicities, as in the non-rotating case. However, another characteristic time comes into play $\tau_\Omega = 1/\Omega$ in addition to the standard non-linear time $\tau_{nl} = v_l/l$. Equating those two time scales yield a new characteristic length, now known as the "Zeman" scale k_Ω. It introduces a thumb threshold between the "large scales" ($k \lesssim k_\Omega$) that feel the rotation, and the small scales ($k \gtrsim k_\Omega$) for which the effect of the rotation is transparent. If the Zeman scale is larger than the dissipation scale, then one can therefore expect to see a small-scale inertial range, with the same dual energy-helicity cascade as in the non-rotating case. The dissipation scale can then be standardly estimated as $k_\nu \simeq \epsilon/\nu^3)^{1/4}$. The condition for the small-scale inertial range to exist is $k_\Omega < k_\nu$. It can be formulated in terms of a condition involving the Rossby number $Ro = U_f/(L_f\Omega)$ and the Reynolds number $Re = U_f L_f/\nu$ – with U_f a typical velocity at injection scale L_f – as $k_\Omega \ll k_\nu$ if and only if $ReRo^2 \gg 1$.

For the scales in between the injection scale and the Zeman scale, the existence of a wave regime has been proposed. It is phenomenologically obtained by assuming that the characteristic time for the transfer of energy to smaller scales is τ_{nl}^2/τ_Ω instead ofτ_{nl}. Such a scenario does not prescribe a power law for the specific spectrum of energy and the specific spectrum of helicity, but rather a "joint behavior" $E(k)H(k) \sim k^{-4}$. Due to the effect of rotation, the energy and the helicity spectra can be expected to be essentially perpendicular.

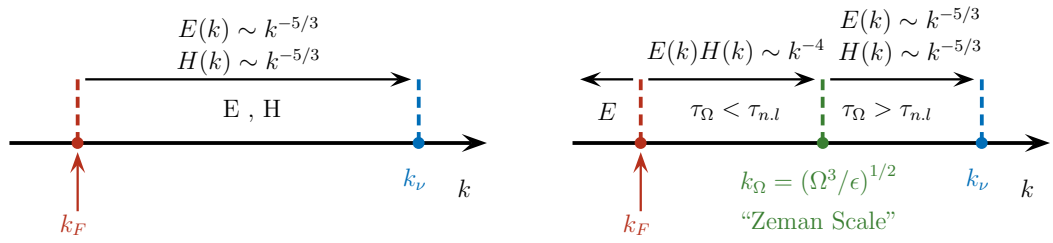

(a) Without rotation **(b)** With rotation

Figure 7.1: Cartoon of the cascades in three dimensional turbulence with and without rotation. The dissipation scale is the standard Kolmogorov-dissipation scale $k_\nu = \left(\frac{\epsilon}{\nu^3}\right)^{1/4}$.

Simulation The scenario does well account for the spectral behavior of the 1536^3 rotating run at use in the numerical simulations, which display k^4 law behavior for the quantity $E(k)H(k)$ – see Figure 7.2. In this run, the Reynolds number can be estimated as $Re \simeq 5.1 \times 10^3$ and $Ro \simeq 0.06$. Hence, $ReRo^2 \simeq 18$. The Zeman scale is therefore only moderately resolved. The moderate resolution is in fact our luck since it allows us to focus on the mesoscale regime without having too much of an interference with a three-dimensional, isotropic, Kolmogorov -like turbulence.

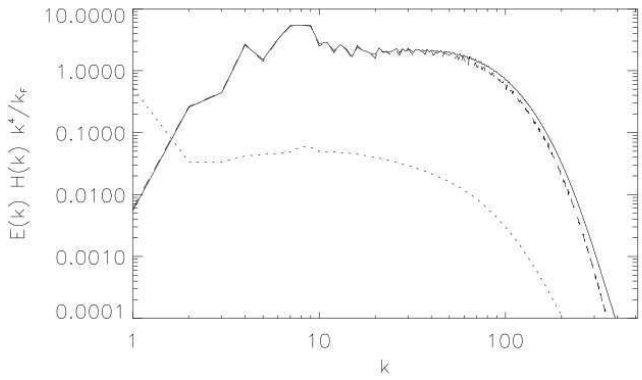

Figure 7.2: Compensated spectrum of energy times the helicity for the 1536^3 rotating helical run at late time. The dotted line represents the parallel (z) component of the spectrum. Taken from [Pouquet and Mininni, 2010].

For the regime under study, there are good indicators of scale-invariance for the increments of velocity field, given by the scaling of the exponents of structure functions. More precisely, longitudinal increments are defined as $\delta v(\mathbf{r}, \mathbf{l}) = [\mathbf{v}(\mathbf{r}+\mathbf{l}) - \mathbf{v}(\mathbf{r}+\mathbf{l})] \cdot \frac{\mathbf{l}}{|\mathbf{l}|}$, and the p-order structure function as $S_p(\mathbf{r}, \mathbf{l}) = \langle \delta v^p(\mathbf{r}, \mathbf{l}) \rangle$, expected to scale as $|\mathbf{l}|^{\xi_P}$. Detailed

measurements for the 1536^3 run are presented in [Mininni and Pouquet, 2009]. It is found that the exponents ξ_p display a linear scaling with p. A similar scaling is found for helical increments and structure functions constructed as $\langle \delta v(\mathbf{r}, \mathbf{l}) \cdot \delta \boldsymbol{\omega} \rangle$.

This is a signature of a scale invariant property for the increments [Frisch, 1996].

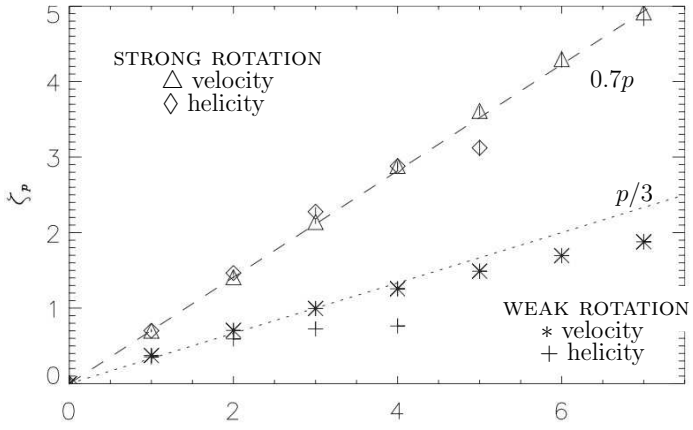

Figure 7.3: Scaling of the exponents of the structure functions for 1536^3 rotating helical run at late time, compared with that obtained for the same run but without rotation.Taken from [Mininni and Pouquet, 2009].

7.4 Addendum : Conformal invariance and "Schramm-Löwner" ensembles.

Most of the present account is inspired by John Cardy's review paper about SLE [Cardy, 2005] and numerical review papers by Tom Kennedy [Kennedy, 2009].

From scale to conformal invariance (Statistical) Scale invariance is the assumption that under the change of variable $\mathbf{r} \to \lambda \mathbf{r} = \mathbf{r}'$ ($\lambda > 0$), the statistical properties of a field $\phi(\mathbf{r}')$ are related to the initial field $\phi(\mathbf{r})$ as $\phi(\lambda \mathbf{r}) \underset{\text{law}}{=} \lambda^h \phi(\mathbf{r})$. Conformal invariance is a generalization of this property to include the set of all maps $\mathbf{r} \to \mathbf{w}(\mathbf{r})$, that locally preserve the angles : $\phi(\mathbf{w}(\mathbf{r})) \underset{\text{law}}{=} |w'|^h \phi(\mathbf{r})$. In two-dimension, the physical domain can be identified with the complex plane, and conformal transformations coincide with holomorphic functions, (*i.e* functions derivable with respects to complex variables). Conformal invariance imposes strong constraints on the shape of n-point correlation functions [Ginsparg, 1988].

Random paths, Invariant measures In two-dimension, an alternative formulation of conformal invariance is the "Schramm-Löwner " formulation, which expresses conformal invariance through the language of random paths, growth processes, conformal mapping... and invariant measures. It stems from the combination of "old" conformal mapping theorems due to Bernhard Riemann (in the 1850's) and Karl Löwner (in the 1920's) with some state-to-the art contemporary mathematical developments in the theory of probability over the past decade, and theorems proven by Gregory Lawler, Oded

Schramm, Wendelin Werner, Stanislav Smirnov among others.

At a basic level of understanding, the global ideas behind Schramm-Löwner Evolutions can however be partly understood intuitively, and used practically to find hints of conformal invariance in two-dimensional physical systems.

Consider a two-dimensional domain $\mathcal{D}$. And define some rules to generate self-avoiding (random) paths from a starting point $\mathbf{r}_0$ to an endpoint $\mathbf{r}_1$ on the frontier of the domain. The paths γ can be seen as continuous functions from $[0;1] \to \mathcal{D}$, such that $\gamma(0) = \mathbf{r}_0$ and $\gamma(1) = \mathbf{r}_1$. We suppose that we can define a probability measure on the set of paths from $\mathbf{r}_0$ to $\mathbf{r}_1$ and we write $\mu_{\mathbf{r}_0 \to \mathbf{r}_1}(\gamma, \mathcal{D})$ the probability of finding a prescribed path γ joining $\mathbf{r}_0$ to $\mathbf{r}_1$ – within a a small distance $\mathrm{d}\gamma$ for a conveniently defined topology.

Naturally, in order to define and build those measures, one might require to use a discretization process and have a lattice picture in mind. One can first consider $N \times N$ regular discretization of the domain $\mathcal{D}$. The number of paths starting from $\mathbf{r}_0$ and ending at $\mathbf{r}_1$ is then necessarily finite, whatever the rules for generating those paths are. One can then define a uniform measure of this finite ensemble of paths and extend this measure to a continuous measure by letting the mesh of the lattice go to zero. The lattice picture is useful to define "interesting rules" in order to define ensembles of non-intersecting paths. Examples of "rules" to generate non intersecting paths include the pivot algorithm to generate so called "Self Avoiding Walks" (SAW), the generation of two-dimensional Brownian motions in which the loops are gradually erased, yielding "Loop Erased Random Walks" (LERW), percolating paths obtained in the percolation problem. One may also think of the frontiers of spin domains in lattice models such as the Ising or the Potts model, and so on.

A Schramm-Löwner ensemble of paths is obtained when the two following properties hold :

(i) (Markov property) : divide a path γ into two subpaths : γ_a starting from $\mathbf{r}_0$ and ending at an intermediate point $\mathbf{r}'$ in the domain $\mathcal{D}$ and γ_b starting from $\mathbf{r}'$ and ending at $\mathbf{r}_1$. Ask that for any such quantities, the probability of finding the path γ_b in the restricted space $\mathcal{D}\backslash\gamma_a$ be the same as the conditional probability of finding γ_b knowing γ_a :

$$\mu_{\mathbf{r}' \to \mathbf{r}_1}(\gamma_b, \mathcal{D}\backslash\gamma_a) = \mu_{\mathbf{r}_0 \to \mathbf{r}_1}(\gamma_b | \gamma_a, \mathcal{D}). \tag{7.1}$$

(ii) (Conformal Invariance property) : given an invertible conformal mapping $\phi : \mathcal{D} \to \tilde{\mathcal{D}}$, ask that μ be an invariant measure for ϕ, that is to say that the probability μ and the image probability $\mu^{\sharp\phi}$ of finding a path $\tilde{\gamma}$ going from $\tilde{\mathbf{r}_0} = \phi(\mathbf{r}_0)$ to $\tilde{\mathbf{r}_1} = \phi(\mathbf{r}_1)$ in $\tilde{\mathcal{D}}$ coincide :

$$\underbrace{\mu^{\sharp\phi}_{\tilde{\mathbf{r}}_0 \to \tilde{\mathbf{r}}_1}(\tilde{\gamma}, \tilde{\mathcal{D}})}_{\mu_{\mathbf{r}_0 \to \mathbf{r}_1}(\gamma, \mathcal{D})} = \mu_{\tilde{\mathbf{r}}_0 \to \tilde{\mathbf{r}}_1}(\tilde{\gamma}, \tilde{\mathcal{D}}). \tag{7.2}$$

Now, it is yet not so clear whether measures defined on ensembles of continuous path are really much easier to handle than correlation functions. It turns out to be the case. It

involves a 1920 equation obtained by Löwner and a 2000 theorem proven by Schramm. The idea is to interpret paths in the two-dimensional domain $\mathcal{D}$ as growth processes.

Löwner equation. For simplicity, let us here take $\mathcal{D}$ as the upper half complex plane. Let us first consider a path γ_1 composed of a segment going from 0 to $\mathbf{z}_1$. It is possible to find a conformal mapping $g_1 : \mathcal{D}\backslash[0;\mathbf{z}_1] \to \mathcal{D}$. If $\mathbf{z}_1$ was imaginary and γ_1 a vertical segment, the application $g_1 : \mathbf{z} \to \left[\mathbf{z}^2 + y^2\right]^{1/2}$, would do the job, with "$x^{1/2}$" meaning the square root located in the upper half-plane. In general, g_1 may not be as simple though. However, because $\mathcal{D}\backslash[0;\mathbf{z}_1]$ and $\mathcal{D}$ are two simply connected domains, the existence of g_1 is nevertheless guaranteed by a now standard theorem called the Riemann theorem. It can be made unique by imposing $g(z) \sim z + 2\delta\tau/z + o(1/z)$ at ∞. The effect of g_1 is clear : it "zips" the slit γ_1 onto the x-axis. In particular; the tip $\mathbf{z}_1$ is sent to a real number $a_1 = g_1(\mathbf{z}_1)$. $\delta\tau$ is necessarily positive. It can be interpreted as a time, which will be called th "Löwner time".

If we now add N vertical slits to the paths γ, we see that we can zip the entire path until z_N with the application $g(z) = g_N \circ g_{N-1} \circ ...g_1$ and map the path onto a sequence a_1,a_2...a_N of real numbers, parametrized by a Löwner time $\tau_1 = \delta\tau_1$, $\tau_2 = \tau_1 + \delta\tau_2$, ... $\tau_N = \tau_N + \delta\tau_N$. Hence, the process maps a "static" complex valued path γ of the upper half-plane the complex plane onto a dynamic real valued process a_τ.

The continuous version of the process has been known since 1920. It was discovered by Löwner. It is described by the Löwner equation :

$$\partial_\tau g_\tau(z) = \frac{2}{g_\tau(z) - a_\tau} \quad \text{with} \quad a_\tau = g_\tau(a_\tau). \tag{7.3}$$

The Löwner equation describes the "Löwner time" evolution of the conformal mapping $g_\tau(z)$ that maps an infinitesimal parcel of the path onto the x-axis at Löwner time τ. ξ_τ is the image of the tip of the path sent onto the x-axis at time τ. It therefore maps the path γ in the two-dimensional space $\mathcal{D}$ onto a one dimensional process $a(\tau)$. The mapping is a one-to-one mapping.

At a numerical level, the discrete Löwner process can be implemented by choosing the functions g_i as $g_i(z) = \Re(z_i) + \left[((z - \Re(z_i))^2 + \Im(z_i)^2\right]^{1/2}$ [Kennedy, 2009]. The function g_i zip the vertical slit $[\Re(z_i); z_i]$ onto the real-axis –instead of zipping the tilted slit $[0 z_i]$. Each zipping "takes" a Löwner time $\delta\tau = \Im(z_i)^2/4$. The Löwner zipping process is made visual on Figure 7.4.

Schramm theorem and "SLE_κ" For ensembles of random curves satisfying both the Markov property (i) and the Conformal property (ii), and which are symmetric with respect to the property $\mathbf{x} \to -\mathbf{x}$, Schramm's theorem tells that the driving functions are proportional to a standard Brownian motion B_τ: $a_\tau = \sqrt{\kappa} B_\tau$.

The diffusivity κ is not prescribed by the theorem. It depends on the ensemble of random paths that is under consideration. Once an ensemble has been identified as SLE_κ,

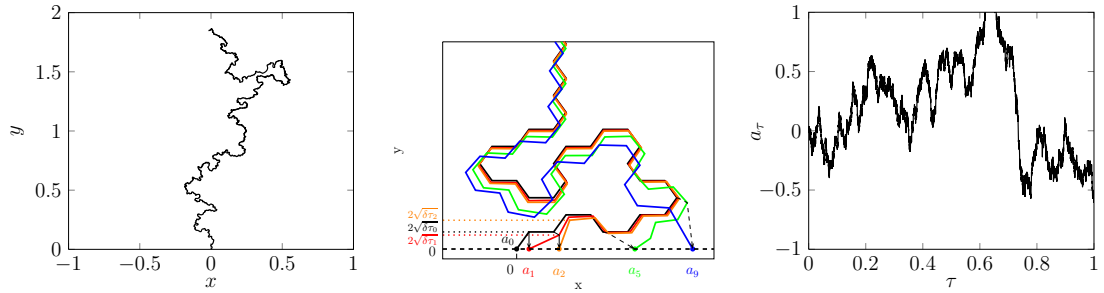

Figure 7.4: (a) A path in the upper plane. (b) the zipping process. (c) The driving function corresponding to (a).

knowing κ allows to compute and deduce both standard and unsuspected geometric properties for the random paths. The fractal dimension $d_f$of an SLE_κ path is $d_f = 1 + \frac{\kappa}{8}$, but less trivial quantities are amenable to an exact expression involving κ : winding angle distributions, distribution of the Radii, typical number of fjords , probabilities to keep a prescribed domain point on one side, crossing probabilities ... examples of which are shown on both papers.

It is believed and sometimes proven that the one parameter SLE_κ family of random paths describe the continuum limit of the interfaces which emerge in many short-range lattice models at critical temperature, including the Ising model ($\kappa = 3$) or Potts model, and of many natural random paths in two-dimensions : critical percolation paths ($\kappa = 6$) , self-avoiding walks ($\kappa = 8/3$), loop erased random walks ($\kappa = 2$)... Both the Markov and the conformal properties are natural properties to expect for such models. They give a translation in the language of random measures on ensemble of paths of the two essential ingredients common to those models : (i) the short range nature of the interactions : the paths keep forgetting their past and (ii) the conformal invariance property, expected to hold at at criticality. Note, that for systems with short range interactions, conformal invariance stems as a consequence of scale invariance, translational invariance ("homogeneity"), and rotational invariance ("isotropy"), as proven by Alexander Polyakov [Polyakov, 1970, Mussardo, 2010]. Note however, that there are only a limited number of cases (critical percolation on hexagonal lattices, loop erased random walks, ...) for which the convergence to the SLE description has indeed been proven at a mathematical level.

Schramm's theorem can be given a very practical use. To check that an ensemble of paths is likely to be described by SLE, it therefore suffices to compute driving functions. To do so one may use the Discrete Zipper Löwner process described previously. Then, the test of whether or not conformal invariance holds can be made at the level of the driving functions. We need to determine whether or not the sets of driving functions have a chance to represent a set of Brownian processes. Statistical tests can then be used to test the linear scaling of the variance, the Gaussianity of the increments, their independence. As noted in [Kennedy, 2009], it is in fact not so obvious to distinguish ensembles "close " to SLE from truly SLE ensembles. Therefore, those tests can only provide hints as to

whether or not sets of the random paths considered are both Markovian and conformal invariant. Due to the intrinsic long-range nature of the interactions, there is no reason to expect that SLE paths should be present in turbulent flows. But such hints of conformal invariance can however be identified in the two quasi-2D situations that we took a look at.

Chapter 8

Conclusion

Contributions. At a theoretical level, we have given some predictions based on counting arguments to argue about non-trivial long time behavior of three different 2D3C flows : magneto-hydro, axisymmetric and Boussinesq flows. Those three examples of 2D3C flows share many properties in common : i) they are incompressible ii) their energies are the sum of two well-identified contributions iii) they possess two families of Casimir invariants iv) the advecting field is not bounded by those. The study reveals that the long-time behavior of 2D3C flows is not generic. It can be expected to be of a very different nature than the long time behavior of two-dimensional hydro and related quasi-geostrophic flows. This substantially implies that ideal arguments based on the quasi-conservation of enstrophy to argue about the existence of long-lived coherent structures in the atmosphere should be handled with care.

Statistical arguments in Fourier space based on the use of rugged invariants show that the behavior of 2D3C flows is not generic : they yield small scales regimes for Boussinesq/Axisymmetric flows; and the possibility of a large scale magnetic regime and a small scale regime for two-dimensional magneto-hydro fluids. We have also extended the argument to a wider class of 2D3C flows, obtained from the magneto-hydro model by changing the integral relations between the vorticity and the stream-function on one hand, and the current and the magnetic potential on the other hand, in such a way that the other rugged invariants were left unchanged. The conclusion is not ground-breaking but deserves some mention : the crucial ingredients for the emergence of large scale structures is not so much the presence of extra-rugged invariants (in addition to the energy) but rather the interplay between those.

To obtain a clearer view, we have proposed a construction of an invariant microcanonical measure for the axisymmetric Euler equations, taking into account all the invariants and the stretching of the vorticity. The construction yields a very clear, but nuanced picture of the axisymmetric equilibria. The energy is essentially toroidal when it is low and essentially poloidal when it is high. In the latter case, the poloidal energy is large scale while the toroidal energy and the helicity are small scale, and the typical poloidal field very irregular at small scale. The construction was extended to the magneto-hydro case, with only a partial success, as no explicit expressions for the average physical quantities

was found in general, except for some very specific regimes. The construction however reveals the existence of at least four different kinds of magneto-hydro regimes, obtained by considering a non-helical situation. Depending on the regularity of the magnetic field, the equilibria either describe axisymmetric-like regimes or a magnetic condensation regime, in which all the energy is magnetic and on the largest scale.

We do not know whether 2D3C flows are well-defined mathematical objects : as mentioned in the introduction, they may very well exhibit a finite-time singularity for a wide range of initial data. It is therefore not so clear whether the ensembles we have constructed are relevant to describe long time properties of such flows. In other words : "if the system blows up, then its long time properties are trivial !". If this was the case, the present construction may provide a physicist proof *ab absurdio* that regularity for the poloidal/kinetic field is lost at long time : this is what the divergence of the high-order cumulants for the poloidal/kinetic equilibrium distributions suggests. More pragmatically, those two constructions [(a)] still provide a useful analogy between ideal flows and some conveniently defined "spin" lattice models that accounts for the interplay between the different geometric constraints provided by the Casimirs. The sought after limit measure is then seen as the thermodynamic limit of a statistical ensemble of spin configurations. The picture allows to account for the difference between the magneto-hydro and the axisymmetric cases from a condensed matter point of view : in the magneto-hydro case the magnetic energy is mapped onto a short-range lattice energy of ferromagnetic type, while in the axisymmetric case the toroidal energy induces no interactions between the toroidal spins. At a thermodynamical level, the analogy reveals three kinds of large scale organizations : the large scale magnetic condensation in magneto-hydro dynamics is a zero (positive) temperature "paramagnetic" self-organization, the large scale vortices in two-dimensional ideal (hydro) fluids are negative temperature states, the axisymmetric large-scale poloidal jets are infinitely-warm states – yet "colder" than the 2D states.

Whether or not those ensembles can be used to describe long-time properties of forced-dissipated flows is even more dubious. It may be that predictions based on those kinds of ideal ensembles dramatically fail when forcing is put into the game. However, a literal and liberal interpretation of the lattice model analogy can again provide some insights about experimental flows : it is the case for the Von Kármán experiments which we described in Chapter 6. The reasons why the interpretation works is not crystal clear, and its scope is surely limited. However, it gives an original definition of a "temperature of turbulence".

Openings. Concerning the ideal theories, one can wonder whether lattice models arguments, which may pave the way to a clean definition of a random ideal measure, might be used for more complicated flows than the incompressible 2D3C ones that we considered. In two-dimensions, a natural model to investigate would be the shallow-water model, which includes a compressibility effect. But the real question might be whether such an approach could be used to describe the equilibria of three-dimensional flows, possibly

[(a)]– or three if we include the straightforward generalization to the Boussinesq case –

stratified. A fruitful example to consider might be the three-dimensional magneto hydrodynamical case, whose Casimir invariants are known [Padhye and Morrison, 1996], and whose rugged invariants lead to an inverse cascade of magnetic helicity $\int \mathbf{A}\cdot(\nabla\times\mathbf{A})$, obtained both Fourier space arguments [Frisch et al., 1975] and observed in magnetically-forced simulations [Alexakis et al., 2006]. The statistical mechanics of such flows could be all the more relevant to describe as the analogy between Stratified Boussinesq turbulence and Magneto-hydro turbulence extends to the three-dimensional situation, [Gibbon and Holm, 2010, Pieri et al., 2013].

Ideal statistical theories provide an enjoyable playground, but are not the ultimate scope of statistical mechanics. They can provide trends, sometimes approximate solutions, usually thermodynamic inequalities to account for non-equilibrium phenomena but certainly not a precise description of those. They can however also provide ideas to develop the non-equilibrium statistical mechanics needed for turbulence. But to transform those ideas into a consistent non-equilibrium framework is far from being understood. Many non-equilibrium statistical theories for turbulence have been proposed, that rely on subtle interpretations of equilibrium physics. The inclusion of additional constraints such as a finite energy dissipation constraint in inferences theory [Verkley,], the parametrization of small scale forcing through the use of mixed ensembles [Ellis et al., 2000] and canonical prior distribution [Chavanis, 2008, Majda and Wang, 2006], the use of "maximum entropy bubbles" [Chavanis and Sommeria, 1998] and more recent reduced partition functions [Herbert, 2013] to account for a possible loss of ergodicity provide such examples.

We note that it could also be that the appropriate non-equilibrium statistical mechanics at use to describe turbulence at a dynamical, coarse-grained level may involve ensembles and concepts that are very distant cousins of the ideas depicted in the present work. The dynamics of coherent structure may be obtained from ensembles of paths [Bouchet et al., 2011, Monthus, 2011], they may be computed from effective equations derived from optimization principles [Turkington, 2013] or maximum entropy production principles [Chavanis et al., 2010, Herbert and Paillard, 2013], and apprehended by the use of direct statistical simulations of turbulence [Marston, 2011]... The applications of statistical physics to describe turbulent flows are potentially many. Much work remains to be done to make them explicit.

Appendix A

Technical computations related to the Bessel-Fourier modes.

This appendix details some technical computations related to the Bessel Fourier modes, as used in chapter 3 and 4. Those computations are akin to computations described in [Leprovost et al., 2006, Naso et al., 2010b].

Contents

A.1 Explicit computation of Bessel-Fourier modes.

Explicit expression. We consider the case of a cylindrical domain with no inner radius (Von Kármán geometry). The radius of the outer cylinder is R. The height of the domain is $2h$. The cylindrical coordinates are (r, θ, z), and we assume no dependence of the fields with respect to θ.

We define the Bessel-Fourier modes as the eigenmodes of the differential operator $\mathcal{L} = -r\Delta_\star(r.)$, defined in chapter 1, with vanishing boundary conditions. We also impose that those modes vanish for $r = 0$.

A Bessel Fourier-mode $\phi_{\mathbf{k}}$ is labeled by an index $\mathbf{k} = (k_r, k_z) \in \mathbb{N}^2$. It is explicitly given by

$$\phi_{\mathbf{k}}(r, z) = A_{\mathbf{k}} \sin \frac{k_z \pi z}{2h} J_1\left(j_{k_r} \frac{r}{R}\right) \quad \text{with} \quad A_{\mathbf{k}} = \left(\frac{1}{2} J_2^2(j_{k_r})\right)^{-1/2}. \tag{A.1}$$

Its corresponding eigenvalue reads

$$\kappa_{\mathbf{k}}^2 = \frac{j_{k_r}^2}{R^2} + \frac{k_z^2 \pi^2}{4h^2}. \tag{A.2}$$

In the last two equations, J_1 and J_2 respectively denote the first and second Bessel functions of the first kind – see for example [Abramowitz and Stegun, 1965] – , and j_{k_r} is the k_r^{th} zero of J_1. Besides,

(a) $\phi_{\mathbf{k}}$ is non trivially zero provided both k_r and k_z are non zero;

(b) the choice of $A_{\mathbf{k}}$ in (A.1) make the $\phi_{\mathbf{k}}$ be an orthonormal family for the scalar product $(,)$ defined through $(f,g) = \frac{1}{hR^2}\int_{r=0}^{R}\int_{h=0}^{2h} r\mathrm{d}r\mathrm{d}z f(r,z)g(r,z)$.

Note, that for large values of k_r, the k_r^{th} zero j_{k_r} of J_1 can be expanded as $j_{k_r} = (k_r + \frac{1}{4})\pi + o(1)$. For large k_r, the coefficients $A_{\mathbf{k}}$ can then be estimated as $A_{\mathbf{k}} = \pi\sqrt{k_r + \frac{1}{4}}(1 + o(1))$. [(a)]

The eigenmodes made explicit (technical computation). Let ϕ be an eigenmode of $\mathcal{L} = -r\Delta_\star(r.)$, such that $\mathcal{L}(\phi) = \kappa^2\phi_{\mathbf{k}}$. Let us assume that ϕ vanishes both at the boundaries and at the center of the cylinder. Note that κ^2 can be negative if κ is imaginary. ϕ satisfies the differential equation :

$$0 = -\mathcal{L}(\phi) + \kappa^2\phi = r^{-1}\partial_{zz}^2 r\phi + \partial_r\left(r^{-1}\partial_r r\phi\right) + \kappa^2\phi = 0. \tag{A.3}$$

We now solve (A.4) by the method of separation of variables. Let us write ϕ as $\phi(r,z) = f(r)g(z)$. In terms of f and g, (A.4) becomes

$$-\left(\frac{g''(z)}{g(z)} + \kappa^2\right) = \frac{f''(r)}{f(r)} + \frac{f'(r)}{rf(r)} - \frac{1}{r^2} = \alpha^2, \tag{A.4}$$

where α is a yet nonprescribed constant, to be determined by the boundary conditions.

g. The differential equation on g reads

$$g'' + \left(\kappa^2 - \alpha^2\right)g = 0. \tag{A.5}$$

ϕ needs to vanish both at the upper wall and at the bottom wall of the domain. The quantity $\kappa^2 - \alpha^2$ is therefore necessarily non negative, and g can be written as $g(z) = A\sin z\sqrt{\kappa^2-\alpha^2} + B\cos z\sqrt{\kappa^2-\alpha^2}$. From $g(0) = g(2h) = 0$, we conclude that $B = 0$ and that $\kappa^2 - \alpha^2$ can be written as $\kappa^2 - \alpha^2 = \left(\frac{n\pi}{2h}\right)^2$, with $n \in \mathbb{N}$.

f. The differential equation on f reads

$$r^2 f''(r) + rf'(r) + \left(r^2\alpha^2 - 1\right)f(r) = 0. \tag{A.6}$$

The change of variables "$x = |r\alpha|$" and "$\tilde{f}(x) = f(r)$", yields more familiar differential equations :

[(a)] This is easily proven by using the estimates $J_\nu(x) \underset{x\to\infty}{\sim} \sqrt{\frac{2}{\pi x}}\cos\left(x - \frac{\pi}{4} - \frac{\nu\pi}{2}\right)$, so that $J_1(x) \underset{x\to\infty}{\sim} -\sqrt{\frac{2}{\pi x}}\sin\left(\frac{\pi}{4} - x\right)$ and $J_2(x) \underset{x\to\infty}{\sim} -\sqrt{\frac{2}{\pi x}}\cos\left(x - \frac{\pi}{4}\right)$. Note, that it is also true that $J_0(x) \underset{x\to\infty}{\sim} \sqrt{\frac{2}{\pi x}}\cos\left(x - \frac{\pi}{4}\right)$ [Abramowitz and Stegun, 1965].

$$x^2\tilde{f}''(x) + x\tilde{f}'(x) + \left(x^2 - 1\right)\tilde{f}(x) = 0, \quad \text{if } \alpha^2 \geq 0 \tag{A.7}$$

$$\text{or} \quad x^2\tilde{f}''(x) + x\tilde{f}'(x) - \left(x^2 + 1\right)\tilde{f}(x) = 0. \quad \text{if } \alpha^2 < 0 \tag{A.8}$$

Equation (A.7) is a Bessel equation and Equation (A.8) is a so called "modified" Bessel equation [Abramowitz and Stegun, 1965]. Solutions of modified Bessel equations are either exponentially growing or decaying and are not oscillating. They cannot describe –non trivial – solutions vanishing both at the center and at the outer wall. We conclude that α^2 is non-negative. The solution of A.7 can be expressed as a linear combination of the first Bessel function of the first kind J_1 and the first Bessel function of the second kind K_1, so that $\tilde{f}(x) = CJ_1(x) + DK_1(x)$. From $\phi(0,z) \equiv 0$, we obtain $D = 0$. From $\phi(R,z) \equiv 0$, we obtain $J_1(\alpha R) = 0$. Therefore, the quantity αR is one of the zeros j_m of J_1.

ϕ. Putting the pieces back together, we therefore get ϕ in terms of two integers m and n as $\phi(r,z) = \phi_{m,n}(r,z) = A_{m,n}J_1\left(\frac{j_m r}{R}\right)\sin\frac{n\pi z}{2h}$. The corresponding eigenvalues κ^2 is non negative, and reads $\kappa^2 = \kappa^2_{m,n} = \frac{n^2\pi^2}{4h^2} + \frac{j_m^2}{R^2}$.

$\phi_{m,n}$ s. From the identity $\int_0^1 x\mathrm{d}x\, J_1(xj_m)J_1(xj_{m'}) = \frac{\delta_{m,m'}}{2}J_2^2(j_m)$ [Abramowitz and Stegun, 1965], we immediately see that (i) the $\phi_{(m,n)}$ are mutually orthogonal for the scalar product defined through $(f,g) = \frac{1}{hR^2}\int_{z=0}^{2h}\int_{r=0}^{R} r\mathrm{d}r\mathrm{d}z f(r,z)g(r,z)$; (ii) the choice $A_{m,n} = \left(\frac{J_2^2(j_m)}{2}\right)^{-1/2}$ makes the set of $\{\phi_{m,n}\}_{(m,n)\in\mathbb{Z}^2}$ orthonormal, namely $\left(\phi_{(m,n)}\phi_{(m',n')}\right) = \delta_{mm'}\delta_{nn'}$.

A.2 Explicit estimates of integrals involving Bessel-Fourier modes.

Below are some estimates of quantities involving the $\phi_{\mathbf{k}}$, valid provided k_r and k_z are both non vanishing. Those quantities appear mostly in chapter 3. They deserve no particular further comment.

Estimate of $(r\phi_{\mathbf{k}})$.

$$(r\phi_{\mathbf{k}}) \underset{k_r\to\infty}{=} \frac{\sqrt{2}R}{\pi^2}(-1)^{k_r+1}\frac{1-(-1)^{k_z}}{k_z\left(k_r+\frac{1}{4}\right)}\left(1+o\left(\frac{k_r}{k_z}\right)\right). \tag{A.9}$$

Proof :

$$\begin{aligned}(r\phi_{\mathbf{k}}) &= \frac{1}{hR^2}\int_0^{2h}\mathrm{d}z\int_0^R \mathrm{d}r r^2\phi_{\mathbf{k}}(r,z) = 2RA_{\mathbf{k}}\int_0^1 \mathrm{d}z\sin k_z\pi z\int_0^1 \mathrm{d}u u^2 J_1(j_{k_r}u)\\ &= 2RA_{\mathbf{k}}\frac{1-(-1)^{k_z}}{k_z\pi}\frac{J_2(j_{k_r})}{j_{k_r}}.\end{aligned}$$

■

Estimate of $(r^{-1}\phi_{\mathbf{k}})$.

$$(r^{-1}\phi_{\mathbf{k}}) \underset{k_r\to\infty}{=} \frac{2}{R\pi}\frac{1-(-1)^{k_z}}{k_z\left(k_r+\frac{1}{4}\right)^{1/2}}\left(1+o\left(\frac{k_r}{k_z}\right)\right). \tag{A.10}$$

$$\begin{aligned}(r^{-1}\phi_{\mathbf{k}}) &= \frac{1}{hR^2}\int_0^{2h}\mathrm{d}z\int_0^R \mathrm{d}r\phi_{\mathbf{k}}(r,z) = 2R^{-1}A_{\mathbf{k}}\int_0^1 \mathrm{d}z\sin k_z\pi z\int_0^1 \mathrm{d}uJ_1(j_{k_r}u)\\ &= 2R^{-1}A_{\mathbf{k}}\frac{1-(-1)^{k_z}}{k_z\pi}\frac{1}{j_{k_r}}\left(1-J_0(j_{k_r})\right).\end{aligned}$$

Estimate of $\alpha_{\mathbf{k}\mathbf{k}'} = (r^2\phi_{\mathbf{k}}\phi_{\mathbf{k}'})$.

$$\alpha_{\mathbf{k}\mathbf{k}'} \simeq \begin{cases} 0 \quad \text{if } k_r \neq k_r' \\ \dfrac{R^2}{3}\left(1-\dfrac{3}{2\pi^2\left(k_r+\frac{1}{4}\right)^2}\right) \quad \text{if } \mathbf{k}=\mathbf{k}' \\ \dfrac{2R^2}{\pi^2}\left(\dfrac{(-1)^{k_r-k_r'}}{(k_r-k_r')^2}-\dfrac{(-1)^{k_r-k_r'}}{(k_r+k_r'+1/2)^2}+\dfrac{1}{\pi(k_r+k_r'+1/2)^3}\right) \quad \text{otherwise.}\end{cases} \tag{A.11}$$

Proof :

$$\begin{aligned}(r^2\phi_{\mathbf{k}}\phi_{\mathbf{k}'}) &= \frac{1}{hR^2}\int_0^{2h}\mathrm{d}z\int_0^R \mathrm{d}r r^3\phi_{\mathbf{k}}(r,z)\phi_{\mathbf{k}'}(r,z)\\ &= 2R^2A_{\mathbf{k}}A_{\mathbf{k}'}\underbrace{\int_0^1 \mathrm{d}z\sin k_z\pi z\sin k_z'\pi z}_{=\frac{1}{2}\delta_{k_zk_z'}}\underbrace{\int_0^1 \mathrm{d}u u^3J_1(j_{k_r}u)J_1(j_{k_r'}u)}_{Q}.\end{aligned}$$

The contribution near 0 being smoothed by the factor x^3, it is legitimate to approximate Q upon estimating J_1 with its asymptotic development $J_1(x)\simeq -\sqrt{\frac{2}{\pi x}}\sin\left(\frac{\pi}{4}-x\right)$. This approximation – combined with liberal substitutions of j_{k_r} by $(k_r+\frac{1}{4})\pi$ – yields an estimate for Q. If $k_r=k_r'$, one gets, using two successive integrations by parts :

$$Q\simeq\frac{2}{\pi j_{k_r}}\int_0^1 \mathrm{d}u u^2\frac{1-\cos\left(\pi/2-2j_{k_r}u\right)}{2} = \frac{1}{\pi^2(k_r+1/4)}\left\{\frac{1}{3}-\frac{1}{2(k_r+1/4)^2\pi^2}\right\}.$$

If $k_r\neq k_r'$, the calculation is slightly more lengthy. With a couple of integration by parts and using the short term notations $S=j_{k_r}+j_{k_r'}'\simeq\pi/2+\pi(k_r+k_r')$ and $\Delta=$

$j_{k'_r} - j_{k_r} \simeq \pi(k'_r - k_r)$, one gets

$$\begin{aligned} Q &\simeq \frac{2}{\pi\sqrt{j_{k_r} j_{k'_r}}} \int_0^1 \mathrm{d}u \frac{u^2}{2} \{\cos u\Delta - \sin uS\} \\ &\simeq \frac{1}{\pi\sqrt{j_{k_r} j_{k'_r}}} \left(\frac{\sin\Delta}{\Delta} + \frac{2\cos\Delta}{\Delta^2} - \frac{2\sin\Delta}{\Delta^3} + \frac{\cos S}{S} - \frac{2\sin S}{S^2} + \frac{2(1-\cos S)}{S^3} \right) \\ &\simeq \frac{1}{\pi^2\sqrt{(k_r+1/4)(k'_r+1/4)}} \left(\frac{2(-1)^{k_r-k'_r}}{\Delta^2} - \frac{2(-1)^{k_r-k'_r}}{S^2} + \frac{2}{S^3} \right). \end{aligned}$$

■

Appendix B

Mock equilibria including nearest neighbor interactions for the peristrophy.

This appendix details the technical computations related to the evaluation of the partition function within a helicity-energy-peristrophy canonical ensemble in the case where we include some nearest neighbor interactions in the approximation of the peristrophy, as sketched in Figure B.1.

Factorization of the partition function. The partition function is

$$\mathcal{Z}_N = \int_{\mathbb{R}^{2N}} \prod_{\mathbf{k}} \mathrm{d}\omega_{\mathbf{k}} \mathrm{d}v_{\mathbf{k}}\, e^{-\epsilon \mathcal{G}_N - \beta \mathcal{E}_N - \gamma \mathcal{H}_N}. \tag{B.1}$$

with $N(\kappa_c) = \text{Card}\,\{\mathbf{k}, \kappa_{\mathbf{k}} < \kappa_c\}$, $\mathcal{H}_N = \sum_{\mathbf{k}} \omega_{\mathbf{k}} v_{\mathbf{k}}$, $\mathcal{E}_N = \sum_{\mathbf{k}} v_{\mathbf{k}}^2 + \kappa_{\mathbf{k}}^{-2} \omega_{\mathbf{k}}^2$ and $\mathcal{G}_N = \sum_{\mathbf{k},\mathbf{k}'} \alpha_{\mathbf{k}\mathbf{k}'} v_{\mathbf{k}} v_{\mathbf{k}'}$ (see the notations of Chapter 3), and

$$\alpha_{\mathbf{k}\mathbf{k}'} = \begin{cases} \dfrac{R^2}{3} & \text{if } \mathbf{k} = \mathbf{k}' \\ -\dfrac{2R^2}{\pi^2} & \text{if } k_z = k'_z \text{ and } |k_r - k'_r| = 1 \\ 0 & \text{otherwise.} \end{cases} \tag{B.2}$$

In this new approximation, the peristrophy can be renormalized and written as

$$\mathcal{G}_N = \frac{1}{2} \sum_{\mathbf{k}} v_{\mathbf{k}}^2 - \alpha \sum_{\mathbf{k}} v_{(k_r,k_z)} v_{(k_r+1,k_z)} \quad \text{with} \quad \alpha = \frac{6}{\pi^2} > 0. \tag{B.3}$$

The partition function $\mathcal{Z}_N$ can be factorized in terms of vertical partial partition functions as

$$\mathcal{Z}_N = \prod_{k_z : |\kappa_{(1,k_z)}| \leq \kappa_c} \tilde{\mathcal{Z}}_n(k_z), \tag{B.4}$$

where $n = n(k_z) = \max\left\{i : |\kappa_{(i,k_z)}| \leq \kappa_c\right\}$ (see Figure B.1 for an illustration). The partial partition function $\tilde{\mathcal{Z}}_n(k_z)$ is defined as

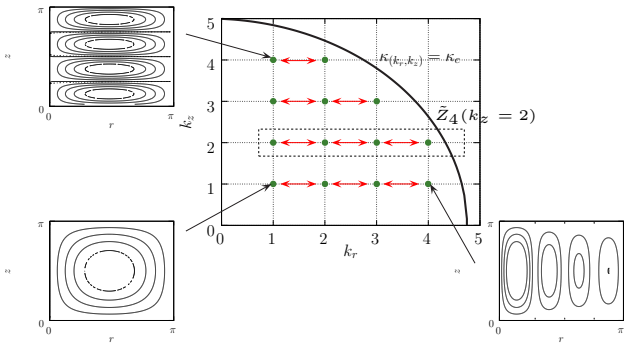

Figure B.1: Bessel-Fourier Modes for $R = 2h = \pi$. The mode $\mathbf{k} = (k_r, k_z)$ has eigenvalue $\kappa^2_{\mathbf{k}} = k_z^2 + (k_r + \frac{1}{4})^2$. For a cutoff $\kappa_c = 5$, the (non trivial) modes that describe the truncated axisymmetric equations in a Von-Kármán geometry are depicted with a green dot. The inserts show contour plots of the modes (1,4),(1,1) and (4,1). The red links show the nearest neighbors couplings induced by the conservation of the peristrophy . The modes within the dotted box are the ones taken into account to compute the vertical partial partition function $\tilde{\mathcal{Z}}_4(2)$ (see the text for a definition).

$$\tilde{\mathcal{Z}}_n(k_z) = \prod_{k_r:|\kappa_{(k_r,k_z)}|\leq\kappa_c} \int_{\mathbb{R}^2} \mathrm{d}\omega_{\mathbf{k}}\mathrm{d}v_{\mathbf{k}} e^{-\frac{1}{2}{}^t X_n A_n X_n}, \qquad \text{and} \quad X_n = {}^t\left(v_{(1,k_z)}, v_{(2,k_z)}, ..., v_{(n,k_z)}, \omega_{(1,k_z)}, \omega_{(2,k_z)}, ..., \omega_{(n,k_z)}\right), \tag{B.5}$$

where

$$A_n = \begin{bmatrix} \beta+\epsilon & -\epsilon\alpha & & 0 & \gamma & & & 0 \\ -\epsilon\alpha & \ddots & \ddots & & & \ddots & & \\ & \ddots & \ddots & -\epsilon\alpha & & & \ddots & \\ 0 & & -\epsilon\alpha & \beta+\epsilon & 0 & & & \gamma \\ \gamma & & & 0 & \beta/\kappa_1^2 & & & 0 \\ & \ddots & & & & \ddots & & \\ & & \ddots & & & & \ddots & \\ 0 & & & \gamma & 0 & & & \beta/\kappa_n^2. \end{bmatrix} \tag{B.6}$$

Computation of the partial partition functions $\tilde{\mathcal{Z}}_n(k_z)$. If A_n is positive definite, one can compute the partial partition function as $\tilde{\mathcal{Z}}_n(k_z) = \sqrt{\frac{2^{2n}\pi^{2n}}{\det A_n}}$. It remains to compute $\det A_n$. To do so, one can first perform the following substitution of the i^{th} : $C_i \to C_i - \gamma\kappa_i^2 C_{i+n}/\beta$. One then obtains

$$\det A_n = \beta^n \left(\prod_{i=1}^{n} \kappa_i^{-2} \right) M_n;$$
$$\text{with} \quad M_n = \begin{vmatrix} \beta + \epsilon - \dfrac{\kappa_1^2 \gamma^2}{\beta} & -\epsilon\alpha & & 0 \\ -\epsilon\alpha & \ddots & \ddots & \\ & \ddots & \ddots & -\epsilon\alpha \\ 0 & & -\epsilon\alpha & \beta + \epsilon - \dfrac{\kappa_n^2 \gamma^2}{\beta}. \end{vmatrix} \tag{B.7}$$

It is straightforward to notice that the determinants M_i obey the recursion relation :

$$M_i = \left(\beta + \epsilon - \frac{\kappa_i^2 \gamma^2}{\beta} \right) M_{i-1} - \epsilon^2 \alpha^2 M_{i-2}. \tag{B.8}$$

In order for A_n to be positive definite, β needs to be strictly positive and every M_i for $i \leq n$ needs to be strictly positive –it is also a sufficient condition.

Non helical case Let us consider the non-helical case, $\gamma = 0$. The M_n can be explicitly found. The discriminant associated to (B.8) reads $\Delta = (\beta + \epsilon)^2 - 4\epsilon^2\alpha^2$. If $\Delta < 0$, the solutions of (B.8) are oscillating solutions and A_n won't be positive. Let us focus on the limiting case $\Delta = 0$. The M_n are then explicitly given by $M_n = (1+n)2^{-n}(\beta + \epsilon)^n$ which are all positive provide $\beta > 0$ and $\Delta = 0$.

The partial partition functions then satisfy up to a constant term

$$\frac{1}{n} \log \tilde{\mathcal{Z}}_n = \frac{1}{2n} \sum_{i=1}^{n} \log \beta \kappa_i^{-2} - \frac{1}{2} \log(\beta + \epsilon). \tag{B.9}$$

The toroidal energy per mode and the poloidal energy per mode are then just as in the case without coupling :

$$\begin{aligned} \langle E^{\text{tor}} \rangle_n = -n^{-1} \frac{\partial \log \tilde{\mathcal{Z}}_n}{\partial \beta + \epsilon} = \frac{1}{2(\beta + \epsilon)} \\ \text{and} \quad \langle E^{\text{pol}} \rangle_n == \frac{1}{2\beta}. \end{aligned} \tag{B.10}$$

As $\beta \to 0$ we find the ratio of poloidal energy to toroidal energy goes to ∞. Note however that the condition $\Delta = 0$ imposes, when $\epsilon < 0$, that $\beta + \epsilon = -2\epsilon\alpha > 0$. This is a difference with the regime (a) depicted in Figure 3.5 : the nearest neighbor interactions prevent the energy from beeing completely toroidal.

Appendix C

A derivation of the shell model preserving energy, helicity and peristrophy-like invariants.

We here show how to derive the shell model defined by the equations (3.52), (3.53), (3.54) and (3.55) of Chapter 3.

Strategy. We wish to find a local dynamics with $2N$ degrees of freedom $(x_1, ..., x_N, y_1, ..., y_N)$ which preserves the following quantities

$$E = \frac{1}{2}\sum_{n=0}^{N} x_n^2 + \gamma_n y_n^2, \qquad H = \sum_{n=0}^{N} x_n y_n, \quad \text{and} \quad G = \frac{1}{2}\sum_{n=0}^{N} \alpha_n x_n^2, \tag{C.1}$$

where the α_n and the γ_n are assumed to be strictly positive.

To achieve such a task, we look for a dynamics involving nearest and next-nearest neighbor coupling, so that the time derivatives of x_n and y_n will be given by a sum of terms of the kind, $a_n^{(ij)} x_{n+i} x_{n+j}$, $b_n^{(ij)} x_{n+i} y_{n+j}$, and $c_n^{(ij)} y_{n+i} y_{n+j}$ with i and j between -2 and 2. Typically, the time derivatives of E, H, N will vanish by telescopic sums : each conservation law either imposes some coefficients to vanish or to cancel out with one another. For example, if the time derivative of x_n contains terms of the kind $a_n^{(-1-2)} x_{n-1} x_{n-2}$, $a_n^{(-11)} x_{n-1} x_{n+1}$ and $a_n^{(12)} x_{n+1} x_{n+2}$, then the conservation of peristrophy imposes that the sum $\alpha_n a_n^{(-1-2)} + \alpha_{n-1} a_{n-1}^{(-1-1)} + \alpha_{n-2} a_{n-2}^{(12)}$ is zero. It also imposes for example that $a_n^{(-12)}$ is zero.

The first step consists in determining for each one of the quantities E, H, and G the terms that need to be vanishing and the pairs or triplets of terms that can cancel out with one another. The second step is to run a manual Sieve algorithm, to determine a small set of modes which needs to be included in the model, in order for both invariants to be conserved. The algorithm can for example be implemented with the help of a piece of transparent paper.

Equations yielding the conservation of E, H, G Among the ninety initial terms, a set is found, which includes only twelve coefficients. They are constrained by eleven equa-

tions. The notations here match the notations of equation (3.53). Those terms are constrained by

the conservation of the Helicity, through

$$\begin{aligned} &a_2^{(n-1)} + a_4^{(n)} + b_6^{(n-2)} = 0 \\ &a_3^{(n-2)} + a_5^{(n-1)} + b_4^{(n)} = 0 \\ &a_1^{(n)} + a_6^{(n-2)} + b_5^{(n-1)} = 0 \\ &b_1^{(n)} + b_2^{(n-1)} + b_3^{(n-2)} = 0 \end{aligned} \quad ; \tag{C.2}$$

the conservation of the Energy, through

$$\begin{aligned} &a_3^{(n-2)} + a_4^{(n)} + \gamma_{n-1} b_2^{(n-1)} = 0 \\ &a_1^{(n)} + a_5^{(n-1)} + \gamma_{n-2} b_3^{(n-2)} = 0 \\ &a_2^{(n-1)} + a_6^{(n-2)} + \gamma_n b_1^{(n)} = 0 \\ &\gamma_n b_4^{(n)} + \gamma_{n-1} b_5^{(n-1)} + \gamma_{n-2} b_6^{(n-2)} = 0 \end{aligned} \quad ; \tag{C.3}$$

and the conservation of the Peristrophy, through

$$\begin{aligned} &\alpha_{n-2} a_3^{(n-2)} + \alpha_n a_4^{(n)} = 0 \\ &\alpha_n a_1^{(n)} + \alpha_{n-1} a_5^{(n-1)} = 0 \\ &\alpha_{n-1} a_2^{(n-1)} + \alpha_{n-2} a_6^{(n-2)} = 0 \end{aligned} \quad . \tag{C.4}$$

Explicit expressions for the coefficients. The set of equations (C.4) tells us that we can eliminate $a_4^{(n)} a_5^{(n-1)} a_6^{(n-2)}$ from the sets of equations (C.3) and (C.2). (C.3) and (C.2) now contain eight equations for nine unknowns. Solving the b_i in terms of $a_3^{(n-2)}$, $a_1^{(n)}$, $a_2^{(n-1)}$ one obtains the compatibility condition :

$$0 = A_1^{(n)} a_1^{(n)} + A_2^{(n)} a_2^{(n-1)} + A_3^{(n)} a_3^{(n-2)} = B_1^{(n)} a_1^{(n)} + B_2^{(n)} a_2^{(n-1)} + B_3^{(n)} a_3^{(n-2)}, \tag{C.5}$$

where

$$\begin{aligned} &A_1^{(n)} = \frac{\alpha_{n-1} - \alpha_n}{\alpha_{n-1}\gamma_{n-2}}, \qquad A_2^{(n)} = \frac{\alpha_{n-2} - \alpha_{n-1}}{\alpha_{n-2}\gamma_n}, \quad \text{and} \quad A_3^{(n)} = \frac{\alpha_n - \alpha_{n-2}}{\alpha_n \gamma_{n-1}}; \\ &B_1^{(n)} = \frac{\alpha_{n-1}\gamma_{n-1} - \alpha_n\gamma_n}{\alpha_{n-1}}, \qquad B_2^{(n)} = \frac{\alpha_{n-2}\gamma_{n-2} - \alpha_{n-1}\gamma_{n-1}}{\alpha_{n-2}}, \\ &\qquad \text{and} \quad B_3^{(n)} = \frac{\alpha_n\gamma_n - \alpha_{n-2}\gamma_{n-2}}{\alpha_n}. \end{aligned} \tag{C.6}$$

In the most general case, α_n and γ_n make the compatibility condition (C.5) be made of two independent equations, from which we obtain

$$\begin{aligned} &a_1^{(n)} = t^{(n)}(A_2^{(n)} B_3^{(n)} - A_3^{(n)} B_2^{(n)}), \qquad a_2^{(n-1)} = t^{(n)}(A_3^{(n)} B_1^{(n)} - A_1^{(n)} B_3^{(n)}) \\ &\quad \text{and} \quad a_3^{(n-2)} = t^{(n)}(A_1^{(n)} B_2^{(n)} - A_2^{(n)} B_1^{(n)}). \end{aligned} \tag{C.7}$$

where $t^{(n)}$ is an arbitrary sequence.

We can then obtain the explicit expressions for the remaining six unknown parameters, given by equations (3.54) and (3.55) for the case $t^{(n)} \equiv 1$.

Comment. Note that if we change the coefficients of (3.54) as

$$\begin{aligned} &a_1^{(n)}, b_1^{(n)}, a_4^{(n)}, b_4^{(n)} \to a_1^{(n)} t^{(n)}, b_1^{(n)} t^{(n)}, a_4^{(n)} t^{(n)}, b_4^{(n)} t^{(n)} \\ &a_2^{(n)}, b_2^{(n)}, a_5^{(n)}, b_5^{(n)} \to a_2^{(n)} t^{(n+1)}, b_2^{(n)} t^{(n+1)}, a_5^{(n)} t^{(n+1)}, b_5^{(n)} t^{(n+1)} \\ &a_3^{(n)}, b_3^{(n)}, a_6^{(n)}, b_6^{(n)} \to a_3^{(n)} t^{(n+2)}, b_3^{(n)} t^{(n+2)}, a_6^{(n)} t^{(n+2)}, b_6^{(n)} t^{(n+2)}. \end{aligned} \tag{C.8}$$

in equation (3.54), with $t^{(n)}$ being any arbitrary sequence of n, the quantities E,H and G are still conserved by the dynamics. $t^{(n)}$ fixes a rate of energy transfer between the modes.

Appendix D

The condensation regime in the "MHD Ising model".

In this appendix, I explain why the extensivity of the magnetic energy for the "2D MHD Ising model" [(a)] yields a condensation regime, if the levels of magnetic potential are chosen to be ± 1. The equilibrium regimes are then described as the "strong A" regimes. The argument is easily generalized to the case where more levels are considered. The non-helical situation is described (section D.1) and comments are then made about the case with cross-helicity (section D.2). I then derive the equilibrium distributions in the "weak A" regime ($a0 \propto 1/N$), in the low energy limit ($E \leq E_c$) under the working hypothesis that the magnetic energy can be expressed as a macrostate constraint (section D.3). The notations at use are the ones of Chapter 5.

D.1 The "strong A", non-helical case.

In this section, the levels of the magnetic potential are ± 1.

Decoupling the kinetic from the magnetic degrees of freedom. Let us play the same game as the one we played for the axisymmetric case, and start by disregarding the helical constraints. In the case of a doubly periodic domain, one should then require for instance that the total circulation is zero, *ie* $\mathcal{X}[\mathcal{C}_N] = 0$. Then, as in the axisymmetric problem, there is a decoupling between the kinetic and the magnetic degrees of freedom. We can consider each of those separately. A straightforward generalizations of the axisymmetric construction yields the definition the M-dependent kinetic entropies and the magnetic entropies, as $S_M^{\text{kin}}(E, X)$ and $S^{\text{mag}}(E, \mu)$.

Kinetic and magnetic entropies. Now, we already know what the M-dependent kinetic entropy $S_M^{\text{kin}}(E^{\text{kin}}, X)$ looks like, for large M. It is the entropy depicted in Figure 4 of [Thalabard et al., 2013]. Note that in our case, $X = 0$, so that $S_M^{\text{kin}}(E^{\text{kin}}, X)$ is maximal for $E^{\text{kin}} = 0$. It remains to known what the entropy of the magnetic part is. The latter

[(a)] The description of the model is given by Table 5.2 of Chapter 5

turns out to be constant, as a consequence of the extensivity of the magnetic energy– see below. Therefore, the most probable state is a state which is purely magnetic : $E^{\text{mag}} = E$ and $E^{\text{kin}} = 0$. Beside, whatever the magnetic energy, the typical state is exactly the typical state corresponding to a (true) Ising model at vanishing energy per site. A typical state is therefore composed of a small number(*i.e* $\ll N^2$) of large islands of magnetic spins pointing in the same direction. If the total magnetization is prescribed to be zero, the ground state is composed of two stripes of same sign spins. For the MHD problem of interest to us here, this state represents a purely magnetic state, where typically two magnetic potential "islands" are separated by a very strong localized current, as represented on figure D.1.

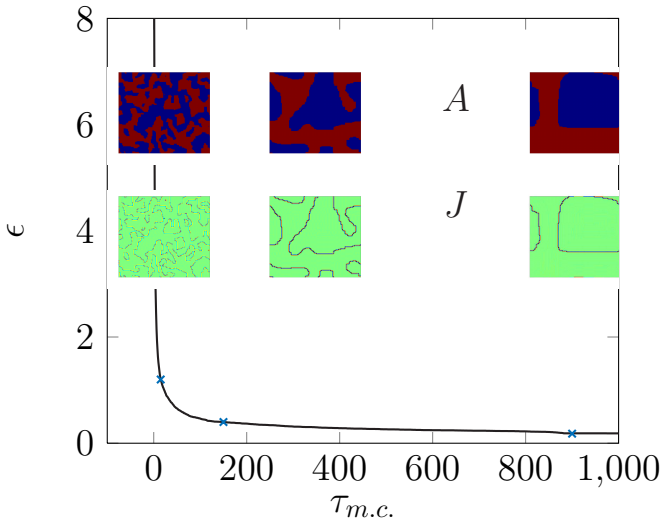

Figure D.1: Examples of low energy configurations for the magnetic potential A and the current J as a function of the Ising energy ϵ, scaled so as to run from 0 to 8. Those configurations were obtained using a Metropolis canonical algorithm at $T = 0$ of the Ising model, initiated with a random configuration ($\epsilon = 4$) and Creutz constraints to keep the magnetization nearly constant.

Proof that "the Magnetic entropy is constant" : Let us recall that the magnetic entropy $S_N^{\text{mag}}(E^{\text{mag}}, \mu)$ is simply defined as the logarithm of the number of configurations of the magnetic Beltrami spins with a prescribed magnetization and a prescribed magnetic energy – up to small fluctuations δE.– divided by N^2. Now, let us make two trivial observations:

(i) Up to a geometric factor C, $\mathcal{E}^{\text{mag}}[\mathcal{C}_N]$ is nothing but N^2 times the hydrodynamical energy of an Ising configuration as defined in the first paragraph of the first section of chapter 5, and as depicted for instance on Figure 5.3. [(a)]

(ii) The magnetization μ of our "MHD Ising model" matches the definition of the magnetization for the Ising model.

Therefore, the limit magnetic entropy $S^{\text{mag}}(E^{\text{mag}}, \mu) = \lim_{N\to\infty} S_N^{\text{mag}}(E^{\text{mag}}, \mu)$ that we look for, can be written in terms of the entropy of the Ising model $S^{Ising}(E/N^2, \mu)$ as $S^{\text{mag}}(E^{\text{mag}}, \mu) = \lim_{N\to\infty} S^{Ising}(E^{\text{mag}}/N^2, \mu) = S^{Ising}(0, \mu)$. It does not depend on the

[(a)] Recall the what we name the hydrodynamical energy is simply the standard (extensive) energy of a spin configuration in the Ising model divided by the number of bonds.

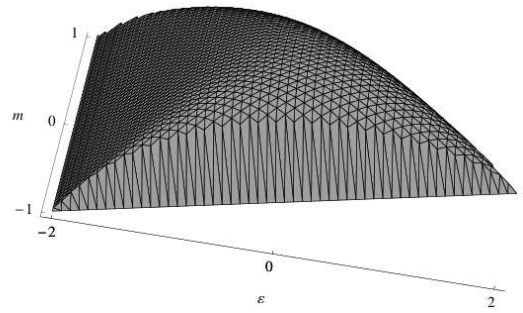

Figure D.2: Approximate graph of the entropy as a function of the energy per site ϵ for the Ising Model. Taken from [Kastner, 2002]. The present "ϵ" is related to the "E" of Figure 5.3 through $\epsilon = 2E - 2$.

magnetic energy E^{mag}. [(b)]. ■

D.2 Remarks on the "strong A" helical case.

Remarks. The case with helicities $X^{\pm} = \pm X_0$ is more subtle to treat, but I think the non-helical case allows at least a heuristic understanding. At a technical level, the problem that we face comes from the fact that the magnetic energy cannot directly be expressed as a constraint on macrostates – defined accordingly to the procedure sketched in Chapter 4. Therefore, the use of Sanov theorem to evaluate the microcanonical volume is not as straightforward as in the axisymmetric case. However one can make the following observations :

1. In the helical case case, the ratio $E^{\text{kin}}/E^{\text{mag}}$ is not necessarily zero. However, the existence of large scale magnetic structures is still guaranteed by the extensivity of the magnetic energy. If E is prescribed, then E^{mag}, is bounded and the ratio $\epsilon = E^{\text{mag}}/N^2$ goes to zero as $N \to \infty$. The consequence of the "Ising hydrodynamic energy"ϵ being zero is the presence of a "ferromagnetic ordering" for the magnetic degrees of freedom of the Beltrami spins.

2. At fixed magnetization, due do the the ferromagnetic ordering a configuration picked at random will be composed of a two macroscopic domains $\mathcal{D}_{\pm}$, in which all the neighboring magnetic spins take the same value ± 1. Typically, one expect to see two stripes of spins.

At a heuristic level one can then expect that the constraint on the helicities will provide a macroscopic correlation between the vorticity and the magnetic potential: in order to satisfy the constraint on $\mathcal{D}_{\pm}$, the distributions of the vorticity field conditioned on $\mathcal{D}_{\pm}$ need to be centered around the value $2X_{\pm}/(1+\mu)$. Hence the emergence of a macroscopic organization of the typical vorticity field.

[(b)] The exact expression of the Ising entropy is not important in the present argument, As a side remark, though, an approximate graph of the Ising entropy, as found in [Kastner, 2002], is shown on Figure D.2

D.3 A counting argument for the "weak A" regime.

In the weak A regime, recall that the levels $\pm a_0$ are simply $\pm 1/N$, so that the magnetic energies and the kinetic energies are both intensive and non-trivially vanishing in the limit $N \to \infty$. Unlike the axisymmetric and the two-dimensional hydro cases, the short range interactions induced by the magnetic energy seem to prevent the use of a counting argument to compute ensemble averages in terms of macrostate probabilities.

We standardly write $p_\pm(\omega, \mathbf{r})\mathrm{d}\omega$ the macrostate probability that the *sign* of the magnetic potential is ± 1 and that the vorticity field lies between ω and $\omega + \mathrm{d}\omega$ in the vicinity of a position $\mathbf{r}$. This defines a macrostate p_M

The sign magnetization $\mu = (A_+ - A_-)/\mathcal{D}$, the conditioned cross-helicities $\mathcal{X}_\pm$ and the kinetic energy can be mapped onto macrostate constraints, as already explained in Chapter 3 :

$$\begin{aligned} &\mu[p_M] = \frac{1}{|\mathcal{D}|}\int_{\mathcal{D}} \mathrm{d}\mathbf{r} \sum_{\pm} \int_{-M}^{M} \mathrm{d}\omega \pm p_\pm(\omega, \mathbf{r}), \qquad \mathcal{X}_\pm[p_M] = \frac{1}{|\mathcal{D}|}\int_{\mathcal{D}} \mathrm{d}\mathbf{r} \int_{-M}^{M} \mathrm{d}\omega \omega p_\pm(\omega, \mathbf{r}) \\ &\text{and} \quad \mathcal{E}_{\text{kin}}[p_M] = \frac{1}{2|\mathcal{D}|}\int_{\mathcal{D}} \mathrm{d}\mathbf{r} \sum_{\pm} \int_{-M}^{M} \mathrm{d}\omega p_\pm(\omega, \mathbf{r}) \omega \psi(\mathbf{r}). \end{aligned} \tag{D.1}$$

Low-energy regime $E < E_c$. By definition, the configurations of the magnetic degrees of freedom exhibit a paramagnetic organization in the low-energy regime. It is therefore reasonable to assume that the magnetic energy can be written in terms of the local sign magnetization $\mu(\mathbf{r})$, and assume that there exists a function f such that

$$\mathcal{E}_{\text{mag}}[p_M] = \frac{1}{\mathcal{D}}\int_{\mathcal{D}} f(\mu(\mathbf{r})) \quad \text{with} \quad \mu(\mathbf{r}) = \sum_{\pm} \int_{-M}^{M} \mathrm{d}\omega \pm p_\pm(\omega, \mathbf{r}). \tag{D.2}$$

The hypothesis is exactly akin to the separation of scale hypothesis used in [Jordan and Turkington, 1997]. The function f might be estimated from a Braggs-Williams type of approximation for the underlying spin model [(a)]. If we assume that f exists and is known, then the maximization of the M-dependent macrostate entropy $S_M = -\frac{1}{|\mathcal{D}|}\int_{\mathcal{D}} \mathrm{d}\mathbf{r} \sum_\pm \int_{-M}^{M} \mathrm{d}\omega p_\pm(\omega, \mathbf{r}) \log p_\pm(\omega, \mathbf{r})$ under the macrostate constraints μ, $\mathcal{E}$ and $\mathcal{X}_\pm$ yields the critical macrostate distribution :

$$\begin{aligned} &p^\star_{\pm,M}(\mathbf{r}, \omega) = \frac{1}{Z^\star_M(\mathbf{r})} \exp\left\{\alpha^{(M)}_\pm + (h^{(M)}_\pm - \beta^{(M)}\frac{\psi(\mathbf{r})}{2})\omega \mp \beta^{(M)} f'(\mu(\mathbf{r}))\right\} \\ &\text{with} \quad Z^\star_M(\mathbf{r}) = \sum_{\pm} \int_{-M}^{M} \exp\left\{\alpha^{(M)}_\pm + (h^{(M)}_\pm - \beta^{(M)}\frac{\psi(\mathbf{r})}{2})\omega \mp \beta^{(M)} f'(\mu(\mathbf{r}))\right\}. \end{aligned} \tag{D.3}$$

In the low energy limit, if we want to let $M \to \infty$, we necessarily need ψ to vanish and the Lagrange multipliers to scale as $\beta^{(M)} \simeq \beta_\star M^0$, $h^{(M)}_\pm \simeq h^\star_\pm M^{-2}$ and $\alpha^{(M)}_\pm \simeq \alpha^\star_\pm M^0$.

[(a)] f is the inverse of the function which link the energy to the spontaneous magnetization in the underlying paramagnetic lattice model with only the magnetic energy acting as a constaint, as for example shown on Figure 5.3.

This for instance yields, in the limit $M \to \infty$:

$$\langle \mu(\mathbf{r}) \rangle = \tanh\left[\alpha - \beta f'(\langle \mu(\mathbf{r}) \rangle)\right] \quad \text{and} \quad \langle \omega(\mathbf{r}) \rangle = \frac{h_+^\star + h_-^\star}{6} + \frac{h_+^\star - h_-^\star}{6} \langle \mu(\mathbf{r}) \rangle. \tag{D.4}$$

In the special case of symmetric levels, $\alpha = 0$ and $h_+ = -h_-$. The vorticity should be proportional to the average magnetization, the latter being locally constant.

Appendix E

Frozen axisymmetric equilibria in the two-level case.

In this appendix, I give some details about the derivation of the frozen axisymmetric equilibria mentioned in Chapters 4,5,6. The notations are the ones at use in Chapter 4.

Description. We work in the two-level case, useful for the practical use of the equilibria in Chapter 5 and 6. At a theoretical level, the quenched regime emerges if one prescribes a "frozen" dependence $h_\pm(\xi_0)$ between the toroidal and the poloidal field at the level of the macrostate probability $p_\pm(\xi_0, \mathbf{r})$ as

$$\underbrace{p_\pm(\xi_0,\mathbf{r})}_{\text{Proba(sign}(\sigma)=\pm \text{ and } \xi=\xi_0 \text{ at } \mathbf{r})} = \overbrace{p_\pm(\mathbf{r})}^{\text{Proba(sign}(\sigma)=\pm \text{ at } \mathbf{r})} \times \underbrace{h_\pm(\xi_0)}_{\text{Proba}(\xi=\xi_0|\text{sign}(\sigma)=\pm)}. \tag{E.1}$$

[(a)].

Frozen Macrostate probabilities. The maximization of the macrostate entropy

$$\mathcal{S}[p_\pm] = -\sum_{\pm}\int_{\mathbb{R}} \mathrm{d}\xi \int_{\mathcal{D}} p_\pm(\xi,\mathbf{r}) \log p_\pm(\xi,\mathbf{r}), \tag{E.2}$$

under the contraints :

$$\mathcal{A}_\pm[p_\pm] = A_\pm, \qquad \mathcal{X}_\pm[p_\pm] = X_\pm, \qquad \mathcal{E}_{\text{pol}}[p_\pm] = E_{\text{pol}} \quad \text{and} \quad \text{Proba}(\xi = \xi_0|\text{sign}(\sigma) = \pm) = h_\pm(\xi_0); \tag{E.3}$$

yields the frozen toroidal critical distributions :

$$p_\pm(\mathbf{r}) = \frac{e^{\alpha_\pm - \frac{\beta\psi(\mathbf{r})\xi_\pm}{2}}}{e^{\alpha_+ - \frac{\beta\psi(\mathbf{r})\xi_+}{2}} + e^{\alpha_- - \frac{\beta\psi(\mathbf{r})\xi_-}{2}}}. \tag{E.4}$$

[(a)] "Proba" denotes a local probability defined through a coarse graining, as explained in details in Chapter 4.

In the latter formula,

$\xi_\pm$ are the average poloidal fields conditioned on the toroidal levels : $\xi_\pm = \int_{\mathrm{d}} \xi h_\pm(\xi)\xi$.

β is the Lagrange multiplier associated to the conservation of the poloidal energy.

$\alpha_\pm$ is a function of the Lagrange multipliers associated to the other constraints. It is explicitly given in the next paragraph.

A comment on the derivation of E.4 can be found in the next paragraph.

How do we obtain equation E.4 ? To achieve the computation, it suffices to use equation (E.1) and prescribe $h_\pm(\xi)$ at the level of the probability measures. That way, one can recast both the macrostate entropy and the macrostate constraints in terms of the toroidal probability $p_\pm$ only. Doing so, we find

$$\begin{aligned} 2\mathcal{E}_{\mathrm{pol}}[p] &= \int_{\mathcal{D}} \mathbf{dr} \sum_{\pm} \int_{\mathbb{R}} \mathrm{d}\xi p_\pm(r) h_\pm(\xi)\xi\psi(\mathbf{r}) = \int_{\mathcal{D}} \mathbf{dr} \sum_{\pm} p_\pm(r)\xi_\pm\psi(\mathbf{r}), \\ \text{and similarly} \quad X_\pm &= \int_{\mathcal{D}} \mathbf{dr}\, p_\pm(r)\xi_\pm = \xi_\pm A_\pm. \end{aligned} \tag{E.5}$$

In the same way, the macrostate entropy can be written as

$$\mathcal{S}[p_\pm] = -\int_{\mathcal{D}} \sum_{\pm} p_\pm(\mathbf{r}) \log p_\pm(\mathbf{r}) - \int_{\mathcal{D}} \sum_{\pm} p_\pm(\mathbf{r}) \underbrace{\int_{\mathbb{R}} \mathrm{d}\xi h_\pm(\xi) \log h_\pm(\xi)}_{=s_\pm}. \tag{E.6}$$

$s_\pm$ is the entropy associated to the prescribed poloidal distributions $h_\pm$.

Equation E.4 is then obtained through the use of Lagrange multipliers to enforce the constraints : $\tilde{\alpha}_\pm$ for the areas, $h_\pm$ for the helicities, and β (for the energy). It is then apparent that $\alpha_\pm = s_\pm + h_\pm\xi_\pm + \tilde{\alpha}_\pm$.

Recall that the total macrostate probability is $p_\pm(\mathbf{r},\xi) = p_\pm(\mathbf{r})h_\pm(\xi)$.

Mean field relations. The quenched average fields are then such that

$$\begin{aligned} \langle\sigma\rangle(\mathbf{r}) &= \sum_{\pm} \sigma_\pm p_\pm(\mathbf{r}) \underbrace{\int_{\mathbb{R}} \mathrm{d}\xi h_\pm(\xi)}_{=1} = \frac{e^{\alpha_+ - \frac{\beta\psi(\mathbf{r})\xi_+}{2}} - e^{\alpha_- - \frac{\beta\psi(\mathbf{r})\xi_-}{2}}}{e^{\alpha_+ - \frac{\beta\psi(\mathbf{r})\xi_+}{2}} + e^{\alpha_- - \frac{\beta\psi(\mathbf{r})\xi_-}{2}}}. \\ \text{and} \quad \langle\xi\rangle(\mathbf{r}) &= \frac{\xi_+ e^{\alpha_+ - \frac{\beta\psi(\mathbf{r})\xi_+}{2}} - \xi_- e^{\alpha_- - \frac{\beta\psi(\mathbf{r})\xi_-}{2}}}{e^{\alpha_+ - \frac{\beta\psi(\mathbf{r})\xi_+}{2}} + e^{\alpha_- - \frac{\beta\psi(\mathbf{r})\xi_-}{2}}}. \end{aligned} \tag{E.7}$$

If the levels are symmetric – $A_+ = A_-$, $X_+ + X_- = 0$, $h_+(\xi) = h_-(-\xi)$ and consequently $\xi_+ + \xi_- = 0$ – we recover $\tanh$ laws, such as

$$\begin{aligned} &\langle\sigma\rangle(\mathbf{r}) = \tanh(B\psi(\mathbf{r})), \qquad \langle\xi\rangle(\mathbf{r}) = \xi_+ \tanh(B\psi(\mathbf{r})), \\ &\quad \text{with} \quad B = -\frac{\beta(\xi_+ - \xi_-)}{2}. \end{aligned} \tag{E.8}$$

Similarly,

$$\langle \mathsf{sign}(\xi)\rangle(\mathbf{r}) = \left(\int_{\mathbb{R}} \mathrm{d}\xi h_+(\xi)(\mathsf{sign}(\xi))\right) \tanh(B\psi(\mathbf{r})). \tag{E.9}$$

Bibliography

[Abarbanel et al., 1986] Abarbanel, H. D., Holm, D. D., Marsden, J. E., and Ratiu, T. S. (1986). Nonlinear stability analysis of stratified fluid equilibria. Philosophical Transactions of the Royal Society of London. Series A, Mathematical and Physical Sciences, 318(1543):349–409.

[Abramowitz and Stegun, 1965] Abramowitz, M. and Stegun, I. A. (1965). Handbook of Mathematical Functions with Formulas, Graph, and Mathematical tables. Applied Mathematics Series, 55:1046.

[Alexakis et al., 2006] Alexakis, A., Mininni, P. D., and Pouquet, A. (2006). On the inverse cascade of magnetic helicity. The Astrophysical Journal, 640(1):335.

[Aref, 2007] Aref, H. (2007). Point vortex dynamics: A classical mathematics playground. Journal of mathematical Physics, 48:065401.

[Bardos and Titi, 2013] Bardos, C. and Titi, E. S. (2013). Mathematics and Turbulence: where do we stand ? arXiv preprint arXiv:1301.0273.

[Batchelor, 1953] Batchelor, G. (1953). The theory of homogeneous turbulence.

[Baxter, 1982] Baxter, R. J. (1982). Exactly solved models in statistical mechanics.

[Bellout et al., 2009] Bellout, H., Neustupa, J., and Penel, P. (2009). On viscosity-continuous solutions of the euler and navier–stokes equations with a navier-type boundary condition. Comptes Rendus Mathematique, 347(19–20):1141 – 1146.

[Berhanu et al., 2007] Berhanu, M., Monchaux, R., Fauve, S., Mordant, N., Pétrélis, F., Chiffaudel, A., Daviaud, F., Dubrulle, B., Marié, L., Ravelet, F., et al. (2007). Magnetic field reversals in an experimental turbulent dynamo. EPL (Europhysics Letters), 77(5):59001.

[Bernard et al., 2006] Bernard, D., Boffetta, G., Celani, A., and Falkovich, G. (2006). Conformal invariance in two-dimensional turbulence. Nature Physics, 2(2):124–128.

[Bernard et al., 2007] Bernard, D., Boffetta, G., Celani, A., and Falkovich, G. (2007). Inverse turbulent cascades and conformally invariant curves. Physical review letters, 98(2):024501.

[Biskamp, 1993] Biskamp, D. (1993). Nonlinear Magnetohydrodynamics. Cambridge Monographs on Plasma Physics.

[Biskamp and Bremer, 1994] Biskamp, D. and Bremer, U. (1994). Dynamics and statistics of inverse cascade processes in 2d magnetohydrodynamic turbulence. Physical review letters, 72(24):3819.

[Boucher et al., 2000] Boucher, C., Ellis, R. S., and Turkington, B. (2000). Derivation of maximum entropy principles in two-dimensional turbulence via large deviations. Journal of Statistical Physics, 98(5-6):1235–1278.

[Bouchet and Barre, 2005] Bouchet, F. and Barre, J. (2005). Classification of phase transitions and ensemble inequivalence, in systems with long range interactions. Journal of statistical physics, 118(5-6):1073–1105.

[Bouchet and Corvellec, 2010] Bouchet, F. and Corvellec, M. (2010). Invariant measures of the 2D Euler and Vlasov equations. Journal of Statistical Mechanics: Theory and Experiment, 2010(08):P08021.

[Bouchet et al., 2011] Bouchet, F., Laurie, J., and Zaboronski, O. (2011). Control and instanton trajectories for random transitions in turbulent flows. In Journal of Physics: Conference Series, volume 318, page 022041. IOP Publishing.

[Bouchet and Simonnet, 2009] Bouchet, F. and Simonnet, E. (2009). Random changes of flow topology in two-dimensional and geophysical turbulence. Physical review letters, 102(9):094504.

[Bouchet and Venaille, 2011] Bouchet, F. and Venaille, A. (2011). Statistical mechanics of two-dimensional and geophysical flows. Arxiv preprint arXiv:1110.6245.

[Brown and Lopez, 1990] Brown, G. and Lopez, J. (1990). Axisymmetric vortex breakdown part 2. physical mechanisms. Journal of Fluid Mechanics, 221(1):553–576.

[Burgers, 1929] Burgers, J. (1929). On the application of statistical mechanics to the theory of turbulent fluid motion. Proc. Roy. Neth. Acad. Soc, 32(414):643.

[Caflisch, 1993] Caflisch, R. E. (1993). Singularity formation for complex solutions of the 3d incompressible euler equations. Physica D: Nonlinear Phenomena, 67(1):1–18.

[Cardy, 2005] Cardy, J. (2005). Sle for theoretical physicists. Annals of Physics, 318(1):81–118.

[Castaing, 1996] Castaing, B. (1996). The temperature of turbulent flows. Journal de Physique II, 6(1):105–114.

[Chavanis et al., 2010] Chavanis, P., Naso, A., and Dubrulle, B. (2010). Relaxation equations for two-dimensional turbulent flows with a prior vorticity distribution. The European Physical Journal B, 77(2):167–186.

[Chavanis and Sommeria, 1996] Chavanis, P. and Sommeria, J. (1996). Classification of self-organized vortices in two-dimensional turbulence: the case of a bounded domain. Journal of Fluid Mechanics, 314:267–298.

[Chavanis and Sommeria, 1998] Chavanis, P. and Sommeria, J. (1998). Classification of robust isolated vortices in two-dimensional hydrodynamics. Journal of Fluid Mechanics, 356:259–296.

[Chavanis, 2005] Chavanis, P.-H. (2005). Statistical mechanics of geophysical turbulence: application to jovian flows and Jupiter's great red spot. Physica D: Nonlinear Phenomena, 200(3):257–272.

[Chavanis, 2008] Chavanis, P.-H. (2008). Statistical mechanics of 2d turbulence with a prior vorticity distribution. Physica D: Nonlinear Phenomena, 237(14):1998–2002.

[Chavanis and Sommeria, 2000] Chavanis, P.-H. and Sommeria, J. (2000). Statistical mechanics of the shallow water system. arXiv preprint physics/0004056.

[Chorin, 1993] Chorin, A. J. (1993). Vorticity and Turbulence. Springer-Verlag.

[Cortet et al., 2011] Cortet, P., Herbert, E., Chiffaudel, A., Daviaud, F., Dubrulle, B., and Padilla, V. (2011). Susceptibility divergence, phase transition and multistability of a highly turbulent closed flow. Journal of Statistical Mechanics: Theory and Experiment, 2011(07):P07012.

[Cortet et al., 2010] Cortet, P.-P., Chiffaudel, A., Daviaud, F., and Dubrulle, B. (2010). Experimental evidence of a phase transition in a closed turbulent flow. Physical review letters, 105(21):214501.

[Creutz, 1983] Creutz, M. (1983). Microcanonical Monte Carlo simulation. Physical Review Letters, 50(19):1411–1414.

[Creutz, 1985] Creutz, M. (1985). Reversible Ising dynamics. In Presented at the Conference on Advances in Lattice Gauge Theory, Coral Gables, Fla., 10 Apr. 1985, volume 1.

[Creutz, 1986] Creutz, M. (1986). Deterministic Ising dynamics. Annals of physics, 167(1):62–72.

[de la Torre and Burguete, 2007] de la Torre, A. and Burguete, J. (2007). Slow dynamics in a turbulent von Kármán swirling flow. Physical review letters, 99(5):054101.

[Dijkstra and Molemaker, 1997] Dijkstra, H. A. and Molemaker, M. (1997). Symmetry breaking and overturning oscillations in thermohaline-driven flows. Journal of Fluid Mechanics, 331:169–198.

[Dubrulle and the VKEteam, 2013] Dubrulle, B. and the VKEteam (2013). Statistical mechanics of Beltrami flows in axisymmetric geometry: Comparison with experiments.

[Ellis et al., 2000] Ellis, R. S., Haven, K., and Turkington, B. (2000). Large deviation principles and complete equivalence and nonequivalence results for pure and mixed ensembles. Journal of Statistical Physics, 101(5-6):999–1064.

[Eyink and Frisch, 2011] Eyink, G. and Frisch, U. (2011). Robert H. Kraichnan. A Voyage Through Turbulence, pages 329–372.

[Eyink and Spohn, 1993] Eyink, G. and Spohn, H. (1993). Negative-temperature states and large-scale, long-lived vortices in two-dimensional turbulence. Journal of statistical physics, 70(3-4):833–886.

[Eyink and Sreenivasan, 2006] Eyink, G. and Sreenivasan, K. (2006). Onsager and the theory of hydrodynamic turbulence. Reviews of modern physics, 78(1):87.

[Fauve et al., 1993] Fauve, S., Laroche, C., and Castaing, B. (1993). Pressure fluctuations in swirling turbulent flows. Journal de physique II, 3(3):271–278.

[Feynman et al., 1964] Feynman, R., Leighton, R., and Sands, M. (1964). The flow of dry water. Lectures on Physics. Reading, MA: Addison-Wesley, 2.

[Fjørtoft, 1953] Fjørtoft, R. (1953). On the changes in the spectral distribution of kinetic energy for twodimensional, nondivergent flow. Tellus, 5(3):225–230.

[Fleury, 2006] Fleury, L. (2006). Equilibres multiples de la circulation thermohaline. PhD thesis, Atelier national de reproduction des thèses.

[Frisch, 1996] Frisch, U. (1996). Turbulence. Turbulence, by Uriel Frisch, pp. 310. ISBN 0521457130. Cambridge, UK: Cambridge University Press, January 1996., 1.

[Frisch et al., 1975] Frisch, U., Pouquet, A., Léorat, J., and Mazure, A. (1975). Possibility of an inverse cascade of magnetic helicity in magnetohydrodynamic turbulence. Journal of Fluid Mechanics, 68:769–778.

[Fyfe and Montgomery, 1976] Fyfe, D. and Montgomery, D. (1976). High-beta turbulence in two-dimensional magnetohydrodynamics.

[Gage, 1979] Gage, K. (1979). Evidence for the-5/3 law inertial range in mesoscale two-dimensional turbulence. Journal of Atmospheric Sciences, 36:1950–1954.

[Gibbon, 2008] Gibbon, J. D. (2008). The three-dimensional Euler equations: Where do we stand ? Physica D: Nonlinear Phenomena, 237(14):1894–1904.

[Gibbon and Holm, 2010] Gibbon, J. D. and Holm, D. (2010). The dynamics of the gradient of potential vorticity. Journal of Physics A: Mathematical and Theoretical, 43(17):172001.

[Ginsparg, 1988] Ginsparg, P. H. (1988). Applied conformal field theory. arXiv preprint hep-th/9108028, 63.

[Grauer and Sideris, 1991] Grauer, R. and Sideris, T. C. (1991). Numerical computation of 3d incompressible ideal fluids with swirl. Physical review letters, 67(25):3511–3514.

[Grauer and Sideris, 1995] Grauer, R. and Sideris, T. C. (1995). Finite time singularities in ideal fluids with swirl. Physica D: Nonlinear Phenomena, 88(2):116–132.

[Hall, 1972] Hall, M. (1972). Vortex breakdown. Annual Review of Fluid Mechanics, 4(1):195–218.

[Herbert, 2013] Herbert, C. (2013). Restricted partition functions and dual energy cascade in parity symmetry breaking flows. to appear.

[Herbert and Paillard, 2013] Herbert, C. and Paillard, D. (2013). Predictive use of the maximum entropy production principle for past and present climates. arXiv preprint arXiv:1301.1062.

[Herbert et al., 2012] Herbert, E., Daviaud, F., Dubrulle, B., Nazarenko, S., and Naso, A. (2012). Dual local and non-local cascades in 3d turbulent beltrami flows. arXiv preprint arXiv:1206.5613.

[Herring, 1999] Herring, J. R. (1999). Some problems and issues in geophysical turbulence. Fluid dynamics research, 24(6):363–373.

[Holm et al., 1985] Holm, D. D., Marsden, J. E., Ratiu, T., and Weinstein, A. (1985). Nonlinear stability of fluid and plasma equilibria. Physics Reports, 123(1):1–116.

[Jaynes, 1957] Jaynes, E. T. (1957). Information theory and statistical mechanics. Physical review, 106(4):620.

[Jordan and Turkington, 1997] Jordan, R. and Turkington, B. (1997). Ideal magnetofluid turbulence in two dimensions. Journal of statistical physics, 87(3-4):661–695.

[Joyce and Montgomery, 1973] Joyce, G. and Montgomery, D. (1973). Negative temperature states for the two-dimensional guiding-centre plasma. Journal of Plasma Physics, 10(01):107–121.

[Julien et al., 1998] Julien, K., Knobloch, E., and Werne, J. (1998). A new class of equations for rotationally constrained flows. Theoretical and Computational Fluid Dynamics, 11(3-4):251–261.

[Kastner, 2002] Kastner, M. (2002). Existence and order of the phase transition of the Ising model with fixed magnetization. Journal of statistical physics, 109(1-2):133–142.

[Kennedy, 2009] Kennedy, T. (2009). Numerical computations for the schramm-loewner evolution. Journal of Statistical Physics, 137(5-6):839–856.

[Khinchin, 1949] Khinchin, A. I. (1949). Mathematical Foundations of Statistical Mechanics. Courier Dover Publications.

[Kim and Dubrulle, 2002] Kim, E.-j. and Dubrulle, B. (2002). Are the energy and magnetic potential cascades direct or inverse in 2D MHD turbulence? Physica D: Nonlinear Phenomena, 165(3):213–227.

[Kraichnan, 1967] Kraichnan, R. H. (1967). Inertial ranges in two-dimensional turbulence. Physics of fluids, 10:1417.

[Kraichnan and Montgomery, 1980] Kraichnan, R. H. and Montgomery, D. (1980). Two-dimensional turbulence. Reports on Progress in Physics, 43:547–619.

[Kuksin, 2007] Kuksin, S. B. (2007). Eulerian limit for 2d navier-stokes equation and damped/driven kdv equation as its model. Proceedings of the Steklov Institute of Mathematics, 259(1):128–136.

[Labbé et al., 1996] Labbé, R., Pinton, J.-F., and Fauve, S. (1996). Power fluctuations in turbulent swirling flows. Journal de Physique II, 6(7):1099–1110.

[Landau and Binder, 2009] Landau, D. P. and Binder, K. (2009). A guide to Monte Carlo simulations in statistical physics. Cambridge university press.

[Lee, 1952] Lee, T. (1952). On some statistical properties of hydrodynamical and magnetohydrodynamical fields. Q. Appl. Math, 10:69.

[Leith, 1968] Leith, C. E. (1968). Diffusion approximation for two-dimensional turbulence. Physics of Fluids, 11:671.

[Leprovost et al., 2006] Leprovost, N., Dubrulle, B., and Chavanis, P.-H. (2006). Dynamics and thermodynamics of axisymmetric flows: Theory. Physical Review E, 73(4):046308.

[Lilly, 1969] Lilly, D. (1969). Tornado dynamics, ncar man. 69-117. Natl. Cent. for Atmos. Res., Boulder, Colo.

[Lilly, 1983] Lilly, D. K. (1983). Stratified turbulence and the mesoscale variability of the atmosphere. Journal of the Atmospheric Sciences, 40(3):749–761.

[Lim, 2003] Lim, C. C. (2003). Coherent structures in an energy-enstrophy theory for axisymmetric flows. Physics of Fluids, 15:478.

[Lindborg, 1999] Lindborg, E. (1999). Can the atmospheric kinetic energy spectrum be explained by two-dimensional turbulence ? Journal of Fluid Mechanics, 388:259–288.

[Mahalov et al., 1990] Mahalov, A., Titi, E., and Leibovich, S. (1990). Invariant helical subspaces for the Navier- Stokes equations. Archive for Rational Mechanics and Analysis, 112(3):193–222.

[Majda and Wang, 2006] Majda, A. and Wang, X. (2006). Nonlinear dynamics and statistical theories for basic geophysical flows. Cambridge University Press.

[Marié, 2003] Marié, L. (2003). Transport de moment cinétique et de champ magnétique par un écoulement tourbillonnaire turbulent: influence de la rotation. PhD thesis, Université Paris-Diderot-Paris VII.

[Marsden and Morrison, 1984] Marsden, J. E. and Morrison, P. J. (1984). Noncanonical Hamiltonian field theory and reduced MHD. Contemp. Math, 28:133–150.

[Marston, 2011] Marston, J. (2011). Planetary atmospheres as non-equilibrium condensed matter. arXiv preprint arXiv:1107.5289.

[Martinus et al., 1995] Martinus, J., Nieuwstadt, F. T., and Steketee, J. (1995). Selected papers of JM Burgers. Kluwer Academic Publishers.

[Metropolis et al., 1953] Metropolis, N., Rosenbluth, A. W., Rosenbluth, M. N., Teller, A. H., and Teller, E. (1953). Equation of state calculations by fast computing machines. The journal of chemical physics, 21:1087.

[Michel and Robert, 1994] Michel, J. and Robert, R. (1994). Statistical mechanical theory of the great red spot of Jupiter. Journal of Statistical Physics, 77(3):645–666.

[Miller, 1990] Miller, J. (1990). Statistical mechanics of Euler equations in two dimensions. Physical review letters, 65(17):2137.

[Miller et al., 1992] Miller, J., Weichman, P. B., and Cross, M. (1992). Statistical mechanics, Euler's equation, and Jupiter's red spot. Physical Review A, 45(4):2328.

[Mininni and Pouquet, 2009] Mininni, P. and Pouquet, A. (2009). Helical rotating turbulence. part ii. intermittency, scale invariance and structures. arXiv preprint arXiv:0909.1275.

[Mohseni, 2001] Mohseni, K. (2001). Statistical equilibrium theory for axisymmetric flows: Kelvin's variational principle and an explanation for the vortex ring pinch-off process. Physics of Fluids, 13:1924.

[Moisy et al., 1999] Moisy, F., Tabeling, P., and Willaime, H. (1999). Kolmogorov equation in a fully developed turbulence experiment. Physical review letters, 82(20):3994.

[Moisy et al., 2001] Moisy, F., Willaime, H., Andersen, J., and Tabeling, P. (2001). Passive scalar intermittency in low temperature helium flows. Physical Review Letters, 86(21):4827.

[Monchaux, 2007] Monchaux, R. (2007). Mécanique statistique et effet dynamo dans un écoulement de von Kármán turbulent. PhD thesis, Université Paris-Diderot-Paris VII.

[Monchaux et al., 2007] Monchaux, R., Berhanu, M., Bourgoin, M., Moulin, M., Odier, P., Pinton, J.-F., Volk, R., Fauve, S., Mordant, N., Pétrélis, F., et al. (2007). Generation of a magnetic field by dynamo action in a turbulent flow of liquid sodium. Physical review letters, 98(4):044502.

[Monchaux et al., 2006] Monchaux, R., Ravelet, F., Dubrulle, B., Chiffaudel, A., and Daviaud, F. (2006). On the properties on steady states in turbulent axisymmetric flows. arXiv preprint arXiv:cond-mat/0601582v1.

[Montgomery and Joyce, 1974] Montgomery, D. and Joyce, G. (1974). Statistical mechanics of "negative temperature" states. Physics of Fluids, 17:1139.

[Montgomery et al., 1992] Montgomery, D., Matthaeus, W., Stribling, W., Martinez, D., and Oughton, S. (1992). Relaxation in two dimensions and the "sinh-poisson"equation. Physics of Fluids A: Fluid Dynamics, 4:3.

[Montgomery and Turner, 1982] Montgomery, D. and Turner, L. (1982). Two-and-a-half-dimensional magnetohydrodynamic turbulence. Physics of Fluids, 25:345.

[Monthus, 2011] Monthus, C. (2011). Non-equilibrium steady states: maximization of the shannon entropy associated with the distribution of dynamical trajectories in the presence of constraints. Journal of Statistical Mechanics: Theory and Experiment, 2011(03):P03008.

[Montroll et al., 1963] Montroll, E. W., Potts, R. B., and Ward, J. C. (1963). Correlations and Spontaneous Magnetization of the Two-Dimensional Ising Model. Journal of Mathematical Physics, 4:308.

[Morrison, 1998] Morrison, P. (1998). Hamiltonian description of the ideal fluid. Reviews of Modern Physics, 70(2):467.

[Morrison, 2005] Morrison, P. (2005). Hamiltonian and action principle formulations of plasma physics. Physics of plasmas, 12:058102.

[Morrison and Hazeltine, 1984] Morrison, P. and Hazeltine, R. (1984). Hamiltonian formulation of reduced magnetohydrodynamics. Physics of Fluids, 27:886.

[Mussardo, 2010] Mussardo, G. (2010). Statistical field theory. Oxford Univ. Press.

[nasa.gov, 2013] nasa.gov (2013).

[Naso et al., 2010a] Naso, A., Monchaux, R., Chavanis, P.-H., and Dubrulle, B. (2010a). Statistical mechanics of Beltrami flows in axisymmetric geometry: Theory reexamined. Physical Review E, 81(6):066318.

[Naso et al., 2010b] Naso, A., Thalabard, S., Collette, G., Chavanis, P.-H., and Dubrulle, B. (2010b). Statistical mechanics of Beltrami flows in axisymmetric geometry: equilibria and bifurcations. Journal of Statistical Mechanics: Theory and Experiment, 2010(06):P06019.

[Nazarenko and Zakharov, 1992] Nazarenko, S. and Zakharov, V. (1992). Kinetic equation for point vortices in a shear flow. Physica D, 56:381–288.

[Onsager, 1949] Onsager, L. (1949). Statistical hydrodynamics. Il Nuovo Cimento (1943-1954), 6:279–287.

[Orszag, 1974] Orszag, S. A. (1974). Lectures on the statistical theory of turbulence. Flow Research Incorporated.

[Orszag and Tang, 1979] Orszag, S. A. and Tang, C.-M. (1979). Small-scale structure of two-dimensional magnetohydrodynamic turbulence. Journal of Fluid Mechanics, 90(01):129–143.

[Padhye and Morrison, 1996] Padhye, N. and Morrison, P. (1996). Relabeling symmetries in hydrodynamics and magnetohydrodynamics. Plasma Physics Reports, 22(10):869–877.

[Pedlosky, 1982] Pedlosky, J. (1982). Geophysical fluid dynamics. New York and Berlin, Springer-Verlag, 1982. 636 p., 1.

[Pieri et al., 2013] Pieri, A., Godeferd, F. S., Cambon, C., Dubrulle, B., and Thalabard, S. (2013). On cross helicity in rotating homegeneous shear-stratified turbulence. to appear.

[Pierrehumbert et al., 1994] Pierrehumbert, R. T., Held, I. M., and Swanson, K. L. (1994). Spectra of local and nonlocal two-dimensional turbulence. Chaos, Solitons & Fractals, 4(6):1111–1116.

[Polyakov, 1970] Polyakov, A. M. (1970). Conformal symmetry of critical fluctuations (originally published in russian volume 12, number 11). Soviet Journal of Experimental and Theoretical Physics Letters, 12:381.

[Potters et al., 2013] Potters, M., Vaillant, T., and Bouchet, F. (2013). Sampling micro-canonical measures of the 2d euler equations through Creutz's algorithm: a phase transition from disorder to order when energy is increased. Journal of Statistical Mechanics: Theory and Experiment, 2013(02):P02017.

[Pouquet, 1978] Pouquet, A. (1978). On two-dimensional magnetohydrodynamic turbulence. Journal of Fluid Mechanics, 88(1):1–16.

[Pouquet and Mininni, 2010] Pouquet, A. and Mininni, P. (2010). The interplay between helicity and rotation in turbulence: implications for scaling laws and small-scale dynamics. Philosophical Transactions of the Royal Society A: Mathematical, Physical and Engineering Sciences, 368(1916):1635–1662.

[Pumir and Siggia, 1992a] Pumir, A. and Siggia, E. D. (1992a). Development of singular solutions to the axisymmetric euler equations. Physics of Fluids A: Fluid Dynamics, 4:1472.

[Pumir and Siggia, 1992b] Pumir, A. and Siggia, E. D. (1992b). Finite-time singularities in the axisymmetric three-dimension euler equations. Physical review letters, 68(10):1511–1514.

[Ravelet, 2005] Ravelet, F. (2005). Bifurcations globales hydrodynamiques et magnétohydrodynamiques dans un écoulement de von Kármán turbulent. PhD thesis, CEA.

[Robert, 2004] Robert, R. (2004). Mathématiques et turbulence. Images des mathématiques, CNRS, pages 91–100.

[Robert and Sommeria, 1991] Robert, R. and Sommeria, J. (1991). Statistical equilibrium states for two-dimensional flows. J. Fluid Mech, 229(29):l–3.

[Saint-Michel, 2013] Saint-Michel, B. (2013). L'expérience von Kármán comme paradigme de la mécanique statistique hors équilibre. PhD thesis, Université Paris-Diderot-Paris VII.

[Saint-Michel et al., 2013a] Saint-Michel, B., Daviaud, F., and Dubrulle, B. (2013a). A zero-mode mechanism for spontaneous symmetry breaking in a turbulent von k\'arm\'an flow. arXiv preprint arXiv:1305.3389.

[Saint-Michel et al., 2013b] Saint-Michel, B., Dubrulle, B., Ravelet, F., and Daviaud, F. (2013b). Forcing-dependent stability of steady turbulent states. arXiv preprint arXiv:1301.1810.

[Salmon, 1983] Salmon, R. (1983). Practical use of Hamilton's principle. Journal of Fluid Mechanics, 132:431–44.

[Salmon, 1988] Salmon, R. (1988). Hamiltonian fluid mechanics. Annual review of fluid mechanics, 20(1):225–256.

[Salmon, 2012] Salmon, R. (2012). Statistical mechanics and ocean circulation. Communications in Nonlinear Science and Numerical Simulation, 17(5):2144–2152.

[Shepherd, 1990] Shepherd, T. G. (1990). Symmetries, conservation laws, and Hamiltonian structure in geophysical fluid dynamics. Adv. Geophys, 32(287-338):2.

[Sommeria, 2001] Sommeria, J. (2001). Two-dimensional turbulence. In New trends in turbulence Turbulence: nouveaux aspects, pages 385–447. Springer.

[Spiegel and Zahn, 1992] Spiegel, E. and Zahn, J.-P. (1992). The solar tachocline. Astronomy and Astrophysics, 265:106–114.

[Szeri and Holmes, 1988] Szeri, A. and Holmes, P. (1988). Nonlinear stability of axisymmetric swirling flows. Philosophical Transactions of the Royal Society of London. Series A, Mathematical and Physical Sciences, 326(1590):327–354.

[Thalabard et al., 2013] Thalabard, S., Dubrulle, B., and Bouchet, F. (2013). Statistical mechanics of the 3D axisymmetric Euler equations in a Taylor-Couette geometry. arXiv preprint arXiv:1306.1081.

[Tisserand and Reggiani, 1970] Tisserand, P. and Reggiani, S. (1970). Le vénusien. Je Voudrais Pas Crever1970 (Polydor, 2393 010). bla bla.

[Tolman, 1938] Tolman, R. C. (1938). The principles of statistical mechanics. Courier Dover Publications.

[Turkington, 2013] Turkington, B. (2013). An optimization principle for deriving nonequilibrium statistical models of hamiltonian dynamics. Journal of Statistical Physics, 152:569–597.

[Turkington and Jordan, 1995] Turkington, B. and Jordan, R. (1995). Turbulent relaxation of a magnetofluid: A statistical equilibrium model. Advances in geometric analysis and continuum mechanics, pages 124–137.

[Turkington et al., 2001] Turkington, B., Majda, A., Haven, K., and DiBattista, M. (2001). Statistical equilibrium predictions of jets and spots on jupiter. Proceedings of the National Academy of Sciences, 98(22):12346–12350.

[Turkington and Whitaker, 1996] Turkington, B. and Whitaker, N. (1996). Statistical equilibrium computations of coherent structures in turbulent shear layers. SIAM Journal on Scientific Computing, 17:1414.

[Verkley,] Verkley, W. The statistical mechanics of turbulent flows.

[Villani, 2006] Villani, C. (2005-2006). Intégration et Analyse de Fourier.

[Vladimirov et al., 1997] Vladimirov, Moffatt, and Ilin (1997). On general transformations and variational principles for the magnetohydrodynamics of ideal fluids. part iii. stability criteria for axisymmetric flows. Journal of Plasma Physics, 57:89–120.

[Weichman, 2012] Weichman, P. (2012). Long-range correlations and coherent structures in magnetohydrodynamic equilibria. Physical review letters, 109(23):235002–235002.

[Weichman and Petrich, 2001] Weichman, P. B. and Petrich, D. M. (2001). Statistical equilibrium solutions of the shallow water equations. Physical Review Letters, 86(9):1761.

[Welander, 1955] Welander, P. (1955). Studies on the general development of motion in a two-dimensional, ideal fluid. Tellus, 7(2):141–156.

[Whitaker and Turkington, 1994] Whitaker, N. and Turkington, B. (1994). Maximum entropy states for rotating vortex patches. Physics of Fluids, 6:3963.

[Wikipedia, 2013b] Wikipedia (08/07/2013b). Wikipedia:probabilite stationnaire d une chaine de markov.

[Wikipedia, 2013a] Wikipedia (10/07/2013a). Wikipedia:five-point stencil.

[Zandbergen and Dijkstra, 1987] Zandbergen, P. and Dijkstra, D. (1987). Von kármán swirling flows. Annual review of fluid mechanics, 19(1):465–491.

[Zeldovich, 1957] Zeldovich, Y. B. (1957). The magnetic field in the two-dimensional motion of a conducting turbulent fluid. Sov. Phys. JETP, 4:460–462.